



## 저작자표시-비영리-변경금지 2.0 대한민국

이용자는 아래의 조건을 따르는 경우에 한하여 자유롭게

- 이 저작물을 복제, 배포, 전송, 전시, 공연 및 방송할 수 있습니다.

다음과 같은 조건을 따라야 합니다:



저작자표시. 귀하는 원저작자를 표시하여야 합니다.



비영리. 귀하는 이 저작물을 영리 목적으로 이용할 수 없습니다.



변경금지. 귀하는 이 저작물을 개작, 변형 또는 가공할 수 없습니다.

- 귀하는, 이 저작물의 재이용이나 배포의 경우, 이 저작물에 적용된 이용허락조건을 명확하게 나타내어야 합니다.
- 저작권자로부터 별도의 허가를 받으면 이러한 조건들은 적용되지 않습니다.

저작권법에 따른 이용자의 권리는 위의 내용에 의하여 영향을 받지 않습니다.

이것은 [이용허락규약\(Legal Code\)](#)을 이해하기 쉽게 요약한 것입니다.

[Disclaimer](#)

공학박사 학위논문

# **Novel synthesis of heteroatoms-doped carbons using one-pot chlorination process:**

**Understanding the synthesis-structure-property  
relationship of CNB and M-CNB materials**

탄질화물, 붕화물 및 전이금속 전구체의 단일  
염소반응 공정을 통한 고기능성 이종원소 치환  
다공성 탄소소재 합성 및 응용과 열역학을 통한  
구조 제어 인자의 이해

2021 년 2 월

서울대학교 대학원

재료공학부

하 대 권 (河 大 權)

**Novel synthesis of heteroatoms-doped  
carbons (CNB and M-CNB) using one-pot  
chlorination process: Understanding the  
structure controlling factor via thermodynamic**

지도 교수 정 인 호

이 논문을 공학박사 학위논문으로 제출함  
2021 년 02 월

서울대학교 대학원  
재료 공 학 부  
하 대 권

하대권의 공학박사 학위논문을 인준함  
2021 년 02 월

위 원 장 박 중 래

부위원장 정 인 호

위 원 이 관 형

위 원 백 중 범

위 원 연 순 화

# **Abstract**

## **Novel synthesis of heteroatoms-doped carbons using one-pot chlorination process: Understanding the synthesis-structure-property relationship of CNB and M-CNB materials**

Dae-Gwon Ha

Department of Materials Science and Engineering

The Graduate School

Seoul National University

The introduction of heteroatoms to the porous carbon materials is one of the most effective strategies to boost the surface reactivity of the porous carbon materials for energy and environment applications. The doping of nitrogen atom to the carbon structure has been studied extensively in the past decades, and the co-doping of other heteroatoms, including boron and transition metals to nitrogen-doped carbon(CN) has gained great interest to enhance the surface reactivity of CN. However, there is still a lack of research for the development of the facile synthetic methodology to the synthesis of the heteroatoms co-doped porous carbon materials based on the comprehensive understanding of the synthesis-structure-property relationship.

The conventional carbide-derived carbon (CDC) synthesized via the chlorination process is one of the representative methods for producing the nanoporous carbon using the selective extraction of the metal or metalloid atom in



the carbide lattice. The CDC is favorable to synthesizing highly nanoporous structure as well as controlling the nano-pore size. However, to extract the metal atom, a reactive etchant, such as the halogen element ( $\text{Cl}_2$ ), is required inevitably; thus, it is challenging to incorporate the heteroatom component into carbon structure. Previously, our research group has demonstrated the availability of the chlorination process to produce heteroatoms-doped (nitrogen and boron) porous carbon materials. However, it is still insufficient to apply the chlorination process to synthesize the high functional heteroatoms-doped porous carbon materials.

In this thesis, new approaches to the development of heteroatom-doped porous carbon materials synthesis, which is based on the thermodynamic and experiments are introduced. The critical factors that decide 1) the incorporation of the h-BN phase in the porous carbon in the synthesis of the CNB and 2) the atomic dispersion of metals in the synthesis of the M-CNB via the chlorination method and pyrolysis method are predicted by the thermodynamic calculations and demonstrated by the experiments. The structure and composition of CNB and M-CNB materials can be precisely controlled by the synthetic parameters such as the raw powder composition and heat-treatment temperature.

In the first part, we focus on the development of the novel synthetic route to synthesizing B-C-N materials using one-pot chlorination of  $\text{Ti}(\text{C}_{1-x}\text{N}_x)\text{-TiB}_2$  mixture. The influence of boron during the formation process of the boron-doped porous carbon (CB) and boron and nitrogen co-doped porous carbon (CNB) is discussed. Boron content supplied from  $\text{TiB}_2$ . It is demonstrated that boron atoms supplied into the carbon structure by the solid-state diffusion serve as the carbon structure linker as well as the dopant. Thus, boron atoms facilitate the development of the

heteroatoms-rich carbon layer, which can effectively enhance the electrocatalytic activity. The oxygen-rich carbon layer in CB and nitrogen-rich carbon shell in CNB result in the increase in the  $2e^-$  pathway and  $4e^-$  pathway oxygen reduction reaction (ORR) performance.

Furthermore, we successfully synthesized BN nanodomains embedded porous carbon by the one-pot chlorination of nitrogen-rich  $Ti(C,N)-TiB_2$ . The formation of h-BN phase and the influence of boron to CN structure are predicted using the thermodynamic calculations. Based on the calculations, the facile synthesis method (direct bond method) that maximizes the contactability of  $Ti(C,N)$  and  $TiB_2$  (C, N, and B precursors, respectively) is introduced. Supplied boron atoms serve as the carbon structure linker as well as the BN formation source, which is the key to the significant development of the h-BN-carbon interface. The abundant h-BN-carbon interfaces in highly porous carbon structure significantly improve the electrocatalytic activity of  $2e^-$  pathway ORR performance. Thus, the h-BN nanodomains embedded porous carbon shows outstanding operation performance in the custom-made full flow cell.

In the second part, we discuss the novel synthesis method for atomically dispersed M-CNB (M= Fe and Ni) via the one-pot chlorination of  $Ti(C,N)-TiB_2-M(acac)_x$  (M= Fe and Ni) mixture. The addition of boron to M (M= Fe and Ni)-CNB causes the formation of metal boride nanoparticles, which is predicted by thermodynamic calculation and demonstrated by the experiments. The formation of boride nanoparticles greatly changes the melting temperature of nanoparticles, which is a major parameter that determines the atomic dispersion of metal in the porous carbon structure. It is revealed that the introduction of boron facilitates the single Fe

atom dispersion in the Fe-CNB system. Hence, Fe-CNB shows superior ORR performance. In contrast, in the Ni-CNB, doping boron is detrimental for the atomic dispersion of Ni, rather intensifies the graphitization of the Ni-CNB, unhelpful to the electrocatalytic properties.

Finally, the novel synthesis method for atomically dispersed M-CNB (M= Fe and Ni) via the one-pot pyrolysis of polyethylene glycol-urea-boric acid-metal nitrate (Fe and Ni) is investigated. It is demonstrated that the addition of boric acid results in the formation of a liquid boron oxide protective layer. The liquid boron oxide layer induces the formation of the heteroatoms-doped carbon nanotube and inhibits the formation of the metal-based nanoparticles during the pyrolysis process, which is predicted by the thermodynamic calculation and verified by the experiments. Metal contents (Fe and Ni) readily incorporates into micro- and mesoporous CNB. Thus, M-N<sub>x</sub> active sites are well-developed in M-CNB (Fe and Ni), and Fe-CNB and Ni-CNB show the excellent electrocatalytic activity for the oxygen reduction reaction (ORR) and CO<sub>2</sub> reduction reaction (CO<sub>2</sub>RR).

All these results can provide the guidelines for the synthesis of the high functional heteroatoms-doped porous carbon materials, which can be used to various applications, including energy and environment.

---

**Keywords:** carbide derived carbon, chlorination process, pyrolysis process, boron and nitrogen co-doped porous carbon, M-N<sub>x</sub> embedded porous carbon, atomic dispersion of metal, oxygen reduction reaction.

**Student number:** 2013-20630

# Table of contents

<b>Abstract.....</b>	<b>iii</b>
<b>List of Tables.....</b>	<b>xi</b>
<b>List of Figures.....</b>	<b>xii</b>
<b>Chapter 1. Introduction .....</b>	<b>1</b>
1.1. Demand for functional porous carbon materials for a sustainable society	
1	
1.2. Issue in porous carbon materials .....	6
1.3. Objectives of the thesis.....	1 8
1.4. Organization of the thesis .....	2 3
<b>Chapter 2. General background .....</b>	<b>2 5</b>
2.1. Carbide derived carbon (CDC).....	2 5
2.2. Role of boron in carbon structure.....	3 9
2.3. Borocarbonitrides (BCN) material.....	4 2
2.4. Graphitization .....	4 9
2.5. Pore structure.....	5 2
2.6. Electrochemistry.....	5 7
2.7. Thermodynamic tools .....	6 9
<b>Chapter 3. Experimental .....</b>	<b>7 4</b>
3.1. Chlorination.....	7 4
3.2. Preparation of CB/CNB materials via the one-pot chlorination process	7
5	
3.3. Preparation of BN embedded porous carbon via one-pot chlorination	
process .....	7 8
3.4. Preparation of M-CN/CNB materials via the one-pot chlorination process	
8 0	
3.5. Preparation of M-CN/CNB materials via the one-pot pyrolysis process	8

3.6. Characterization.....	8 3
3.7. Thermodynamic calculation .....	8 9
3.8. Oxidation stability .....	9 1

## **Chapter 4. Synthesis of heteroatoms (B, N, and O) doped carbon via one-pot chlorination process ..... 9 2**

4.1. Research highlight .....	9 2
4.2. Introduction .....	9 3
<b>4.3. Structural variation of CBs and CNBs .....</b>	<b>9 7</b>
<b>4.4. Surface chemistry variation of CBs and CNBs .....</b>	<b>1 0 4</b>
<b>4.5. Oxidation stability of CBs and CNBs .....</b>	<b>1 0 6</b>
<b>4.6. Influence of boron in CBs and CNBs .....</b>	<b>1 0 7</b>
<b>4.7. Electrocatalytic properties of CBs and CNBs for oxygen reduction reaction.....</b>	<b>1 1 1</b>
4.8. Conclusions .....	1 2 1

## **Chapter 5. Synthesis of BN embedded porous carbon via one-pot chlorination process and its application for the H<sub>2</sub>O<sub>2</sub> production 1 2 3**

5.1. Research highlight .....	1 2 3
5.2. Introduction .....	1 2 4
<b>5.3. Thermodynamic analysis on the chlorination reaction of carbonitride and boride mixture.....</b>	<b>1 2 8</b>
<b>5.4. Challenging in h-BN implant in porous carbon substrate .....</b>	<b>1 3 2</b>
<b>5.5. Variation of D-BNC characteristics with chlorination temperature 1 3 4</b>	
<b>5.6. Variation of D-BNC characteristics with raw powder composition 1 4 7</b>	
<b>5.7. Formation mechanism of BNC .....</b>	<b>1 5 3</b>
<b>5.8. Oxygen reduction reaction performance of D-BNC .....</b>	<b>1 5 5</b>
5.9. Conclusions .....	1 6 1

<b>Chapter 6. Synthesis of atomically dispersed metal-CNB via one step chlorination.....</b>	<b>1 6 3</b>
6.1. Research highlight.....	1 6 3
6.2. Introduction .....	1 6 4
<b>6.3. The ORR activity of Fe-CN/CNB and Ni-CN/CNB.....</b>	<b>1 6 7</b>
<b>6.4. Structural variation of Fe-CN/CNB and Ni- CN/CNB.....</b>	<b>1 6 9</b>
<b>6.5. Formation of metal-based particles during the synthetic process of Fe-CN/CNB and Ni-CN/CNB .....</b>	<b>1 7 9</b>
<b>6.6. Thermodynamic calculation for the chlorination process .....</b>	<b>1 8 3</b>
<b>6.7. Phase diagrams for the nano-sized M-C and MxB-C systems. 1 8 7</b>	<b>1 8 7</b>
<b>6.8. The proposed formation mechanism of Fe-CNB and Ni-CNB 1 9 1</b>	<b>1 9 1</b>
6.9. Conclusions .....	1 9 4
<b>Chapter 7. Synthesis of atomically dispersed M (Fe or Ni)-CNB via one-pot pyrolysis method .....</b>	<b>1 9 6</b>
7.1. Research highlight.....	1 9 6
7.2. Introduction .....	1 9 7
<b>7.3. Structural analysis of Fe-CN/CNB.....</b>	<b>1 9 9</b>
<b>7.4. Chemical configuration of Fe-CN/CNB .....</b>	<b>2 0 7</b>
<b>7.5. Effect of boric acid for atomic dispersion of Fe in CNB .....</b>	<b>2 1 0</b>
<b>7.6. Proposed formation mechanism of Fe-CNB.....</b>	<b>2 2 0</b>
<b>7.7. Electrocatalytic performance evaluation.....</b>	<b>2 2 2</b>
<b>7.8. Synthesis of Ni-CNB .....</b>	<b>2 2 3</b>
7.9. Conclusions .....	2 2 9
<b>Chapter 8. Overall Conclusion.....</b>	<b>2 3 0</b>
8.1. Summary of results.....	2 3 0
8.2. Original contribution .....	2 3 5
8.3. Future suggestion.....	2 3 7
<b>Reference.....</b>	<b>i</b>
<b>요약 (국문 초록).....</b>	<b>xxviii</b>

<b>Appendix .....</b>	<b>xxxiii</b>
-----------------------	---------------

## List of Tables

- Table 2.1.** Thermodynamic electrode potentials of ORR electrode.
- Table 4.1.** The yield, BET SSA and pore volumes of C, CBs, CN, and CNBs
- Table 4.2.** The chemical composition of C, CBs, CN and CNBs measured via XPS.  
The values in the parentheses are for bulk compositions taken by ICP measurement for B.
- Table 4.3.** Observed the separation of anodic/cathodic peak potential( $\Delta E_p = E_{pa} - E_{pc}$ ), dimensionless rate parameter ( $\Psi$ ), and electron transfer constants ( $k^0$ ) of CBs and CNBs.
- Table 5.1.** The chemical composition of D-BNCs measured by XPS.
- Table 5.2.** Summary of the content of bond configuration of D-BNCs.
- Table 5.3.** BET SSA and pore volumes of D-BNCs
- Table 5.4.** The chemical composition of D-BNC-700s measured by XPS and N/C ratio calculated by XPS and EA
- Table 5.5.** Summary of the content of bond configuration of D-BNC-700-LB and -HB
- Table 5.6.** The BET SSA and pore volumes of BNC-700s
- Table 6.1.** BET specific surface area and pore volumes of CN, CNB, Fe-CN, Fe-CNB, Ni-CN, Ni-CNB
- Table 7.1.** BET specific surface area and pore volumes of Fe-CNB and Fe-CN
- Table 7.2.** The composition of Fe-CNB(20)-950 and Fe-CN-950 measured by XPS analysis
- Table 7.3.** BET specific surface area and pore volumes of Ni-CNB(20)-950 and Ni-CN-950.



## List of Figures

**Figure 1.1.** Molecular models of different types of  $sp^2$ -like hybridized carbon nanostructures exhibiting different dimensionalities, 0D, 1D, 2D and 3D:

**Figure 1.2.** Various applications of carbon materials.

**Figure 1.3.** Schematic of a sustainable energy landscape based on electrocatalysis.

**Figure 1.4.** Schematic illustration of functional strategies and applications of porous carbon materials.

**Figure 1.5.** The research trend of heteroatoms-doped porous carbon

**Figure 1.6.** Schematic illustrate the changes of surface free energy and specific activity per metal atom with metal particle size and the support effects.

**Figure 1.7.** Endowing the functionalities to hierarchical porous carbon materials.

**Figure 1.8.** The major parameters that determining the electrocatalytic properties of porous carbon materials.

**Figure 1.9.** The research scope of this thesis about the functional porous carbon materials.

**Figure 1.10.** The research scope of this thesis about the functional porous carbon materials.

**Figure 1.11.** Overview of the thesis

**Figure 2.1.** Transmission electron microscopy images of various CDC structures as obtained from carbide chlorination and vacuum decomposition of SiC:

**Figure 2.2.** Synthesis of CDC by the chlorination of binary carbide.

**Figure 2.3.** Schematic of the atomic structure of  $Ti_3SiC_2$  (a) and 3C-SiC (b) and

the corresponding CDC structures after halogenation.

**Figure 2.4.** Pore size distribution, calculated according to NLDFT method by using the so-called slit-shaped pores model, for different micro- and mesoporous carbide-derived carbon materials.

**Figure 2.5.** Average pore sizes for selected binary and ternary carbides

**Figure 2.6.** a-e) TEM images of TiC-CDCs obtained by chlorination at various temperatures. f-i) Slab of 2 nm thickness of simulated TiC-CDCs after annealing at T1= 1500 K, T2 = 2000 K, T3 = 3000 K, T4 = 4000 K and T5 = 4500 K. Red, green and blue spheres denote sp, sp<sup>2</sup>, and sp<sup>3</sup> bonding, respectively.

**Figure 2.7.** Timeline of synthesis of heteroatoms-doped carbon materials using chlorination process.

**Figure 2.8.** The schematic presentation of BC<sub>x</sub> materials (left) top view and (right) side view. [2.47]

**Figure 2.9.** Molecular models showing the effect of intercalated B atoms between SWNTs.

**Figure 2.10.** The expected band structure of B/C/N materials. [2.56]

**Figure 2.11.** a) Schematics of three compositions BC<sub>7</sub>N<sub>2</sub> (I), B<sub>2</sub>C<sub>2</sub>N<sub>2</sub> (II), and BC<sub>8</sub>N (III), along with their symmetrically inequivalent configurations. C (black), B (green), and N (red). b1) DOS for four configurations of BC<sub>7</sub>N<sub>2</sub> (I). b2) Projected DOS of Ia. b3) DOS of IIIa and IIIb configurations of BC<sub>8</sub>N. b4) Projected DOS of II configuration of B<sub>2</sub>C<sub>2</sub>N<sub>2</sub>. c) Study of the effect of BN and the CN domains on HER activity of B<sub>x</sub>C<sub>y</sub>N<sub>z</sub>. Schematic of B<sub>2</sub>C<sub>6</sub>N<sub>2</sub> (IV), (b) B<sub>2</sub>C<sub>5</sub>N<sub>3</sub> (V) (C–N ring is marked by black circle) and their

corresponding DOS. d) The comparison of the Fermi energies and HER energy level with the conduction and valence band edge positions. Valence band and conduction band is denoted by black and red, respectively. Green dots are the Fermi levels.

**Figure 2.12.** Schematic diagram of Chemical vapor deposition (CVD) method and pyrolysis method.

**Figure 2.13.** Overall crystallization stages of cokes.

**Figure 2.14.** Diagrams of dissolution-precipitation mechanism (a) and decomposition of metal carbides mechanism (b) of catalytic graphitization.

**Figure 2.15.** IUPAC classification of (a) physisorption isotherms (x-axis: relative pressure ( $p/p_0$ ) and y-axis: amount of adsorbate (V) and (b) hysteresis loops of adsorbent materials.

**Figure 2.16.** Ellingham diagram for considering the standard Gibbs free energy of various oxide compounds according to the temperature.

**Figure 2.17.** The electrochemical reduction reaction in the cathode with the change of electron energy of the electrode.

**Figure 2.18.** The charge transfer and mass transfer at the surface of electrode.

**Figure 2.19.** The electrochemical reaction in electrolytic cell.

**Figure 2.20.** The current variation with the potential in the cathode and anode in electrolytic cell.

**Figure 2.21.** The electrochemical reaction in Galvanic cell.

**Figure 2.22.** The current variation with the potential in the cathode and anode in Galvanic cell.

**Figure 2.23.** Proposed pathways for ORR. (black spheres: catalyst atoms; red

spheres: oxygen atoms; white spheres: hydrogen atoms; yellow arrows: O–O bond cleavage; and blue arrows: the proton or electron transfer.)

**Figure 2.24.** Volcano plots for metal ORR catalysts (a), and for heteroatoms-doped graphene catalysts.

**Figure 2.25.** The derivation of phase diagram of binary system (left) from the minimum Gibbs free energy assemblage of given system in equilibrium condition (right).

**Figure 2.26.** Ellingham diagram for considering the standard Gibbs free energy of various oxide compounds according to the temperature.

**Figure 3.1.** Schematic diagram representing chlorination reactor setup.

**Figure 3.2.** The heating schedule of the chlorination process to synthesize the porous carbon materials.

**Figure 3.3.** The heating schedule of the pyrolysis process to synthesize the porous carbon materials.

**Figure 4.1.** Boron doping methods used in the present study.

**Figure 4.2.** TEM images of C (a), G-CB (b), D-CB (c), CN (d), G-CNB (e), D-CNB (f).

**Figure 4.3.** TEM images and of C (a-c), G-CB(e-g), and D-CB (i-k) and HR TEM image of C (d), G-CB (h), and D-CB (l).

**Figure 4.4.** TEM images and of CN (a-c), G-CNB, (e-g), and D-CNB (i-k) and HR-TEM images of CN (d), G-CNB (h), and D-CNB (l).

**Figure 4.5.** FE-SEM images of C (a), G-CB (b), D-CB (c), CN (d), G-CNB (e), and D-CNB (f).

**Figure 4.6.** XRD patterns of C and CBs (a), CN and CNBs (b). Raman spectra of

C and CBs (c), CN and CNBs (d). ID/IG values of C, CBs, CN, and CNBs (e)

**Figure 4.7.** N<sub>2</sub> sorption isotherm of C and CBs (a) CN and CNBs (b). The pore size distribution (PSD) of C and CBs (c) and CN and CNBs (d).

**Figure 4.8.** Characterization of C and CBs: The oxygen content and oxidation onset potential from DTG analysis (a), and deconvoluted HR XPS spectra of C1s (b). Polarization curves at 1600 rpm (solid lines), H<sub>2</sub>O<sub>2</sub> detection currents at the ring electrode (dashed lines) (c), and the calculated selectivity at 0.1 M KOH (d). Peak potential separation values and heterogeneous electron transfer rate constant (e).

**Figure 4.9.** Characterization of CN and CNBs: The nitrogen/oxygen contents and oxidation onset potential from DTG analysis (a), and deconvoluted HR XPS spectra of C1s (b). Polarization curves at 1600 rpm (solid lines), H<sub>2</sub>O<sub>2</sub> detection currents at the ring electrode (dashed lines) (c), and the calculated selectivity at 0.1 M KOH (d). Peak potential separation values and heterogeneous electron transfer rate constant (e).

**Figure 4.10.** High resolution XPS C 1s spectra of CN (a), G-CNB (b), and D-CNB

**Figure 4.11.** High resolution XPS B1s spectra of G-CNB and D-CNB.

**Figure 4.12.** The distribution of nitrogen species in CN, G-CNB, and D-CNB calculated from deconvolution peaks of N1s spectra.

**Figure 4.13.** TG curve of C and CBs (a), and CN and CNBs (b), and DTG analysis (c, d) of the C, CN, CBs, and CNBs.

**Figure 4.14.** Average shell thickness of CN, G-CNB, and D-CNB

**Figure 4.15.** Tafel plots of the CB and CNB carbons for oxygen reduction reaction. The numbers represent the Tafel slopes.

**Figure 4.16.** Cyclic voltammetry of the C and CN series carbons; C (a), G-CB (b), D-CB (c), CN (d), G-CNB (e), and D-CNB (f), measured in Ar-saturated 1 mM  $[\text{Ru}(\text{NH}_3)_6]\text{Cl}_2$ + 0.1 M KCl electrolytes at a scan rate of  $50 \text{ mV s}^{-1}$ .

**Figure 4.17.** ORR mechanism on CDC-CB and CDC-CNB carbons in alkaline medium. The nitrogen-doped sites of D-CNB, especially pyridinic N, can mostly catalyze direct  $4\text{e}^-$  and  $(2\text{e}^-+2\text{e}^-)$  ORR mechanism. In the other hand, the oxygen-rich defective sites of D-CB, induced by boron atoms in CDC-process, can facilitate the outer-sphere electron transfer and boost  $2\text{e}^-$  ORR kinetics.

**Figure 4.18.** ORR curves of D-CNB and Pt/C 20wt.% (Johnson Matthey) in  $\text{O}_2$ -saturated 0.1 M KOH electrolyte with  $5 \text{ mV s}^{-1}$  on 1600 rpm.

**Figure 5.1.** Thermodynamic calculations for the chlorination of titanium carbonitride and boride mixture. The synthesized products varying with amount of  $\text{Cl}_2$  in  $\text{Ti}(\text{C}_{0.3},\text{N}_{0.7})\text{-TiB}_2$  system (a),  $\text{Ti}(\text{C}_{0.3},\text{N}_{0.7})$  system (b) at  $700^\circ\text{C}$ . Thermodynamic calculations for the  $\text{Ti}(\text{C}_{0.3},\text{N}_{0.7})\text{-TiB}_2$  system (a),  $\text{Ti}(\text{C}_{0.3},\text{N}_{0.7})$  system (b) at  $800^\circ\text{C}$  and identical calculations for the  $\text{Ti}(\text{C}_{0.3},\text{N}_{0.7})\text{-TiB}_2$  system (c),  $\text{Ti}(\text{C}_{0.3},\text{N}_{0.7})$  system (d) at  $600^\circ\text{C}$  (Synthesized products vs. mole of  $\text{Cl}_2$ ).

**Figure 5.2.** Synthesized products varying with the chlorination temperature at the  $\text{Cl}_2$  to precursors ( $\text{Ti}(\text{C}_{0.3},\text{N}_{0.7})\text{-TiB}_2$ ) molar ratio of 1:1 (a) 2:1 (b), and 5:1(c).

**Figure 5.3.** TEM images of D-BNC-600 (a-c), D-BNC-700 (e-g), and D-BNC-800 (i-k). HR-TEM images of D-BNC-600 (d), D-BNC-700 (h), and D-BNC-800 (l)

- Figure 5.4.** TEM images of D-BNC-400 (a-c) and D-BNC-1000 (e-g). HR-TEM images of D-BNC-400 (d) and D-BNC-1000 (h).
- Figure 5.5.** FE-SEM images of D-BNC-600 (a), -700 (b), and -800 (c).
- Figure 5.6.** XRD of D-BNCs varying with the chlorination temperature.
- Figure 5.7.** HR-XPS B 1s spectra of D-BNC-600 (a), D-BNC-700 (b), D-BNC-800 (c) and N 1s spectra of D-BNC-600 (d), D-BNC-700 (e), D-BNC-800 (f). NXANES spectra of N-K edge (g) and B-K edge (h) for D-BNC-600, 700, and 800, CN-800, and bulk BN (ref.).
- Figure 5.8.** High resolution (HR) XPS C 1s spectra of D-BNC-600 (a), D-BNC-700 (b), and D-BNC-800 (c).
- Figure 5.9.** Elemental mapping of boron(a), carbon (a), and nitrogen (c), and EELS spectrum (d) of D-BNC-700.
- Figure 5.10.** High resolution XPS B 1s spectra of D-BNC-400 (a) and D-BNC-1000 (b), N 1s spectra of D-BNC-400 (c) and D-BNC-1000 (d), and C1s spectra of D-BNC-400 (e) and D-BNC-1000 (f).
- Figure 5.11.** FT-IR spectrum of D-BNCs.
- Figure 5.12.** The N<sub>2</sub> sorption isotherm (a) and pore size distribution (b) of D-BNCs.
- Figure 5.13.** TEM image of D-BNC-700-LB (a-c), D-BNC-700-HB (e-g). HR-TEM images of D-BNC-700-LB (d) and D-BNC-700-HB (h).
- Figure 5.14.** FE-SEM images of D-BNC-700-LB (a) and D-BNC-700-HB (b).
- Figure 5.15.** XRD of D-BNC-700-LB and -HB.
- Figure 5.16.** High resolution XPS B 1s spectra of D-BNC-700-LB (a) and D-BNC-700-HB (b), N 1s spectra of D-BNC-700-LB (c) and D-BNC-HB (d), and C1s spectra of D-BNC-700-LB (e) and D-BNC-700-HB (f).
- Figure 5.17.** The N<sub>2</sub> sorption isotherm (a) and pore size distribution (b) of D-BNC-

700s.

**Figure 5.18** The scheme of the formation mechanism of D-CNBs.

**Figure 5.19.** Polarization curves (solid lines) and simultaneous  $\text{H}_2\text{O}_2$  detection current at the ring electrode (dashed lines) at 1600 rpm with D-BNC materials, which were heat-treated under different temperature with  $\text{Cl}_2$  (a). Calculated selectivity for  $\text{H}_2\text{O}_2$  production of samples (b), and the stability measurement of D-BNC-700 samples at 0.1 M KOH electrolyte (c). Imaginary capacitances plot for the complex capacitance analysis from EIS measurement (d). Digital images of our custom-made  $\text{H}_2\text{O}_2$  electrosynthetic flow cell (e) and  $\text{H}_2\text{O}_2$  generation performance in 1.0 M KOH electrolyte (f).

**Figure 5.20.** Nyquist plots of EIS results (a), and real capacitances plot for the complex capacitance analysis (b).

**Figure 5.21.** ORR polarization curves (a) and the selectivity for  $\text{H}_2\text{O}_2$  production (b) of D-BNC-700s using RRDE setup heat-treated at 700 °C.

**Figure 5.22**  $\text{H}_2\text{O}_2$  generation performance of D-BNC-700 in the custom-made flow cell with the neutral 1.0 M  $\text{Na}_2\text{CO}_3$  electrolyte.

**Figure 6.1.** ORR activity comparison between (a) Fe-CN and Fe-CNB, and (b) Ni-CN and Ni-CNB in 0.1 M KOH. The measurements were conducted with the electrode rotation of 1600 rpm.

**Figure 6.2.** TEM images of (a,b) CN, (c-h) Fe-CN.

**Figure 6.3.** TEM images of Ni-CN.

**Figure 6.4.** TEM images of (a-c) Fe-CNB and (d-f) Ni-CNB.

**Figure 6.5.** XRD patterns of (a) CN, CNB, Fe-CN, and Fe-CNB, and (b) Ni-CN and Ni-CNB.



**Figure 6.6.** RDFs of FT k3-weighted (a) Fe K-edge EXAFS spectra of Fe-CN and Fe-CNB and (b) Ni K-edge EXAFS spectra of Ni-CN and Ni-CNB.

**Figure 6.7.** N<sub>2</sub> sorption isotherm of (a) CN, Fe-CN, and Ni-CN, and (b) CNB, Fe-CNB, and Ni-CNB. The pore size distribution (PSD) of (c) CN, Fe-CN, and Ni-CN, and (d) CNB, Fe-CNB, and Ni-CNB.

**Figure 6.8.** TEM images of just before chlorination (800 °C, Ar, 0 m) of (a,b) Fe-CNB and (c,d) Ni-CNB.

**Figure 6.9.** Ellingham diagram for the oxidation tendency of C and various metal (Fe, Ni, and Co):  $2C + O_2 = 2CO$ ,  $CO + O_2 = 2CO_2$ , and  $2M + O_2 = 2MO$ .

**Figure 6.10.** Thermodynamic calculation for chlorination of M-CN. FeO-CN (a,b), Fe-CN (c,d), and Ni-CN (e,f).

**Figure 6.11.** Thermodynamic calculation for chlorination of M-CNB. FeO-CNB (a,b), Fe-CNB (c,d), and Ni-CNB (e,f).

**Figure 6.12.** The existence of nickel boride particle (Ni<sub>3</sub>B) observed by TEM analysis.

**Figure 6.13.** Phase diagrams of (a) Ni-C system, (b) Ni<sub>2</sub>B-C, (c) Ni<sub>3</sub>B-C system: bulk (black solid line), 50 nm (blue dashed line), and 10 nm (red dashed line)

**Figure 6.14.** Phase diagrams of (a) Fe-C and (b) Fe<sub>2</sub>B-C: bulk (black solid line), 50 nm (blue dashed line), and 10 nm (red dashed line)

**Figure 6.15.** The proposed formation mechanism of Fe-CNB and Ni-CNB.

**Figure 7.1.** TEM images (a,b,c), HR-TEM image (d), and SEM images (e,f) of Fe-CNB(20)-950.

**Figure 7.2.** HADDF image (a) and EDS elemental mapping images (b-f) of Fe-CNB(20)-950.

**Figure 7.3.** TEM images (a,b), HR-TEM image (c), HADDF images (d), and SEM images (e,f) of Fe-CN-950.

**Figure 7.4.** The optical images of Fe-CNB(20)-950 (left) and Fe-CN (right) that obtain to investigate the magnetism using magnet.

**Figure 7.5.** The XRD patterns of Fe-CNB(20)-950 and Fe-CN-950.

**Figure 7.6.** The N<sub>2</sub> sorption isotherm (a) and pore size distribution (b) of Fe-CNB and Fe-CN

**Figure 7.7.** The wide scan XPS spectra of Fe-CNB(20)-950 and Fe-CN-950 (a). HR-B1s XPS spectra of Fe-CNB(20)-950 (b). HR-XPS N1s spectra (c) and F2p spectra (d) of Fe-CNB(20)-950 and Fe-CN-950.

**Figure 7.8.** The XRD patterns of Fe-CNB(5)-950 and Fe-CNB(1)-950.

**Figure 7.9.** The BET specific surface area, boron, and nitrogen content of Fe-CN-950 and Fe-CNB(1, 5, and 20)-950 (a), and the content of deconvoluted peaks in N1s and B1s XPS of Fe-CN-950 and Fe-CNB(1, 5, and 20)-950, calculated by the peak area.

**Figure 7.10.** Phase diagram of the Fe-B<sub>2</sub>O<sub>3</sub> system at (p<sub>O2</sub>=10<sup>-5</sup> atm), calculated from the thermodynamic software.

**Figure 7.11.** Phase diagram of the Fe-B<sub>2</sub>O<sub>3</sub>-O<sub>2</sub> system with oxygen partial pressure at 950 °C, calculated from the thermodynamic software.

**Figure 7.12.** Thermodynamic calculations for the Fe-CN (PEG-urea-Fe) (a) and Fe-CNB(20) (PEG-urea-Fe-B<sub>2</sub>O<sub>3</sub>) (b).

**Figure 7.13.** TEM image (a), HR-TEM image (b), HADDF image (c) of Fe-CN-700-1 min

**Figure 7.14.** TEM images (a-c), HR-TEM image (d), HADDF image (e), and EDS elemental mappings (iron, nitrogen, and boron) (f-h) of Fe-CNB(20)-700-1 min.

**Figure 7.15.** Formation mechanism of Fe-CNB(20)-950 and Fe-CN-950

**Figure 7.16.** LSV curves of CN-950, CNB(20)-950, Fe-CN-950, Fe-CNB(20)-950, and commercial 20 wt.% Pt/C exhibiting ORR activity in 0.1 M KOH. The measurements were conducted with the electrode rotation of 1600 rpm.

**Figure 7.17.** TEM images (a,b), HR-TEM image (c,d), HADDF image (e), and EDS elemental mappings (nickel) (f) of Ni-CN-950

**Figure 7.18.** TEM images (a-c), HR-TEM image (d), HADDF image (e), and EDS elemental mappings (nickel, nitrogen, and boron) (f-h) of Ni-CNB(20)-950

**Figure 7.19.** The XRD patterns of Ni-CNB(20)-950 and Ni-CN-950.

**Figure 7.20.** The N<sub>2</sub> sorption isotherm (a) and pore size distribution (b) of Ni-CNB(20)-950 and Ni-CN-950.

**Figure 7.21.** LSV curves of Ni-CNB(20)-950 and Ni-CN-950 measured in the Ar saturated or CO<sub>2</sub> saturated 0.5 M KHCO<sub>3</sub> electrolyte.

# **Chapter 1. Introduction**

## **1.1. Demand for functional porous carbon materials for a sustainable society**

Carbon is one of the most earth-abundant elements and is one of the key elements proving the basis for life on earth. [1.1] Carbon can form a variety of allotropes in the form of zero to three dimensional, having a unique electronic structure. [1.1,2] Not only limited to graphite and diamond that naturally existed carbon allotropes, starting with the discovery of fullerenes (1985), the era of synthetic carbon allotropes has begun. In particular, the discovery of carbon nanotubes (1991) and the rediscovery of graphene (2004) dramatically expanded the applicability of carbon materials. [1.1, 3, 4] Depending on the type of allotrope, carbon materials can manifest different properties. [1.1, 3, 5] At the same time, the remarkable development of nanotechnology, including the synthetic and observation techniques, has been further increased the commercialization potential of these carbon allotropes. [1.2, 6, 7] For the 21st century, on the basis of these fortuitous discoveries and advent in nanotechnology, various carbon materials are applied to a wide range of academic and industrial fields, briefly described in Figure 1.1 and 1.2.

Meanwhile, after the industrial revolution, the significant development of energy-intensive industries and energy production based the fossil fuel in the 20th century make the remarkable progress of humanity. However, as the cost of this progress, the global environmental problems involving global warming attributed to a significant increase in CO<sub>2</sub> concentration in the atmosphere have threatened the

future of humanity. [1.6, 8] In the 21st century, as industrial development accompanying the improvement of individuals' quality of life expands around the world, the world energy consumption and demand for production of various industrial materials are rapidly increasing by the minute. For example, the world energy consumption incredibly fast increases predicted to double from 13.5 TW in 2001 to 27 TW by 2050 and to triple to 43 TW by 2100. [1.6, 9] Unfortunately, in the current fossil-fuel-based society, it is challenging to achieve both the improvement of quality of life through industrial development for every individual and the survival of humankind at the same time. Therefore, the global agenda of the 21st century is the establishment of a sustainable society. [1.6, 9] Hence, to achieve a sustainable society, many researchers in academia and industries have been struggling to develop a sustainable energy source and the green industries. In line with this, they have also been challenging to develop the advanced materials suitable for new industrial structure and energy sources.

The carbon materials having the versatility and greenness has been recognized as the suitable material for a sustainable society. [1.5, 10, 11] Especially, nanoporous carbon materials have recently been spotlighted as a key material. [1.12] Figure 1.3 showed an overview of the cycle of a sustainable society. One of the main issues in the sustainable society is the decentralized production of clean energy and industrial chemical, which are based the electrochemistry and energy storage. The porous carbon materials have high applicability in electrochemical production, energy storage, filtration, and adsorption. [1.7, 9, 13, 14] Because the nano-pore structure of porous carbon materials is favorable for the interaction with reactant or adsorption

of the adsorbent, also, they have high chemical inertness makes them usable in a variety of mediums. [1.12, 13]

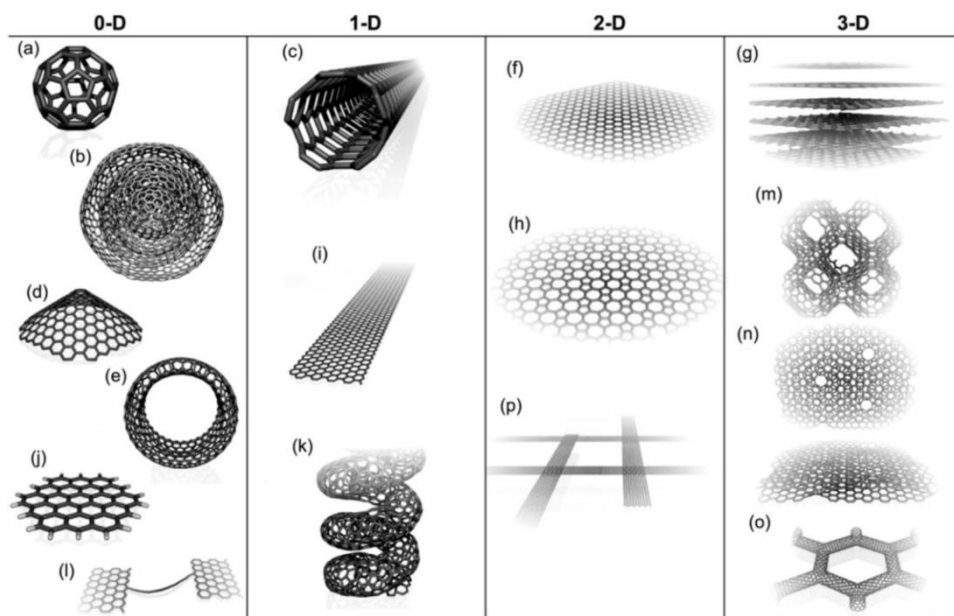


**Figure 1.1.** Molecular models of different types of  $sp^2$ -like hybridized carbon nanostructures exhibiting different dimensionalities, 0D, 1D, 2D and 3D: (a) C<sub>60</sub>: Buckminsterfullerene; (b) nested giant fullerenes or graphitic onions; (c) carbon nanotube; (d) nanocones or nanohorns; (e) nanotoroids; (f) graphene surface; (g) 3D graphite crystal; (h) Haeckelite surface; (i) graphene nanoribbons; (j) graphene clusters; (k) helicoidal carbon nanotube; (l) short carbon chains; (m) 3D Schwarzite crystals; (n) carbon nanofoams (interconnected graphene surfaces with channels); (o) 3D nanotube networks, and (p) nanoribbons 2D networks. [1.15] Copyright 2010, Elsevier.

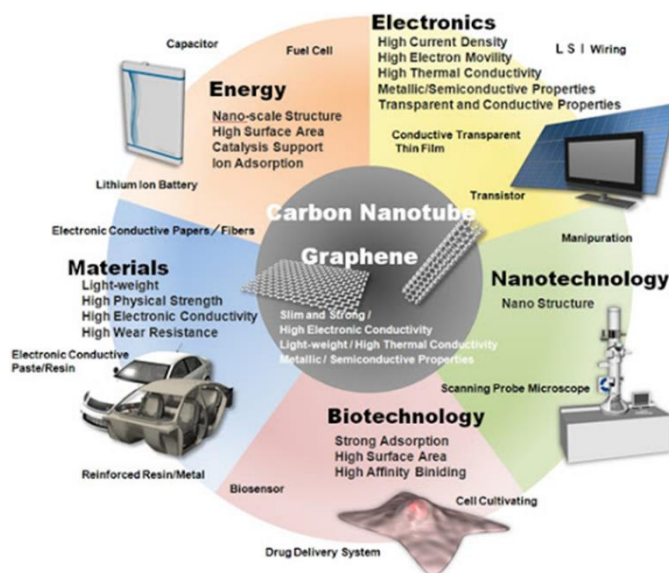


**Figure 1.2.** Various applications of carbon materials. [1.87] Copyright Meijo Nano Carbon.

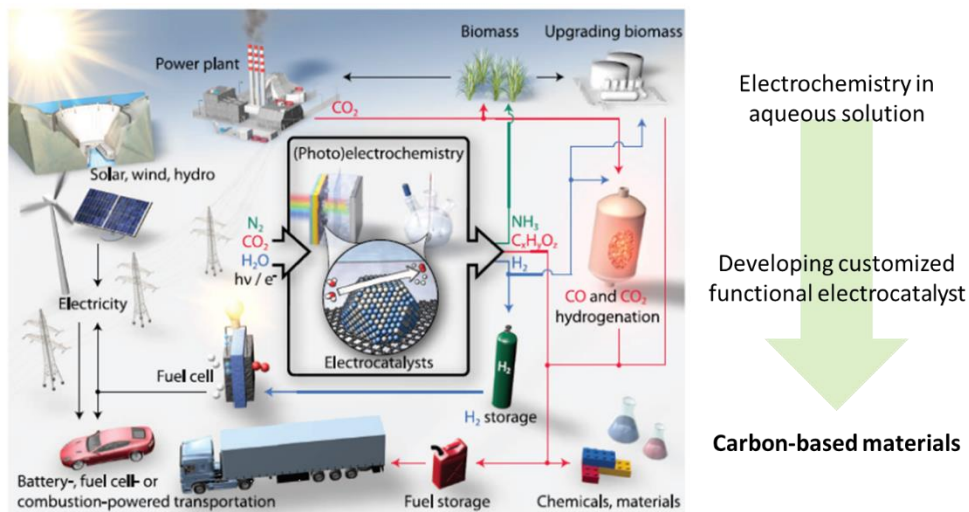


**Figure 1.3.** Schematic of a sustainable energy landscape based on electrocatalysis. [1.6] Copyright 2017, AAAS.



## **1.2. Issue in porous carbon materials**

### **1.2.1. Limitation of pristine porous carbon material**

Pristine porous carbon materials, such as the activated carbon, carbon black, etc., have already been used in certain applications. However, they have the inert surfaces having low activity with reactants, which is the one major drawback of the porous carbon materials for the energy and environmental applications. To overcome this obstruct, many researchers have been focused on the functionalization of porous carbon materials via the various strategies, as shown in Figure 1.4. [1.16, 17] The introduction of heteroatoms species into the pristine carbon materials is one of the most effective strategies that mutates the characteristic of carbon materials. [1.8, 18] For example, pristine graphene is a zero-bandgap semiconductor. The incorporation of guest atoms in graphene opens up the bandgap, which accompanies the variation of electronic properties. [1.19] Thus, tremendous research has been undertaken to apply these modified carbon materials to energy-related applications, and the research trend was briefly summarized in Figures 1.5. Starting with the introduction of the single component, especially nitrogen, into carbon material, the type and number of doping components have been gradually expanding. Recently, the research on the metal species incorporated nitrogen-doped carbon (M-N-C) has been actively conducted since M-N-C materials exhibit a wide range of applicability as the electrocatalyst for the various electrochemical reactions. [1.20, 21]

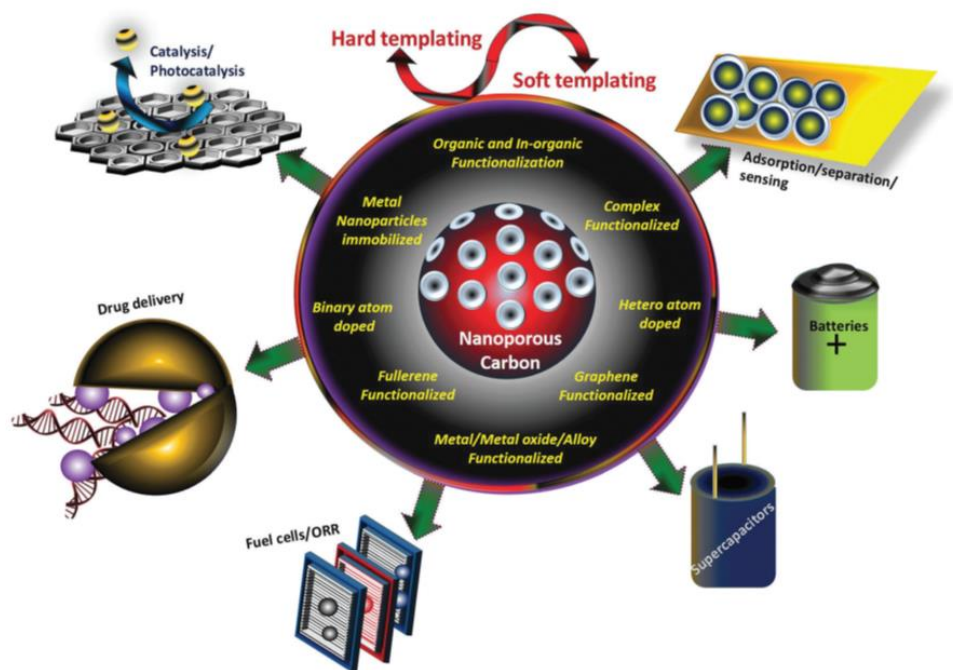


**Figure 1.4.** Schematic illustration of functional strategies and applications of porous carbon materials. [1.7] Copyright 2018, Chemical society review.

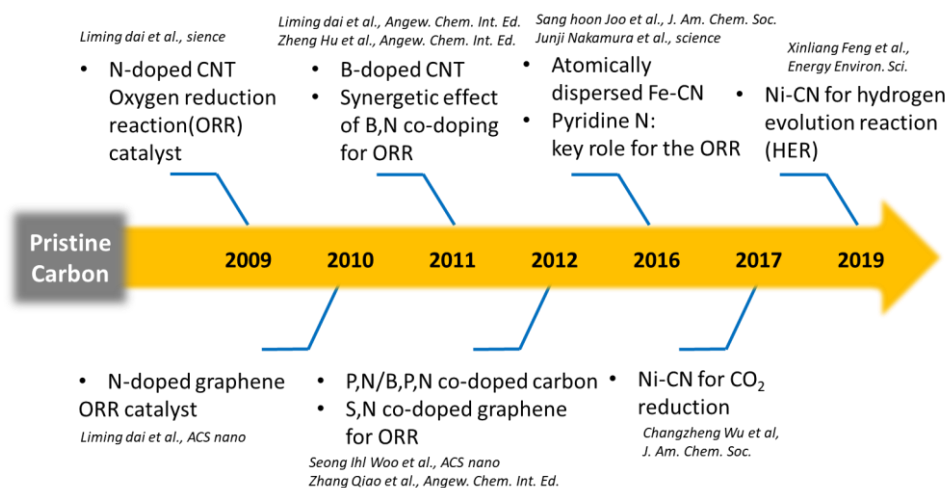


**Figure 1.5.** Timeline showing the research trend of heteroatoms-doped porous carbon.

### 1.2.2. Metal-free heteroatoms doped porous carbon

Among the numerous heteroatoms that can introduce in carbon substrate, the nitrogen is representatives for energy-related applications, and the mono-nitrogen doping strategy is the beginning of doped carbon studies. [1.18] Nitrogen is located right next to carbon in the periodic table, having a similar atomic radius of carbon. Also, its electronegative (3.04) is higher than that of carbon (2.55). [1.18] For these reasons, nitrogen can readily incorporate into the carbon network and induces the local polarization of the carbon network, which can greatly improve the interaction with the reactant or adsorbate. The nitrogen-doped porous carbon (CN) for energy application has been actively studied since Jasinski et al. demonstrated the applicability of N-doped carbon as the electrocatalyst for oxygen reduction reaction (ORR) for the first time in 1964. [1.22] Numerous CN synthetic methods have been reported. Post-treatment of carbon in the nitrogen-containing atmosphere and direct pyrolysis of nitrogen-rich precursors, such as melamine, urea, dicyandiamide, aniline, and pyrrole has been most commonly used. [1.23-27]

Not only the nitrogen, the introduction of other non-metal atoms such as boron, sulfur, and phosphorus to the carbon structure has also been investigated. Among them, boron has been recognized as a highly interesting candidate since it has low electronegativity (2.04) lower than carbon (2.55) and easily incorporated into  $sp^2$ -carbon network. [1.28] Comparing to CN, however, boron-doped porous carbon (CB) has been less studied due to the difficulty in boron doping in the carbon matrix. In general, the boron doping in carbon is required high temperature ( $>1000$  °C) and the material preparation (boron-contained precursors) is quite limited. [1.28-30]

Therefore, further studies are required on the boron effect on C and facile synthesis for CB.

Beyond the mono-atom doping, the co-doping two or three non-metal components tactic has been attempted to achieve to maximize the characteristic variation of carbon materials. The co-doping of boron and nitrogen is most commonly used since boron and nitrogen have the complementary relationship. [1.18, 31] Boron can act as an electron donor, and nitrogen can act as an electron acceptor in the carbon substrate due to the difference of the electronegativity. [1.31] Thus boron and nitrogen play a complementary role when they are substituted into a carbon network simultaneously. [1.31, 32] This synergetic effect triggers a change in the physicochemical properties of the carbon materials. [1.31-33] Thus, boron and nitrogen co-doping porous carbons (CNBs) that show superior optical, electrical, and electrochemical properties have been actively reported. [1.34-37] In most previous studies for CNB synthesis, they mainly focused on the substitution effect of boron and nitrogen in carbon structure to understand the improvement of properties of CNB.

### 1.2.3. Non-precious metal-doped porous carbon

Recently, not only limited to the introduction of non-metallic atoms, the incorporation of metal species into porous carbon materials has been attracted great attention. [1. 17, 38, 39] Notably, many researchers try to introduce the transition metal species into carbon materials since transition metals are cost-effective compared with precious metals. Also, they manifest unique properties that are hard to achieve by nonmetal doped carbon and appropriate to energy-related applications. [1.40-42] In particular, as the size of metal species decreases, their properties can be greatly intensified, shown in Figure 1.6. [1.40-42]

There are two types of TM decorated carbon. One is that the hybridization of TM-based nanoparticles with carbon materials. Various transition metal-based nanoparticles, such as metal, oxide, carbide, nitride, boride, and etc. [1.17, 43-45] They are generally synthesized using the pyrolysis method and show high electrocatalytic performance for the miscellaneous electrochemical reactions. [1.17] The other is that the atomic dispersion of TM in carbon networks, which attracts great interest currently. In particular, atomically dispersed transition metal- $N_x$  ( $M-N_x$ ) embed carbon ( $M-N-C$ ) has been the most actively studied and expected to be a promising electrocatalyst for energy-related applications. [1.4, 18, 46]  $M-N_x$  structure showed the extraordinary electrocatalytic activity, and embedding the  $M-N_x$  moieties into porous carbon support can significantly improve the stability, recyclability, and also performance. [1.18, 40, 47] Because nitrogen can readily incorporate into the carbon support and carbon can construct a strong covalent bond with  $M-N_x$  moieties, which not only stabilizes the  $M-N_x$  moieties but also modifies

the electronic structure of both carbon and M-N<sub>x</sub> moieties to optimize the adsorption and desorption of intermediates for improving catalytic performance. [1.40, 47] Furthermore, the carbon support has a high electrically conductivity enhancing the electron transfer during the electrochemical reaction. [1.40, 47] Depending on the type of transition metal, M-N-C materials can show the extraordinary catalytic performance in the various electrocatalytic reactions including oxygen reduction reaction (ORR) [1.48-53], H<sub>2</sub> evolution reaction (HER) [1.54-56], and CO<sub>2</sub> reduction reaction (CO<sub>2</sub>RR). [1.57-61]

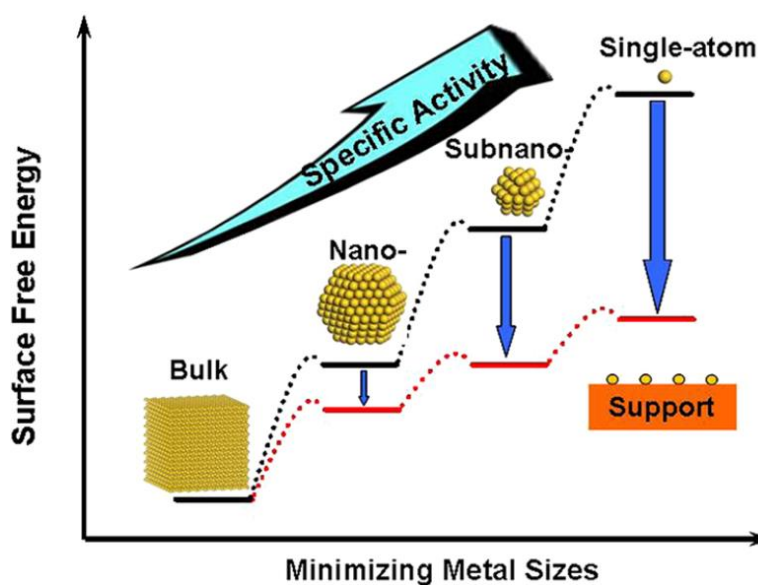


**Figure 1.6.** Schematic illustrate the changes of surface free energy and specific activity per metal atom with metal particle size and the support effects. [1.40] Copyright 2013, ACS Publications.

#### **1.2.4. Synthetic issues in high functional porous carbon material**

As shown in the research trend mentioned above, the introduction of heteroatoms in porous carbon with hierarchical pore structure is one of the mainstreams in porous carbon materials studies, which can endow the specific functionality suitable for each application (Figure 1.7). The research trend moved from doping of the unary system to doping of multi-nary system in porous carbon materials, customized for the specific applications. [1. 2, 7, 18, 62] Numerous studies theoretical studies based on the first-principle calculation demonstrated the relationship between various types of active sites and catalytic activities. [1.14, 18, 63] However, the development of the facile synthetic process to produce robust porous carbon materials is still in an immature stage. To commercialize the heteroatom doped porous carbon material having high functionalities, it is most important to develop the facile synthetic process based on the comprehension of synthesis-structure-property, which is still insufficient. [1.64]

One of the reasons for synthesis difficulty is the complexity of synthetic variables. The major parameters of heteroatoms-doped porous carbon that determine the electrocatalytic activity were summarized in Figure 1.8. To achieve the superior properties appropriate for practical application, all these characteristics should be optimized. [1.16, 65] However, the optimization of these characteristics requires a delicate strategy since all these characteristics are correlated. Moreover, some characteristics, such as the specific surface area (SSA) and the conductivity have a trade-off relationship in general. Furthermore, in the synthetic process of the heteroatom-doped porous carbon, the incorporated heteroatom significantly

influences the overall characteristics of the carbon substrate. In particular, the metallic species can serve as the graphitization catalyst, changing the pore structure, morphology, and electronic properties of carbon materials as well as the dopant, developing the active site in carbon materials. [1.64, 66] The major role of metallic species different depending on synthetic conditions even if the initial composition of precursors is identical, which dramatically affects the properties. Therefore, the understanding of the interaction between the metallic component and the carbon substrate during the synthesis according to specific synthetic conditions is a prerequisite for developing a practical synthesis method.

This synthetic issue is becoming more prominent with the progress of the metal atom dispersed carbon (M-N-C) research for electrochemical reaction. The maximizing the density of M-N<sub>x</sub> active sites embedded in micropore of porous carbon substrate is essential for maximizing the electrocatalytic activity of the M-N-C catalyst. [1.64] Most of M-N-C catalyst synthesis involved the pyrolysis of metal, nitrogen, and carbon precursors mixture accompanying high-temperature treatment (> 800 °C), which is inevitably required to endow the electric conductivity to the carbon support and the stability to M-N<sub>x</sub> active sites. [1.47, 50] During the pyrolysis step, however, the atomic metals not only can establish M-N<sub>x</sub> moieties but also can aggregate and form metal-based nanoparticles. The preference of each phenomenon can vary greatly depending on experimental conditions. The formation of the metal-based nanoparticles, especially transition metal, has a profound effect on the carbon structure since the transition metal-based particle acts as the strong graphitization catalyst well known in various carbon studies. [1.66-68] The controlling the formation of metal-based particle is essential to develop the practical synthesis



process of high functional heteroatoms-doped porous carbon materials. However, the strategy for controlling the formation of the metal-based particle is still in its infancy phase.

Therefore, the innovative approach based on the understanding of the synthesis-structure-property relationship is highly required to develop the practical synthetic method of multi-nary heteroatoms-doped porous carbon materials. To achieve this, an in-depth study of the synthesis-structure relationship is prerequisite. Some previous research combined the thermodynamic to understand the synthesis of the carbon-based materials. Nam et al. reported that the structure of metal (Co, Ni, Cu, and Pt)/carbon nanofiber hybrid material can be controlled and predicted through the thermodynamic evaluation of redox between metal ion and C, as briefly shown in Figure 1.9. [1.69] However, identifying the major synthesis parameters that determine the structure, composition, and property of heteroatoms-doped porous carbon based on the thermodynamic considering the nanosize effect has not been attempted before.

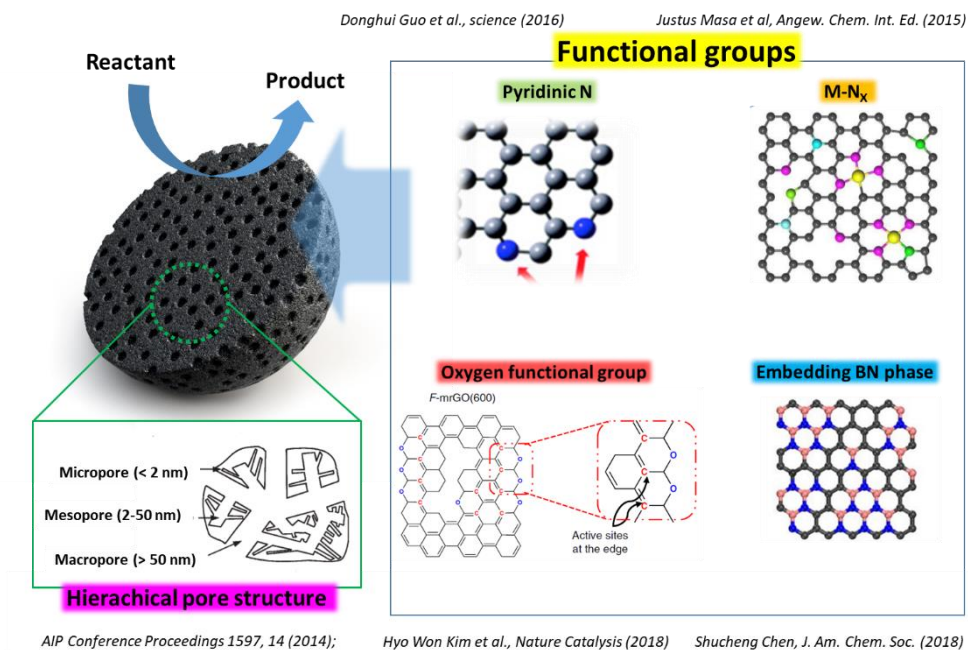


**Figure 1.7.** Endowing the functionalities to hierarchal porous carbon materials.

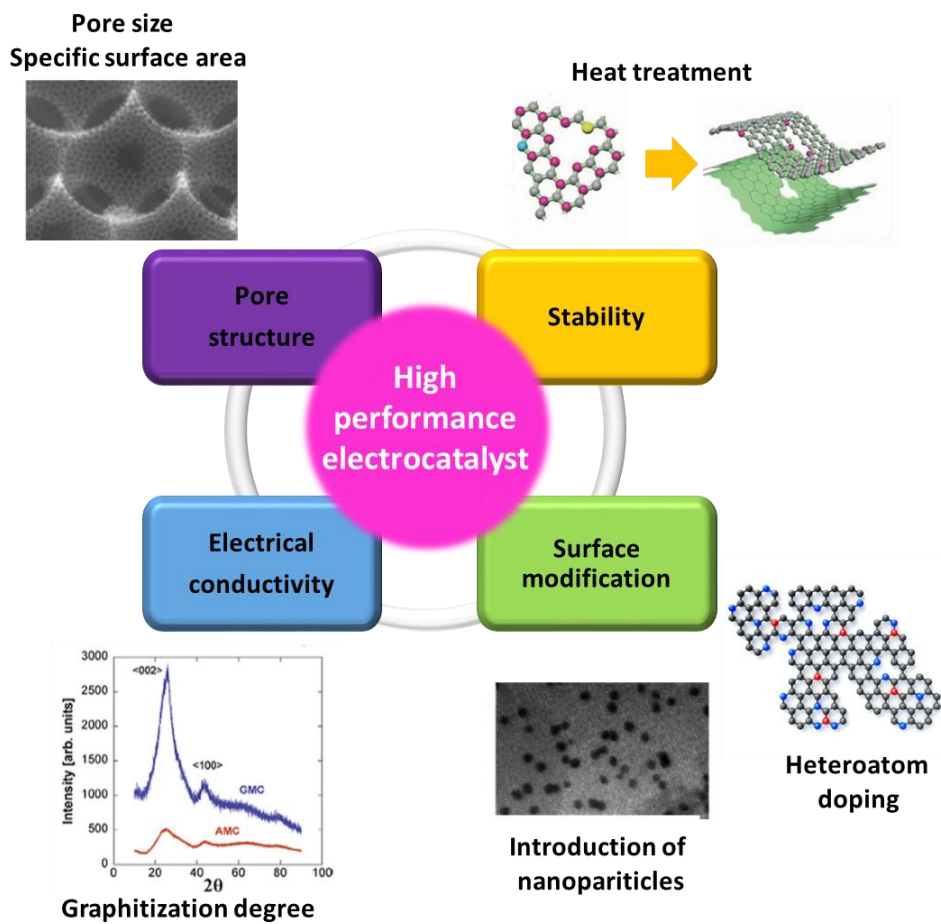


**Figure 1.8.** The major parameters that determining the electrocatalytic properties of porous carbon materials.

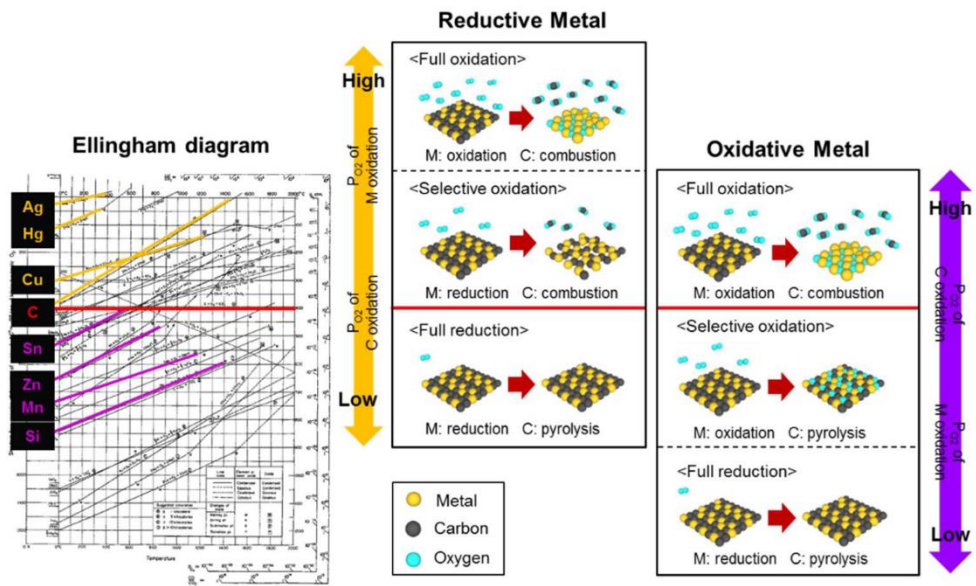


**Figure 1.9.** Categorization of redox reactions of metal and C according to the Gibbs free energy of oxidation in Ellingham diagram. Aspects of phase transformation of metal ion and C decomposition are classified as full oxidation, full reduction, and selective oxidation. [1.69]

### 1.3. Objectives of the thesis

The objective of the thesis is the demonstration of a novel synthetic methodology for high functional heteroatoms doped carbon material (Figure 1.10). In particular, this thesis focuses on three aspects as follows.

First, in terms of synthetic process development, this thesis addresses the demonstration of the novel synthesis methodology for high functional heteroatoms doped carbon via the chlorination process. The conventional carbide-derived carbon (CDC) process, which will be discussed in detail in the general background section (2.1.), is one of the representative methods for produce nanoporous carbon using selective extraction of metal or metalloid atom in carbide lattice. [1.70] CDC is favorable for synthesizing highly nanoporous structure as well as controlling the nano-pore size. Thus, various research for CDCs that carbon structure and pore structure were elaborately designed and show high performance in various energy and environmental applications. [1.71-74] However, to extract the metal atom, reactive etchant, such as halogen element ( $\text{Cl}_2$ ), is required inevitably; thus, it is challenging to incorporate the heteroatom component into carbon, which is a limitation for the synthesis of heteroatom-doped carbon through chlorination process.

Our group previously showed that the synthesis of heteroatoms (N, B, and Fe)-doped porous carbon is feasible by the chlorination process (more detail in the general background section (2.1.4.)). The obtained heteroatoms (N, B, and Fe)-doped porous carbon showed high applicability for the gas storage and

electrocatalyst. However, the doping amount of heteroatoms in the carbon substrate is limited. Moreover, the understanding of the synthesis-structure relationship in the synthesis of porous carbon materials by the chlorination is insufficient. The practical application of chlorination process to synthesizing porous carbon materials still remained in question.

This thesis tried to find a breakthrough and improve the versatility of the chlorination process. Carbonitride was introduced as an N-doped carbon precursor, and also titanium boride was introduced as a B doping precursor. Also, metal acetylacetonates are added as metal dopant precursors. The CNB and M-CNB materials suitable for the electrochemical application can be successfully synthesized using the one-pot chlorination process. These results demonstrate the applicability of the chlorination process to the synthesis of the multi-nary atoms doped nanoporous carbon materials.

Second, in terms of the component of the heteroatom doping system, this thesis focuses on the applicability of the CNB system and the M-CNB system as the electrocatalyst for energy-related applications. Numerous previous studies reported the introduction of boron in CN could bring complementary effect and endow the high catalytic activity for various electrochemical reactions. Thus, boron has been recognized as the promising candidate as the additional dopant of porous nitrogen-doped carbon. Interestingly, boron has a metallic characteristic, [1.75-77] which is differentiated from other nonmetallic dopants (nitrogen, sulfur, oxygen, and phosphorous). Boron can serve the catalyst that facilitated the formation of  $sp^2$ -bond as well as the dopant. [1.78, 79] Also, boron can readily interact with metal elements.

[1.80] Thus, the introduction of boron to the synthesis of CN and M-CNB can significantly alter the overall characteristics of CN and M-CN materials, including structure, surface chemistry, and the electrocatalytic properties. However, the research for the synthesis of CNB and M-CNB is still in its infancy phase, only begun to discover its potential. [1.81, 82] Also, most studies are biased toward the structure (active sites)-the electrochemical properties relationship.

Finally, in terms of the methodology of study on the synthesis of heteroatoms-doped carbon materials, this thesis focuses on the breakthrough approaches for the development of the synthesis process of heteroatoms-doped porous carbon materials. Conventional heteroatoms-doped porous carbon materials study focuses on the structure-property relationship, identifying the specific active sites that endow the specific properties. Conventional studies are dominantly based on the Ab initio quantum chemistry method and the experiments. They are useful to understand the structure (active sites)-property relationship. However, it is imperative to understand the synthesis-structure relationship for the development of a practical synthesis method for heteroatoms-doped carbon materials. The introduction of thermodynamic to the synthesis of functional nanomaterials has been attempted in some previous studies [1.83-1.86] to identify the synthesis-structure relationship. However, it is still in the early stage and has not been applied to heteroatoms-doped porous carbon synthesis yet. In this thesis, the equilibrium thermodynamic calculation and phase diagram in nano-scale are introduced to predict the critical synthesis factors that determines the structure, composition, and the properties of heteroatoms-doped porous carbon materials. The predicted synthesis factors are verified by the experiment. Through the thermodynamic calculation and experiment, the facile

synthesis methods for the heteroatoms-doped porous carbon materials are suggested.

In sum, this thesis aims for a comprehensive understanding of interactions between precursor that occurs throughout the synthetic process of the CNB and M-CNB materials based on the sophisticated controlled experiments, thermodynamics analyses, and various characterizations, including structural, surface chemistry, and electrochemical analyses. Based on these, this thesis addresses the facile synthetic strategies of the CNB and M-CNB materials (Figure 1.11) using one-pot chlorination which can be utilized to the various applications, including the electronics, energy, and environment.



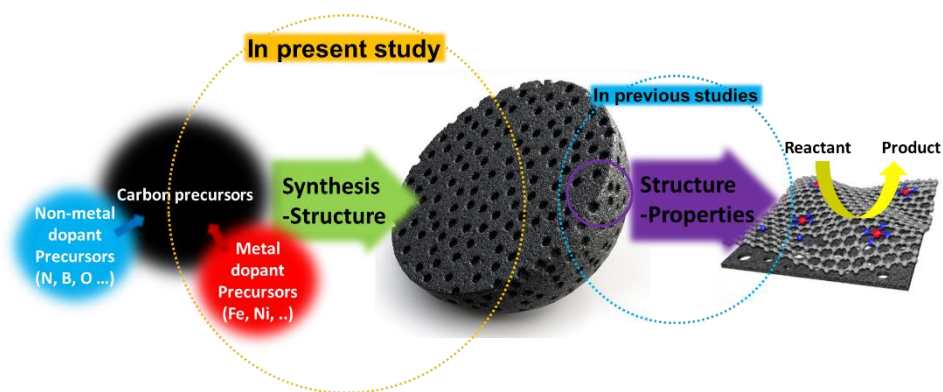


**Figure 1.10.** The research scope of this thesis about the functional porous carbon materials.

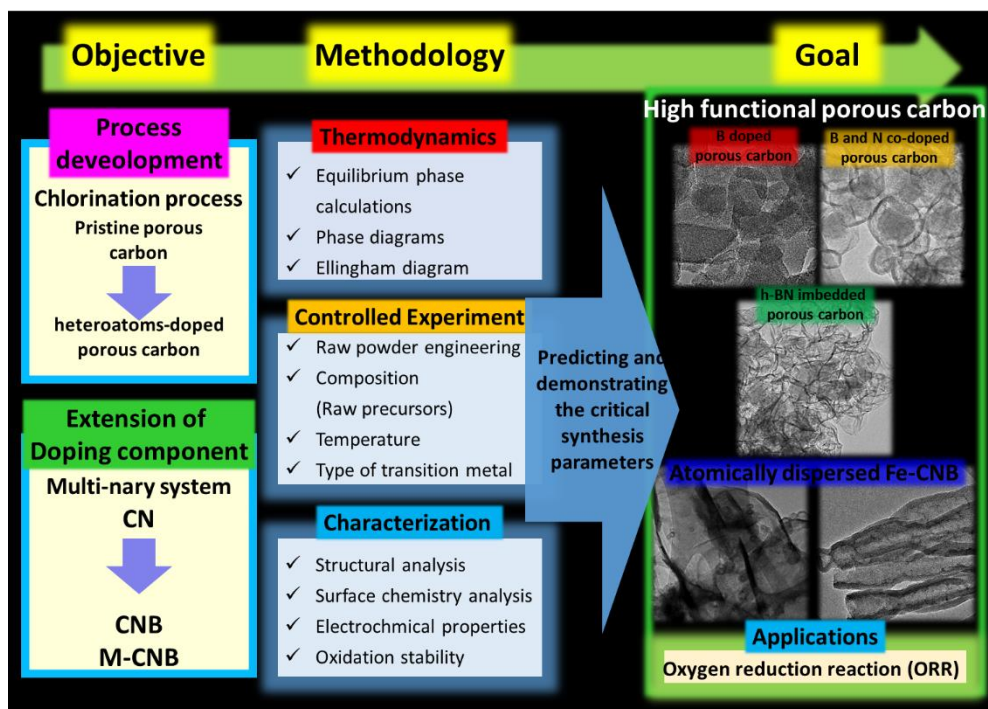


**Figure 1.11.** Overview of the thesis.

## 1.4. Organization of the thesis

This thesis consists of eight chapters. In chapter 2, the fundamental knowledge for carbide-derived carbon (CDC), the role of boron in carbon, BCN materials, graphitization mechanism, pore structure, electrochemistry, and thermodynamics are summarized. Chapter 3 described the experimental procedure, including the preparation of raw carbonitride, boride, and transitional metal source precursor, the chlorination process, and the examination of obtained porous carbon's properties.

Chapter 4 addresses the synthesis of heteroatoms (B, N, and O) doped porous carbons via the chlorination of the carbonitride (or carbide)-boride mixture. The formation mechanism of obtained porous carbons, focusing on the influence of boron in the carbon structure, is also discussed.

Chapter 5 suggest the novel synthesis of BN embedded porous carbon using the chlorination of the nitrogen-rich carbonitride-boride mixture, having excellent electrocatalytic activity for  $\text{H}_2\text{O}_2$  production. The influence of the addition of boron to the formation of carbon structure is predicted using the thermodynamic equilibrium calculation. Based on the thermodynamic calculation results, the optimum synthesis process to synthesize the nano BN moieties embedded porous carbon is designed. The formation mechanism and applicability as the electrocatalyst for  $\text{H}_2\text{O}_2$  production of BN embedded porous carbon are also investigated.

Chapter 6 addresses the novel synthetic strategy of the chlorination process to

obtain of atomically dispersed M-CNB material. The investigation of interaction among carbon, boron, and transition metal species in the synthetic process is conducted based on the thermodynamic analysis and comparative experiments between Fe-CNB and Ni-CNB. The melting temperature of formed metal compounds during the chlorination is predicted as the critical synthesis factor that determines the atomic dispersion of metal atoms to porous carbon. The thermodynamic calculation and phase diagrams in the nano-scale used as the predication tools. The comparative experiments verified the prediction of synthesis factor. Furthermore, the electrocatalytic activity of obtained M-CNBs for oxygen reduction reaction (ORR) is estimated.

Chapter 7 addresses the expandability of the M-CNB system to the other synthetic method (pyrolysis) and discusses the influence of boron precursor (boric acid) for the production of atomically dispersed M (Fe and Ni)-CNB during the synthetic process. The role of boric acid that induces the atomic dispersion of metal to carbon substrate through the formation of liquid solid solution is predicted using the thermodynamic calculations and phase-diagram. This is also demonstrated by the controlled experiment. In Chapter 8, all the results were summarized with the novelty of this thesis, and also the future works are suggested.

## **Chapter 2. General background**

### **2.1. Carbide derived carbon (CDC)**

Carbide derived carbon (CDC) process is one of the promising synthetic methods for synthesizing functional nano-carbon materials ranging from disorder to ordered structures (Figure 2.1). The basic concept of the CDC process is the construction of carbon networks using the extraction of the metal or metalloid atoms from the carbide structure. There are several tactics to remove the metal species, such as halogenation, hydrothermal treatment, vacuum decomposition, and etc. and halogenation, especially chlorination, was recognized as the most suitable for use in large-scale production of CDC. [2.1]

CDC has two unique characteristics that are distinct from the conventional porous carbon materials synthesized by other synthetic methods. First, it is highly microporous. The vacancies having atomic size formed by the removal of metal atoms can be homogeneously distributed in the CDC. Micropore acts as an active site that readily interacts with a reactant or adsorbate, essential for energy and environmental application. [2.1] Second, CDC retains the original morphology of precursors. The selective extraction of metal atoms enables the conformational transformation that maintains the original shape and volume of the precursor, which is favorable for the morphology control. [2.1, 2] Thus, CDCs show high performance in various energy and environmental application such as supercapacitor, water desalination, gas storage, electrochemical reaction. [2.3-9]

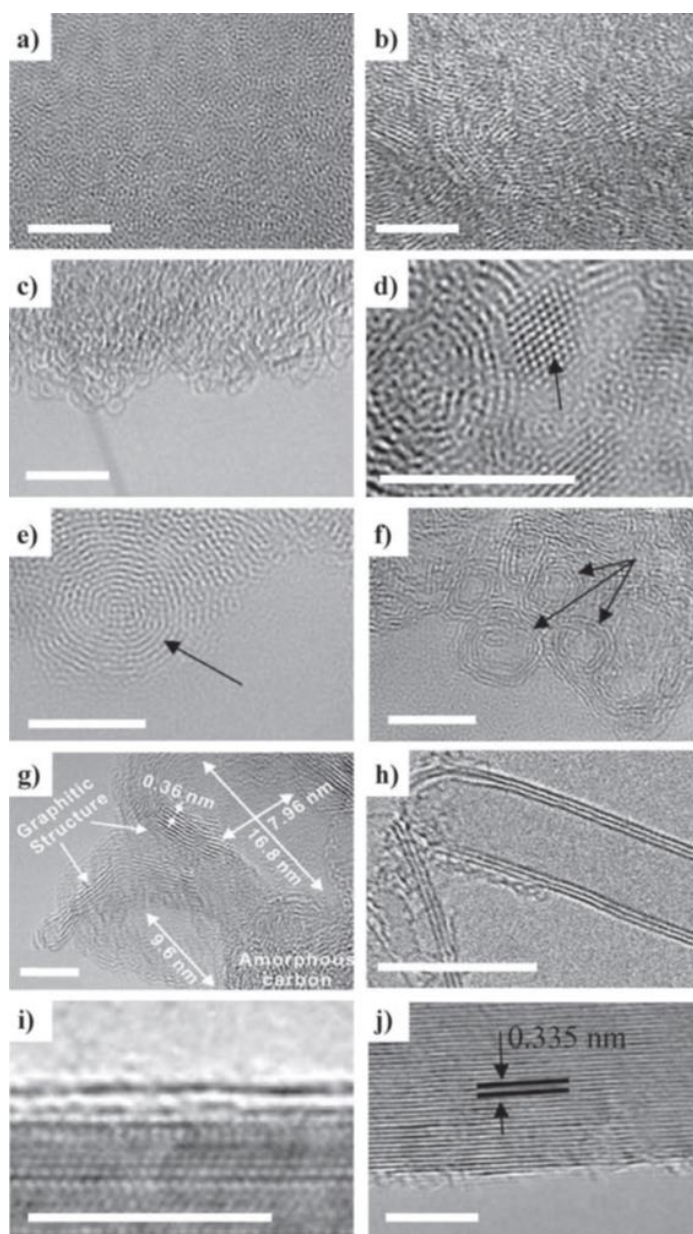
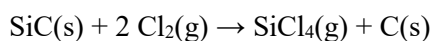


**Figure 2.1.** Transmission electron microscopy images of various CDC structures as obtained from carbide chlorination and vacuum decomposition of SiC: Amorphous carbon (a), turbostratic carbon (b), fullerene-like carbon (c), nano-diamond (d), onion-like carbon (e), carbon nano-barrels (f), mesoporous carbon (g), carbon nanotubes (h), epitaxial graphene (i), graphite (j). The scale bar is 5 nm. [2.1] Copyright 2006, CRC Taylor & Francis. Copyright 2008-2010, Elsevier.

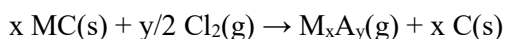
### 2.1.1. CDC synthesized by chlorination

The first synthesis of the CDC via the chlorination of carbide was reported by Otis Hutchins in 1918. [2.10] By exposing the silicon carbide (SiC) to dry chlorine (Cl<sub>2</sub>) gas at 1000 °C or above, silicon tetrachloride and carbon were obtained following equation.



This chlorination process initially targeted to obtain the silicon chloride product which is a key chemical for the semiconductor industry, and the obtained CDC was considered as an undesired residue. However, later, this byproduct CDC classified as the mineral carbon and has been recognized as the useful material since its unique nanoporous structure was discovered.

The general reaction equation for producing CDC through chlorination of binary carbide is as followed equation (Figure 2.2):



where M<sub>x</sub>A<sub>y</sub>(g) is a gaseous reaction byproduct.

This CDC synthetic process basically consists of two simple successive heat treatment steps. [2.1] The first step is chlorination step. The raw carbide precursor ramped into targeted temperature in inert gas and at target temperature, the precursor was exposed to dry chlorine gas and chlorination occurs. The second step is annealing in hydrogen gas to remove residual chlorine and chlorides. Using this technique, numerous CDCs were derived from various binary carbides and ternary carbides, such as Al<sub>4</sub>C<sub>3</sub>, B<sub>4</sub>C, BaC<sub>2</sub>, CaC<sub>2</sub>, Cr<sub>3</sub>C<sub>2</sub>, Fe<sub>3</sub>C, Mo<sub>2</sub>C, MoC, Nb<sub>2</sub>C, NbC, SiC, SrC<sub>2</sub>, Ta<sub>2</sub>C, TaC, Ti<sub>2</sub>AlC, Ti<sub>3</sub>AlC<sub>2</sub>, Ti<sub>3</sub>SiC<sub>2</sub>, TiC, VC, W<sub>2</sub>C, WC, and ZrC. [2.1, 11-15]

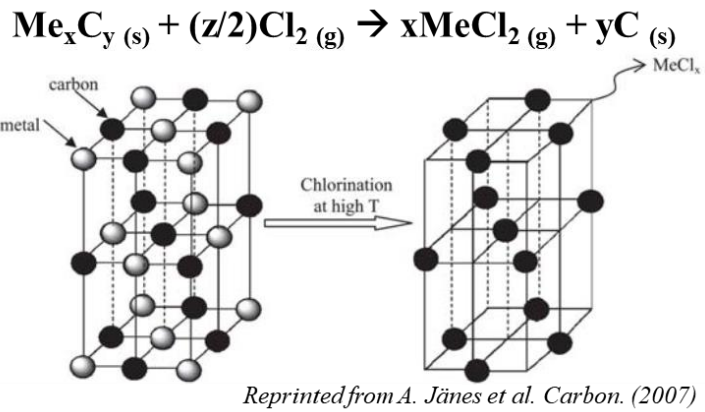


**Figure 2.2.** Synthesis of CDC by the chlorination of binary carbide. [2.16]

### 2.1.2. Effect of type of precursors on the structure of CDC

The morphology and pore structure of CDC can be controlled by the variation of precursors. The overall morphology of CDC followed the morphology of precursor carbides thus CDCs having various shape have been synthesized, such as sintered carbide bodies, whiskers, thin films, micro and nano-sized powders, and single crystal. [2.2, 17-20] Furthermore, the pore structure of CDC varied with precursor carbides, which came from the specificity of chlorination of carbide. The bulk porosity of CDC is dominantly determined by the structure of the precursor carbide, having high porosity in general (> 50 vol.%). [2.1] While, micro- and mesoporosity can be controlled by the type of metal atom in the precursor carbide lattice and crystal structure of carbide, the parameters that determine the distribution of carbon atoms in carbide lattices. Figure 2.3 explains pore structure controlling mechanism through the comparison of pore structure of CDCs synthesized by ternary carbide ( $\text{Ti}_3\text{SiC}_2$ ) and binary carbide (3C-SiC). These two carbides have different crystal structure causing the different carbon atoms distribution in carbide lattice. Thus, two CDCs exhibits totally different pore size distribution at the same chlorination temperature (1200 °C), evaluated using gas adsorption analysis.  $\text{Ti}_3\text{SiC}_2$ -CDC has a broad distribution in 0.5-4 nm range while 3C-SiC-CDC has a narrow distribution in small micropore region (below 1 nm) [2.21, 22]. Also, the TEM images of this two CDCs demonstrated that their ordering tendency is different. Their bulk porosity can be predicted by the calculation of the total weight-based theoretical pore volume  $V_{\text{total}}$  using as followed equation: [2.1]

$$V_{\text{total}} = \frac{1}{X_{\text{carbon}} * \rho_{\text{carbide}}} - \frac{1}{\rho_{\text{carbon}}}$$

Where  $X_{\text{carbon}}$  is the weight fraction of carbon in the carbide,  $\rho_{\text{carbon}}$  is the density of



carbon, and  $\rho_{\text{carbide}}$  is the density of carbide precursor. Calculated  $V_{\text{total}}$  values of two CDC is quite different, 86 vol.% and 58 vol.% for  $\text{Ti}_3\text{SiC}_2$ -CDC and 3C-SiC-CDC, respectively, and they are in agreement with real measured bulk porosity values.

Likewise, the pore structure of CDCs can be greatly varied with the types of carbide precursors. The CDC originated from binary carbide with NaCl structure and wurtzite/zinc blend structure has a narrow pore size distribution. While, orthorhombic or rhombohedral carbide CDCs has a large and uniform pore size distribution. [2.23, 24] Even if the crystal structure of carbide precursors is the same, depending on the type of metal atoms, the carbon-carbon distance in carbide lattice can be varied thus CDCs synthesized by same structure type carbides also have different pore size distribution and bulk porosity. [2.25] Therefore, according to the selection of the carbide precursor, the overall porosity, from micropore to macropore, can be tuned. Figure 2.4 displayed the pore size distribution of other CDCs produced by different carbide precursors, which further demonstrated the advantage of CDCs for modifying the nanoporous structure.

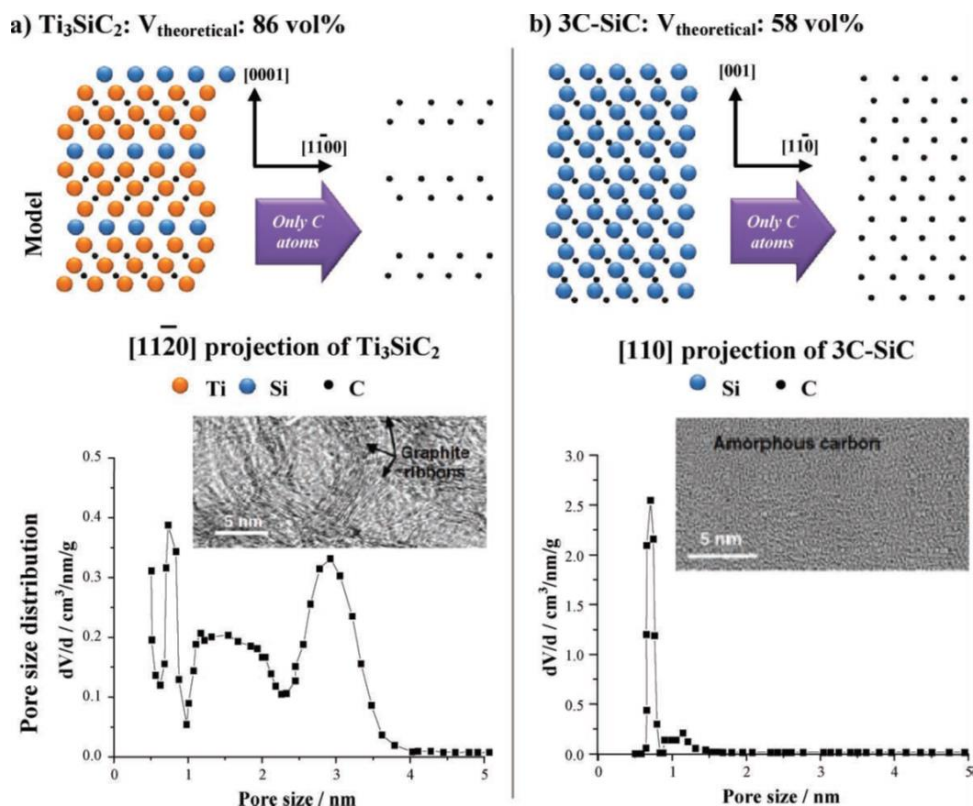


**Figure 2.3.** Schematic of the atomic structure of  $\text{Ti}_3\text{SiC}_2$  (a) and  $3\text{C-SiC}$  (b) and the corresponding CDC structures after halogenation. As seen from the pore size distribution, the ternary carbide shows a broader pore size distribution than the binary carbide at 1200 °C. (The data are from argon sorption obtained from NLDFT.) Also, the resulting carbon structure can be very different – while SiC CDC still consists of predominantly amorphous carbon,  $\text{Ti}_3\text{SiC}_2$  shows significant graphitization at the same temperature. [2.1, 22] Copyright 2006, CRC Taylor & Francis.

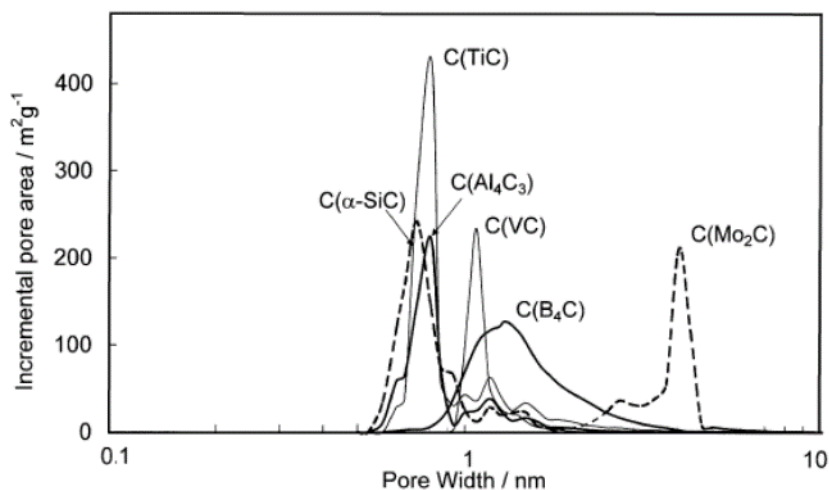


**Figure 2.4.** Pore size distribution, calculated according to NLDFT method by using the so-called slit-shaped pores model, for different micro- and mesoporous carbide-derived carbon materials. The corresponding synthesis temperatures (°C) were used: 1150 °C ( $\alpha$ -SiC), 950 °C (TiC), 400 °C ( $\text{Al}_4\text{C}_3$ ), 900 °C (VC), 1100 °C ( $\text{B}_4\text{C}$ ) and 750 °C ( $\text{Mo}_2\text{C}$ ). [2.26] Copyright 2007, Elsevier.

### **2.1.3. Effect of chlorination temperature on pore structure of CDC**

The chlorination temperature is one of the main parameters that determines the pore structure including pore size, pore sized distribution (PSD), and specific surface area (SSA) of CDC since carbon atoms mobility directly relates to carbon ordering tendency changes varying the temperature. The pore structure including pore size distribution (PSD) of CDC is mainly templated by the crystal structure of carbide precursor as mentioned in the above section. While, at higher chlorination temperature, the pore size of the CDC tends to increase attributed to self-organization and increment of crystallinity due to the high carbon mobility. [2.27, 28] Therefore, fine pore tuning with sub-Ångstrom accuracy is feasible by controlling the chlorination temperature. The example of pore controlling exhibited in Figure 2.5. Figure 2.5a show the average pore sizes in various CDCs varying with chlorination temperature. The pore sizes increase in the sub-nano unit as the chlorination temperature increases. Figure 2.5b,c exhibited the PSDs of specific CDCs ( $\text{Ti}_3\text{SiC}_2$ -CDC and PDC SiCN-CDC) varying with chlorination temperature. They clearly show the shift to large size as the chlorination temperature increases.

Meanwhile, the specific area (SSA) also varied with temperature. In general, the SSA variation of CDCs with increment in the chlorination temperature shows a bell-shape trend. [2.12, 29] This is because there are limiting factors that inhibit the increase in SSA at low and high chlorination temperature. At the low chlorination temperature, pores are directly templated by original carbide lattice (vacancy of metal atoms), resulting in the significant development of small micropores, which is

beneficial for an increase of SSA. But, two limiting factors lowering the SSA exist. One is that the size of developed micropore is less than 0.5 nm too small that gas species used for conventional gas adsorption technique cannot access thus these micropores are barely measured by conventional gas adsorption technique. The other is residual chlorides. The kinetics of formation and removal of chlorides produced during the chlorination is slow thus some chloride residues are trapped in micropores. Meanwhile, at the high chlorination temperature, graphitization and consolidation of the CDC occur, which drastically degenerates the developed pore. For these reasons, in general, the intermediate chlorination temperature (800-1000°C) is appropriate for achieving maximum SSA with the development of proper ordering of carbon structure. [2.12, 29]

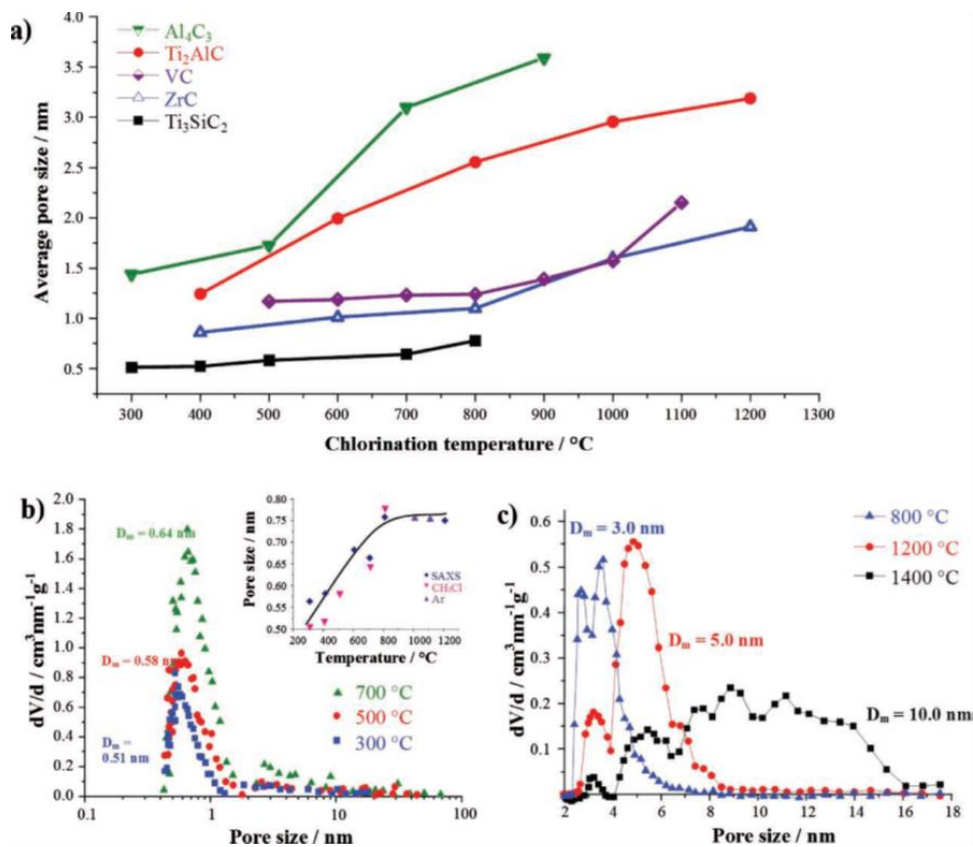


**Figure 2.5.** Average pore sizes for selected binary and ternary carbides (a):  $Al_4C_3$ ,  $Ti_2AlC$ , VC, ZrC,  $Ti_3SiC_2$ . Comparison between the PSD of  $Ti_3SiC_2$  -CDC (b) and SiCN PDC-CDC (c) from nitrogen sorption using NLDFT. [2.1]

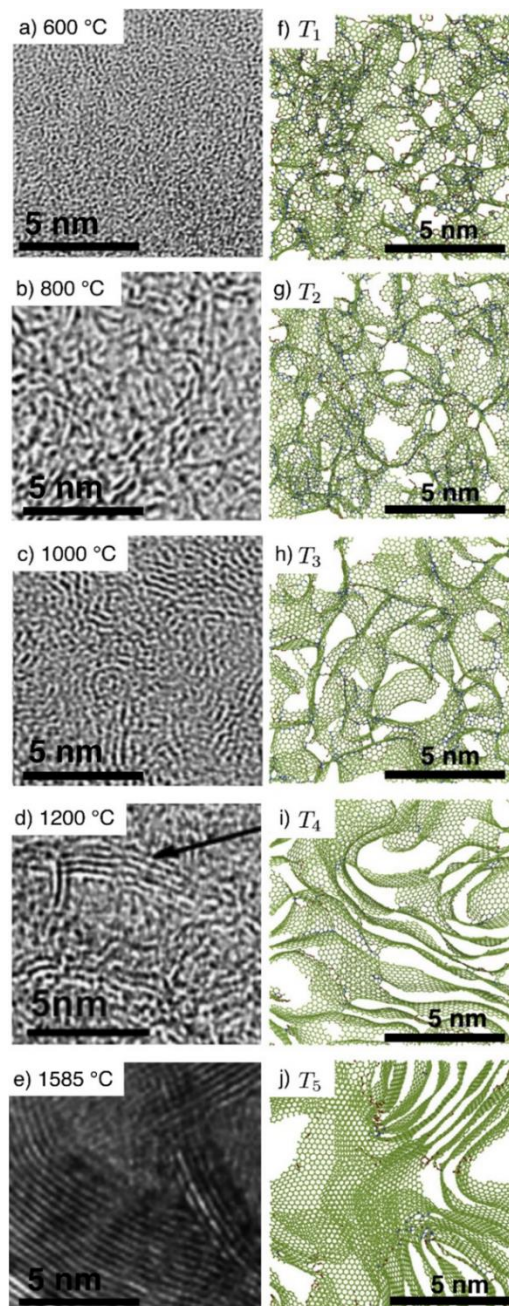


**Figure 2.6.** a-e) TEM images of TiC-CDCs obtained by chlorination at various temperatures. f-i) Slab of 2 nm thickness of simulated TiC-CDCs after annealing at  $T_1 = 1500$  K,  $T_2 = 2000$  K,  $T_3 = 3000$  K,  $T_4 = 4000$  K and  $T_5 = 4500$  K. Red, green and blue spheres denote  $sp$ ,  $sp^2$ , and  $sp^3$  bonding, respectively. [2.30] Copyright 2017, Elsevier.

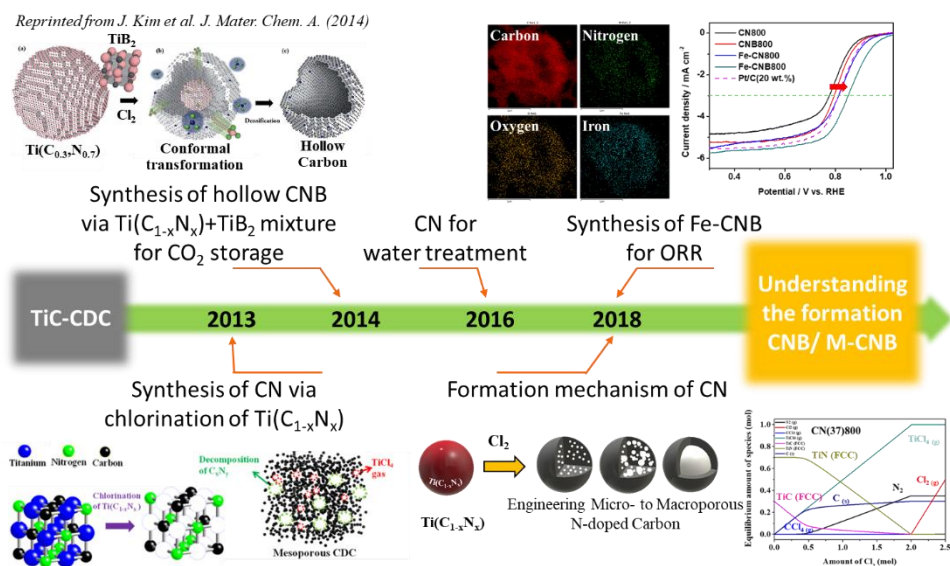
#### **2.1.4. Synthesis of heteroatoms-doped porous carbon using chlorination process**

As mentioned above sections, CDC has great strength in terms of microporosity, which is one of the major contributions guaranteeing high performance in energy and environmental application. However, CDC also has a severe drawback, the difficulties in heteroatom doping, due to the harsh chlorination condition. In chlorination condition, elements other than carbon, such as nitrogen or metallic species, are hard to survive.

To overcome this limitation, our research group introduced the solid-solution of titanium carbide ( $\text{Ti(C,N)}$  and  $\text{Ti(C,O)}$ ) as the precursor of chlorination, instead of carbide (Figure 2.7). Hetero atoms (nitrogen and oxygen) already exists in the lattice of precursors thus hetero atom readily incorporates to the carbon structure. [2.31] Moreover, especially in the case of  $\text{Ti(C,N)}$ -CDC (CN), not only micropore, but also meso- and macropore can be developed due to the decrease of carbon density in precursor lattice and gasification of unstable nitrogen and carbon as the form of  $\text{CCl}_4$  (g),  $\text{N}_2$  (g),  $\text{C}_x\text{N}_y$  (g). [2.32] Thus, CN has hierarchical pore structure. The incorporation of nitrogen atoms and the hierarchical pore structure of CN exhibit synergetic effect thus CN shows the superior performance for supercapacitor and water treatment application. [2.32, 33] Beyond the mono atom doping, additional boron doping in CN was achieved successfully via the chlorination of  $\text{Ti(C,N)}$  and  $\text{TiB}_2$  hand mixture. [2.34]  $\text{TiB}_2$  served as the boron doping source and boron was supplied into CN through two routes; solid-state diffusion (the direct route) and  $\text{BCl}_3$



(g) (the indirect route). It was presumed that introduction small amount of boron in CN could stabilize the unstable CN structure and facilitate the nitrogen incorporation. Thus, boron and nitrogen co-doped porous carbon (CNB) having hollow structure could obtained by the chlorination of  $\text{Ti}(\text{C}_{0.3},\text{N}_{0.7})$  and  $\text{TiB}_2$  hand mixture. [34] This hollow CNB had the excellent  $\text{CO}_2$  gas storage capacity and outstanding oxygen reduction reaction peferomance due to the hollow structure and abundant nitrogen species, especially pyridinic N. [2.34, 35] The introduction of Fe in CNB was also attempted to synthesize atomically dispersed Fe-CNB by the chlorination of  $\text{Ti}(\text{C},\text{N})$ - $\text{TiB}_2$ -iron acetylacetonate hand mixture. It was experimentally observed that the addition of boron facilitates the atomic dispersion of Fe atoms and incorporation of abundant nitrogen functional groups in Fe-CNB, resulting in significant development of  $\text{Fe-N}_x$  active sites. [2.32] Thus, Fe-CNB shows an outstanding electrocatalytic performance for oxygen reduction reaction (ORR).



Reprinted from M. Seo et al. Carbon. (2013) and M. LEE, Ph.D thesis (2019)

**Figure 2.7.** Timeline of synthesis of heteroatoms-doped carbon materials using chlorination process.

## 2.2. Role of boron in carbon structure

Boron can act as a dopant that substitutes into the carbon layer and accepts electrons from the adjacent carbon atoms shown in Figure 2.8. Because its atomic radius is slightly small than carbon, and its electronegativity (2.0) is less than carbon (2.5) which modifies the electronic structure of the carbon layer. [2.36, 37] Lowell reported that the solid solubility of boron in graphite is 2.35 at.% at 2350 °C. [2.38] R. Faccio et al. reported the ad-initio-DFT/GGA study for the introduction of boron atom to carbon layer, and demonstrated that substituted boron atom can induce the structural distortion of the carbon layer, resulting in change of electronic and magnetic properties of carbon layer. [2.39]

Meanwhile, Boron also serves as a structural linker, promoting the formation of the carbon structure. X. Blase et al. reported that boron atoms can catalyze the growth of carbon nanotube. [2.40] The M. Terrones group reported that boron interstitial atoms act as efficient double-walled carbon nanotube (DWNT) welders, as shown in Figure 2.9. [2.41-43] Boron atom creates a covalent junction between DWNTs; thus, significantly lowering the temperature that the coalescence of nanotubes occurs. [2.41] The facilitation of carbon structure formation by boron was also reported in the previous studies on the diamond. Bernholc et al. reported that carbon self-diffusion activation energy in diamond could be decreased by the highly charged vacancy. [2.44] These studies indicate that the introduction of boron can facilitate the formation of robust carbon structure.

In addition, Boron serves as the graphitization catalyst. A.Oya et al demonstrated that the boron accelerate the homogenous continuous graphitization

during the high temperature heat-treatment (1800 – 2600 °C) of several carbon precursors. [2.45] Pu et al. reported that the introduction of a small amount boron could facilitate the  $sp^2$  bonding formation and graphitization in the synthesis of diamond-like carbon. [2.46]

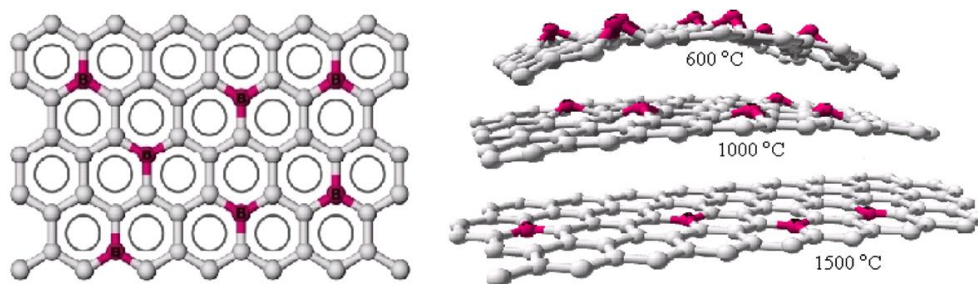


**Figure 2.8.** The schematic presentation of BC<sub>x</sub> materials (left) top view and (right) side view. [2.47] Copyright 2010, Elsevier.

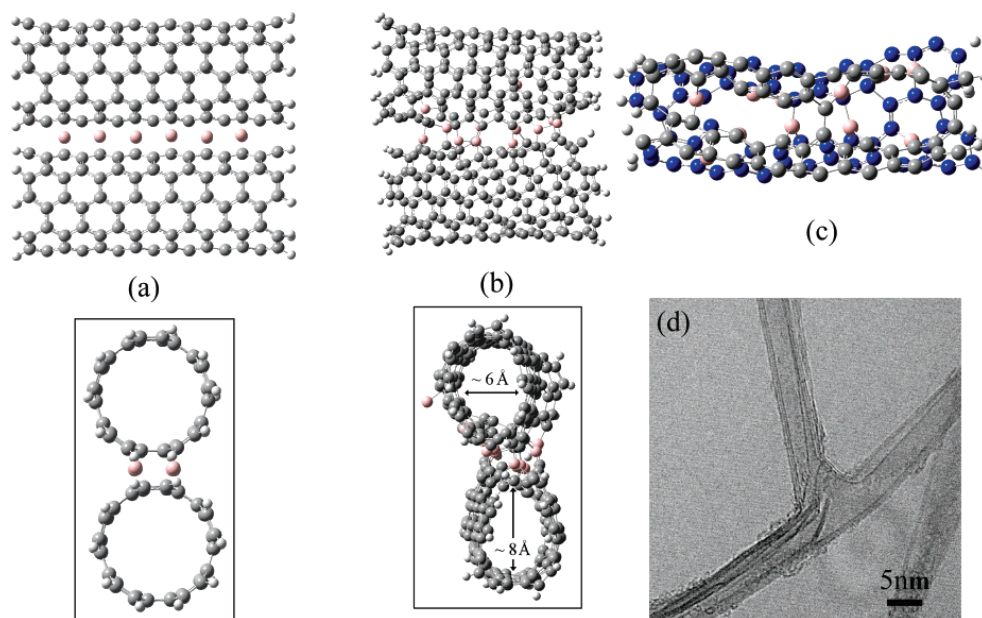


**Figure 2.9.** Molecular models showing the effect of intercalated B atoms between SWNTs. (a) Front and side view of the starting system for the MD calculations: two adjacent C150H20 (5,5) open carbon nanotubes with 12 intercalated boron atoms. (b) Front and side view of the system after 5 picoseconds of calculation, with the indication of the nanotube diameter (Å). The boron atoms start to bridge the two nanotubes, inducing a strong interaction between them. (c) Crosssectional view of the atoms between both nanotubes after 5 picoseconds, with the C atoms of the back nanotube colored in blue for better visualization. Large “holes” are created in both ideal structures and the two lips of the nanotubes are only connected with a few bonds. (d) HRTEM image of triple-walled nanotube T-junction derived from boron catalyzed DWNTs annealing. [2.41] Copyright 2005, ACS Publications.

### 2.3. Borocarbonitrides (BCN) material

Graphite is a versatile material having unique semi-metallic properties. In opposition to graphite, hexagonal boron nitride (h-BN), also called white graphite due to the structural similarity with graphite, having unique insulating properties. The structural similarity and the similar atomic radius of boron, carbon, and nitrogen enable graphite and h-BN to hybridize. The hybrids of these layered materials, called  $B_xC_yN_z$  (for brevity abbreviated to BCN) material, are generally anticipated to have semiconducting properties [2.48, 49], as described in Figure 2.10. As the re-discovery of monolayer graphite (so-called graphene) by Geim and co-workers in 2004 opened a new horizon of two dimensional (2D) layered materials [2.50], the interest for the hybridization of graphene and h-BN has increased dramatically. Pioneering research in graphene reveals that Hall effect (electron acts as massless Dirac fermions) can occur in graphene thus graphene has extraordinarily high electron mobility and also shows semi metal or zero bandgap semiconducting property along with unique thermal and mechanical properties. [2.48] Unlike graphene, h-BN monolayer is an insulator, its bandgap could be up to  $\sim 6$  eV. [2.51, 52] Theoretically, the introduction of B-C-N ternary system into layered hexagonal structures, the bandgap tuning, from zero bandgap to insulator, is feasible depending on the configuration. The h-BN domain in BCN can act like an “infinite” barrier, which results in the quantum confinement and/or spin-polarization at a particular graphene-h-BN boundary. [2.53-55] Thus, small bandgaps opening can occur in graphene, which endows the unique properties, such as magnetic, electrical, optical, mechanical, and electrochemical properties, appropriate for a wide range of

application. [2.49, 56]

Currently, BCN material has been applied to the sensor, transistor, gas adsorbent, electrocatalyst, and energy storage field. [2.48, 49, 57-59] In particular, BCN materials have been attracted great interest as the promising electrocatalyst. [2.36, 60, 61] Heteroatoms (nitrogen and boron) doping sites or carbon atoms near heteroatoms can serve as the active site at the surface of BCN materials. Also, depending on the configuration of boron, carbon, and nitrogen atoms, the electronic properties can be varied, which enables BCN material to have versatility as the electrocatalyst for various electrochemical reactions (Figure 11). [2.36, 62] The abundance and cost of the elements further enhance the applicability. However, the development of a cost-effective and robust synthetic process is still insufficient, which is a bottleneck of the practical application of BCN materials. Gas phase synthetic routes, typically chemical vapor deposition (CVD) method and solid phase synthetic routes (pyrolysis) are the most representative method for BCN material synthesis (Figure 2.12).

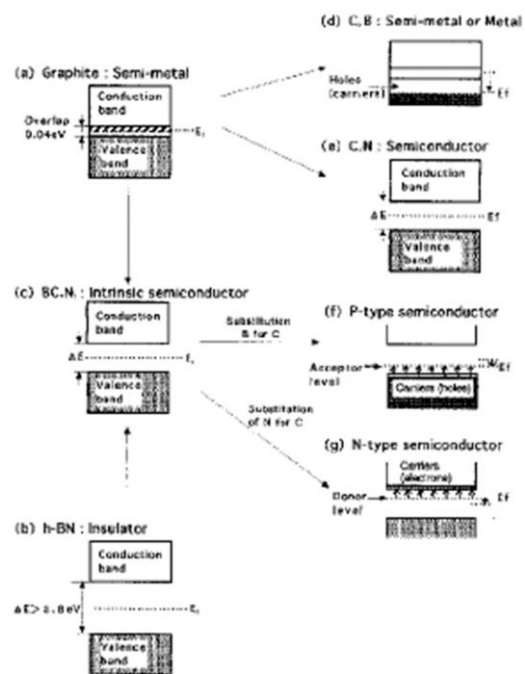


**Figure 2.10.** The expected band structure of B/C/N materials. [2.56] Copyright 1997, John Wiley & Sons, Inc.

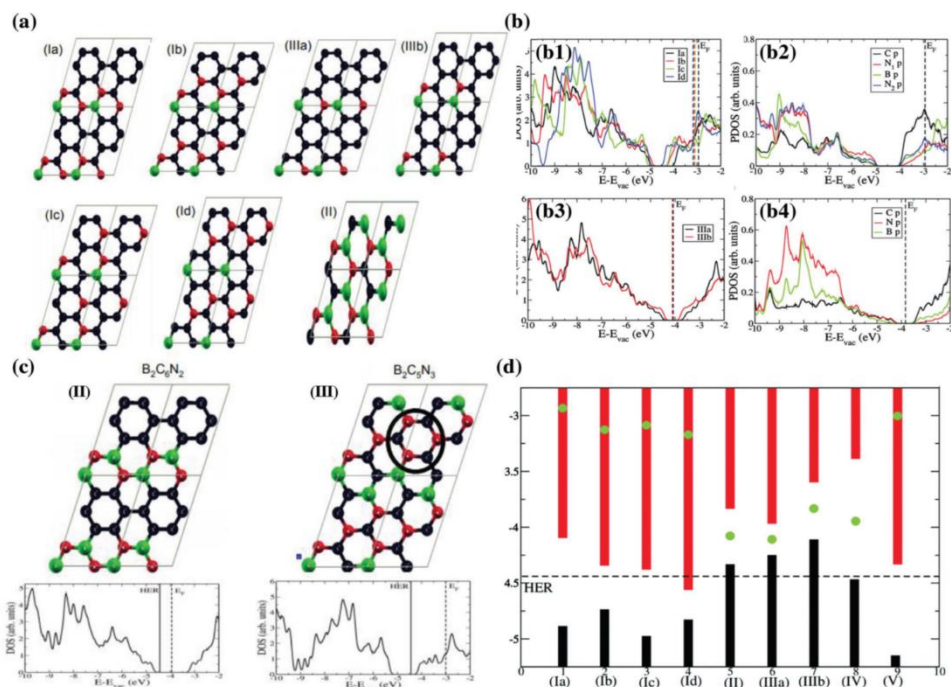
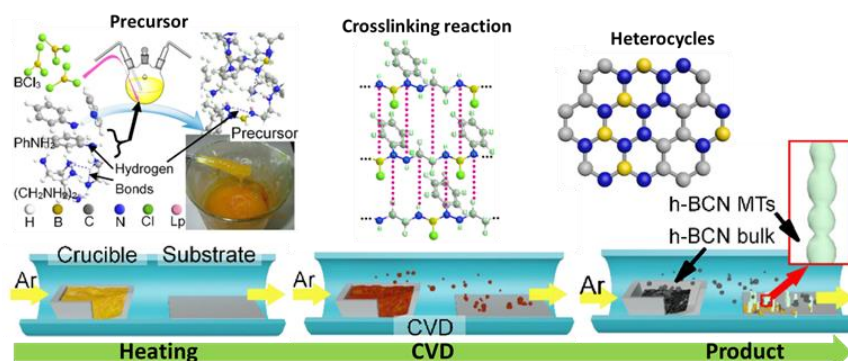


**Figure 2.11.** a) Schematics of three compositions BC<sub>7</sub>N<sub>2</sub> (I), B<sub>2</sub>C<sub>2</sub>N<sub>2</sub> (II), and BC<sub>8</sub>N (III), along with their symmetrically inequivalent configurations. C (black), B (green), and N (red). b1) DOS for four configurations of BC<sub>7</sub>N<sub>2</sub> (I). b2) Projected DOS of Ia. b3) DOS of IIIa and IIIb configurations of BC<sub>8</sub>N. b4) Projected DOS of II configuration of B<sub>2</sub>C<sub>2</sub>N<sub>2</sub>. c) Study of the effect of BN and the CN domains on HER activity of B<sub>x</sub>C<sub>y</sub>N<sub>z</sub>. Schematic of B<sub>2</sub>C<sub>6</sub>N<sub>2</sub> (IV), (b) B<sub>2</sub>C<sub>5</sub>N<sub>3</sub> (V) (C–N ring is marked by black circle) and their corresponding DOS. d) The comparison of the Fermi energies and HER energy level with the conduction and valence band edge positions. Valence band and conduction band is denoted by black and red, respectively. Green dots are the Fermi levels. [2.62] Copyright 2016, Royal Society of Chemistry.



## ❖ Chemical vapor deposition



*Reprinted from Tao Zhang et al., carbon (2018)*

## ❖ Pyrolysis/carbonization

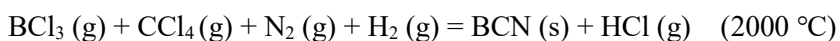


*Reprinted from Bin Liu et al., Adv. Funct. Mat. (2018)*

**Figure 2.12.** Schematic diagram of Chemical vapor deposition (CVD) method and pyrolysis method. Copyright 2018, Elsevier. Copyright 2018, John Wiley & Sons, Inc.

### 2.3.1. Synthesis of BCN material using gas phase synthetic route

Chemical vapor deposition (CVD) method has been generally used to produce the graphene and boron nitride. Combining the synthetic process of graphene and boron nitride, many research reported the synthesis of BCN having graphene-BN heterojunction via CVD method. Badzian et al. firstly applied CVD process to synthesizing BCN material. [2.56] They used the chloride of carbon and born as the precursors and heated these precursor gases in the mixture of hydrogen and nitrogen atmosphere to 2000 °C



The boron trichloride is one of the representative boron sources. The reaction between boron trichloride and hydrocarbon-containing compounds accompanying the elimination of formed HCl has been a common strategy for constructing B-C linkage. Kaner, Bartlett, and co-workers synthesized B/C/N hybrid film by the CVD method using reaction, as shown in following Equation. [2.63]

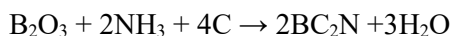
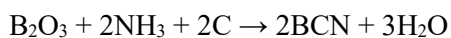
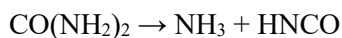
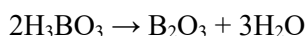


In addition,  $\text{B}_{0.485}\text{C}_{0.02}\text{N}_{0.485}$  and  $\text{B}_{0.35}\text{C}_{0.30}\text{N}_{0.35}$  were produced at 400 and 700 °C, respectively.  $\text{BC}_{1.6}\text{N}$  was obtained by gas phase reaction using  $\text{BBr}_3$ ,  $\text{NH}_3$ , and ethylene as the precursors. [2.64] L. Ci et al. reported the synthesis of BCN sheets on Cu substrates using the decomposition of methane and ammoniaborane precursors at 1000 °C and controlled the composition of BCN sheets in a wide range. [2.65] G. Han et al. reported the synthesis of graphene/BN nanosheets on Cu foil

synthesized by atmospheric pressure CVD (using CH<sub>4</sub>-Ar mixture gas and ammonia borane at 1057 °C). [2.66] Y. Gong et al. devised the conversion of graphene to BCN using heat treatment of boric acid powder in a flow of NH<sub>3</sub>-Ar mixture gas at 1000 °C. [2.67]

### **2.3.2. Synthesis of BCN material using solid phase synthetic routes**

The pyrolysis of the mixture of urea (nitrogen source), boric acid (boron source), carbon precursor, such as exfoliated graphene (EG), glucose, and activated carbon, is one of the representative method to produce BCN material. [2.68-71] In a typical pyrolysis synthesis, nitrogen, boron, and carbon source are mixed in water with different ratios and dried to obtain slurry or powder. This dried mixture is then heated at targeted temperature, generally 900 -1000 °C, in nitrogen or argon atmosphere. The key reactions during the pyrolysis may be represented by the following equations:



During the heat treatment, boric acid is transformed to boron oxide and urea is transformed to ammonia gas phase. The composition of produced BCN can be varied depending on the precursor mixture ratio as well as heat treating temperature.

## 2.4. Graphitization

In the synthesis of the porous carbon material, the graphitization is one of the critical effect that must be controlled. Since the degree of the graphitization in the porous carbon material greatly affects the electronic properties and the pore structure. In the perspective of degree of the graphitization, carbon materials can be classified into two categories after high temperature heat treatment (above 2800 °C), graphitizable carbon (GC) and non-graphitizable carbon (NGC). [2.72] Previous research demonstrated that initial stacking and arrangement of carbon atoms (carbon domain) in precursors is one of the major determinants, forming GC or NGC. [2.72] Figure 2.13 shows the overall crystallization process through treatment of carbon precursor (cokes).

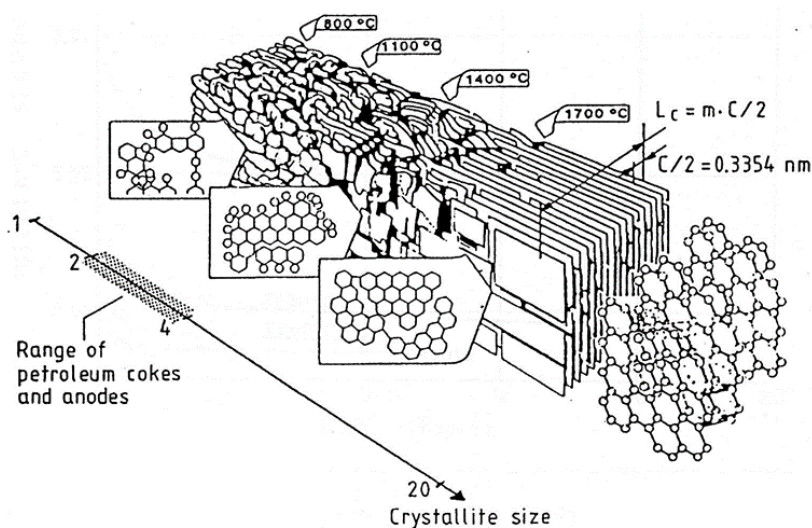


**Figure 2.13.** Overall crystallization stages of cokes.

### **2.4.1. Mechanism of graphitization catalytic effect of metal based particles**

The graphitization of GC can be facilitated by the metal-based particles. Even NGC can be graphitized due to the catalytic effect of metal-based particles. The catalytic graphitization has been investigated for decades and one of the key that synthesis of various carbon nanostructure materials including carbon nanotube, carbon onion, and carbon aerogel. [2.73-76]

The dissolution-precipitation mechanism and decomposition of metal carbides has been accepted as the general mechanism of the catalytic graphitization. [2.75-77] as shown in Figure 2.14. The dominant mechanism and the kinetic graphitization is determined depending on the experimental conditions, including the phase of supplied carbon, type and size of the metal-based particle, temperature, pressure, and atmosphere. [2. 76, 78, 79]

In particular, the size of metal-based particle can be critical factor that affects the kinetic of graphitization when its size is decreased below specific size (generally less than 50 nm). [2.78-80] Since, the melting point of the metal-based nanoparticle and eutectic temperature can be varied depending on the size of metal-based nanoparticle and surface melting metal-based particle can accelerate the graphitization.

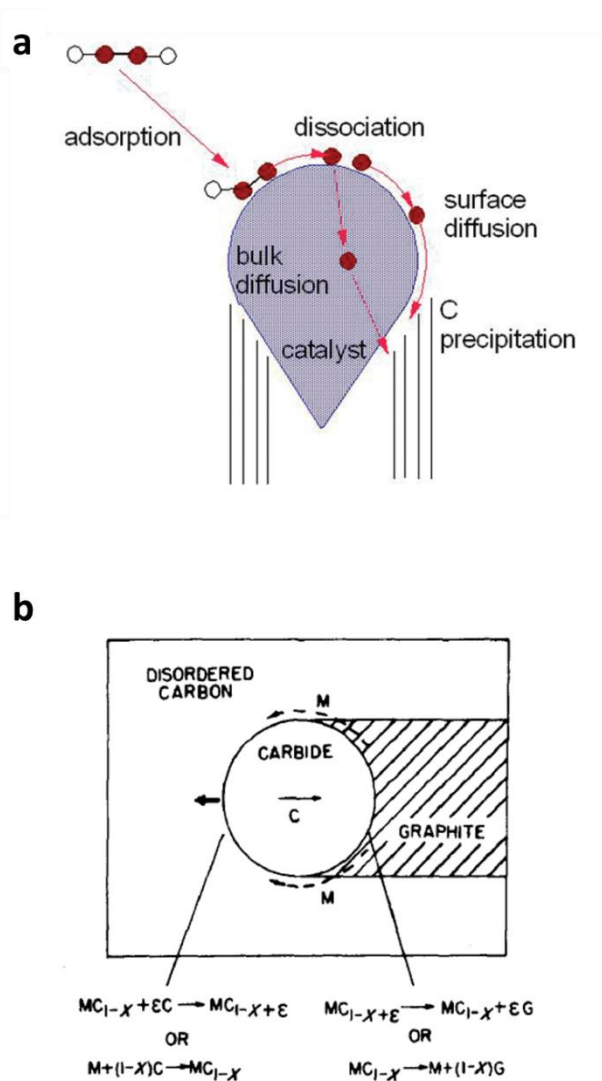


**Figure 2.14.** Diagrams of dissolution-precipitation mechanism (a) and decomposition of metal carbides mechanism (b) of catalytic graphitization. [2.75, 2.77] Copyright 2009, ACS Publications. Copyright 1982, Springer Nature.

## **2.5. Pore structure**

### **2.5.1. Adsorption isotherm**

Adsorption is a surface phenomenon that the adsorbates including atoms, molecules, or ions from the bulk of the gas, liquid, dissolved solids adhere to the surface of adsorbent. The concentration of the adsorbates at the surface has a higher than that of the adsorbates in the bulk, and the formation of a film of the adsorbate occurs. [2.81] There are two adsorption types: chemical adsorption (chemisorption) and physical adsorption (physisorption). Chemisorption, which involves the direct chemical bond formation between the adsorbate and the adsorbent surface. [2.82] While physisorption does not involve chemical bonding, and Van der Waals (VDW) attraction is fundamental interaction force. [2.83] The adsorption amount of the adsorbate as a function of its pressure (for gas) or concentration (for liquid) at the constant temperature is referred an adsorption isotherm.

The interpretation of the physisorption isotherm is essential to understanding pore structure of adsorbent materials. The physisorption isotherms are classified as six types based on the existence of pores and the strength of the adsorbate-adsorbent interaction, shown in Figure 2.15.(a). [2.84] The Type I is an isotherm that has a relative high adsorption value and saturates at low relative pressures. It demonstrates the strong adsorbate-adsorbent interaction and the development of micropores. The Type II isotherm represents unrestricted monolayer-multilayer adsorption and typical for non-porous or macro-porous materials. The Type III isotherm indicates a weak adsorbate-adsorbent interaction and a strong adsorbate-adsorbate interaction.

It generally is observed in materials that have low adsorption potential on surfaces, like organic polymers. The Type IV isotherm is similar to the Type II isotherm, the difference is the existence of hysteresis loop attributed to capillary condensation occurring in mesopores and the adsorption maximum before the saturation pressure is reached. It is a typical isotherm for mesoporous materials. The Type V isotherm appears in some porous adsorbents, where the adsorbent-adsorbate interaction is exceptionally weak, comparing with the adsorbate-adsorbate interaction, for example water vapor adsorption on microporous carbons. Finally, The Type VI isotherm demonstrates the stepwise multilayer adsorption on uniform non-porous surfaces. The step height in the isotherm corresponds to the monolayer capacity. [2.85]

### **2.5.2. Hysteresis of isotherm**

The hysteresis commonly appears in mesoporous materials' adsorption-desorption isotherms attributed to the difference in trend of adsorption and desorption. [2.85] It has been extensively studied but its origin is not fully understood yet. It has been accepted that the capillary condensation, evaporation in pores, and network effects with different neck sizes of pores can induce the hysteresis. [2.86] In the context of pore structure characterization, the understanding of physisorption hysteresis is essential. Thus, measurement of adsorption-desorption isotherms using nitrogen sorption at 77K has been routinely used for characterizing porous materials.

The hysteresis loop can be categorized to four types, adopted by the IUPAC (show in Figure 2.15.(b)). For the type H1 loop, the adsorption and desorption isotherms are close to the vertical and parallel to each other over a narrow range in



partial pressures. It represents the development of the mesopore channel having good pore connectivity and narrow pore size distribution. [2.87, 2.88] The H2 type loop is observed in more complex pore structures having high interconnectivity of pores. [2.89] Network effects of pores are prominent. The distribution of pore sizes and the pore shape is not well defined or irregular. Either pore-blocking/percolation in pore necks in a narrow size range or cavitation induced evaporation can cause a steep branch on the desorption isotherm. [2.90] The H3 type loop is obtained by non-rigid aggregates of plate-like particles and adsorbent that possesses the macroporous pore network not fully filled with the adsorbates. The lower limit of the desorption isotherm appears at the cavitation-induced  $p/p_o$ . [2.90] For Type H4 hysteresis loop, adsorption and desorption isotherms are almost horizontal and parallel over a wide range of partial pressures. It can be given by adsorbent materials that have large mesopores embedded with abundant micropores. [2.91] It is noteworthy that the lower limit of hysteresis loops is determined by the nature of adsorbate, not the nature of adsorbent (e.g. for nitrogen at 77K, the lower limit of hysteresis is at  $p/p_o \approx 0.42$ ). [2.91]

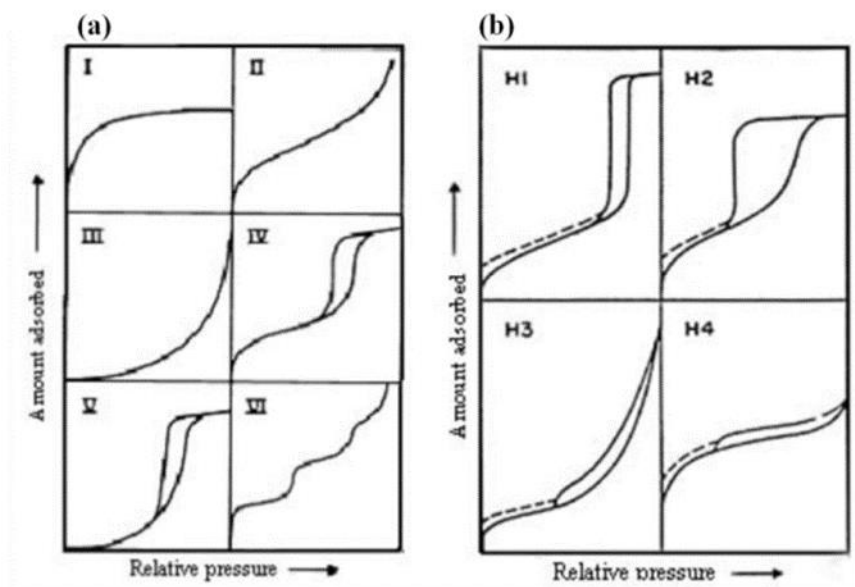


**Figure 2.15.** IUPAC classification of (a) physisorption isotherms (x-axis: relative pressure ( $p/p_0$ ) and y-axis: amount of adsorbate ( $V$ ) and (b) hysteresis loops of adsorbent materials.

### 2.5.3. BET method

In 1938, Brunauer, Emmett and Teller suggested the multilayer adsorption theory (BET theory), extending the Langmuir's monolayer theory to multilayer adsorption. The BET equation has been widely used for evaluating the surface area of adsorbent materials. The BET method is based on the following hypotheses: [2.85] 1) the surface is energetically homogeneous, indicating that all adsorption sites have the identical adsorption energy; 2) no lateral interaction between adsorbates; 3) the second and higher layers' adsorption energy values are equal to adsorbate' condensation energy; [2.91]

The practical BET equation in the linear form for evaluating the surface area is as following equation: [2.90]

$$\frac{\frac{p}{p_0}}{n(\frac{1-p}{p_0})} = \frac{1}{n_m C} + \frac{C-1}{C} \left( \frac{p}{p_0} \right)$$

where  $n$  is the specific amount adsorbate;  $n_m$  is the specific monolayer capacity; and  $C$  is the fitting parameter.

On practical usage of BET method, the measured physisorption is transformed into the 'BET plot' obtained by BET equation, and  $n_m$  can be derived from the proper linear region of the plot. The specific surface area ( $a$ ) is obtained as following relation: [2.90]

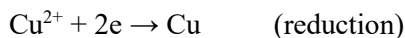
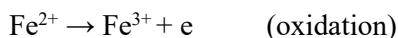
$$a = n_m \times L \times \sigma_m / m$$

in which  $\sigma_m$  is the molecular cross-sectional area.

## 2.6. Electrochemistry

### 2.6.1. Electrochemistry kinetic

The electrochemical reaction is oxidation reaction or reduction reaction i.e. chemical reaction involving electron transfer. Oxidation reaction in electrochemistry is electron generating process, and reduction reaction in electrochemistry is electron consuming process. [2.92]



The electrochemical system can be obtained by constructing a closed loop including more than two electrodes (the work electrode and counter electrode) where oxidation reaction and reduction reaction occur respectively. The basic electrochemical system consists of anode, cathode, electrolyte and external circuit, as shown in Figure 2.16.

The anode is electrode that oxidation reaction occurs, and cathode is electrode that reduction reaction occurs. Electrons produced in the anode move to cathode through the external circuit, thus current is generated in the electrochemical system. In response to current, the charge transfer is also accompanied by the cation and anion through the electrolyte.

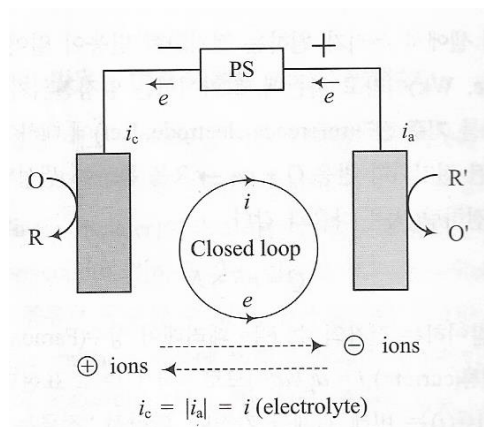


**Figure 2.16.** Configuration of electrochemical system with the closed loop. [2.92]

Copyright 2014, FREEACADEMY INC.

The electrochemical reaction of the electrode can be induced by the electron energy in the electrode using the potentiostat. As shown in Figure 2.17, in the cathode, when electron energy of electrode is sufficiently increased, the electron energy in electrode is higher than the energy level of the lowest unoccupied molecular orbital (LUMO) of chemical compound (reactant). Then, electrons in electrode can be transferred to reactant, and reduction reaction occurs. Vice versa in the anode. The electron energy of electrode is represented as the electrochemical potential, and equilibrium potential that electrochemical reaction can spontaneously occur can be formulated as followed, so-called Nernst equation; [2.92, 2.93]

$$E_{eq} = E^0 + \frac{nF}{RT} \left( \sum_i \ln a_i^O - \sum_j \ln a_j^R \right)$$

where,  $E_{eq}$  is equilibrium potential;  $E^0$  is standard electrode potential;  $n$  is number of electrons;  $F$  is Faradaic constant;  $R$  is ideal gas constant;  $a^O$  is activity of oxidants; and  $a^R$  is activity of reductants.

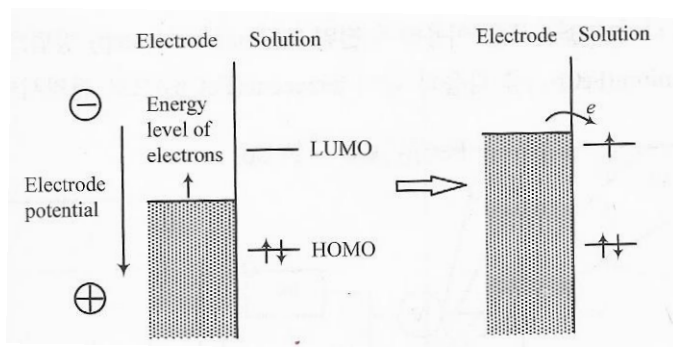


**Figure 2.17.** The electrochemical reduction reaction in the cathode with the change of electron energy of the electrode. [2.92] Copyright 2014, FREEACADEMY INC.

Meanwhile, Nernst equation is based on the view of thermodynamic, i.e. providing guideline for the standard that reaction can occur spontaneously, however cannot explain the how fast the reaction occurs. In the electrochemical reaction in electrode, the reaction progresses through the multi-steps (Figure 2.18). Basically, the reactant should transfer from the solution to the surface of electrode since reactant should be close enough to electrode for the electron tunneling. This is defined as mass transfer. The reactant near to the surface electrode forms the product through charge transfer reaction induced by the electron. The slowest step is the rate-determining step, which determines the kinetics of the electrochemical reaction. [2.92]

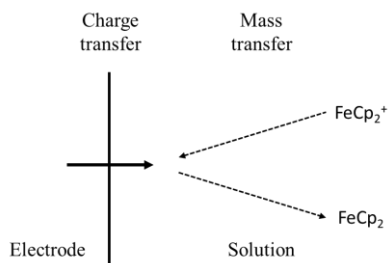


**Figure 2.18.** The charge transfer and mass transfer at the surface of electrode. [2.92] Copyright 2014, FREEACADEMY INC.

The kinetics of the electrochemical reaction is consistent with the net current of the electrochemical system. The correlation between the potential (voltage) of the electrochemical system and the net current of system ( $i_{net}$ ) can be expressed by the following equation: [2.92, 2.93]

$$i_{net} = i_0 \left[ \frac{C_O(0,t)}{C_O^*} e^{-\frac{\beta nF(E_{appl}-E_{eq})}{RT}} - \frac{C_R(0,t)}{C_R^*} e^{-\frac{(1-\beta)nF(E_{appl}-E_{eq})}{RT}} \right]$$

where,  $i_0$  is exchange current;  $\beta$  is symmetry factor;  $E$  is applied potential;  $E_{eq}$  is equilibrium potential;  $C_O^*$  and  $C_R^*$  are the bulk concentrations of oxidant and reductants, respectively;  $C_O$  and  $C_R$  are the concentrations of oxidant and reductants at the surface of anode and cathode, respectively.

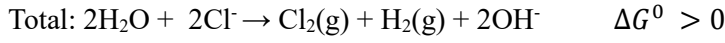
When, the charge transfer is the rate-determining step in the reaction,  $C_O(0,t)/C_O^* = C_R(0,t)/C_R^* = 1$ , the equation can be rewritten as follow, so called Butler-Volmer equation: [2.92, 2.93]

$$i_{net} = i_0 \left[ e^{-\frac{\beta nF(E_{appl}-E_{eq})}{RT}} - e^{-\frac{(1-\beta)nF(E_{appl}-E_{eq})}{RT}} \right]$$

The representative electrochemical systems are electrolytic cell and Galvanic cell. The electrolytic cell is used to synthesize the targeted chemical compound through the electrochemical reaction by supplying additional electrical energy. While Galvanic cell is used to produce electrical energy using the spontaneous electrochemical reaction. [2.92]

The example of electrolytic cell for electrolysis of NaCl solution shown in Figure 2.19, the electrochemical reactions that occur in the two electrodes are as followed; [2.92]





The electrochemical reactions are not spontaneous ( $\Delta G^0 > 0$ ) thus addition electrical energy should be supplied. The relationship between the potential of electrodes and current is plotted in Figure 2.20. If the potential of cathode has a more negative value based on  $E_{eq}^c$  (-0.84 V), the current (cathodic current,  $i_c$ ) increases exponentially. For the anode, anodic current ( $i_a$ ) exponentially increases as the potential of anode has a more positive value based on  $E_{eq}^a$  (1.36 V). The electrode current represents the electrochemical reaction rate. The applied potential ( $E_{appl}$ ) that should be supplied to the cell is determined by the thermodynamic and kinetics, as shown in a following equations: [2.92]

$$E^c = E_{eq}^c - \eta_c, E^a = E_{eq}^a + \eta_a \quad (|i_a| = i_c \neq 0)$$

$$E_{cell} = E_{eq}^a - E_{eq}^c \quad (|i_a| = i_c = 0)$$

$$E_{appl} = (E^a - E^c) + iR_{total}$$

$$E_{appl} = E_{cell} + \eta_a + \eta_c + iR_{total}$$

$$R_{total} = R_{solution} + R_{separator} + R_{circuit}$$

$E_{cell}$  is thermodynamic decomposition potential (voltage) that determines by the difference between the equilibrium potential (voltage) of the cathode and anode. When  $E_{cell}$  is applied to the cell, although the electrochemical reaction can occur thermodynamically, the current is zero in the cell. In addition to  $E_{cell}$ , additional potential is required to induce the electrolysis of NaCl solution, which is denoted as the overpotential ( $\eta_a$  and  $\eta_c$ ). Not only the overpotential of electrode, the additional voltage that compensates the  $iR$  drop, sum of all resistances (attributed to solution, separator, and circuit) in the cell should be applied.

Therefore, to induce the electrolysis of NaCl solution,  $E_{appl}$  should be applied to



the cell, and the reaction rate of electrolysis (current) is increased as  $E_{appl}$  increases.

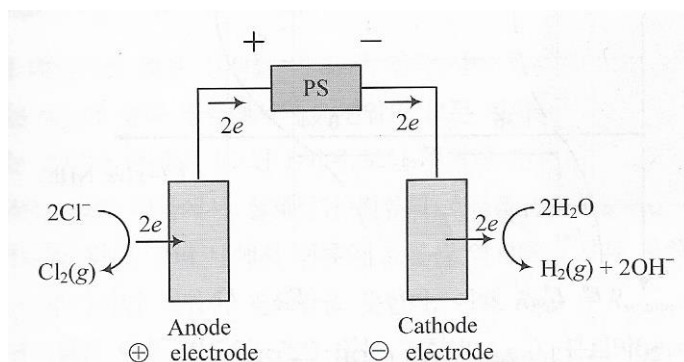


**Figure 2.19.** The electrochemical reaction in electrolytic cell. [2.92] Copyright 2014, FREEACADEMY INC.

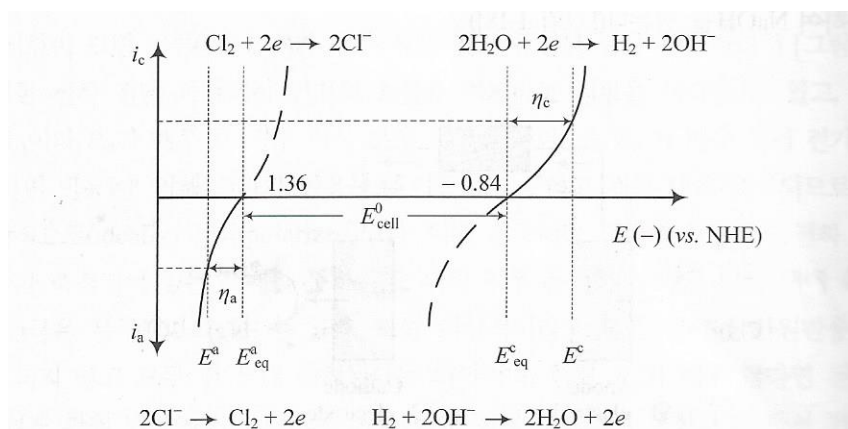


**Figure 2.20.** The current variation with the potential in the cathode and anode in electrolytic cell. [2.92] Copyright 2014, FREEACADEMY INC.

The example of Galvanic cell is fuel cell (Figure 2.21.), the electrochemical reactions that occur in the two electrodes are as followed; [2.92]



The reactions are spontaneous ( $\Delta G^0 > 0$ ), the potential between the two electrodes can be derived by the  $\Delta G^0 = -nFE_{cell}^0$  equation, having 1.23 V. This potential (voltage) is denoted as electromotive force, attributed to thermodynamic of the electrodes. However, the actual working voltage of the cell is less than electromotive force. Figure 2.22. shows the potential-current relationship of the electrodes. When the potential difference between the electrodes is  $E_{cell}^0$ , the current is zero. Due to the overpotentials of electrodes and  $iR$  drop of cell, the current is generated in lower voltage than  $E_{cell}^0$ . The working voltage of the cell ( $E_{wk}$ ) is expressed as follow; [2.92]

$$E^c = E_{eq}^c - \eta_c, \quad E^a = E_{eq}^a + \eta_a \quad (|i_a| = |i_c| \neq 0)$$

$$E_{wk} = (E^c - E^a) - iR_{total}$$

$$E_{cell} = (E_{eq}^c - E_{eq}^a) \quad (|i_a| = |i_c| = 0)$$

$$E_{wk} = E_{cell} - \eta_a - \eta_c - iR_{total}$$

To maximize the cell efficiency, it is crucial to minimize the overpotential of electrodes and the resistance of the cell.

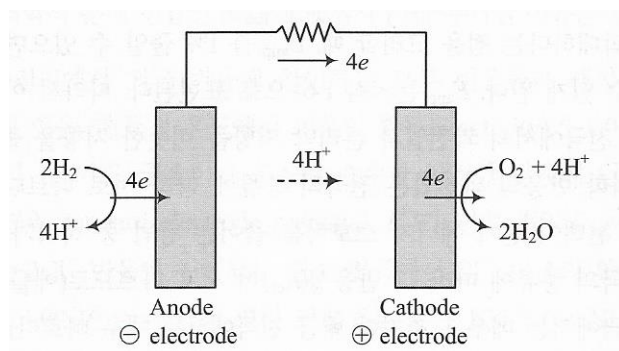


**Figure 2.21.** The electrochemical reaction in Galvanic cell. [2.92] Copyright 2014, FREEACADEMY INC.

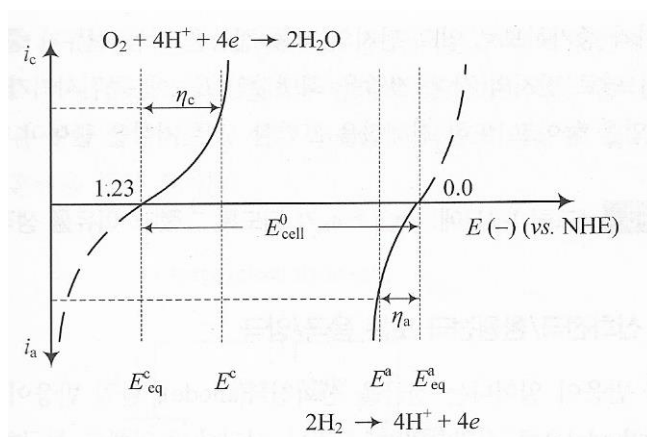


**Figure 2.22.** The current variation with the potential in the cathode and anode in Galvanic cell. [2.92] Copyright 2014, FREEACADEMY INC.

### 2.6.2. Electrocatalytic reaction (ORR)

Among the various types of the fuel cell using the different electrolyte, the proton exchange membrane fuel cell (PEMFC) has been actively studied. Because PEMFC can generate the electrical energy at low temperature ( $< 100\text{ }^{\circ}\text{C}$ ) at ambient condition appropriate for transport application and portable device application. The oxygen reduction reaction (ORR) occurs at the cathode. The typical ORR with the type of the electrolyte is summarized in Table 2.1.

The current-overpotential is following equation: [2.95]

$$i_c = i_{O_2}^0 \left( e^{-\frac{n_{aO}\alpha_O F \eta_c}{RT}} - e^{-\frac{n_{aO}(1-\alpha_O) F \eta_c}{RT}} \right)$$

where  $i_c$  is the ORR current density;  $i_{O_2}^0$  is the exchange current density;  $n_{aO}$  is the number of electrons transferred in the rate-determining step;  $\alpha_O$  is the transfer coefficient;  $F$  is the Faraday constant;  $\eta_c$  is the overpotential of ORR;  $R$  is the gas constant; and  $T$  is the temperature.

$i_{O_2}^0$  is an essential kinetic parameter that represents the electrochemical reaction rate at equilibrium. The higher  $i_{O_2}^0$  value indicates the rapid reaction.

The ORR proceeds through two pathways: i) oxygen is directly reduced to water ( $\text{H}_2\text{O}$ ) via  $4e^-$  ORR; ii) oxygen is firstly reduced to hydrogen peroxide ( $\text{H}_2\text{O}_2$ ) via  $2e^-$  ORR, followed by the additional reduction to  $\text{H}_2\text{O}$  via  $2e^-$  ORR.  $\text{H}_2\text{O}_2$  also can be remained as the final product and can be diffused to the electrolyte. [2.95]

Although there has been active the debate on elucidating ORR mechanism at atomic scale, the ORR mechanisms are still not fully understood. The prevalent mechanisms of ORR are summarized in Figure 2.23. The oxygen molecule ( $\text{O}_2$ )

diffuses to the surface of electrode, and adsorbed  $O_2$  is formed ( $O_2^*$ ).  $O_2^*$  can be reduced through the three pathways. [2.96] 1) the dissociation pathway: the O–O bond of  $O_2^*$  breaks directly, and an  $O^*$  intermediate is formed. The as formed  $O^*$  is reduced to  $OH^*$  and to  $H_2O^*$ . 2) the associative pathway:  $O_2^*$  is reduced to  $OOH^*$  and then the cleave of the O–O bond occurs, forming the  $O^*$  and  $OH^*$  intermediate. 3) the peroxo (or 2nd associative) pathway:  $O_2^*$  is reduced to  $OOH^*$  and to  $HOOH^*$ . The dominant pathway is determined with the reaction condition and electrode materials. The Density functional theory (DFT) calculations reported that the dissociation pathway and associative pathway can be dominant ORR process at low oxygen coverage and at high oxygen coverage, respectively. [2.97]

Generally, the kinetics of ORR is very slow and hinders the practical usage of ORR to applications, including PEMFC and  $H_2O_2$  production. In order to improve the kinetics of ORR, the electrocatalyst is required. Considering ORR mechanisms, the adsorption of intermediates ( $O^*$ ,  $OOH^*$ , and  $HOOH^*$ ) is crucial to ORR kinetics. Nørskov's group suggests that the adsorption of oxygen molecules on the electrode can be the origin of the overpotential of ORR. [2.98, 2.99] The binding energy of intermediates adsorbed to the electrode surface determines the ORR activity. If the binding energy is too weak, the charge transfer by the electron and proton to the adsorbed oxygen is limited. If the binding energy is too strong, the desorption of product ( $H_2O$ ) is sluggish, resulting in the blocking of the ORR active site for further oxygen adsorption. Therefore, an electrocatalyst which has a moderate binding energy to the intermediates is necessary.

So far, Pt-based catalyst has been dominantly used for practical application. It is expensive, and have other problems, including CO deactivation. [2.99] There is still enough room for improving the performance of ORR electrocatalyst and

tremendous efforts has been given to identifying an alternative ORR electrocatalyst. The relation between the ORR activity and the intermediate binding energy for various electrocatalysts including noble-metal, earth-abundant metal, doped graphene are identified and exhibits volcano-like trend, as shown in Figure 2.24. The electronic structure of these catalyst is the key that determines the binding energy of the intermediates. [2.99] Therefore, the controlling the electronic structure of electrocatalyst to have the appropriate binding energy of the intermediates is essential for improving the catalytic properties of ORR. [2.96, 2.99]

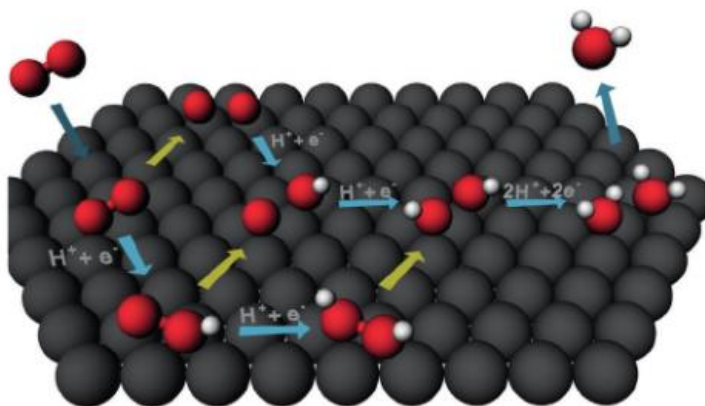


**Figure 2.23.** Proposed pathways for ORR. (black spheres: catalyst atoms; red spheres: oxygen atoms; white spheres: hydrogen atoms; yellow arrows: O–O bond cleavage; and blue arrows: the proton or electron transfer.) [2.96] Copyright 2016, John Wiley & Sons

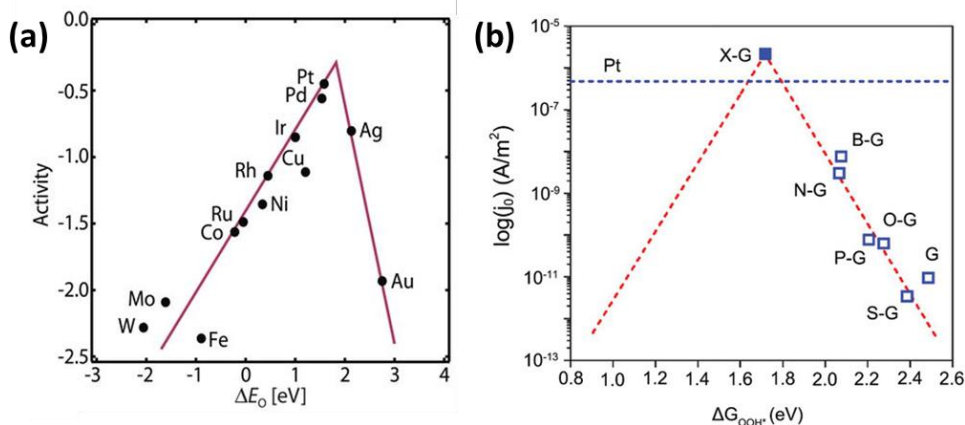


**Figure 2.24.** Volcano plot for metal ORR catalysts (a), and for heteroatoms-doped graphene catalysts. [2.100, 2.101] Copyright 2004, 2014, ACS Publications.

**Table 2.1.** Thermodynamic electrode potentials of ORR electrode. [2.94]

Electrolyte	ORR reactions	Thermodynamic electrode potential at standard conditions, V
Acidic aqueous solution	$O_2 + 4H^+ + 4e^- \rightarrow H_2O$	1.229
	$O_2 + 2H^+ + 2e^- \rightarrow H_2O_2$	0.70
	$H_2O_2 + 2H^+ + 2e^- \rightarrow H_2O$	1.76
Alkaline aqueous solution	$O_2 + H_2O + 4e^- \rightarrow 4OH^-$	0.401
	$O_2 + H_2O + 2e^- \rightarrow HO_2^- + OH^-$	− 0.065
	$HO_2^- + H_2O + 2e^- \rightarrow 3OH^-$	0.867
Non-aqueous aprotic solvents	$O_2 + e^- \rightarrow O_2^-$	Dependent on the type of solvent
	$O_2^- + e^- \rightarrow O_2^{2-}$	

## 2.7. Thermodynamic tools

The standard Gibbs free energy of a pure compound can be defined as follow: [2.102]

$$G_T^o = H_T^o - TS_T^o$$

where  $G_T^o$  represents the standard Gibbs free energy;  $H_T^o$  is the standard enthalpy of A;  $S_T^o$  is the standard entropy of A, and T is the absolute temperature.

$H_T^o$  and  $S_T^o$  have relationship with  $C_p$  as follows: [2.102]

$$H_T^o = \Delta H_{298\text{ K}}^o + \int_{298\text{ K}}^T C_p dT, \quad S_T^o = S_{298\text{ K}}^o + \int_{298\text{ K}}^T \frac{C_p}{T} dT$$

where  $C_p$  is isobaric specific heat capacity;  $\Delta H_{298\text{ K}}^o$  is enthalpy for compound at 298 K with reference of enthalpy of pure stable elemental species;  $S_{298\text{ K}}^o$  is standard entropy at 298 K.

The Gibbs free energy of gas species  $i$  can be written as follows:

$$G_i = G_i^o + RT \ln p_i$$

where  $G_i^o$  is molar Gibbs free energy of gas species  $i$  in standard state;  $p_i$  is pressure of gas species  $i$ ;  $R$  is gas constant; T is absolute temperature.

In the solid or liquid solution, the Gibbs free energy of A solid or liquid solution can be expressed as follows; [2.102]

$$G_{A(\text{in soln})} = G_{A(\text{pure})}^o + RT \ln a_A$$

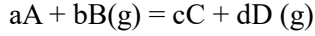
in which,  $G_A^o$  is molar Gibbs free energy of pure A;  $a_A$  is activity of A in solution.  $RT \ln a_A$  term represents the change of Gibbs free energy of A in solution due to the interaction with surrounding species, and  $a_A$  in dilute solution showing Henrian behavior is defined as follows: [2.102]

$$a_A = \frac{p_A}{p_A^o} = \gamma_A x_A$$



where  $p_A$  is vapor pressure of A in solution;  $p_A^o$  is vapor pressure in equilibrium of pure A;  $\gamma_A$  is activity coefficient.

For the chemical reaction involving solid or liquid solution,



the change of Gibbs free energy of the reaction is obtained by  $\Delta G_{rxn} =$

$$\sum G_{products} - \sum G_{reaction}.$$

In equilibrium condition,  $\Delta G_{rxn} = 0$  and  $\Delta G^o = -RT \ln \left( \frac{a_C^c a_D^d}{a_A^a a_B^b} \right)$ .

In A-B solution (solid or liquid solution), the Gibbs free energy of A-B solution is expressed as follow; [2.102]

$$\begin{aligned} G_{solution} &= \sum x_i G_i \\ &= (x_A G_A^o + x_B G_B^o) + RT(x_A \ln a_A + x_B \ln a_B) \end{aligned}$$

When A and B are ideal solution,  $\gamma_A = 1$ ,  $\gamma_B = 1$

$$G_{solution} = (x_A G_A^o + x_B G_B^o) + RT(x_A \ln x_A + x_B \ln x_B)$$

When A and B are regular solution,  $RT \ln \gamma_A = \Omega_{AB} x_B^2$

$$G_{solution} = (x_A G_A^o + x_B G_B^o) + RT(x_A \ln x_A + x_B \ln x_B) + \Omega_{AB} x_A x_B$$

in which  $\Omega_{AB}$  is regular solution parameter.

When A and B are general solution,  $\gamma_A = f(x, T)$

$$G_{solution} = (x_A G_A^o + x_B G_B^o) + RT(x_A \ln x_A + x_B \ln x_B) + G^{ex}$$

$$G^{ex} = \sum_{i,j \geq 1} \omega_{AB}^{ij} x_A^i x_B^j$$

in which  $\omega_{AB}^{ij}$  is general solution parameter.

### 2.7.1. Phase diagram

Phase diagram is the collection of minimum Gibbs free energy assemblage of given system in equilibrium condition, as shown in Figure 2.25. The thermodynamically stable phases in the condition of given system, including temperature, pressure, and composition, can be predicted using phase diagram.

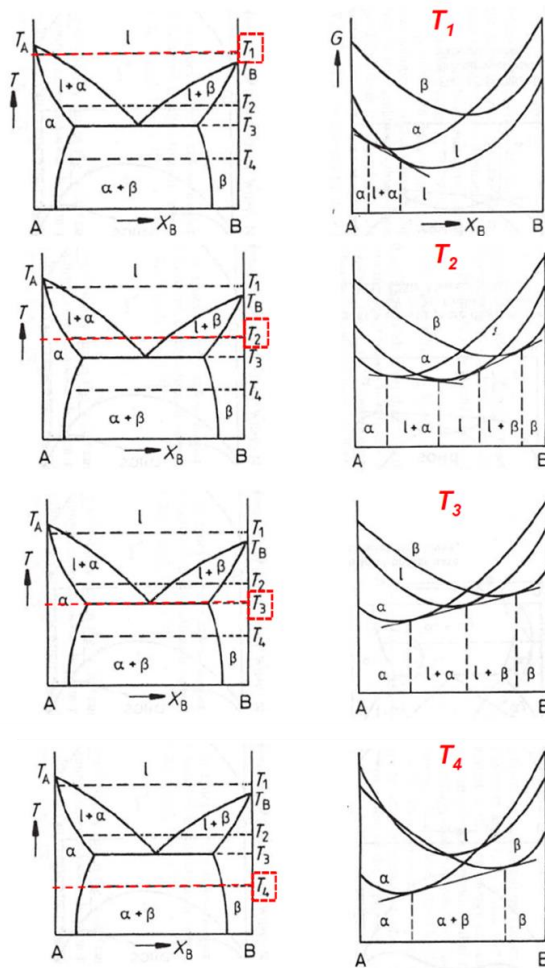


**Figure 2.25.** The derivation of phase diagram of binary system (left) from the minimum Gibbs free energy assemblage of given system in equilibrium condition (right). [2.103] Copyright 2009, CRC press.

### 2.7.2. Ellingham diagram

Ellingham diagram is a graphical form that give a guideline for the feasibility of chemical reaction based on the thermodynamic (the change of the Gibbs free energy of the reaction,  $\Delta G_{rxn}$ ). It is practically used for the gas involving reaction, various metal compounds, including carbides, nitrides, oxides, and sulfides.

Figure 2.26 shows Ellingham diagram of the metal oxidation reactions. [2.102] The left y-axis represents the change of standard Gibbs free energy of the oxidation reaction ( $\Delta G^o$ ) and right y-axis correspond to the oxygen partial pressure ( $p_{O_2}$ ) in Figure 2.16. For comparison, all  $\Delta G^o$  values for oxidation reaction are calculated by the reactions involved the same quantity of oxygen (one mole  $O_2$ ).  $\Delta G_{rxn}$  varying with  $p_{O_2}$  can be calculated by the superimposition of an  $\Delta G^o = RT \ln p_{O_2}$  line on Ellingham diagram. [2.102] The thermodynamic stability of the metal oxide is increased, as the position of the oxidation reaction line is lower. By comparing the  $\Delta G^o$  values, the preference of oxidation and reduction between the different metal compounds can be predicted using this Ellingham diagram.

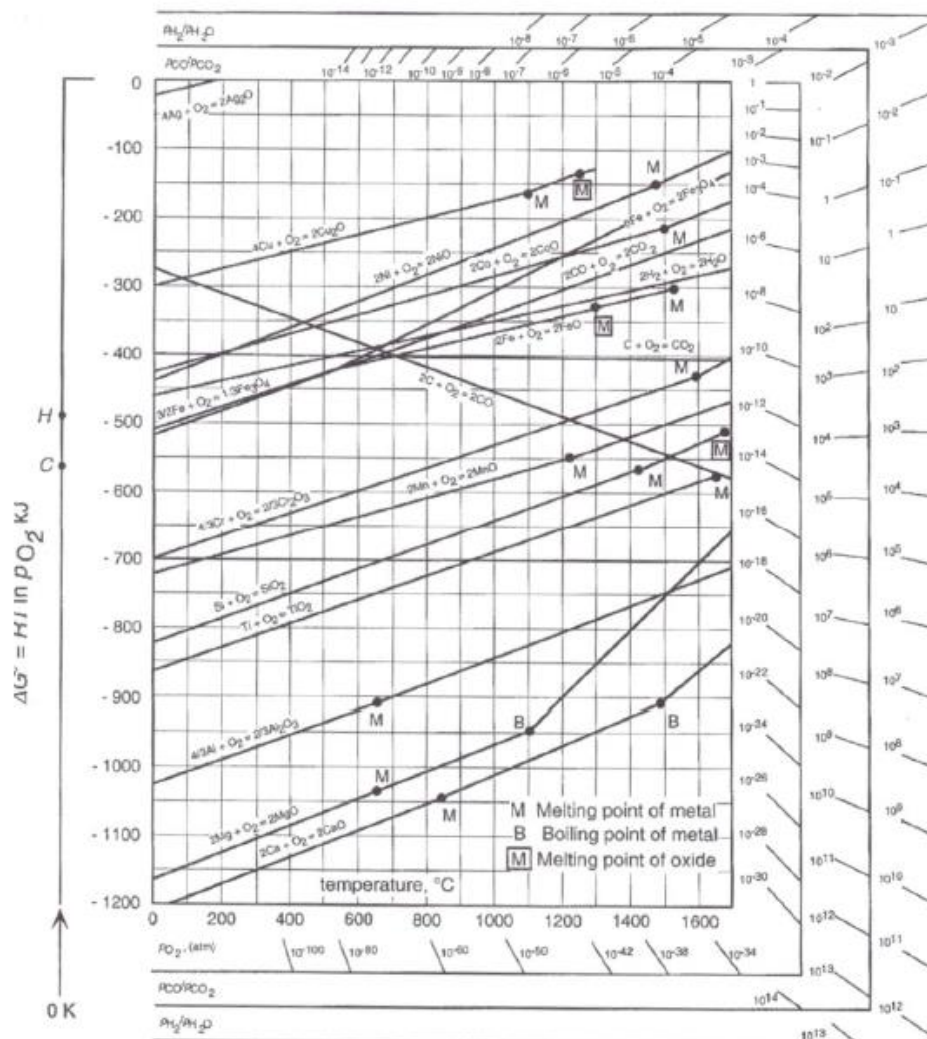


**Figure 2.26.** Ellingham diagram for considering the standard Gibbs free energy of various oxide compounds according to the temperature. [2.102] Copyright 2014, FREEACADEMY INC. Copyright 2017, CRC press.

## Chapter 3. Experimental

### 3.1. Chlorination

The chlorination process was conducted in a customized chlorination reactor setup, schematized in Figure 3.1.

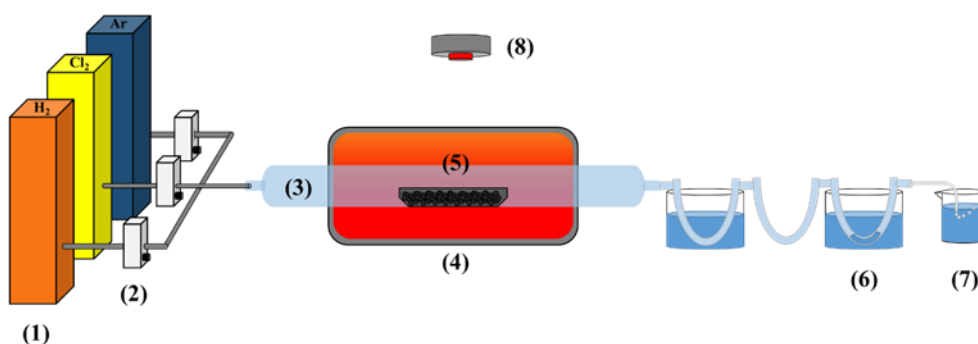


**Figure 3.1.** Schematic diagram representing chlorination reactor setup: (1) gas cabinet, (2) flowmeter, (3) horizontal quartz-tube, (4) tube furnace, (5) crucible containing starting materials, (6) H<sub>2</sub>SO<sub>4</sub> solution, (7) KOH solution, and (8) gas detector.

The procedure of chlorination process is summarized in Figure 3.2.

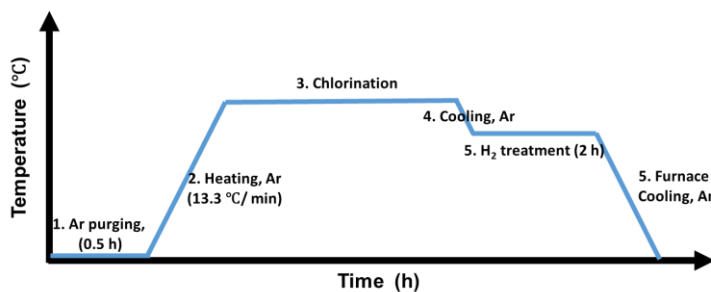
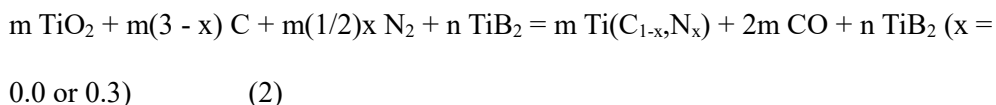
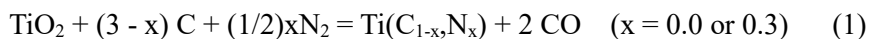


**Figure 3.2.** The heating schedule of the chlorination process to synthesize the porous carbon materials.

## 3.2. Preparation of CB/CNB materials via the one-pot chlorination process

### 3.2.1. Raw powder synthesis

Raw powder synthesis:  $\text{Ti}(\text{C}_{1-x}\text{N}_x)$  powders and in-situ  $\text{Ti}(\text{C}_{1-x}\text{N}_x)\text{-TiB}_2$  composite powders were synthesized via high-energy ball milling and carbothermal reduction, which is a the general method for transition metal compound nano-powder. The starting powders were  $\text{TiO}_2$  (particle size:  $\leq 20 \mu\text{m}$ , purity: 99%, Sigma-Aldrich, St.Louis, MO, USA), graphite (particle size:  $1.65 \mu\text{m}$ , purity: 99%, SeungLim Carbon Metal Co., Ansan, Korea), and  $\text{TiB}_2$  (particle size:  $< 10 \mu\text{m}$ , Sigma-Aldrich, St.Louis, MO, USA). These raw materials with appropriate molar ratios according to Eqs. (1) and Eq. (2) were mixed dry to obtain target compositions of  $\text{Ti}(\text{C}_{1-x}\text{N}_x)$ . m and n values in Eq.(2) were set to meet the mixing molar ratio of carbon to boron in the precursors (the ratio was fixed to 1:1 in all specimens), depending on x value in  $\text{Ti}(\text{C}_{1-x}\text{N}_x)$ ,  $x = 0.0$  and  $0.3$ . The mixtures were ground using a planetary mill (Pulverisette 7, Fritsch, Idar-Oberstein, Germany) at 200 rpm for 5 h. The milling was conducted at a ball-to-powder weight ratio of 40:1. WC-Co balls and a WC-Co coated steel jar were used for milling.



The milled powder mixtures of various compositions were loaded into a graphite furnace, and the carbothermal reduction was conducted at  $1400^\circ\text{C}$  in  $10^{-2}$  torr vacuum for 2 h to synthesize TiC and TiC-TiB<sub>2</sub> composite. The same procedure was

followed to synthesize  $\text{Ti}(\text{C}_{0.7}\text{N}_{0.3})$  and  $\text{Ti}(\text{C}_{0.7}\text{N}_{0.3})\text{-TiB}_2$  composite except that the atmosphere was changed to 10 torr  $\text{N}_2$ . The successful synthesis of  $\text{Ti}(\text{C}_{0.7}\text{N}_{0.3})$  (or  $\text{TiC}$ ) and  $\text{Ti}(\text{C}_{0.7}\text{N}_{0.3})\text{-TiB}_2$  (or  $\text{TiC-TiB}_2$ ) composite is verified by XRD and FE-SEM analysis, as shown in the appendix 1.1 section.

### 3.2.2. Synthesis of samples

*Chlorination:* High purity  $\text{Cl}_2$  (99.995 %), Ar-10 vol.%  $\text{H}_2$ , and  $\text{H}_2$  (99.999 %) gases were introduced as reactive and purging gases to a reaction chamber equipped with a carbon sheet boat installed in the horizontal quartz tube. All the gas flow rates were controlled with the flowmeter. Two grams of starting material ( $\text{Ti}(\text{C}_{1-x}\text{N}_x)$  or  $\text{Ti}(\text{C}_{1-x}\text{N}_x)\text{-TiB}_2$  composite) was loaded in the carbon boat. The temperature of the reaction chamber was controlled by SiC heating materials and R-type thermocouple was installed to measure the specimen temperature. The quartz tube was purged with Ar-10 vol.%  $\text{H}_2$  mixture gas (100 SCCM) over 30 minutes prior to each experiment and the furnace was heated to 800 °C in the same atmosphere with a ramp rate of 13.3 °C/min. During the chlorination experiment, only pure  $\text{Cl}_2$  gas was supplied for 3 h at the flow rate of 12 SCCM. After the chlorination reaction,  $\text{Cl}_2$  gas was replaced by Ar-10 vol.%  $\text{H}_2$  gas (50 SCCM) and the furnace was cooled down to 600 °C. At this temperature,  $\text{H}_2$  gas (20 SCCM) was employed for 2 h in order to remove any residual  $\text{Cl}_2$  gas and residual chlorides trapped in the pores of final products.

*Synthesis of C and CN:* C and CN were synthesized via the chlorination of synthesized  $\text{TiC}$  and  $\text{Ti}(\text{C}_{0.7}\text{N}_{0.3})$ , respectively. They were set as a control group to examine the effect of boron on C and CN.

*Synthesis of G-CB and G-CNB:* G-CB and G-CNB were synthesized by the gas transport method. The commercial micron-size  $\text{TiB}_2$ , and synthesized  $\text{TiC}$  and  $\text{Ti}(\text{C}_{0.7},\text{N}_{0.3})$  were separately located in reaction crucible. The C:B molar ratio in raw  $\text{Ti}(\text{C}_{1-x},\text{N}_x)$  and  $\text{TiB}_2$  was fixed to be 1:1. During the chlorination process, boron was supplied to the surface of C and CN only in the form of  $\text{BCl}_3$  gas produced by chlorination of  $\text{TiB}_2$ .

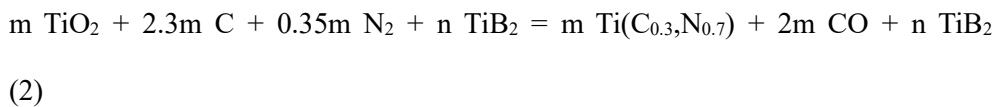
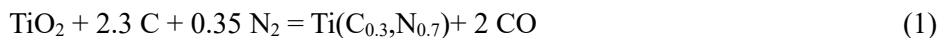
*Synthesis of D-CB and D-CNB:* D-CB and D-CNB were synthesized by the direct bond method. The preparation of powder was just the same as  $\text{TiC}$  or  $\text{Ti}(\text{C}_{0.7},\text{N}_{0.3})$  except a proper amount of commercial micron-size  $\text{TiB}_2$  powder added into oxide and graphite mixture. During the carbothermal reduction,  $\text{TiC}$  and  $\text{Ti}(\text{C}_{0.7},\text{N}_{0.3})$  formed on the surface of  $\text{TiB}_2$ . Thus, direct junction of  $\text{TiC}$  (or  $\text{Ti}(\text{C}_{0.7},\text{N}_{0.3})$ )- $\text{TiB}_2$  was established well and their contact area was maximized as shown in the appendix 1.1 section. Therefore, during the chlorination, boron atoms could be readily supplied to C and CN structure through solid-state atomic diffusion. The C:B molar ratio in all samples was fixed to be 1:1 which was exactly the same ratio as used in G-CB and G-CNB.



### 3.3. Preparation of BN embedded porous carbon via one-pot chlorination process

#### 3.3.1. Raw powder synthesis

Ti(C<sub>0.3</sub>N<sub>0.7</sub>) powder and Ti(C<sub>0.3</sub>N<sub>0.7</sub>)-TiB<sub>2</sub> composite powder were synthesized via the high-energy ball milling and the carbothermal reduction in nitrogen atmosphere. TiO<sub>2</sub> (particle size: ≤ 20 μm, purity: 99%, Sigma-Aldrich, St.Louis, MO, USA), graphite (particle size: 1.65 μm, purity: 99%, SeungLim Carbon Metal Co., Ansan, Korea), and TiB<sub>2</sub> (particle size: < 10 μm, Sigma-Aldrich, St.Louis, MO, USA) were used as the raw materials. These powders were mixed dry with appropriate molar ratios according to Eqs. (1) and (2). m and n values were set to meet the 4:1, 4:4, and 1:4 mixing molar ratios of carbon to boron in the precursors. The mixtures were ground using a planetary mill (Pulverisette 7, Fritsch, Idar-Oberstein, Germany) at 200 rpm for 5 h. The milling was performed at a ball-to-powder weight ratio of 40:1. WC-Co balls and a WC-Co coated steel jar were used.



The milled powder mixtures were loaded into a graphite furnace, and the carbothermal reduction was conducted at 1400 °C in 10 torr N<sub>2</sub> atmosphere.

### 3.3.2. Synthesis of D-BNC

Two grams of starting  $\text{Ti}(\text{C}_{0.3}\text{N}_{0.7})$  or  $\text{Ti}(\text{C}_{0.3}\text{N}_{0.7})\text{-TiB}_2$  materials were loaded in the carbon boat and installed in the horizontal quartz tube. High purity  $\text{Cl}_2$  (99.995 %), Ar-10 vol.%  $\text{H}_2$ , and  $\text{H}_2$  (99.999 %) gases were supplied as reactive and purging gases, and their flow rates were controlled with the flowmeters. The temperature of the tube furnace was controlled by SiC heating materials and a R-type thermocouple was installed to measure the temperature of reaction zone. Samples were loaded into the tube furnace at room temperature. The quartz tube was purged with Ar-10 vol.%  $\text{H}_2$  mixture gas (100 sccm) over 30 min prior to each experiment and the furnace was heated to a targeted temperature (400, 600, 700, 800, and 1000 °C) with a heating rate of 13.3 °C/min. During the chlorination,  $\text{Cl}_2$  gas was supplied for 3 h at the flow rate of 12 sccm. After the chlorination,  $\text{Cl}_2$  gas was replaced with Ar-10 vol.%  $\text{H}_2$  gas (50 sccm) and the furnace was cooled down to 600 °C. At this temperature,  $\text{H}_2$  gas (20 sccm) was supplied for 2 h in order to remove any residual  $\text{Cl}_2$  gas and chlorides trapped in the pores of final products. Then, the furnace was cool down to room temperature, and the sample was taken out after the experiment.

### **3.4. Preparation of M-CN/CNB materials via the one-pot chlorination process**

#### **3.4.1. Chemical**

Starting materials were commercially available micron-sized  $\text{Ti}(\text{C}_{0.5}\text{N}_{0.5})$  solid solutions (Treibacher Industrie AG, 99.5 %; 1 – 2  $\mu\text{m}$ ), micron-sized  $\text{TiB}_2$  (particle size: < 10  $\mu\text{m}$ , Sigma-Aldrich, St.Louis, MO, USA), iron (III) acetylacetonate ( $\text{Fe}(\text{acac})_3$ ,  $\geq 99.9$  % trace metal basis, Sigma-Aldrich, St.Louis, MO, USA), and nickel (II) acetylacetonate ( $\text{Ni}(\text{acac})_3$ ,  $\geq 99.9$  % trace metal basis, Sigma-Aldrich, St.Louis, MO, USA).

#### **3.4.2. Synthesis of M-CNB**

M-CNB were synthesized via the chlorination of commercial  $\text{Ti}(\text{C}_{0.5}\text{N}_{0.5})$ , micron  $\text{TiB}_2$  and  $\text{M}(\text{acac})_x$  ( $\text{Fe}(\text{acac})_3$ ,  $\text{Ni}(\text{acac})_2$ ) mixture. Precursors were mixed by hand in an agate mortar for fifteen minutes before the chlorination reaction. The chlorination reaction was proceeded at 800 °C for five hours at same heating rate to the previous section. For controlled experiment, M-CN were also synthesized in the same procedure as synthesis of M-CN, but without boron precursor.  $\text{Ti}(\text{C}_{0.5}\text{N}_{0.5})$  and  $\text{M}(\text{acac})_x$  ( $\text{Fe}(\text{acac})_3$ ,  $\text{Ni}(\text{acac})_2$ , or  $\text{Co}(\text{acac})_2$ ) were mixed by hand in an agate mortar for fifteen minutes before the chlorination reaction. The chlorination reaction was progressed for five hours at 800 °C.

### **3.5. Preparation of M-CN/CNB materials via the one-pot pyrolysis process**

#### **3.5.1. Chemical**

Iron nitrate (III) nonahydrate (99.99 % trace metal basis, Sigma-Aldrich), Nickel (II) nitrate hexahydrate (puriss. p.a, > 98.5 % (KT), Sigma-Aldrich), Urea (99.0-100.5 %, Sigma-Aldrich), boric acid ( $\text{H}_3\text{BO}_3$ , 99.5 %, Cica-Reagent, Kanto chemical Co., Inc ), and Poly(Ethylene Glycol) (PEG) (average Mn 2,050, chips, Sigma-Aldrich) are used as the source of Fe, Ni, N, B, and C in the present study. All chemicals were used directly in the experiment without additional purification process.

#### **3.5.2. Synthesis of M-CN**

Synthesis of the M-CN(20)-T and M-CN-T: The metal nitrate (Iron nitrate (III) nonahydrate (12.0 mg, mmol) or Nickel (II) nitrate hexahydrate (4.4 mg, mmol)) was mixed with urea (5.0 g), PEG (0.5 g) and boric acid (0.15 g) for M-CN(20)-T and zero amount for CN in 100 ml DI water. This mixture was stirred and dried at 80 °C overnight. The obtained powder was ground and contained in an alumina crucible. Then, the sample in an alumina crucible was loaded into an alumina tube furnace for next treatment. The Ar gas purging was initially conducted for 1 h at room temperature. The heat treatment was then carried out at the target temperature (600, 700, 800, 900, 950 and/or 1000 °C) for 4 h according to the heating schedule as shown in Figure 3.3.

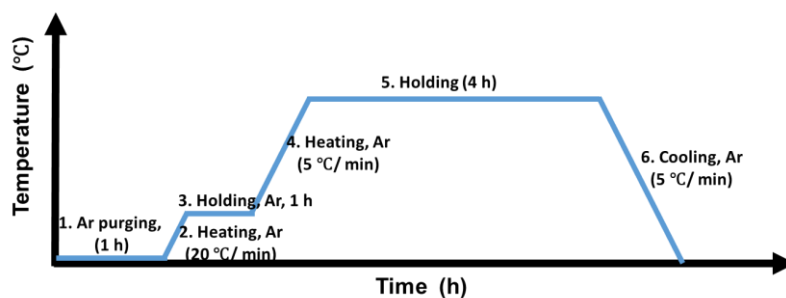


**Figure 3.3.** The heating schedule of the pyrolysis process to synthesize the porous carbon materials.

Synthesis of the controlled sample: The Fe-CNB(1)-950 and Fe-CNB(5)-950 were synthesized using the same process as Fe-CNB(20)-950. The amount of boric acid for these two samples were 7.5 mg and 37.5 mg, respectively. The Fe-CN-700-1min and Fe-CNB(20)-700-1min were also prepared by doing 1 min heat treatment at 700 °C.

### 3.6. Characterization

The average yield for carbon products obtained after chlorination was calculated by the following equation and Three samples were tested under the same experimental condition:

$$Yield(\%) = \frac{\text{Obtained mass (g)}}{\text{Theoretical mass of C+N in Ti(C}_{1-x}\text{N}_x)} \times 100 \quad (1)$$

#### 3.6.1. Structural analysis

Morphological analysis and Eenergy Dispersive Spectrometry (EDS) analysis were carried out using High Resolution-Transmission Electron Microscopy (HR-TEM, JEM-2100F, JEOL Ltd., Japan) and Field Emission-Scanning Electron Microscopy (FE-SEM, MERLIN Compact, ZEISS, German). X-ray diffraction (XRD) spectra were obtained using X-ray diffractometer (D-MAX2500-PC, Rigaku, Japan) with Cu-K $\alpha$  radiation ( $\lambda$ : 1.54Å) operated at 200 mA and 40 kV. Raman analysis was conducted using Raman spectroscopy (LabRamn HV Evolution, HORIBA, Japan) using an Ar ion laser (514.5 nm) at 50x magnification (~2  $\mu$ m spot size). Gas adsorption analysis was performed using BELSORP-MAX (BEL JAPAN INC., Japan) with N<sub>2</sub> adsorbate at 77 K. The BET SSA was determined from P/P<sub>0</sub> range between 0.01 atm to 0.15 atm. Before each gas adsorption measurement, the specimen was pre-heated at 300 °C for 24 hours under vacuum to remove any residual water and other physically adsorbed impurities.

### 3.6.2. Chemical analysis

X-ray photoelectron spectroscopy (XPS) analysis was carried out at Pohang Accelerator Laboratory (PAL) 10A2 beamline (HRPES-II,  $h\nu = 650$  eV). The binding energy of 284.5 eV was selected as a reference for C 1s. X-ray photoelectron spectroscopy (XPS) analysis was carried out using an Electron Spectroscopy for Chemical Analysis (AXIS SUPRA, Kratos Axis Supra, UK). A binding energy of 284.5 eV was selected as a reference for C 1s. Electron Energy Loss Spectroscopy (EELS) measurements and the corresponding elemental mapping were conducted by Tecnai Fe20 (FEI) at 200 kV. Fourier transform infrared spectra (FTIR) were recorded in Vacuum FT-IR/Microscope spectrometer (Vertex-80V/Hyperion2000, BRUKER, German). Elemental analysis for carbon and nitrogen element was carried out using Elemental analyzer (Flash 2000, Thermo Fisher Scientific, Germany). The Inductively Coupled Plasma spectrometer (ICP) analysis was performed to measure the content of boron and metal element by ICP-Atomic Emission Spectrometer (AES) (OTIMA 4300DV, Perkin-Elmer, USA). X-ray absorption near edge structure (XANES) was used for the chemical state analysis and coordination symmetry, and extended X-ray absorption fine structure (EXAFS) was used to elucidate the local geometric factor around iron. XANES analysis was conducted after background subtraction and normalization. The EXAFS signals for the Fe K-edge of the samples were extracted and were Fourier-transformed (FT) over the k-space range of 2.5 – 10 Å<sup>-1</sup>, using k3 weight and a Hanning window. All experimental measurements are conducted from 10C Wide-Energy XAFS beamline of Pohang Light Source (PLS-II).

### 3.6.3. Oxygen reduction reaction (ORR) activity measurement

The electrochemical measurements for the H<sub>2</sub>O<sub>2</sub> production of CBs, CNBs, and D-BNCs were performed using an Autolab electrochemical potentiostat (PGSTAT302N, Metrohm). For the rotating ring-disk electrode (RRDE) measurements (Pine Instruments Corporation), a standard three-electrode cell was used for the electrochemical tests. Ag/AgCl electrode was used as a reference electrode, a graphite rod was used as a counter electrode and the catalyst film coated disk electrode of RRDE (glassy carbon electrode, 0.2475 cm<sup>2</sup> area) was used as the working electrode. Before measurement, the working electrode was polished mechanically with alumina suspension (Buehler) and rinsed with deionized water. To prepare the ink, as-synthesized catalysts (5 mg) were mixed in 1 mL of solution containing 950  $\mu$ L of isopropanol (Sigma aldrich) and 50  $\mu$ L of 5 wt.% Nafion solution (Sigma aldrich), followed by ultrasonication for 20 min to form homogeneous inks. 4.95  $\mu$ L of the catalyst ink was then drop-casted onto a disk electrode of the RRDE tip spinning at an initial rate of 100 rpm and advanced to 400 rpm to achieve uniform catalyst layer and electrode coverage, then the electrode catalyst loading was 100  $\mu$ g cm<sup>-2</sup>. ORR performance was evaluated with cyclic voltammetry (CV) measurement between 0.05 and 1.05 V (vs. RHE) in O<sub>2</sub>-saturated 0.1 M KOH electrolyte at a scan rate of 5 mV s<sup>-1</sup> and a rotation speed of 1600 rpm, while holding the potential of Pt ring electrode at 1.2 V (vs. RHE). All measured ring currents were also corrected using the collection efficiency of RRDE setup. The reduction currents for ORR were corrected by subtracting the current obtained in an Ar-saturated electrolyte from that measured in O<sub>2</sub>-saturated conditions. The H<sub>2</sub>O<sub>2</sub> selectivity was calculated using the following equation:



$$Selectivity\ (\%) = 200 \times \frac{I_r/N}{I_d + I_r/N} \quad (2)$$

where  $I_r$  and  $I_d$  denote the ring current and disk current, respectively, and  $N$  is the collection efficiency of RRDE set-up. The outer-sphere electron transfer kinetics were evaluated using Nicholson method. We employed the  $[Ru(NH_3)_6]^{2+/3+}$  as a redox probe to characterize the electrochemical properties of carbon based electrodes. CV was performed from -0.6 to 0.2 V (vs Ag/AgCl) at a scan rate of 50 mV s<sup>-1</sup> in Ar-saturated electrolyte of 0.1 M KCl + 1 mM  $[Ru(NH_3)_6]Cl_2$ . The CV data were iR-corrected with 97%. The redox peak ex-situ ( $\Delta E_p$ ) was used to calculate the electron transfer with the following equation:

$$k^0 = \Psi \sqrt{\frac{\pi D \nu n F}{RT}} \quad (3)$$

where  $k^0$ ,  $\Psi$ ,  $D$ ,  $\nu$  and  $n$  represent the rate constant, charge transfer parameter, diffusion coefficient of  $[Ru(NH_3)_6]^{2+/3+}$  in 0.1 M KCl ( $8.43 \times 10^{-6}$  cm<sup>2</sup> s<sup>-1</sup>),<sup>50</sup> scan rate, electron transfer number (1 for the Ru redox complex). The  $\Psi$  is determined by the  $\Delta E_p$  value, then the rate constant is able to be derived with  $\Delta E_p$ . The equation is as follow:

$$k^0 = 1.54 \times \sqrt{\frac{D \nu n F}{RT}} \cdot \exp\left[-\frac{n F \Delta E_p}{4 RT}\right] \quad (4)$$

The CV measurement was repeated several times and averaged  $\Delta E_p$  was able to be obtained.

To quantitate the amount of H<sub>2</sub>O<sub>2</sub> molecules and achieve high peroxide concentrations, we performed the electrochemical ORR in a microfluidic cell. For the electrosynthetic flow cell test, 0.1 mg/cm<sup>2</sup> of carbon catalyst was air-brushed onto 5 cm<sup>2</sup> JNT-30A GDL electrodes as ORR cathode. 5cm<sup>2</sup> of nickel foam (pressed) electrode was used as anode. The two electrodes were placed on opposite sides in the flow cell without a membrane separator. O<sub>2</sub>-saturated KOH (1.0 M concentrated) with 10 mM EDTA was used as electrolyte and stabilizer each. The cathode was open to the atmosphere. The flow rate of KOH solution was 10 mL/min, as controlled by a peristaltic pump, and the electrolyte (total 40 mL) was reflux to obtain the concentrated H<sub>2</sub>O<sub>2</sub> product solution. Two types of flow field were used with or without the hole for reference electrode (Ag/AgCl, RE-1CP, ALS), to conduct two- or three-electrode cell configuration. A current of 250 mA was employed for H<sub>2</sub>O<sub>2</sub> production. After the electrochemical reaction, the generated amount of H<sub>2</sub>O<sub>2</sub> was detected by titrating with standard ceric sulfate solution. The Faradaic efficiency (FE) of the electrosynthetic cell for H<sub>2</sub>O<sub>2</sub> production is calculated using the following equations.

$$FE_{\text{cell}} = (\text{generated H}_2\text{O}_2 \text{ [mol]}) \cdot 2 \cdot 96485 / (\text{total amount of charge [C]})$$

The 4<sup>-</sup> electron pathway ORR performance for M-CN and M-CNB materials was measured with an Autolab potentiostat (PGSTAT302N, Metrohm) in a standard three-electrode cell with a graphite rod as a counter electrode and a saturated Ag/AgCl as a reference electrode. The catalyst ink was prepared by dispersing 10 mg catalyst in 500  $\mu$ L Nafion solution (400  $\mu$ L 2-propanol (Sigma-Aldrich), 50  $\mu$ L water, and 50  $\mu$ L Nafion solution (5 wt%, Simga-Aldrich)). The working electrode

was prepared by dropping the catalyst ink (8.66  $\mu\text{L}$ ) onto the glassy carbon (0.248  $\text{cm}^2$ ) of the rotating ring-disk electrode (RRDE, Pine, E7R9 series tips) which was left for drying at room temperature. This resulted in a catalyst loading of 700  $\mu\text{g}/\text{cm}^2$ . Before the electrochemical experiments, the Ag/AgCl reference electrode was calibrated against a Pt electrode in the  $\text{H}_2$  purged electrolyte. Accordingly, all of the potentials shown are the RHE scale. The ORR performance was measured in an  $\text{O}_2$ -saturated 0.1 M KOH (Sigma-Aldrich, 99.99 wt%) solution at a rotating rate of 1600 rpm and a scan rate of 10 mV/s at 293 K in a water bath. The non-Faradaic capacitance term was calibrated by reduction of cyclic voltammetry under Ar at the same scan rate. The total electron transfer number was calculated from the disk/ring current of the RRDE system, setting the Pt ring potential at 1.2 VRHE. Supercapacitor performance was conducted by using the same system. The specific capacitance of these carbonaceous materials were measured in a 1 M KOH solution purged with Ar gas.

#### **3.6.4. Electrical conductivity**

We conducted the Electrochemical impedance spectroscopy (EIS) with three-electrode cell which is same with the electrochemical ORR measurement using EIS instrument (Zennium, Zahner). The measurement was obtained under a constant voltage (0 V vs. RHE) in Ar-saturated 1.0 M KOH electrolyte. The frequency range is from 100 mHz to 100 kHz with a 5 mV amplitude.

### **3.7. Theromdynamic calculation**

#### **3.7.1. Thermodynamic equilibrium calculation**

The FactSage thermochemical software (version 7.3) [3.1] was employed to perform the thermodynamic equilibrium calculations and phase-diagram calculations. The stable phases formed by the chlorination of the Ti(C,N) solid solution and Ti(C,N) solid solution-TiB<sub>2</sub> mixture were calculated depending on the mole of Cl<sub>2</sub>(g) and temperatures. FACTPS databases and FSSStel database were used for all stoichiometric solids and Ti(C,N) solid solutions, and gas species in the Ti-C-N-Cl and Ti-C-N-B-Cl system. The identical thermodynamic equilibrium calculations were conducted in the chlorination of 1) Fe- Ti(C,N) solid solution system, 2) Fe- Ti(C,N) solid solution-TiB<sub>2</sub> system 3) Ni- Ti(C,N) solid solution system, 4) Ni- Ti(C,N) solid solution-TiB<sub>2</sub> system. All thermodynamic calculations were performed for a closed system at a constant total pressure of 1 atm. The thermodynamic calculation was used to simulate Fe-CN and Fe-CNB(20) synthesis process. In the calculation, both PEG and Urea for carbon and nitrogen source are considered together with Fe and B<sub>2</sub>O<sub>3</sub>. All possible solids, liquid oxide, and gas phase were considered in the equilibrium calculation.

#### **3.7.2. Phase diagram calculation**

The phase diagrams of Fe-C, Fe<sub>2</sub>B-C, Ni-C, Ni<sub>2</sub>B-C, and Ni<sub>3</sub>B-C system at constant total pressure of 1atm were calculated using the FactSage thermochemical software (version 7.3)

To calculate the phase diagram in nano-scale, The surface energy contribution on the molar Gibbs free energy of solid phases is calculated as follows assuming a spherical shape of radius  $r$  [3.2].

$$G^{surface} = \frac{3 \cdot \gamma_i(T) \cdot V_i(T)}{r}$$

where  $\gamma_i$  is the surface tension and  $V_i$  is the molar volume. The surface tension of pure elements is determined based on the relationship between the empirical surface tension and thermodynamic property of various elements [3.3].

$$\gamma_i = \frac{\Delta H_{SG,i}}{A_i} \approx \frac{\Delta H_{SG,i}}{1.091 \cdot N_{av}^{1/3} \cdot V_i^{2/3}}$$

where  $\Delta H_{SG,i}$  is the heat for solid-gas transformation,  $A_i$  is the molar surface area, and  $N_{av}$  is the Avogadro number. The temperature dependence of surface tension is derived through a similar approach using the entropy for solid-gas transformation. The molar volume temperature dependence is derived assuming a typical volume expansion of 10 percent from solid phase at 0 K to liquid phase at melting temperature.

For the surface tension and molar volume of stoichiometric compounds, the sum of fractions of each constituent is applied to calculate the surface term of the Gibbs free energy. The Gibbs free energy of solid solutions modeled using the Compound Energy Formalism (CEF) [3.4] is modified by introducing the Gibbs free energy of the surface term to the endmembers of each solid solutions while maintaining the identical interaction parameters. The Gibbs free energy of liquid phase remains identical as the Gibbs free energy of bulk term without any surface energy contribution.

The CALPHAD method using thermochemical software FactSage [3.1] with the reassessed Gibbs free energy of each phases composed of the bulk and surface term is used to predict the phase diagram in nanoscale.

### **3.8. Oxidation stability**

The thermal gravimetric analysis (TGA) was carried out using at air condition. The samples are heated to 1000 °C and the heating rate was 5 °C/min.

## **Chapter 4. Synthesis of heteroatoms (B, N, and O) doped carbon via one-pot chlorination process**

### **4.1. Research highlight**

- B-doped carbon (CB) and B and N Co-doped carbon (CNB) were successfully synthesized using a one-pot chlorination process.
- TiC-TiB<sub>2</sub> powder Ti(C<sub>0.7</sub>,N<sub>0.3</sub>)-TiB<sub>2</sub> powder used as the original raw precursors to produce CB and CNB, respectively.
- To maximize the atomic diffusion of boron in TiB<sub>2</sub> into carbon structure during the chlorination, the direct bond method was used, maximizing the interface between TiC (or Ti(C<sub>0.7</sub>,N<sub>0.3</sub>))-TiB<sub>2</sub>.
- The samples obtained by chlorination of direct bonded TiC-TiB<sub>2</sub> and Ti(C<sub>0.7</sub>,N<sub>0.3</sub>)-TiB<sub>2</sub> powder are denoted as D-CB and D-CNB, respectively.
- D-CB has oxygen rich carbon layer and D-CNB has nitrogen-rich (Pyridinic N) carbon layer at the surface. Boron atoms in TiB<sub>2</sub> readily diffuse into carbon structure during the carbon structure formation stage in the chlorination, and significantly facilitates the development of hetero-atom doped carbon structure.
- The oxidation stability and electrocatalytic activity for oxygen reduction reaction (ORR) of D-CB and D-CNB are greatly changed. D-CB and D-CNB show excellent 2e<sup>-</sup> pathway and 4e<sup>-</sup> pathway ORR performance, respectively.

## 4.2. Introduction

The porous carbon material is a key material for a sustainable society. However, its high chemical inertness brings out low activity in a chemical reaction on the surface. Thus, porous carbon material (C) without any dopant has obvious limitations in the energy and environmental applications. To overcome this drawback, introducing heteroatoms into carbon, which is an effective strategy that mutates carbon's characteristics, has been actively studied. [4.1-4] Boron and nitrogen are the most representative dopant elements. Nitrogen can be easily doped in and out of the carbon layer. Numerous synthetic methods for nitrogen-doped porous carbon (CN) have been reported. Post-treatment of carbon in the nitrogen-containing atmosphere and direct pyrolysis of nitrogen-rich precursors have been most commonly used. [4.5-9] Comparing with CN, boron-doped porous carbon (CB) has been less studied due to the difficulty in doping boron in carbon matrix. In general, boron doping requires high temperature ( $>1000\text{ }^{\circ}\text{C}$ ) and special material preparation (boron contained precursors). [4.10-12]

Beyond the mono-atom doping, co-doping of boron and nitrogen has attracted great attention. Boron and nitrogen co-doped porous carbons (CNBs) show superior optical, electrical, and electrochemical properties. [4.13-16] Boron and nitrogen can act as an electron donor and acceptor, respectively, due to the difference between their electronegativity in the carbon substrate. Thus, boron and nitrogen play a complementary role when they are substituted into a carbon network simultaneously. This synergetic effect enhances the physicochemical properties of carbon material. [4.17-19] In many CNB synthesis methods including pyrolysis and chemical vapor



deposition, nitrogen and boron are introduced to carbon during the formation of carbon structure. Boron is also known to act as a carbon structure former as well as a substituent. Blase et al. [4.20] reported that boron atoms could catalyze the growth of carbon nanotube. Endo et al. [4.21] showed that boron interstitial atoms could act as carbon nanotube welders and coalescence accelerator by creating covalent connections among nanotubes.

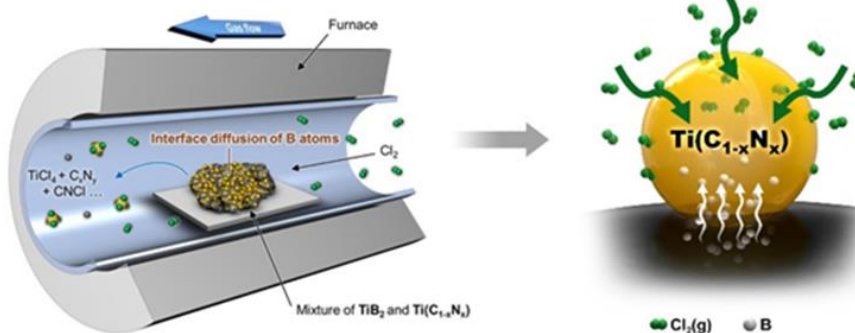
Our research group successfully synthesized C and CN via the chlorination of TiC and Ti(C,N), respectively, [4.22] which is a carbide-derived carbon (CDC)-motivated process. [4.23, 24] Chlorine gas selectively extracts Ti metal atoms in the form of  $\text{TiCl}_4$  gas. As a result, highly nanoporous C and CN can be obtained without any template. Furthermore, we also reported the facile synthesis of CNB that had a hollow morphology along with a highly micro-and mesoporous pore structure via the chlorination of Ti(C,N)- $\text{TiB}_2$  mixture. We demonstrated that a small amount of boron from  $\text{TiB}_2$  could stabilize the CN structure with significant amount of nitrogen functional groups. [4.25, 26] However, the role of boron during the formation of carbon structure was not clearly understood in the previous studies.

In this study, we designed two different boron doping methods (gas transfer and direct diffusion) to C and CN during the chlorination process to elucidate the role of boron in the development of porous carbon structure. The schematic diagram in Figure 4.1 presents two different boron supply routes adopted in the present study. In the direct bond method (solid-state boron diffusion), the  $\text{TiB}_2$  and TiC or Ti(C,N) mixture produced by mechanically milling was employed as starting materials in chlorination process. The carbon materials produced in this method are denoted to D-CB and D-CNB. For the gas transfer route,  $\text{TiB}_2$  and TiC or Ti(C,N) starting

materials were placed separately during the chlorination process.  $\text{TiB}_2$  was reacted to  $\text{Cl}_2$  gas, and  $\text{BCl}_3$  gas species could be transferred to  $\text{TiC}$  or  $\text{Ti}(\text{C},\text{N})$  during the formation of the C or CN. The C and CN materials produced by this method are denoted as G-CB and G-CNB materials.

We demonstrate that the addition of boron via the direct bond method more effectively induce the formation of the heteroatoms-rich (oxygen and/or nitrogen) carbon structure. The resultant D-CB and D-CNB show improved 2  $e^-$  and 4 $e^-$  pathway oxygen reduction reaction (ORR) performance, respectively. This result is expected to provide useful guideline for boron doping to synthesize functional heteroatoms doped porous carbon materials.

### <Direct-bond method>



### <Gas-transport method>

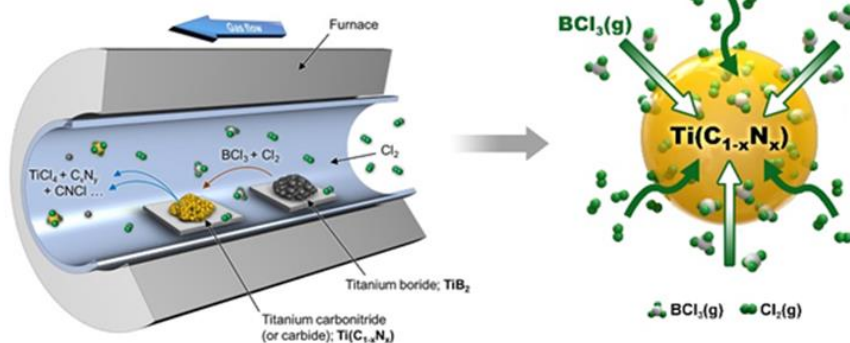


**Figure 4.1.** Boron doping methods used in the present study: Direct-bond method (physical contact of C,N, and B precursors) and gas-transport method (separation of B precursor with C and N precursors ).

### 4.3. Structural variation of CBs and CNBs

The transmission electron microscopy (TEM) analysis (Figure 4.2) was conducted to investigate the influence of boron to the morphology variation of porous carbon materials. The C chlorinated only from TiC (Figure 4.2a) retained the morphology of original TiC powder. In the case of CBs, the coalescence of carbon particles occurs in G-CB (Figure 4.2b) and more prominent in D-CB (Figure 4.2c). The coalescence is also observed in FE-SEM images (Figures 4.5a-c). Moreover, the high-resolution TEM (HR-TEM) images of D-CB presented in Figures 4.3k,l show the growth of disorder carbon layers at the surface, which could result from the effect of direct diffusion of boron atoms. CN and CNBs have a core-shell structure, as shown in Figures 4.2d-f and 4. The morphology of CN is uneven and partially collapsed, losing the shape of the original Ti(C,N) particle (Figure 4.2d). The overall morphology of G-CNB (Figure 4.2e) is similar to that of CN. In contrast, D-CNB has a thick and distinct carbon shell, and the original shape of each Ti(C,N) particle is maintained (Figure 2f, also see in SEM images Figure 4.5). All specimens have a turbostratic structure which is the typical structure of carbide-derived carbon. [4.27] This is verified through HR-TEM images (Figures 4.3 and 4.4) and the selected area electron diffraction (SAED) patterns (inset of Figures 4.3 and 4.4). The SAED shows two diffusive rings, (100)/(101) and (110)/(112) patterns with 0.21 nm and 0.12 nm d-spacing, respectively, and one broad diffraction ring indicating inhomogeneity of the (002) interlayer distance. In addition, partially ordered carbon layers were observed particularly prominent in D-CNB (shown in Figure 4.4l).

XRD patterns and Raman spectra in Figure 4.6 are consistent with the results

from TEM analysis. In the XRD patterns (Figures 4.6a,b), all specimens have broad (002) peak and (10) peak, located around  $26.4^\circ$  and  $43^\circ$ , respectively, indicating the turbostratic structure of carbon. [4.28] The Raman spectra of all specimens (Figures 4.6c,d) exhibit a broad D-band ( $\sim 1356\text{ cm}^{-1}$ ) and G-band ( $\sim 1579\text{ cm}^{-1}$ ), which correspond to the out of plane lattice vibration from  $A_{1g}$  modes of graphitic carbon (D-band) and an ideal graphitic lattice vibrations mode with  $E_{2g}$  symmetry (G-band), respectively. [4.29] The simultaneous development of D- and G-band is typical for a turbostratic carbon and is in agreement with the previous TiC-CDC study. [4.28] The sharp (002) peak at  $26.4^\circ$  is detected in the XRD pattern of D-CNB, and  $I_D/I_G$  value of D-CNB is marginally lower than those of CN and G-CNB, as shown in Figure 4.6e. Similarly,  $I_D/I_G$  value of D-CB is lower than those of C and G-CB. The decrease in  $I_D/I_G$  value confirms the partial ordering in the D-CB and D-CNB.

The  $N_2$  adsorption and desorption isotherms at 77 K (Figures 4.7a,b) demonstrate the change in the pore structure of carbon materials due to the introduction of boron. C and CBs have type I pores that only micro-pore less than 1 nm is dominantly developed, as exhibited by pore size distribution (PSD) plotted in Figure 4.7c. In contrast, CN and CNBs have type I and IV pores, which indicate the simultaneous development of micro- and mesopore, as shown in the PSD plot (Figure 4.7d). [4.30, 31] In addition, all specimens show a sharp increase in the adsorption at  $P/P_0=0.90-0.99$  in isotherms, which demonstrates well-developed macro-pores attributed to the agglomeration of original raw powders. The quantitative values of pore texture are summarized in Table 4.1. The Brunauer-Emmett-Teller (BET) specific surface areas of all specimens are as high as  $1500\text{ m}^2/\text{g}$  or more, indicating that all samples are highly microporous. The formation of

mesopore in CN and CNBs is due to the outflow of nitrogen gas and the decomposition of  $C_xN_y$  because nitrogen exists in the raw powder ( $Ti(C,N)$ ). [4.22] The notable decrease of meso- and total pore volume more prominent in D-CNB can be attributable to the development of robust carbon shell in CNBs accompanying the reduction of large meso- and macropore originated from cavities developed by the collapse of CN particles.

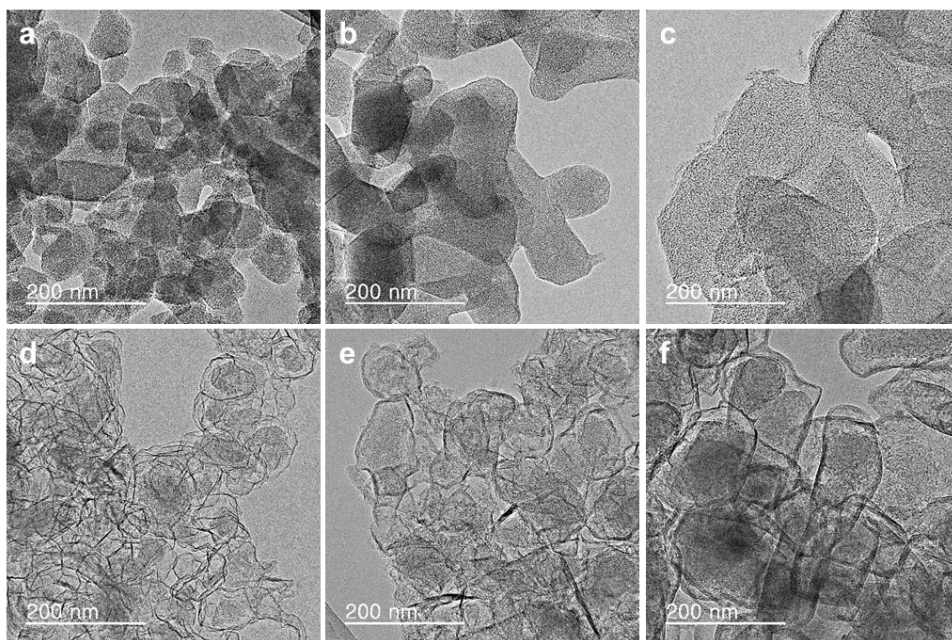


**Figure 4.2.** TEM images of C (a), G-CB (b), D-CB (c), CN (d), G-CNB (e), D-CNB (f).

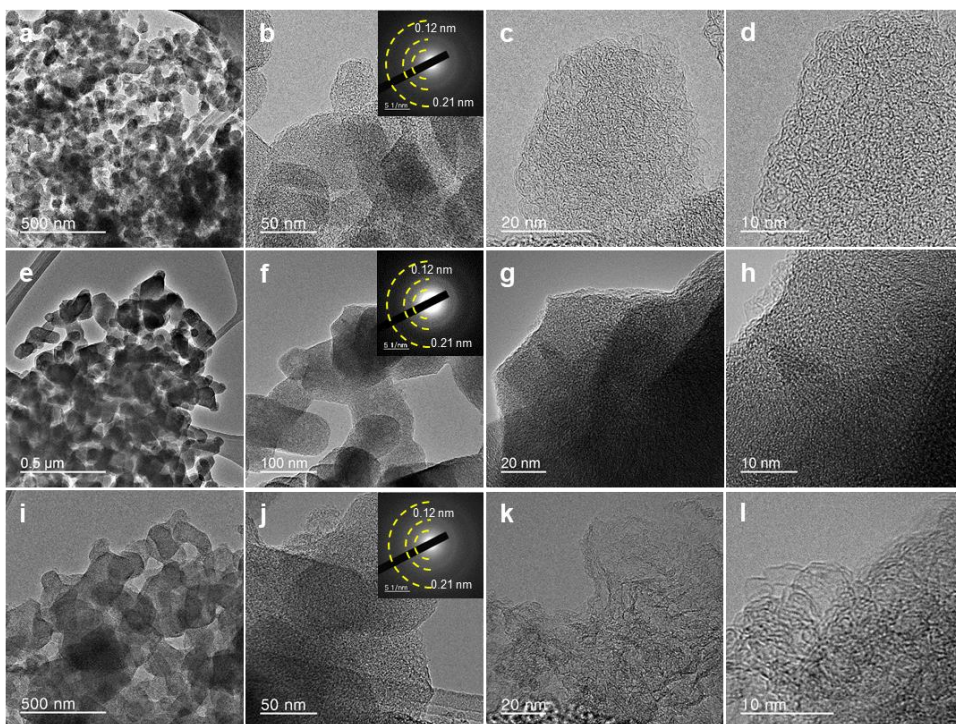


**Figure 4.3.** TEM images and of C (a-c), G-CB(e-g), and D-CB (i-k) and HR TEM image of C (d), G-CB (h), and D-CB (l).



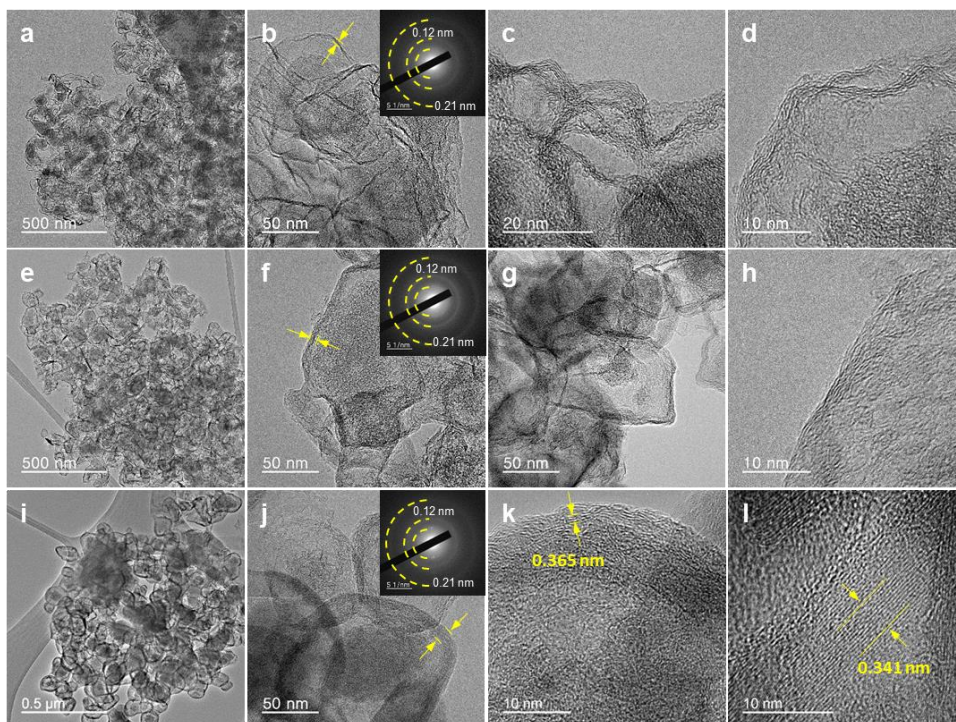


**Figure 4.4.** TEM images and of CN (a-c), G-CNB, (e-g), and D-CNB (i-k) and HR-TEM images of CN (d), G-CNB (h), and D-CNB (l).

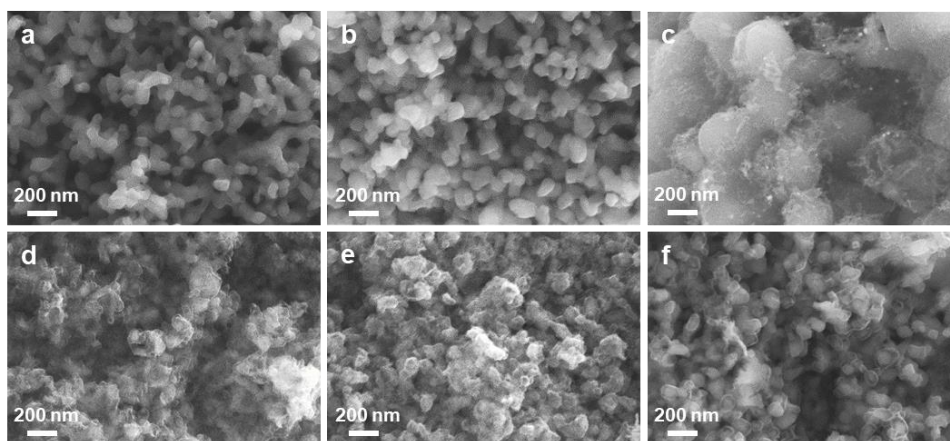


**Figure 4.5.** FE-SEM images of C (a), G-CB (b), D-CB (c), CN (d), G-CNB (e), and D-CNB (f).



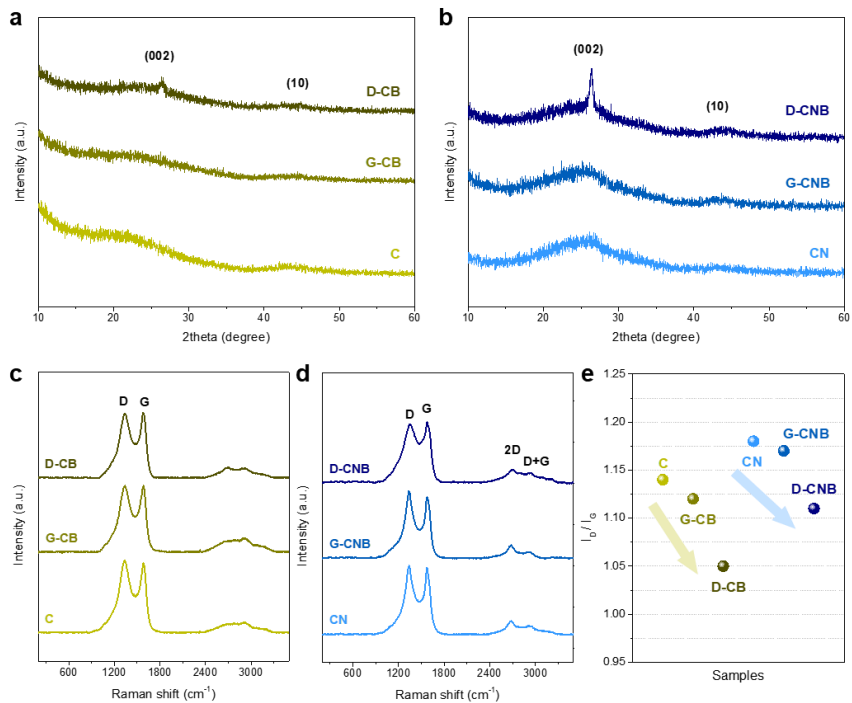


**Figure 4.6.** XRD patterns of C and CBs (a), CN and CNBs (b). Raman spectra of C and CBs (c), CN and CNBs (d). ID/IG values of C, CBs, CN, and CNBs (e)

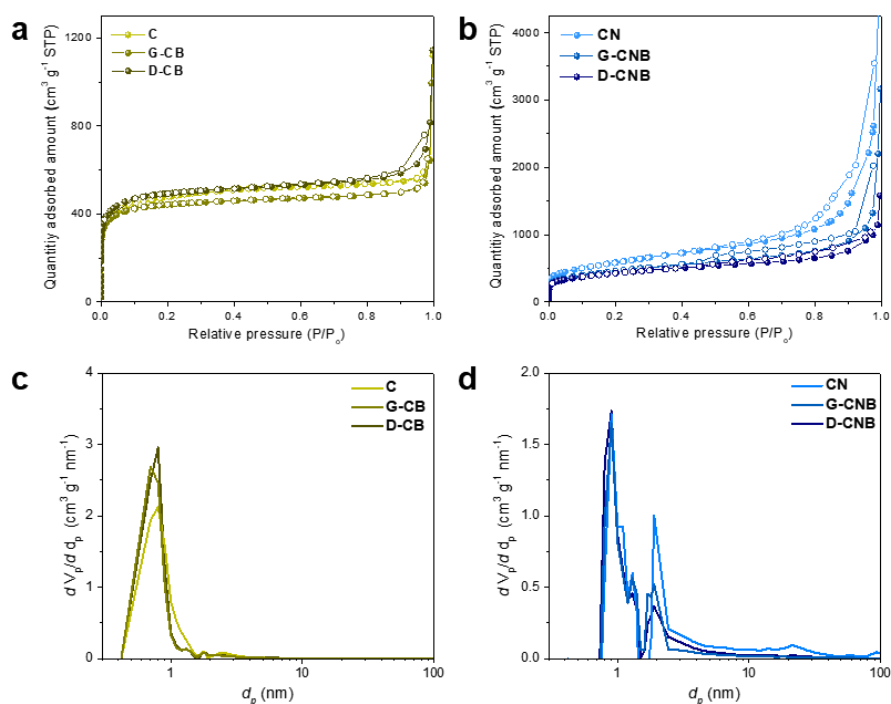


**Figure 4.7.** N<sub>2</sub> sorption isotherm of C and CBs (a) CN and CNBs (b). The pore size distribution (PSD) of C and CBs (c) and CN and CNBs (d).

**Table 4.1.** The yield, BET SSA and pore volumes of C, CBs, CN, and CNBs

Sample	Yield (%, C+N(raw mater.))	BET SSA(m <sup>2</sup> /g)	Micro pore volume (cm <sup>3</sup> /g)	Meso pore volume (cm <sup>3</sup> /g)	Total pore volume (cm <sup>3</sup> /g)
C	82.8	1700	0.69	0.16	1.14
G-CB	84.5	1537	0.65	0.11	1.12
D-CB	89.1	1740	0.73	0.18	1.34
CN	42.2	2099	0.77	1.51	6.54
G-CNB	49.1	1636	0.61	0.79	3.45
D-CNB	54.7	1533	0.58	0.60	1.93

#### 4.4. Surface chemistry variation of CBs and CNBs

The incorporation of boron modified the composition and the bonding configuration at the surface of CBs and CNBs, which is demonstrated by X-ray photoelectron spectroscopy (XPS). The quantitative analysis (Table 4.2) shows that oxygen and nitrogen content are also increased with the addition of boron. It is noteworthy that D-CB and D-CNB have the highest oxygen and nitrogen content, respectively. The oxygen content of D-CB was 6.07 wt.% higher than those of C (2.05 wt.%) and G-CB (5.04 wt.%). The nitrogen content of D-CNB was 4.22 wt. % higher than those of CN (2.00 wt.%) and G-CNB (3.25 wt.%). In contrast to the significant increase in oxygen and nitrogen content, the boron content is still very low in all CBs and CNBs. Although boron was barely detected in CBs by XPS analysis, it was observed by inductively coupled plasma (ICP) analysis: 0.42 and 0.20 wt.% for G-CB and D-CB, respectively. Boron was more readily detected in CNBs by both XPS and ICP analysis, and the content was still very low ( $< 0.5$  wt.%).

According to the high-resolution XPS spectra analysis, the C1s spectra of CBs (Figure 4.8b) were deconvoluted into five components at 284.5, 285.4, 286.1, 288.7 and 290.5 eV, corresponding to  $sp^2$  hybridized carbon,  $sp^3$  hybridized carbon, C-O, -O-C=O, and  $\pi-\pi^*$  transition, respectively. [4, 32, 33] The increased area ratio of C-O peaks, prominent in D-CB, exhibits that the introduction of boron induced the development of edges, defects, and oxygen functional groups (C-O). The C1s spectra of CNBs (Figure 4.10) are divided into six components, the same as CBs except an extra peak at 285.2 eV. This extra peak is attributed to a C-N bond, indicating that nitrogen atoms are incorporated into the carbon structure of CNBs. The N1s spectra (Figure 4.9b) of CNBs are divided into three sharp peaks from pyridinic N (398.3

eV), pyrrolic N (400.1 eV), and graphitic N (401 eV), along with two small peaks from B-N (397.8 eV) and oxidic N (403.2 eV). [4.34-36] The contents of pyridinic N (398 eV) and pyrrolic N (399 eV) in CNBs are significantly increased compared with CN. Moreover, the increase in pyridinic N is more pronounced in D-CNB, also shown in Table 4.2 and Figure 4.12. The B1s spectra of G-CNB and D-CNB (Figure 4.11) were deconvoluted into three and four components, respectively. Three peaks located at 190.7, 191.9, and 193.1 eV in G-CNB are assigned to  $\text{BC}_2\text{O}/\text{h-BN}$ ,  $\text{BCO}_2/\text{BN}_3$ , and B-O bonds, respectively. [4.34-36] These three peaks are also exhibited in D-CNB. Furthermore, a small  $\text{BC}_3$  peak appears at 189.7 eV, which is the evidence that shows the carbon network linking effect of boron. The oxygen content in CBs and nitrogen content in CNBs originate dominantly from the increment of C-O bond and pyridinic N, respectively, despite low boron content. The XPS results demonstrate that the introduction of a small amount of boron can trigger the overall surface change in CBs and CNBs, particularly conspicuous in D-CB and D-CNB.

## 4.5. Oxidation stability of CBs and CNBs

The oxidation stability of CBs and CNBs was measured using thermal gravimetric analysis (TGA), and the results are plotted in Figures 4.8a, 9a, and 13. The weight loss of specimens in ambient air was measured with the variation of temperature. The initial weight loss up to about 10 wt.% observed below 400 °C in all samples was originated from the desorption of physically absorbed water and other impurities. Thus, the results above 400 °C were mainly considered in this study. In the CB system (Figure 4.13a), the oxidation onset temperature (the temperature that the rate of weight loss reached 1 %/min) of D-CB was lower than C by 60 °C, see also Figure 4.8a. Furthermore, the differential thermal gravimetry (DTG) curves shown in Figure 4.13c exhibit that D-CB has the accelerated carbon oxidative gasification at a much lower temperature than C. Similarly, in the CNB system (Figure 4.13b), D-CNB also has lower oxidation onset temperature and faster weight loss compared with CN. On the other hand, G-CB and G-CNB show much higher oxidation stability compared with D-CB and D-CNB, respectively.

## 4.6. Influence of boron in CBs and CNBs

By combining the experimental results in the present study and the previous literature, the influence of the addition of boron in the C and CN structure can be explained as followed. During the chlorination of TiC and  $\text{Ti}(\text{C}_{0.7}\text{N}_{0.3})$ , carbon and/or nitrogen atoms instantly lose their bonds with titanium atoms due to the selective extraction of titanium in the form of  $\text{TiCl}_4(\text{g})$ . Unbonded carbon and/or nitrogen atoms are very unstable. Thus, they tend to be promptly rearranged and to bond each other to re-form the carbon structure. When boron was supplied through direct-bond method (direct contact between TiC (or  $\text{Ti}(\text{C},\text{N})$ ) and  $\text{TiB}_2$ ), boron atoms could directly diffuse into carbon structure form covalent bonds with carbon and/or nitrogen atoms during the chlorination process. In this case, boron atoms acted as the structure linker, as reported in previous carbon nanotube studies. [4.20, 21] Boron atoms readily diffuse in carbon structure due their small atomic size [4.37] and anchor the defect-rich and heteroatom-rich carbon layers that were hard to survive in the harsh chlorination condition without the aid of boron by establishing a covalent bond with carbon and heteroatoms (oxygen and nitrogen) and facilitated the partial ordering in carbon structure by improving self-diffusion of carbon atoms. [4.38] In addition, some boron atoms served as the dopants, facilitating the incorporation of heteroatoms (oxygen and nitrogen) and the formation of vacancies in the carbon layer. [4.39, 40] Therefore, atomically diffused boron atoms significantly promoted the development of defective and heteroatom-doped carbon networks, resulting in noticeable structure and surface chemistry alteration of D-CB and D-CNB, as shown in previous sections.

On the other hand, when boron was supplied in the form of  $\text{BCl}_3(\text{g})$  (gas transport method), boron atoms could limitedly participate in the formation process of carbon structure. B-Cl bond-breaking must be preceded to boron incorporation to the carbon structure, [4.41] which seems to impede the immediate introduction of boron in the early stage of carbon and nitrogen atoms rearrangement. Hence, when boron was supplied by the gas transport method. Boron's role as the structure linker was limited, and boron dominantly acted as a dopant that substituted into unstable sites, such as the edge and defects in already formed carbon layer inducing the minor structure and surface characteristic change of G-CB and G-CNB.

In addition, the difference in oxidation stability can be the one of indicators that shows the development of heteroatoms-rich carbon layers. According to previous studies about the oxidation behavior of carbon material, substitutional boron can enhance the oxidation stability of carbon material. [4.42, 43] Boron atoms bond with the specific surface reactive sites such as edges, defects, oxygen, and nitrogen-doped functional groups which are vulnerable to oxidation in the carbon layers. Doped boron can be oxidized to boron oxide, which inhibits the gasification of reactive sites. [4.42, 43] On the other hand, boron enables to induce the development of defective heteroatom-doped (oxygen or nitrogen) carbon layer, which undermines the oxidation stability of carbon material. [4.5] Depending on the degree of these two opposite effects of boron, the apparent oxidation stability of CBs and CNBs can be determined.

The structure, surface chemistry, and oxidation stability variation of the CBs and CNBs materials by the chlorination process depending on the boron supply methods can be demonstrated as follows:

**C system:** In the case of D-CB, atomically diffused boron atoms in solid-state serve as both dopants and carbon structure connectors. As a result, the coalescence of D-CB particles is prominent (Figure 4.2c), which seems to be attributed to the structural linking effect of boron. The oxygen-rich carbon layers are well-developed in D-CB along with the increment in the yield (89.1 %), compared with C (82.8 %) with no boron, as shown in the XPS results (Figure 4.8b) and Table 4.2. Thus, D-CB shows the lowest oxidation stability compared to C and G-CB, as shown in Figures 4.8a and 4.13a,c.

In the case of G-CB, boron supplied through  $\text{BCl}_3(\text{g})$  serves dominantly as a dopant. The coalescence of G-CB particles is limited (Figure 4.2b). They incorporated into the near edge and defect in the carbon layer and induced the additional doping of oxygen. However, the increase in the oxygen content, yield, and structure variation were limited in the case of G-CB compared with C without boron. It should be noted that oxygen was unintended, but it always exists in raw powder and chlorination gas as an impurity.

**CN system:** Formation of carbon structure can be influenced by both nitrogen and boron. Comparing with TiC, the volumetric density of carbon in  $\text{Ti}(\text{C},\text{N})$  is low due to the existence of nitrogen. As C-N bond is unstable in high temperature ( $> 600\text{ }^\circ\text{C}$ ), most of the nitrogen atoms and some carbon atoms can transform to  $\text{N}_2$ ,  $\text{C}_x\text{N}_y$ , and  $\text{CNCl}$  gas species during the chlorination process. Thus, when the CN structure is developed at the surface of  $\text{Ti}(\text{C},\text{N})$ , unstable carbon and nitrogen atoms unbonded from Ti located below the surface could actively diffuse into the surface to form the stable nitrogen doped-carbon shell or transform to gas species. [4.44] Resultant CN has an irregular carbon core-shell structure, as shown in the TEM result (Figures



4.2d and 4.4a).

In the case of D-CNB, boron atoms can diffuse into the surface of carbon in the early stage of shell formation, and serve as both the structure linker and dopant. Thus, the formation of the boron and nitrogen co-doped carbon shell accompanying partial ordering of some carbon layer in the shell could be facilitated. The development of carbon shell of D-CNB is prominent and the thickness of shell was 8.77 nm, much thicker than that of CN (3.02 nm), which led to a significant increase in yield (54.7 %) compared with CN (34.6 %), as exhibited in the TEM results (Figures 4.4 and 14). Furthermore, even though the content of boron was small ( $< 0.5$  wt.%) in D-CNB, the nitrogen content, especially in the form of pyridinic N, is increased remarkably, as illustrated in the XPS results (Figure 4.9b). This indicates the significant development of pyridinic N-rich carbon shell in D-CNB. Thus, the oxidation stability of D-CNB is significantly decreased, compared to the CN and D-CNB, as shown in Figures 4.9a and 13b,d.

When boron was supplied via the gas-transport method, the role of boron as the carbon structure linker was limited, and boron atoms predominantly acted as the dopant. This may happen because boron supply could be insufficient to participate in the early stage of carbon structure formation. As a result, the development of nitrogen-rich carbon layers is limited. G-CNB showed only a small increase in nitrogen content (3.25 wt.%), shell thickness (4.57 nm), and yield (49.1 %) compared with CN. In addition, G-CNB shows the higher oxidation stability since the active site protecting effect by doped boron is predominant.

## 4.7. Electrocatalytic properties of CBs and CNBs for oxygen reduction reaction

The electrochemical performances of CBs and CNBs for the oxygen reduction reaction (ORR) were examined in O<sub>2</sub>-saturated 0.1 M KOH electrolyte with the rotating ring-disk electrode (RRDE). The ORR activity and H<sub>2</sub>O<sub>2</sub> selectivity of CBs and CNBs are presented in Figures 4.8 and 9, respectively, and the ring current was adjusted by the collection efficiency of RRDE set-up. It revealed that the introduction of boron via the direct bond method could further improve the ORR activity in both C and CN systems, as indicated by the positively shifted polarization curve of CBs and CNBs compared with C and CN. Notably, the CBs deliver much higher H<sub>2</sub>O<sub>2</sub> production current than CNBs, showing selectivity towards 2e<sup>-</sup> ORR kinetics (Figures 4.8c, d). On the other hand, when the boron atoms were introduced into the CN surfaces, the H<sub>2</sub>O<sub>2</sub> selectivity decreased and predominantly produced H<sub>2</sub>O by 4e<sup>-</sup> ORR reaction path (Figures 4.9c, d).

In the case of CBs, oxygen doped defective carbon layers could enhance the electrocatalytic activity better than regular turbostratic carbon layer in C, which seems to be the effect of boron doping. Recently, oxygen functional groups in carbon edge sites turn out to be effective for enhancing the ORR performance, especially for 2e<sup>-</sup> mechanism. [4.32, 33, 45] The oxygen-rich and defective nature of D-CB was verified by Raman spectroscopy (Figure 4.6c) and the higher C 1s XPS signals (Figure 4.8b) for the oxygenated carbon species and ones placed on defect sites. We provided the experimental evidence elucidating the role of oxygen doping sites on

the ORR activity. Tafel slopes for C and CBs were similarly close to 59 mV dec<sup>-1</sup>, indicating that the ORR kinetics is limited by the first electron transfer to the O<sub>2</sub> under the Temkin adsorption conditions (Figure 4.15). [4.46] Thus, the outer-sphere electron transfer ability of these C and CBs would modulate their ORR activities. To assess the electron transfer rates of them, an outer-sphere redox system of [Ru(NH<sub>3</sub>)<sub>6</sub>]<sup>2+/3+</sup> was conducted (more details are described in Supplementary information). The difference between two peak potentials of cyclic voltammograms (CV), shown in Figure 4.16, decreased as boron sources are incorporated in carbon lattice, implying the electron transfer rate was enhanced (Figure 4.8e). Therefore, the further developed carbon edge sites, O-doping sites, on the surface of D-CB (compared to C and G-CB) can boost the reaction rates while maintaining a high selectivity of H<sub>2</sub>O<sub>2</sub> production, not affecting the ORR mechanism.

For the CN structures, the increase in pyridinic N among nitrogen components was more pronounced in D-CNB, as shown in Figure 4.12. Generally, pyridinic N that prefer to be located on the edges or defects of the carbon materials is considered as the most efficient nitrogen species for 4e<sup>-</sup> pathway ORR, [4.47,48] but it is difficult to selectively generate pyridinic nitrogen atoms. The introduction of boron atoms via the direct bond method can be the breakthrough methodology to selectively increase pyridinic N (25 % of N in CN to 56 % in D-CNB). In the case of CN catalysts, the CV measurements with Ru complexes were also conducted to evaluate the outer-sphere electron transfer rates (Figure 4.9e). The calculated rate constants of CN catalysts were somewhat higher than those of C and CBs catalyst, but there was no pronounced tendency to the outer-sphere electron transfer kinetics as the amount of nitrogen components changed. These results showed that the

nitrogen dopants could offer a difference in the reaction mechanism for ORR, supporting mainly the  $4e^-$  pathway reduction. That is, the ORR kinetics on the most of nitrogen-doped carbon catalysts is prone to progress via an inner-sphere electron transfer mechanism, in which  $O_2$  chemisorbs directly on the pyridinic N (or graphitic N) active sites. [4.49] The ORR mechanism of CBs and CNBs is schematically depicted in Figure 4.17. Consequently, it demonstrated that introducing boron through the direct bond method was effective to synthesize the surface-activated C and CN, resulting in improved electrocatalytic performance.

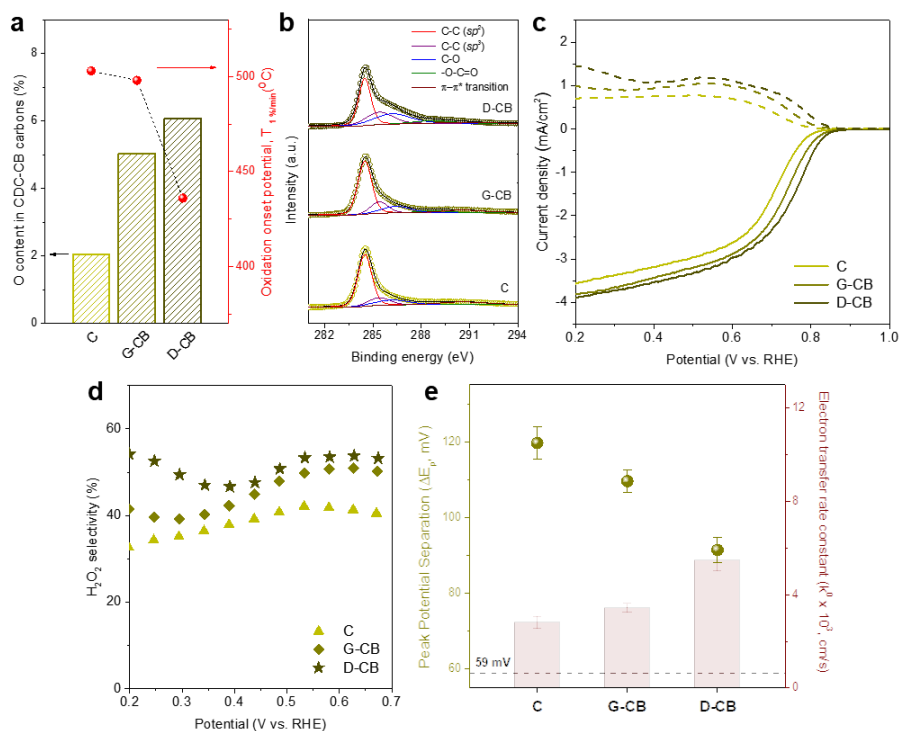


**Figure 4.8.** Characterization of C and CBs: The oxygen content and oxidation onset potential from DTG analysis (a), and deconvoluted HR XPS spectra of C1s (b). Polarization curves at 1600 rpm (solid lines), H<sub>2</sub>O<sub>2</sub> detection currents at the ring

electrode (dashed lines) (c), and the calculated selectivity at 0.1 M KOH (d). Peak potential separation values and heterogeneous electron transfer rate constant (e).

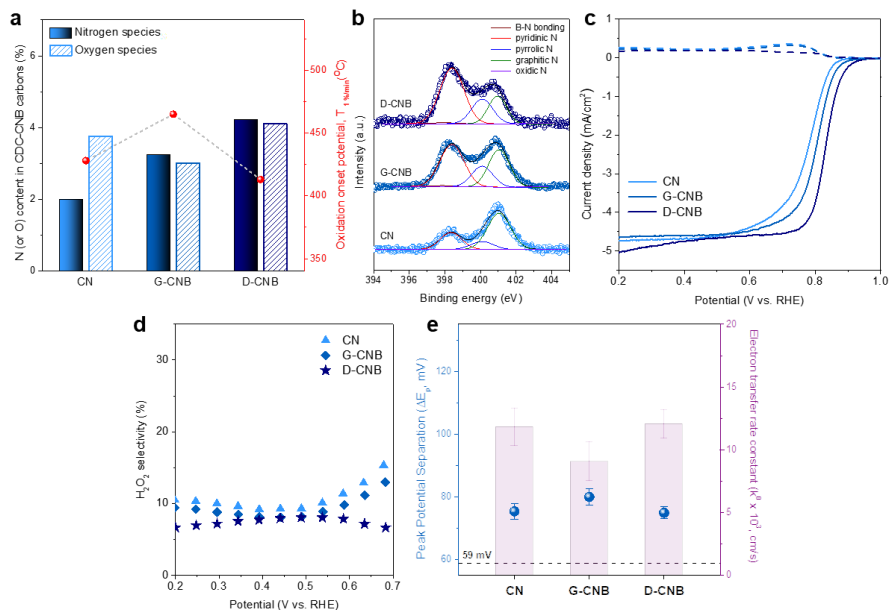


**Figure 4.9.** Characterization of CN and CNBs: The nitrogen/oxygen contents and oxidation onset potential from DTG analysis (a), and deconvoluted HR XPS spectra of C1s (b). Polarization curves at 1600 rpm (solid lines), H<sub>2</sub>O<sub>2</sub> detection currents at the ring electrode (dashed lines) (c), and the calculated selectivity at 0.1 M KOH (d). Peak potential separation values and heterogeneous electron transfer rate constant (e).

**Table 4.2.** The chemical composition of C, CBs, CN and CNBs measured via XPS. The values in the parentheses are for bulk compositions taken by ICP measurement for B.

Sample	C (wt.%)	N (wt.%)	B (wt.%)	O (wt.%)	Nitrogen functional groups				
					BN bonding	Pyridinic N	Pyrrolic N	Graphitic N	Oxidic N
<b>CB system</b> (TiC+TiB <sub>2</sub> -CDC)	<b>C</b>	97.84	N/A	N/A	2.05	-	-	-	-
	<b>G-CB</b>	94.79	N/A	0.03 (0.42)	5.04	-	-	-	-
	<b>D-CB</b>	93.78	N/A	0.04 (0.20)	6.07	-	-	-	-
<b>CNB system</b> (TiCN+TiB <sub>2</sub> -CNCDC)	<b>CN</b>	94.03	2.00	N/A	3.75	0.73	26.05	12.70	60.13
	<b>G-CNB</b>	93.36	3.25	0.37 (0.34)	3.02	1.20	44.39	19.16	34.36
	<b>D-CNB</b>	91.21	4.22	0.46 (0.34)	4.11	0.97	56.44	20.70	21.42

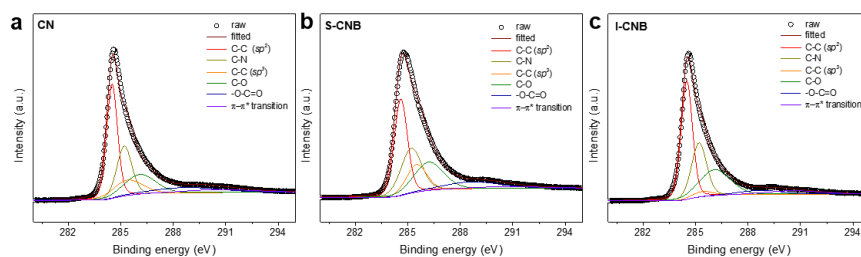


**Figure 4.10.** High resolution XPS C 1s spectra of CN (a), G-CNB (b), and D-CNB (c).

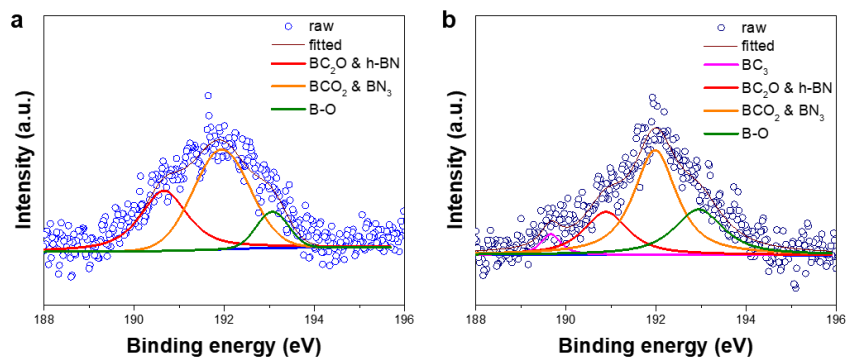


**Figure 4.11.** High resolution XPS B1s spectra of G-CNB and D-CNB.

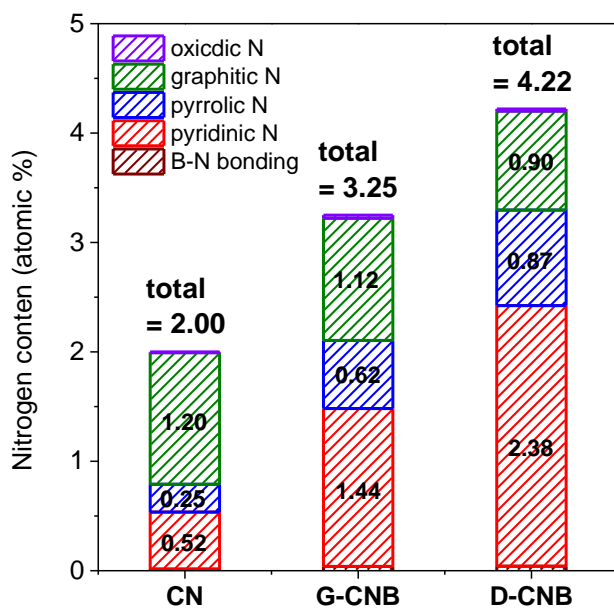


**Figure 4.12.** The distribution of nitrogen species in CN, G-CNB, and D-CNB calculated from deconvolution peaks of N1s spectra.

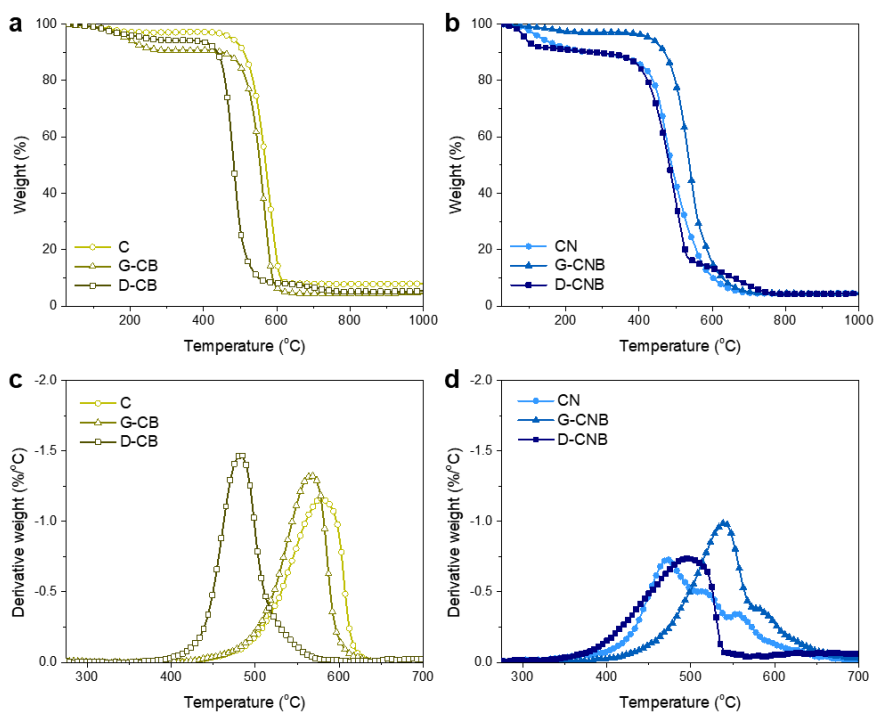


**Figure 4.13.** TG curve of C and CBs (a), and CN and CNBs (b), and DTG analysis (c, d) of the C, CN, CBs, and CNBs.

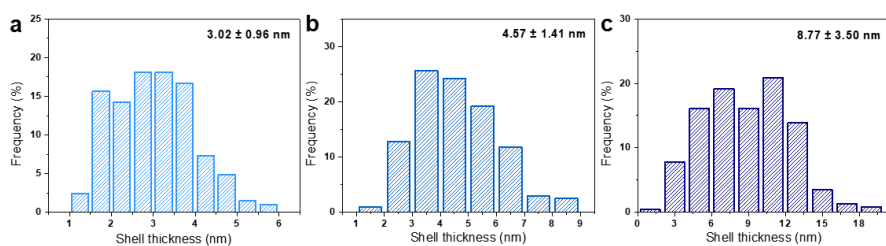


**Figure 4.14.** Average shell thickness of CN, G-CNB, and D-CNB.



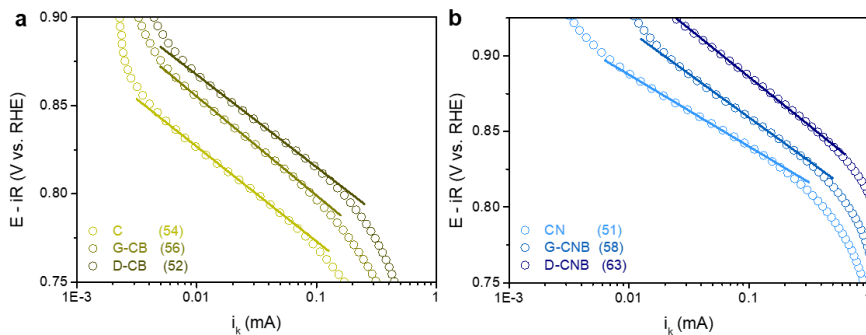


**Figure 4.15.** Tafel plots of the CB and CNB carbons for oxygen reduction reaction.

The numbers represent the Tafel slopes.

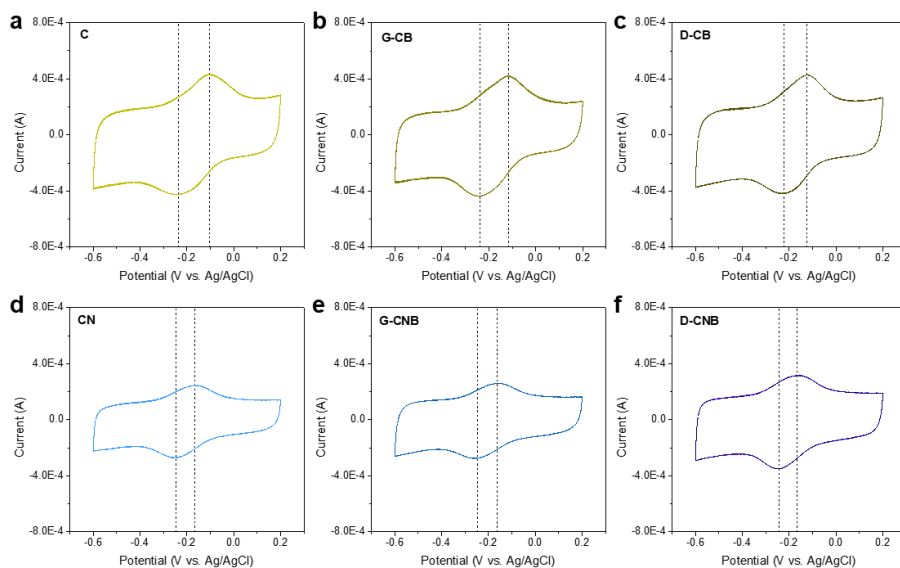


**Figure 4.16.** Cyclic voltammetry of the C and CN series carbons; C (a), G-CB (b), D-CB (c), CN (d), G-CNB (e), and D-CNB (f), measured in Ar-saturated 1 mM  $[\text{Ru}(\text{NH}_3)_6]\text{Cl}_2 + 0.1 \text{ M KCl}$  electrolytes at a scan rate of  $50 \text{ mV s}^{-1}$ .

**Table 4.3.** Observed the separation of anodic/cathodic peak potential ( $\Delta E_p = E_{pa} - E_{pc}$ ), dimensionless rate parameter ( $\Psi$ ), and electron transfer constants ( $k^0$ ) of CBs and CNBs.

	Sample	$\Delta E_p$	$\Psi$	$k^0$
TiC-TiB <sub>2</sub>	C	119.6 ( $\pm$ 4.3)	0.378 ( $\pm$ 0.036)	2.81 ( $\pm$ 0.26)
	G-CB	109.6 ( $\pm$ 2.9)	0.462 ( $\pm$ 0.025)	3.43 ( $\pm$ 0.18)
	D-CB	91.4 ( $\pm$ 3.3)	0.736 ( $\pm$ 0.057)	5.46 ( $\pm$ 0.43)
Ti(C <sub>0.7</sub> N <sub>0.3</sub> )-TiB <sub>2</sub>	CN	75.4 ( $\pm$ 2.5)	1.59 ( $\pm$ 0.20)	11.8 ( $\pm$ 1.5)
	G-CNB	80.0 ( $\pm$ 2.6)	1.22 ( $\pm$ 0.21)	9.1 ( $\pm$ 1.6)
	D-CNB	74.9 ( $\pm$ 1.9)	1.63 ( $\pm$ 0.15)	12.1 ( $\pm$ 1.1)

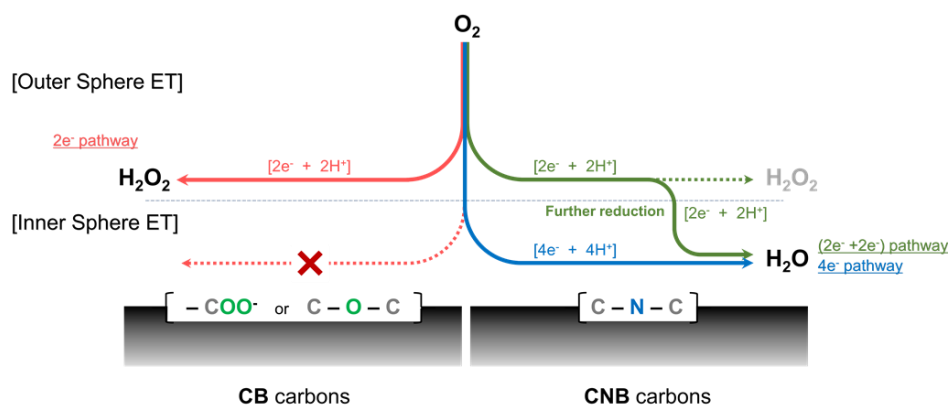


**Figure 4.17.** ORR mechanism on CDC-CB and CDC-CNB carbons in alkaline medium. The nitrogen-doped sites of D-CNB, especially pyridinic N, can mostly catalyze direct 4e<sup>-</sup> and (2e<sup>-</sup>+2e<sup>-</sup>) ORR mechanism. In the other hand, the oxygen-rich defective sites of D-CB, induced by boron atoms in CDC-process, can facilitate the outer-sphere electron transfer and boost 2e<sup>-</sup> ORR kinetics.

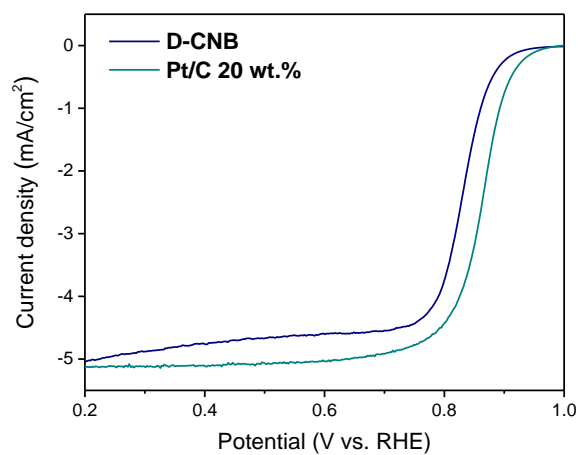


**Figure 4.18.** ORR curves of D-CNB and Pt/C 20wt.% (Johnson Matthey) in O<sub>2</sub>-saturated 0.1 M KOH electrolyte with 5 mV s<sup>-1</sup> on 1600 rpm.

## 4.8. Conclusions

Boron atoms were introduced to the carbide-derived porous carbon and the carbonitride-derived nitrogen-containing porous carbon in order to modify the overall physicochemical characteristic of porous carbon. Two methods were used to introduce boron to porous carbon in the chlorination process: Direct bond method using a mixture of  $\text{TiB}_2$  and  $\text{Ti}(\text{C},\text{N})$  powder and gas transport method where  $\text{BCl}_3$  gas supplies boron to  $\text{Ti}(\text{C},\text{N})$  during the chlorination process. In the direct bond method, boron atoms originated from  $\text{TiB}_2$  could instantaneously diffuse into carbon structure constructed by the chlorination of  $\text{Ti}(\text{C},\text{N})$  from the early stage of the chlorination process. Diffused boron atoms played a pivotal role in the development of the active site-rich surface of CB and CNB. Diffused boron atoms served as not only the dopant but also the structure linker that anchored the unstable defective carbon layer and induced the partial ordering of carbon layer by establishing covalent connections with carbon and nitrogen atoms. As a result, D-CB had oxygen-rich defective carbon layers developed at the surface facilitating the outer-sphere electron transfer, which mainly contributed to the improvement of  $2\text{e}^-$  ORR kinetics. D-CNB had thick boron and nitrogen co-doped shell where pyridinic N was exclusively developed. Therefore, D-CNB exhibited excellent  $4\text{e}^-$  ORR performance. In addition, D-CB and D-CNB had lower oxidation stability compared with C and CN. These results clearly indicated that the introduction of boron atoms during the carbon structure formation process could facilitate the development of porous carbon having

a reactive surface. Therefore, the direct bond method can be a simple and cost-effective method to maximize the electrochemical properties of porous C and CN. Furthermore, our result can improve the versatility of the chlorination process for synthesizing the functional carbon material and also can provide the reassessment for the role of boron in the porous carbon material synthesis.

# **Chapter 5. Synthesis of BN embedded porous carbon via one-pot chlorination process and its application for the H<sub>2</sub>O<sub>2</sub> production**

## **5.1. Research highlight**

- BN nanodomains embedded porous carbon (BNC) was successfully synthesized a one-pot chlorination process.
- Direct bonded Ti(C<sub>0.3</sub>,N<sub>0.7</sub>)-TiB<sub>2</sub> powder used as the original raw precursors to produce CNB. The sample obtained by chlorination of direct bonded Ti(C<sub>0.3</sub>,N<sub>0.7</sub>)-TiB<sub>2</sub> powder is denoted as D-CNB-T (T = chlorination temperature).
- Boron atoms in TiB<sub>2</sub> diffuse into CN during the chlorination, and act as both BN formation source and carbon structure stabilizer, which induce the formation of BN nanodomains embedded porous carbon structure.
- For achieving the high loading BN nanodomain carbon layers and highly nanoporous structure simultaneously, 700 °C and 1:1:2.3 are decided as the optimum chlorination temperature and optimum B:C:N molar ratio in the raw precursors based on thermodynamic calculation and experiments.
- D-CNB-700 applied as the electrocatalyst shows outstanding H<sub>2</sub>O<sub>2</sub> production performance in alkaline medium. (H<sub>2</sub>O<sub>2</sub> selectivity = 88.3 %, H<sub>2</sub>O<sub>2</sub> production rate = 4.65 mmol/h, durability = 10 h, faradaic efficiency = ~61 %)

## 5.2. Introduction

Hydrogen peroxide ( $\text{H}_2\text{O}_2$ ) is one of the essential chemicals for various applications, including pulp and textile bleaching, wastewater treatment, chemical synthesis, and semiconductor cleaning, and the demand for  $\text{H}_2\text{O}_2$  has been increased significantly. [5.1-3] For the large-scale  $\text{H}_2\text{O}_2$  production, the anthraquinone process has been widely used. [5.1] Although this process is appropriate for centralized production, it is an energy-intensive process and requires massive infrastructure, inevitably accompanying the environmental problems. [5.1] Currently, there is a high demand for decentralized production of  $\text{H}_2\text{O}_2$ . Thus, many researchers have focused on the production of  $\text{H}_2\text{O}_2$  through electrochemical synthetic route, and  $2\text{e}^-$  oxygen reduction reaction (ORR) is one of the promising candidates. [5.1, 2] Because it can produce  $\text{H}_2\text{O}_2$  in room temperature and atmospheric pressure, is eco-friendly due to the direct production of  $\text{H}_2\text{O}_2$  from  $\text{O}_2$  and  $\text{H}_2$ . To commercialize the ORR synthetic process, the selection of the proper electrocatalyst is a prerequisite. The noble metal-based electrocatalysts are ranked the first in terms of performance, but its high price is always pointed out as a fatal drawback.[5.3] Thus, other alternative electrocatalysts such as transition metal-based and carbon-based electrocatalyst have been actively studied. [5.3-5]

In particular, great progress has been achieved in the metal-free carbon-based catalysts. Numerous research has been performed to produce the heteroatom doped porous carbon to improve the electrocatalytic activity for  $2\text{e}^-$  pathway ORR. [5.6-10] The introduction of nitrogen or oxygen functional groups into porous carbon can

significantly enhance the  $2e^-$  pathway ORR performance. [5.6, 7] Beyond the mono-atom doped carbon, the boron-carbon-nitrogen (B-C-N) materials could be a suitable candidate for the  $H_2O_2$  production electrocatalyst. The B-C-N materials have already been applied in various optical, electrical, and electrochemical applications [5.11-13] because its characteristics can be widely tuned with the variation of composition from pure graphene to pure boron nitride (h-BN). [5.14] The B-C-N materials manifested its high performance for  $4e^-$  ORR. [5.15-19] Recently, the applicability of the B-C-N materials as the electrocatalyst for the  $H_2O_2$  production has been revealed, and the implantation of the h-BN nanodomains in porous carbon substrate is demonstrated as the key for achieving high  $2e^-$  pathway ORR performance. [5.20]

Nevertheless, the structure-property relationships and the nature of active sites in the B-C-N materials that endow the electrocatalytic activity are still less understood. Moreover, there is a still lack of research on the control of a synthesis-structure relationship to establish the practical B-C-N materials synthesis route. Chemical vapor deposition (CVD) and pyrolysis method are the representatives for synthesizing the B-C-N materials, but there are still limitations in the mass production using such methods. The CVD method requires expensive chemicals and sophisticated equipment. While the pyrolysis method inevitably involves the high temperature (above  $800\text{ }^{\circ}\text{C}$ ) treatment. [5.11, 21] Furthermore, both methods are difficult to control the pore structure of carbon, especially, such as micro- and mesopore and the doping level of boron and nitrogen, which are the major factors determining the properties of the B-C-N material. [5.22] Therefore, the development of alternative and economic B-C-N materials synthesis methods based on the understanding of their synthesis-structure-property relationship is highly required.



Carbide-derived carbon (CDC) method that synthesizes carbon through selectively extracting metal or metalloid atom in carbide lattice is one of the representative methods for the synthesis of various carbon materials such as CNT, diamond, and porous carbon. [5.23] In particular, the CDCs have two advantages which are distinctive from other conventional carbon synthesis methods. The CDCs synthesized through a conformational transformation reaction retain the original morphology of raw materials. The CDCs are also highly microporous and has a specific size of micro-pore which can be controlled depending on various carbide precursors. [5.23, 24] Thus, the CDCs show high performance in various energy and environmental applications, including supercapacitor, water desalination, and gas storage. [5.25-28] However, to extract the metal atom, a reactive etchant such as the halogen element ( $\text{Cl}_2$ ) is required inevitably, which makes the CDC method to synthesize only pristine carbon materials. This is an explicit limitation of the CDC process.

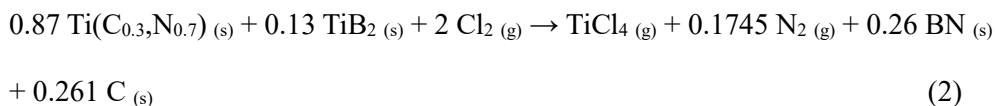
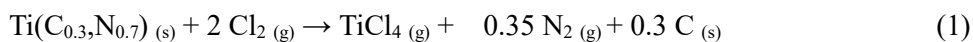
To overcome the limitation of the conventional CDC process, our research group proposed a synthesis method for the nitrogen-doped carbon via the chlorination of  $\text{Ti}(\text{C},\text{N})$  instead of  $\text{TiC}$ . [5.29] Beyond the N-doped carbon, we also synthesized B and N co-doped carbon having the hollow structure via the chlorination of the  $\text{Ti}(\text{C},\text{N})\text{-TiB}_2$  mixture. This hollow B and N co-doped carbon (less than 1 at.% B and 10 at.% N) showed the excellent  $\text{CO}_2$  gas storage and electrochemical catalyst performance. [5.30, 31] We also reported the synthesis of nanoporous boron nitride having a high  $\text{H}_2$  storage capacity using the chlorination of the  $\text{TiN-TiB}_2$  mixture. [5.32] In a series of our previous studies, however, there has

been no research to effectively control the doping concentration of boron and nitrogen in the CDCs.

In this study, the breakthrough technology to synthesize the BN embedded nanoporous carbon (BNC) is proposed using the chlorination of the Ti(C,N)-TiB<sub>2</sub> mixture. The well-established interface between nano-sized Ti(C,N) and micron TiB<sub>2</sub> powders are obtained using the simple raw powder engineering (the direct bond method). This interface enables boron atoms from TiB<sub>2</sub> to diffuse directly into CN structure during the porous carbon formation stage, which is the key for implantation of BN nano-domain in the carbon structure. The samples synthesized by the direct bond method is denoted as the D-BNC-T, where T is the chlorination temperature. By controlling the chlorination temperature and the composition of original raw powder precursors, the B and N composition and pore structure of porous carbon can be readily tuned. In particular, D-BNC-700 has abundant BN nano-domains in porous carbon having a hierarchical pore structure. Thus, it exhibits the outstanding electrocatalytic performance of the H<sub>2</sub>O<sub>2</sub> production by 2e<sup>-</sup> pathway oxygen reduction reaction (ORR). This study demonstrates that the high applicability of the nanoporous B-C-N materials as the 2e<sup>-</sup> ORR electrocatalyst.

### 5.3. Thermodynamic analysis on the chlorination reaction of carbonitride and boride mixture

Thermodynamic calculations for the chlorination of  $\text{Ti}(\text{C}_{0.3}\text{N}_{0.7})\text{-TiB}_2$  and  $\text{Ti}(\text{C}_{0.3}\text{N}_{0.7})$  were performed using the FactSage thermodynamic calculation software to understand the chemical reactions in the chlorination process. [5.33] Although the nano-size effect and doping effect were not considered in calculations, the thermodynamic calculations could still provide the key reactions in the chlorination process under the full thermodynamic equilibrium condition. The chlorination of  $\text{Ti}(\text{C}_{0.3}\text{N}_{0.7})\text{-TiB}_2$  and  $\text{Ti}(\text{C}_{0.3}\text{N}_{0.7})$  at 600 to 800 °C were calculated with varying amount of chlorine, and the results are summarized in Figures 5.1a-f. The overall chlorination reactions of  $\text{Ti}(\text{C}_{0.3}\text{N}_{0.7})$  solid-solution and  $\text{Ti}(\text{C}_{0.3}\text{N}_{0.7})\text{-TiB}_2$  mixture based on 1 mole of Ti and 2 moles of  $\text{Cl}_2$  can be expressed as follows:



The calculation results for each starting material at 600 to 800 °C are almost the same regardless of the temperature. Compared to the chlorination of  $\text{Ti}(\text{C}_{0.3}\text{N}_{0.7})$  at 700 °C (Figure 5.1b), the chlorination of  $\text{Ti}(\text{C}_{0.3}\text{N}_{0.7})\text{-TiB}_2$  at 700 °C (Figure 5.1a) shows two distinct differences. The first is the formation of the BN phase in  $\text{Ti}(\text{C},\text{N})\text{-TiB}_2$  mixture. The h-BN phase can form from  $\text{TiB}_2$  in the initial chlorination stage, and it can be transformed to  $\text{BCl}_3$  gas with the progress of chlorination process

(above 2.4 mole  $\text{Cl}_2$ ). Thermodynamic instability of the h-BN phase in high  $\text{Cl}_2$  region is also calculated at 600 °C and 800 °C, as shown in Figure 5.1c-f. The other difference is the order of chlorination reaction of TiC and TiN content in  $\text{Ti}(\text{C}_{0.3}, \text{N}_{0.7})$  solid solution. In the case of  $\text{Ti}(\text{C}_{0.3}, \text{N}_{0.7})\text{-TiB}_2$ , TiN and  $\text{TiB}_2$  react with  $\text{Cl}_2$  gas to form h-BN, followed by the chlorination of TiC to form C. That is h-BN formation with  $\text{Cl}_2$  gas is thermodynamically more favorable than the chlorination of TiC. On the other hand, in the case of  $\text{Ti}(\text{C}_{0.3}, \text{N}_{0.7})$  powder, TiC is reduced first to form C, followed by the chlorination of TiN to nitrogen gas. This means that h-BN or high amounts of atomic B can be available during the formation of carbon structure and thus may significantly influence to the carbon structure construction. In addition, carbon stability is relatively low at 600 °C while it is increased as the chlorination temperature increases. Figure 5.2 shows the thermodynamic calculation results of three different mixture of  $\text{Cl}_2$  gas and  $\text{Ti}(\text{C}_{0.3}, \text{N}_{0.7})\text{-TiB}_2$  at the temperatures from 0 to 1200 °C. From our experience, the chlorination reaction kinetic is very slow below 500 °C. The calculation results for all three mixtures above 500 °C are nearly independent of temperature. But the BN is calculated to be less stable above 1100 °C.

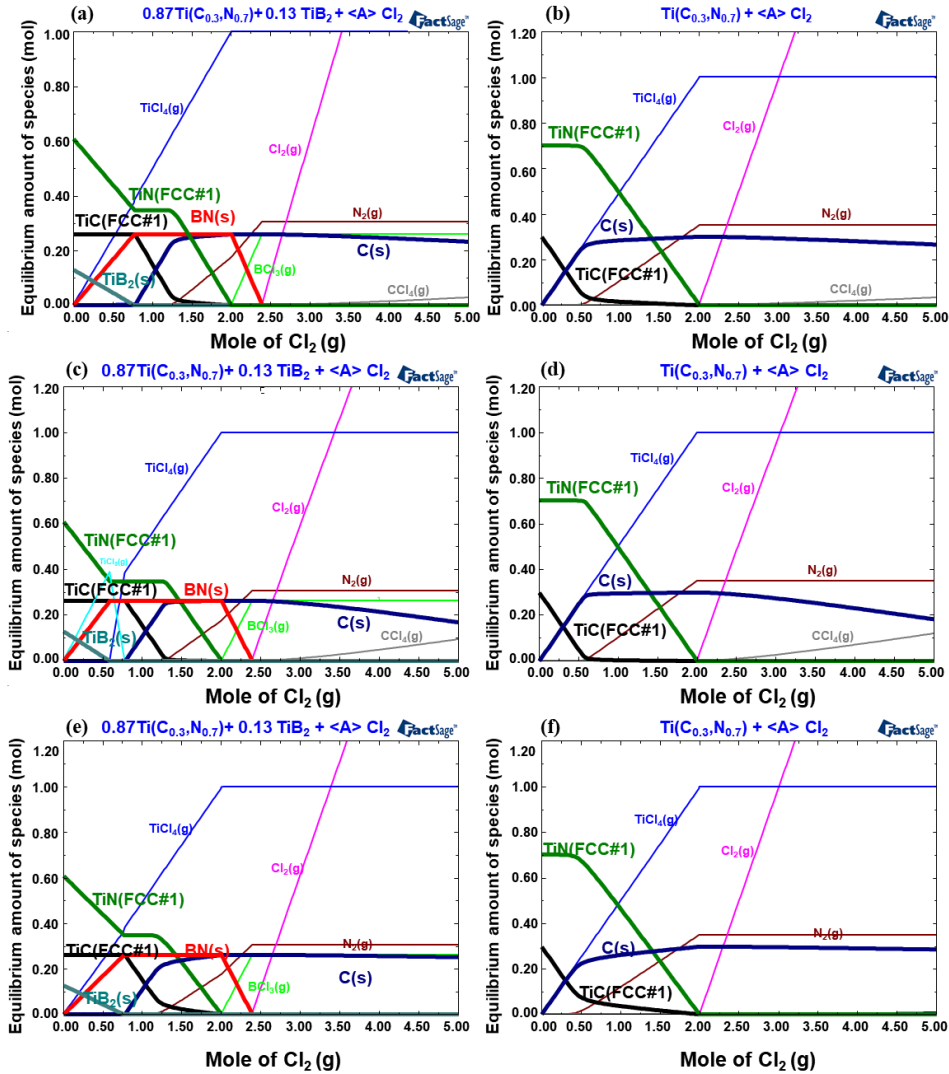


**Figure 5.1.** Thermodynamic calculations for the chlorination of titanium carbonitride and boride mixture. The synthesized products varying with amount of  $\text{Cl}_2$  in  $\text{Ti}(\text{C}_{0.3}\text{N}_{0.7})\text{-TiB}_2$  system (a),  $\text{Ti}(\text{C}_{0.3}\text{N}_{0.7})$  system (b) at 700 °C. Thermodynamic calculations for the  $\text{Ti}(\text{C}_{0.3}\text{N}_{0.7})\text{-TiB}_2$  system (a),  $\text{Ti}(\text{C}_{0.3}\text{N}_{0.7})$  system (b) at 800 °C and identical calculations for the  $\text{Ti}(\text{C}_{0.3}\text{N}_{0.7})\text{-TiB}_2$  system (c),  $\text{Ti}(\text{C}_{0.3}\text{N}_{0.7})$  system (d) at 600 °C (Synthesized products vs. mole of  $\text{Cl}_2$ ).

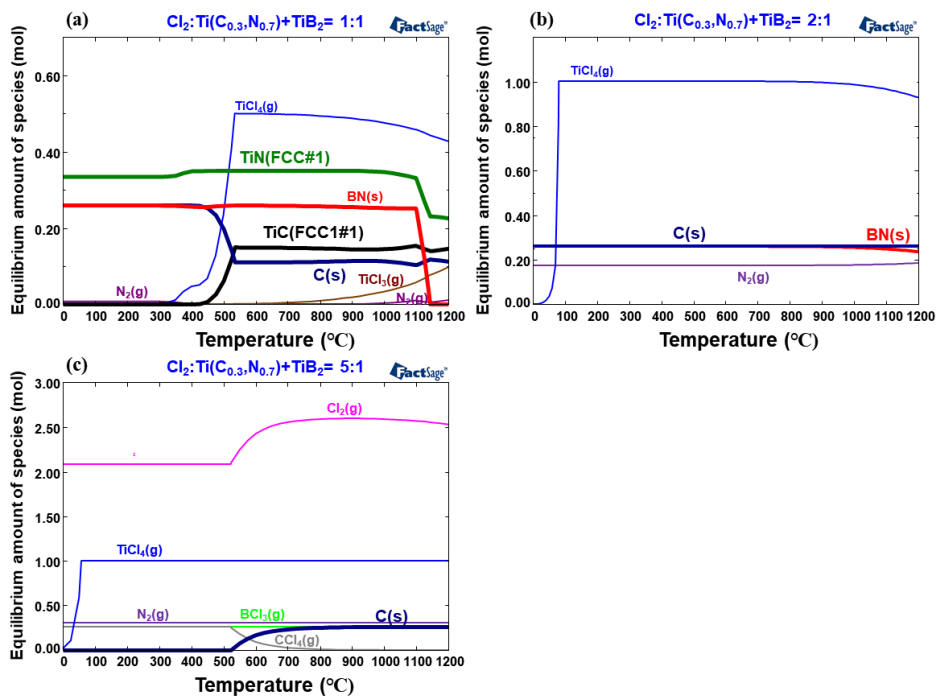


**Figure 5.2.** Synthesized products varying with the chlorination temperature at the  $\text{Cl}_2$  to precursors ( $\text{Ti}(\text{C}_{0.3}\text{N}_{0.7})\text{-TiB}_2$ ) molar ratio of 1:1 (a) 2:1 (b), and 5:1(c).

## 5.4. Challenging in h-BN implant in porous carbon substrate

Previous research presented the applicability of the B-C-N materials as the electrocatalyst for  $\text{H}_2\text{O}_2$  production, and the interface of BN-carbon is demonstrated the effective active site for  $2\text{e}^-$  pathway ORR. [5.20] The importance of BN-carbon interface for  $2\text{e}^-$  pathway activity is also demonstrated by our experiment, the evaluation of electrocatalytic properties of the graphene-BN sheet mixture, shown in the appendix 1.2.1 section. Although the formation of the interface between graphene and BN sheet in micron-scale brings the enhancement of  $2\text{e}^-$  pathway ORR performance, the improvement is limited. Because maximizing the BN-C interface is less effective in micron-scale. Therefore, the implantation of BN nano-domains in the porous carbon substrate is essential to maximize the  $2\text{e}^-$  pathway ORR performance.

As well known, because B-N and C-C bonds have high stability, and C-N and C-B bond stability are relatively low [5.21], the h-BN phase can be more likely formed as a separate phase rather than being embedded into CN structure. Secondly, CN formed by the chlorination of  $\text{Ti}(\text{C},\text{N})$  has the low thermal stability and form various  $\text{C}_x\text{N}_y$  and  $\text{CNCl}$  gas species above  $600\text{ }^\circ\text{C}$  due to its high nitrogen content. [5.29, 34] As boron can easily form BN, both nitrogen and Ti can be consumed during the chlorination process of  $\text{Ti}(\text{C},\text{N})$  which can promote the gasification of the remained carbon atoms in original  $\text{Ti}(\text{C},\text{N})$  powder. This is, a solid carbon structure may not be developed well under the existence of B source. The difficulty in the implantation of BN in the carbon substrate by the chlorination process is evident in

controlled the experiment summarized in the appendix 1.2.2 section. When the B precursor ( $\text{TiB}_2$ ) and C and N precursor ( $\text{Ti(C,N)}$ ) are physically separated during the chlorination process, only  $\text{BCl}_3(\text{g})$  supplied to CN as the boron source. In this case, most carbons atoms are gasified, and a small amount of BN-rich phase remains as an impurity. Therefore, although the thermodynamic calculations show the formation of BN and carbon in the chlorination process at above 600 °C, the synthesis of BN embedded porous carbon material can be very challenging. In order to successfully obtain the BN embedded porous carbon, an innovative idea in the chlorination process is needed.

For achieving this, we introduce the direct bond method and synthesize the D-BNC. By mechanical milling of micron-sized commercial  $\text{TiB}_2$  particles with  $\text{TiO}_2$  and C under the  $\text{N}_2$  atmosphere, nano-size  $\text{Ti(C}_{0.3}\text{,N}_{0.7})$  aggregated on the surface of micron-sized  $\text{TiB}_2$  were obtained, as shown in appendix 1.1 section. Details of the synthesis are described in the experimental section. In this way, the contact between  $\text{Ti(C}_{0.3}\text{,N}_{0.7})$  and  $\text{TiB}_2$  could be maximized in the starting materials prior to the chlorination process. Thus, boron atoms from  $\text{TiB}_2$  can directly diffuse to the surface  $\text{Ti(C}_{0.3}\text{,N}_{0.7})$  and interact with both nitrogen and carbon during the chlorination process,.

In the present study, two main process parameters, chlorination temperature and starting material composition, were investigated for the synthesis of D-BNC.



## 5.5. Variation of D-BNC characteristics with chlorination temperature

The chlorination temperature is certainly a major process parameter determining the morphology, boron and nitrogen content, and pore structure of D-BNCs. The morphology variation of D-BNCs depending on the chlorination temperature was analyzed using TEM, as shown in Figures 5.3 and 5.4. D-BNC-400 has a turbostratic carbon structure, and maintains the same shape of the original raw Ti(C,N) powder. No hollow structure is observed. D-BNC-600 has the crumpled and collapsed shells wrapping some remaining  $C_xN_y$  cores. D-BNC-700 also exhibits a similar structure, but less amount of  $C_xN_y$  cores is observed. D-BNC-800 and -1000, on the other hand, show the hollow structure that solid shells retain the raw powder shape with a small amount of remaining core. The morphology of D-BNCs observed by FE-SEM analysis (Figure 5.5) is analogous to the results of TEM analysis. All D-BNCs have a turbostratic structure verified by the High-resolution (HR) TEM images in Figures 5.3d,h,l and 5.4d,h. This is further confirmed in the selected area electron diffraction (SAED) patterns of D-BNCs (insets of Figures 5.3c,g,k and 5.4c,g). Two diffusive rings which indicate (100)/(101) and (110)/(112) with 0.21 nm and 0.12 nm d-spacing, respectively, and one broad diffraction ring proving inhomogeneity of the (002) interlayer distance are observed in the SAED pattern. The structural analysis of D-BNCs was also conducted by X-ray powder diffraction(XRD), shown in Figure 5.6. The two broad peaks centered at around  $26.0^\circ$  and  $42.2^\circ$  corresponding to (002) and (10), respectively, appear in all D-BNCs regardless of the chlorination

temperature. These data indicate that all D-BNCs have a turbostratic structure, which are consistent with HR-TEM analysis results.

X-ray photoelectron spectroscopy (XPS) analysis shows that boron and nitrogen content in D-BNC is significantly varied with the chlorination temperature. The quantitative analysis (Table 5.1) exhibits that D-BNC-700 contains a very high content of boron (15.5 at.%) and nitrogen (22.0 at.%), while D-BNC-800 and 1000 contain a low amount of boron and nitrogen. In particular, boron content is less than 2.0 at.%. In the case of D-BNC-400 and 600, their boron and nitrogen contents are high, but carbon contents are very low (below 26.0 at.%). In addition, there is a significant amount of oxygen in the D-BNCs at the low temperature, originated from gas or original raw powder as an impurity.

The high-resolution (HR) spectra analysis was performed to examine the bond configuration at the surface D-BNCs shown in Figures 5.7, 5.8, and 5.10. The B1s bands of D-BNC-400, 600, and 800 (Figures 5.10a and 5.7a,c respectively) can be separated into three components located around 190.1, 191, and 192.3 eV, corresponding to h-BN,  $\text{BC}_2\text{O}$ , and  $\text{BCO}_2/\text{BN}_3$ , respectively. [5.17, 35, 36] While the B1s band of D-BNC-700 (Figure 5.7b) exhibits only two peaks, h-BN and  $\text{BC}_2\text{O}$ . In the case of D-BNC-1000 shown in Figure 5.10b, the B1s band was divided into four peaks, assigning to h-BN,  $\text{BC}_2\text{O}$ ,  $\text{BCO}_2/\text{BN}_3$ , and  $\text{BC}_3$  (189.5 eV). [5.17] The N1s band of D-BNC-400 (Figure 5.10c) can be deconvoluted into four components at 397.9, 398.5, 399.5, and 400.5, corresponding to B-N bond, pyridinic N, C-N-B, and pyrrolic N, respectively. [5.17, 35, 36] The N1s bands of D-BNC-600 and 700 (Figures 5.7d,e) are divided into five components, identical with D-BNC-400 except

for the appearance of a small peak at 401.5 eV attributed to graphitic N. [5.37] It seems that nano-graphene carbon network was gradually developed in the carbon shell as the chlorination temperature increased. In the N1s bands of D-BNC-800 and 1000 (Figures 5.7f and 5.10d), the N-oxide peak (402.5 eV) appears additionally along with five peaks observed for D-BNC-700. [5.37] The C1s bands of D-BNC-400, 600, and 700 (Figures 5.10e and 5.8a,b, respectively) are split into five components at 284.5, 285.5, 286.5, 287.7, 299 eV, corresponding to  $sp^2$  hybridized C-C bond,  $sp^3$  hybridized C-C bond, C-O, C=O/C=N/C≡N, and O-C=O/C-N, respectively. [5.7, 38] In the case of D-BNC-800 and 1000 (Figures 5.8c and 5.10f), one additional peak at 291 eV related to  $\pi$ - $\pi$  shake-up is recorded to five components. [5.7]

The quantitative analysis of the bonding configuration is summarized in Table 5.2. In the case of D-BNC-400, although BN content is considerably high (16 at.%), the single B doping ( $BC_2O$  and  $BCO_2$ ) and single N doping (pyridinic N and pyrrolic N) content are equally high, 11.3 at.% and 18.1 at.%, respectively, indicating that boron and nitrogen bond by themselves as well as with carbon and oxygen. In addition,  $sp^2$ -hybridized carbon content is very low (9.4 at.%). D-BNC-600 shows a similar trend with D-BNC-400, but its BN content (26.8 at.%) and  $sp^2$ -hybridized carbon content (15.4 at.%) are higher. In contrast, in the case of D-BNC-700, a significant increase in  $sp^2$ -hybridized carbon content (36.5 at.%) was observed. Also, the content of h-BN (32.2 at.%) is increased along with a significant decrease in single N (6.3 at.%) and B doping (2.8 at.%). The  $sp^2$ -hybridized carbon content was much higher in D-BNC-800 and 1000, 49.1, and 45.9 at.%, respectively. The h-BN content, however, is sharply decreased to less than 2.5 at.%.

Near-edge X-ray absorption fine structure spectroscopy (NEXAFS) is further carried out to understand the chemical structure of boron and nitrogen at the surface of D-BNCs, and the results are shown in Figures 5.7g,h. The B and N-K edge NEXAFS of D-BNC-600, 700, and 800 are compared with bulk h-BN. They exhibit the development of  $sp^2$ -hybridized B-N bond (h-BN), especially in D-BNC-700. In the B-K edge spectrum, bulk h-BN has a sharp  $B1s \rightarrow \pi^*$  peak at 191.8 eV, two  $B1s \rightarrow \sigma^*$  resonance peaks at 198 and 199.3 eV, and one broad peak at 204 eV originated from the N-K edge appears in B-K edge NEXAFS. [5.12, 39] These four peaks are also detected in D-BNC-600, 700, and 800. In addition, the two incidental peaks at 192.3 and 193.0 eV attributed to boron atoms bound to two nitrogen atoms and single atoms, respectively, which are the defects of h-BN are detected in D-BNC-600. [5.40] This indicates the incomplete development of h-BN due to the low chlorination temperature. One additional peak at 193.7 eV assigning to B-O bond appears in D-BNC-600 and 800. These additional peaks are barely observed in D-BNC-700, which demonstrates that boron atoms in D-BNC-700 predominantly exist as the h-BN configuration. The N-K edge spectrum of bulk h-BN exhibits three peaks at 403.4, 410.0, and 417.4 eV, which also appear in D-BNC-600, 700, and 800. The peak at 403.4 is ascribed to  $\pi^*$  resonance transitions, and the other two peaks are corresponded to  $\sigma^*$  resonance transitions. [5.12, 39] In addition, the peaks originated from the single nitrogen doping sites are also detected in D-BNCs, although their intensities are relatively low. Two peaks at 396.8 and 399.7 eV corresponding to pyridinic N and graphitic N, respectively, [5.41] exist in D-BNCs and are gradually intensified with increasing chlorination temperature.

FT-IR spectra of D-BNCs also demonstrate the formation of h-BN exhibited, as shown in Figure 5.11. The strong peak at  $1398\text{ cm}^{-1}$  appears in D-BNC-400, 600, and 700, along with an additional peak at  $772\text{ cm}^{-1}$ . These two peaks are corresponded to in-plane stretching and out-of-plane bending vibration of h-BN, respectively. [5.42] On the other hand, only a small peak at  $1398\text{ cm}^{-1}$  is observed in D-BNC-800. The C=N bond also exists in all D-BNCs. [5.42] In addition, the broad band at  $3398\text{ cm}^{-1}$  attributed to O-H or N-H stretching or water molecules is detected in all D-BNCs. [5.42] In D-BNC-400, both h-BN and C=N peak are developed significantly, whereas h-BN peaks are prevailed in D-BNC-600 and 700. While, in D-BNC-800, the C=N peak is dominant and h-BN peaks were barely observed.

According to XPS, NEXAFS, and FT-IR analysis results, the optimum chlorination temperature to synthesize the BN embedded porous carbon is  $700\text{ }^{\circ}\text{C}$ . If the chlorination temperature is less than  $700\text{ }^{\circ}\text{C}$ , the h-BN phase is well-formed, but the graphitic nature of D-BNC cannot be well-established (low  $sp^2$ -hybridized carbon, but high C-O and C-N content. Conversely, if the chlorination temperature is higher than  $700\text{ }^{\circ}\text{C}$ , the robust carbon layer can be constructed, but the h-BN phase is barely developed in the carbon shell of D-BNC.

Furthermore, Electron energy loss spectroscopy (EELS) analysis of D-BNC-700 clearly illustrated the BN embedded carbon structure. Elemental mapping analysis (Figures 5.9a-c) showed that boron, carbon, and nitrogen were homogeneously dispersed throughout D-BNC-700. In addition, the K-edge absorption for boron, carbon, and nitrogen located at 191, 284, and 401eV, respectively, is displayed in Figure 5.9d. A pair of peaks originated from  $1s \rightarrow \pi^*$  and

1s $\rightarrow\sigma^*$  appears at each absorption region, indicating that boron, carbon, and nitrogen atoms have sp<sup>2</sup> hybridization states. [5.14, 37, 43]

The N<sub>2</sub> adsorption and desorption isotherms of D-BNCs at 77 K are illustrated in Figure 5.12a. All isotherms present type I and IV pores, which indicates the simultaneous development of the micro- and mesopore in D-BNCs. [5.44, 45] Pore size distribution (PSD) of D-BNCs is plotted in Figure 5.12b. A sharp increase in the adsorption at P/P<sub>0</sub>=0.90-0.99 in all isotherms tells the development of macro-pore originated from the agglomeration of raw powders. The quantitative analysis of pore texture is summarized in Table 5.3. D-BNC-400 has the lowest Brunauer-Emmett-Teller (BET) specific surface area value of 447 m<sup>2</sup>/g. An increase in chlorination temperature causes an increase in BET specific surface area of D-BNCs. This is due to the development of micro and small meso-pore attributed by the rearrangement of carbon atoms and decomposition of nitrogen and carbon atoms inside the particles during the chlorination, as reported in the previous chlorination. [5.29, 46] In particular, D-CBN37(44)-700 and 800 have a very high BET surface area of 1215 and 1613 m<sup>2</sup>/g, respectively, and also show both high micropore volume and mesopore volume along with high total pore volume. These results indicate the hierarchical pore structure, which is favorable for the kinetics of the electrochemical reaction. [5.47]

In brief, integrating all the characterizations of D-BNCs, the chlorination temperature of 700 °C is determined as the optimum temperature for synthesizing the robust BN incorporated porous carbon having hierarchical pore structure.

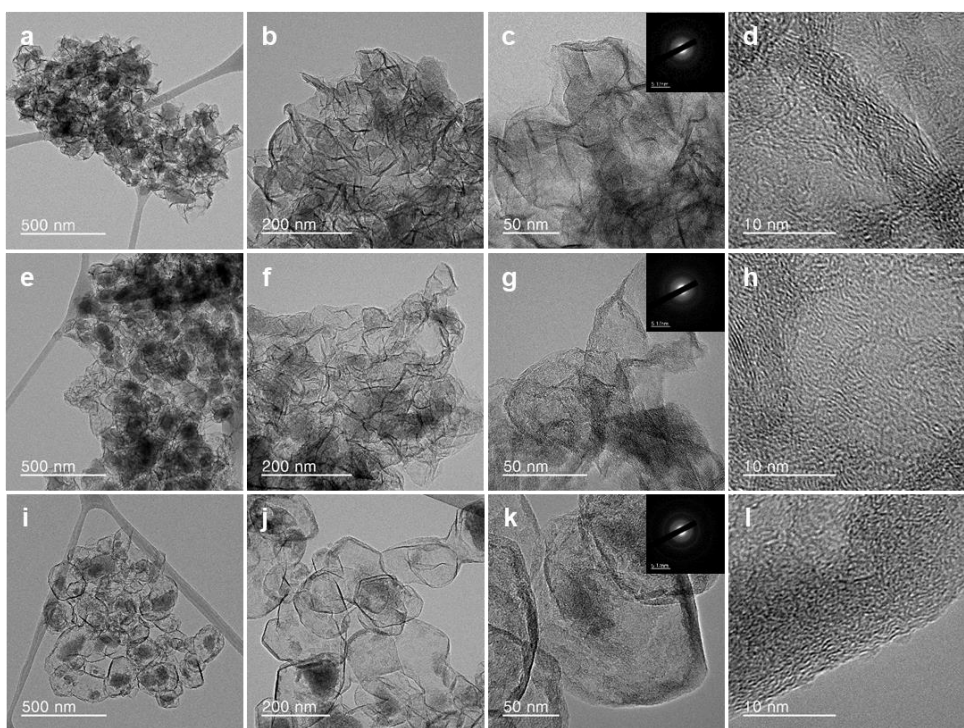


**Figure 5.3.** TEM images of D-BNC-600 (a-c), D-BNC-700 (e-g), and D-BNC-800 (i-k). HR-TEM images of D-BNC-600 (d), D-BNC-700 (h), and D-BNC-800 (l).

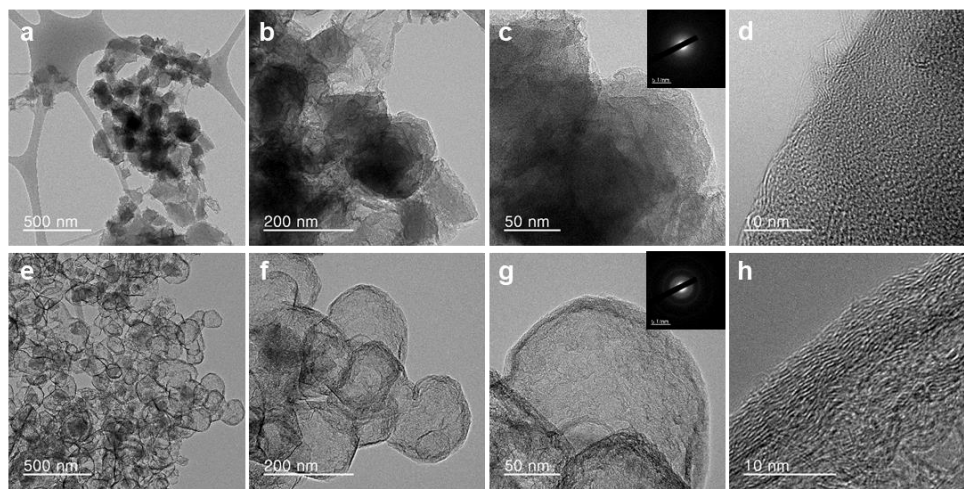


**Figure 5.4.** TEM images of D-BNC-400 (a-c) and D-BNC-1000 (e-g). HR-TEM images of D-BNC-400 (d) and D-BNC-1000 (h).

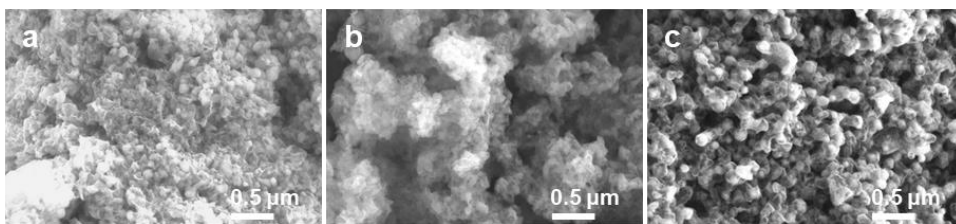


**Figure 5.5.** FE-SEM images of D-BNC-600 (a), -700 (b), and -800 (c).

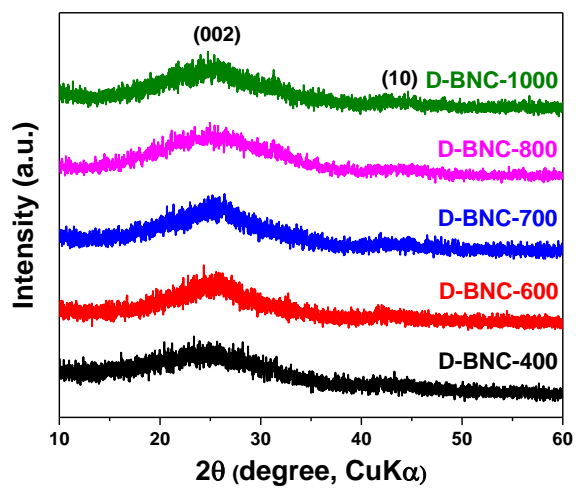


**Figure 5.6.** XRD of D-BNCs varying with the chlorination temperature.



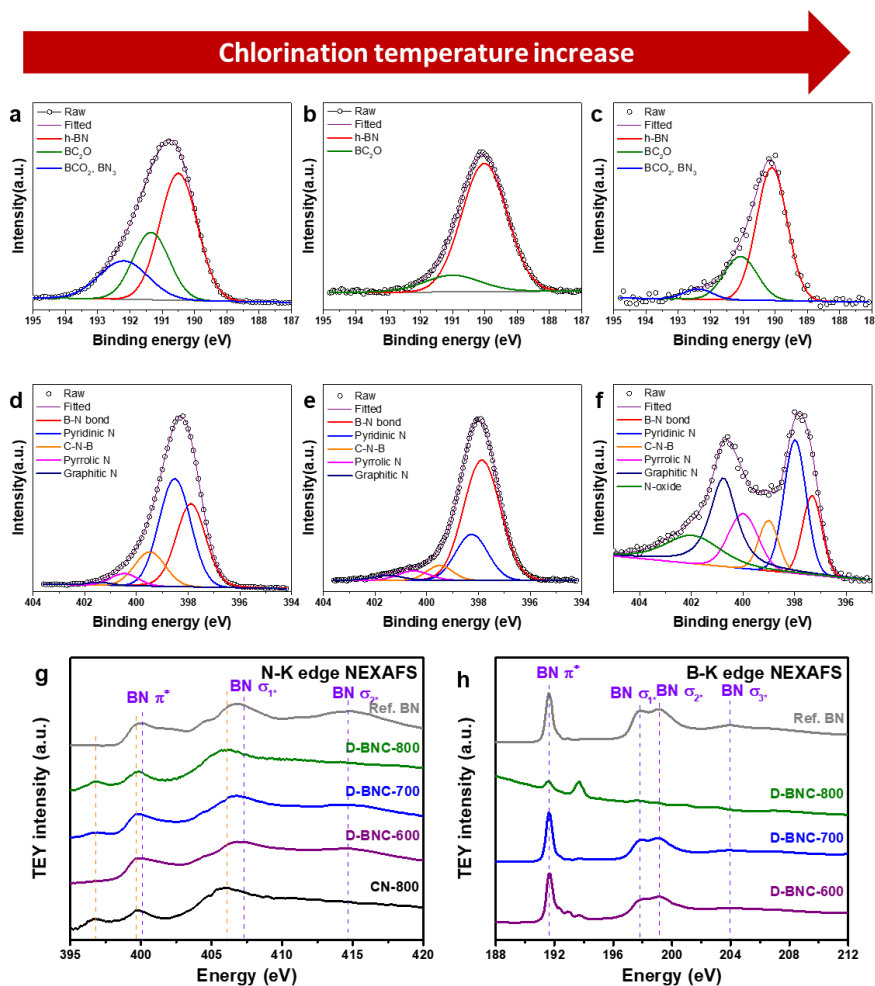


**Figure 5.7.** HR-XPS B 1s spectra of D-BNC-600 (a), D-BNC-700 (b), D-BNC-800 (c) and N 1s spectra of D-BNC-600 (d), D-BNC-700 (e), D-BNC-800 (f). NXAFS spectra of N-K edge (g) and B-K edge (h) for D-BNC-600, 700, and 800, CN-800, and bulk BN (ref.).

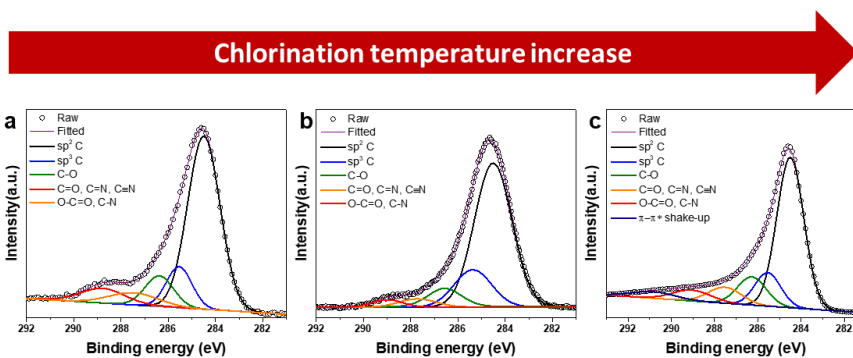


**Figure 5.8.** High resolution (HR) XPS C 1s spectra of D-BNC-600 (a), D-BNC-700 (b), and D-BNC-800 (c).

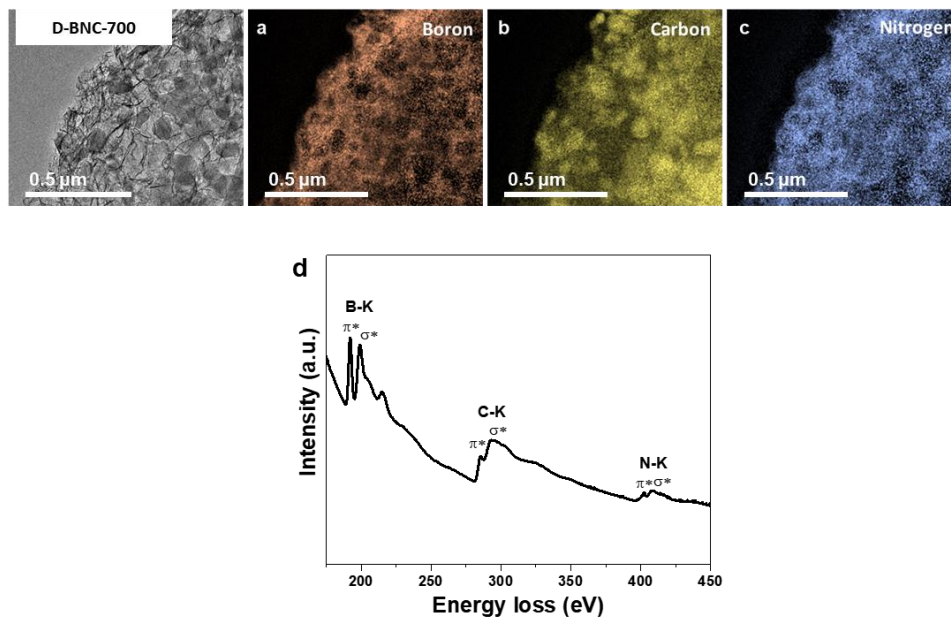


**Figure 5.9.** Elemental mapping of boron(a), carbon (a), and nitrogen (c), and EELS spectrum (d) of D-BNC-700.

**Table 5.1.** The chemical composition of D-BNCs measured by XPS.

Samples	XPS (at. %)			
	C	N	B	O
D-BNC-400	24.9	35.9	22.8	13.7
D-BNC-600	25.4	33.7	29.8	10.2
D-BNC-700	56.9	22.0	15.5	4.1
D-BNC-800	84.2	8.7	1.6	2.6
D-BNC-1000	95.1	2.6	0.7	1.2

**Table 5.2.** Summary of the content of bond configuration of D-BNCs.

Samples	sp <sup>2</sup> C (at.%)	h-BN (at.%)	BC <sub>2</sub> O (at.%)	BCO <sub>2</sub> (at.%)	Pyridi cic N (at.%)	Pyrroli c N	Graph itic N	N- oxide
D-BNC-400	9.4	16.0	8.8	2.5	14.7	3.4	-	-
D-BNC-600	15.4	26.8	6.8	5.3	17.1	1.7	0.3	-
D-BNC-700	36.5	32.2	2.8	-	5.3	1.0	0.6	-
D-BNC-800	49.1	2.2	0.4	0.1	2.1	1.1	2.3	1.3
D-BNC-1000	45.9	0.4	0.2	0.1	0.4	0.5	0.7	0.5

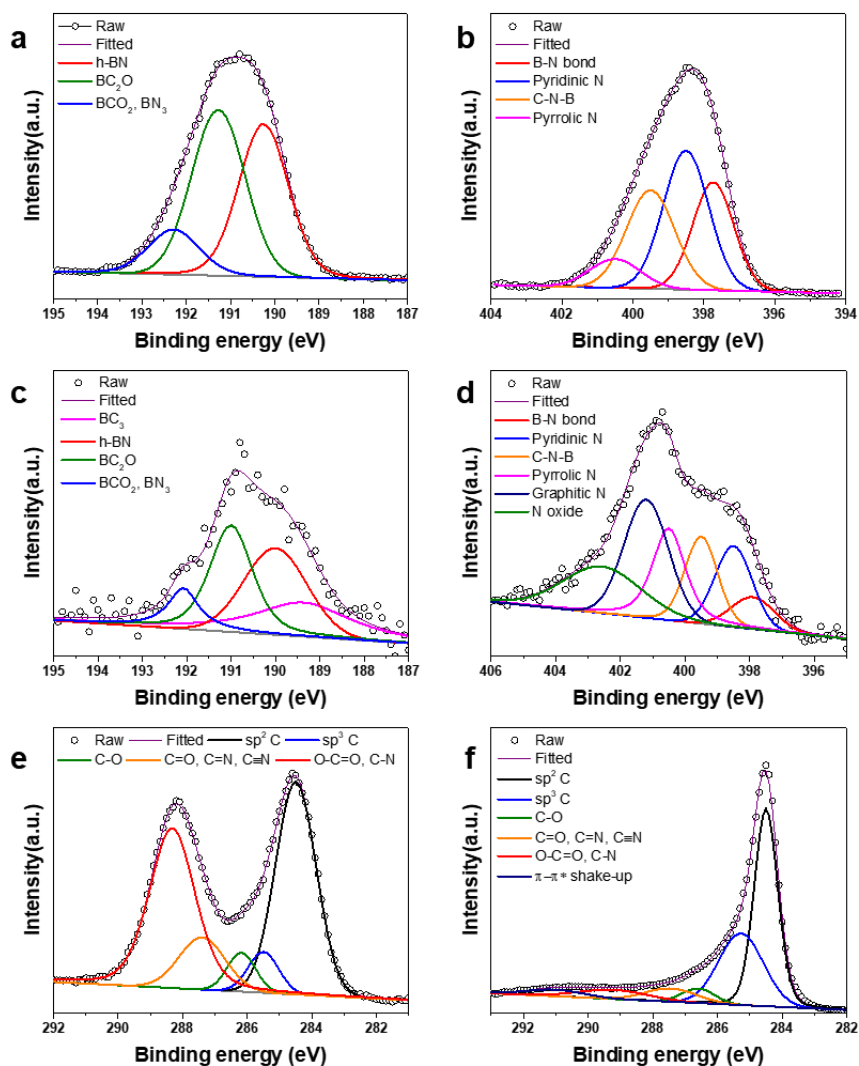


**Figure 5.10.** High resolution XPS B 1s spectra of D-BNC-400 (a) and D-BNC-1000 (b), N 1s spectra of D-BNC-400 (c) and D-BNC-1000 (d), and C 1s spectra of D-BNC-400 (e) and D-BNC-1000 (f).

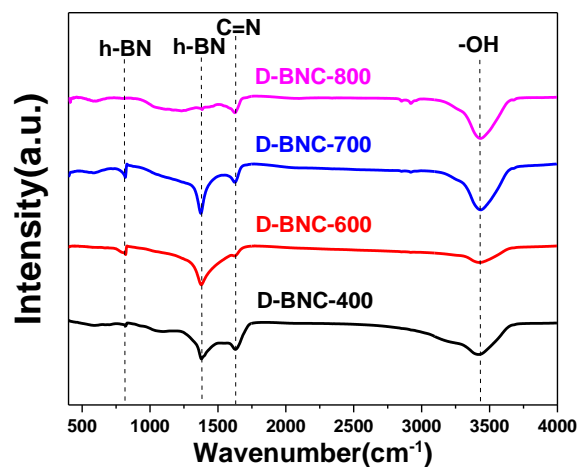


Figure 5.11. FT-IR spectrum of D-BNCs.

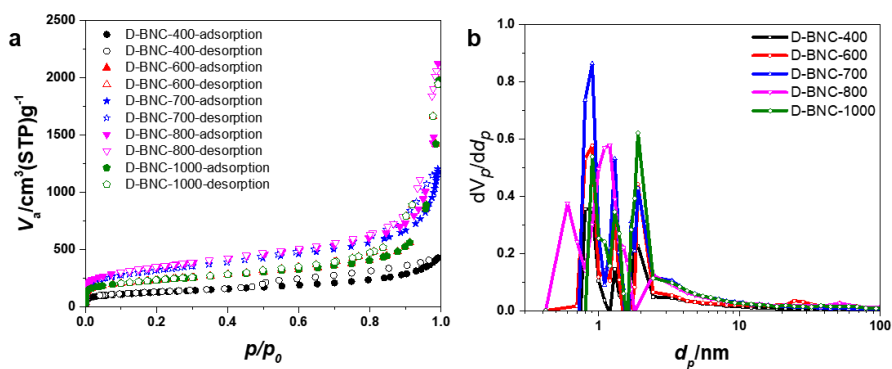


Figure 5.12. The N<sub>2</sub> sorption isotherm (a) and pore size distribution (b) of D-BNCs.

Table 5.3. BET SSA and pore volumes of D-BNCs.

Sample	BET SSA(m <sup>2</sup> /g)	Micro-pore volume (cm <sup>3</sup> /g)	Meso pore volume (cm <sup>3</sup> /g)	Total pore volume (cm <sup>3</sup> /g)
D-BNC-400	447	0.17	0.20	0.65
D-BNC-600	816	0.31	0.50	2.64
D-BNC-700	1130	0.43	0.44	1.83
D-BNC-800	1613	0.59	0.83	4.01
D-BNC-1000	959	0.35	0.45	2.31

## 5.6. Variation of D-BNC characteristics with raw powder composition

The starting raw powder composition (C:B ratio) is one of the main factors that can change the morphology and composition of D-BNCs. Compared to D-BNC-700 using a moderate amount of boron precursor (B:C:N molar ratio in precursors = 1:1:2.3) shown in the previous section, the samples that used insufficient boron precursor (D-BNC-700-LB, B:C:N molar ratio in precursors = 0.25:1:2.3) and excessive boron precursor (D-BNC-700-HB, B:C:N molar ratio in precursors = 4:1:2.3) show significant difference in the structure and surface chemistry.

In Figure 5.13, TEM images show the morphology of D-BNC-700s varying with the mixture ratio of precursor. In the case of D-BNC-700-LB, the lack of boron impedes the development of BNC shell. In contrast, in D-BNC-700-HB, spherical CN aggregates were retained inside the shell. Excess supply of boron seems to reinforce the formation of BN-rich carbon shells, and the carbon and nitrogen could not escape well through the shells, which leaves CN aggregates. The difference in morphology also exhibited in the SEM images of D-BNC-700-LB and -HB (Figure 5.14). The HR-TEM images of both D-BNC-700-LB and D-BNC-700-HB (Figures 5.13 d,h) showed a turbostratic structure regardless of the boron precursor ratio. This is further corroborated by the selected area electron diffraction (SAED) patterns (insets of Figures 5.13c,g) displaying two diffusive rings which indicate (100)/(101) and (110)/(112), respectively, and one broad diffraction ring originated from inhomogeneity of the (002) interlayer distance. X-ray powder diffraction(XRD)

patterns of D-BNC-700-LB and D-BNC-700-HB, shown in Figure 5.15 presents the same results as the TEM analysis. They only have two broad peaks located at around 26.1 ° and 42.4 ° assigned to (002) and (10), respectively, indicating the turbostratic structure.

The variation of boron and nitrogen content is measured using the XPS quantitative analysis. Table 5.4 shows the composition of D-BNC-700-LB and D-BNC-700-HB. Comparing with D-BNC-700, the boron and nitrogen content of D-BNC-700-LB are lower while carbon content is higher. On the other hand, in the case of D-BNC-700-HB, even though its boron content in starting raw powder was much higher than D-BNC-700, its final boron content was significantly less than D-BNC-700, and the nitrogen content was similar level. The low boron content in D-BNC-700-HB is due to the remaining CN inside carbon shells, as shown in above TEM analysis (Figure 5.13e).

The HR spectra analysis was performed to examine the bond configuration of boron and nitrogen at the surface (Figure 5.16), and bond configuration contents were calculated and summarized in Table 5.5. Comparing with the results of D-BNC-700 (Figures 5.7b,e and 5.8b, and Table 5.2), D-BNC-700-LB has lower h-BN content, but higher  $sp^2$ -hybridized carbon and single N doping sites content. D-BNC-700-HB has lower  $sp^2$ -hybridized and h-BN content, while C-O and C-N content are greatly increased, as shown in the C 1s band (Figure 5.16f). These results indicate that the development of h-BN is insufficient in D-BNC-700-LB due to the lack of boron, whereas the excess supplied boron in D-BNC-700-HB impedes the decomposition of CN inside carbon shell resulting in the inhomogeneity of phase

distribution inner and outer area. This is also confirmed with the huge difference in N/C ratio of D-BNC37-700-HB between XPS (0.37) result and elemental analysis (EA) result (0.6) listed in table 5.5. The N/C ratios measured by XPS and EA are 0.37 and 0.60, respectively, demonstrating the inhomogeneity of phase distribution, not observed in D-BNC-700.

The pore structures of D-BNC-700-LB and D-BNC-700-HB are compared using the N<sub>2</sub> adsorption and desorption isotherms at 77 K, as shown in Figure 5.17a. Both D-BNCs show type I and IV pores, indicating the simultaneous development of the micro- and mesopore, also shown in PSD (Figure 5.17b). The BET specific area and pore texture values are summarized in Table 5.6. D-BNC-700-LB and D-BNC-700-HB have lower BET specific surface area and micropore volume than D-BNC-700 due to the residue of CN that lowers the micropore and small mesopore volume inside the D-BNC. This trend is more intensified in D-BNC-700-HB due to the development of agglomerated CN, as demonstrated in TEM analysis. Based on the analysis result of structural and chemical configuration, it is found that the precursor mixture ratio of B:C:N=1:1:2.3 is the optimum value for maximizing the uniformly distributed BN nanodomains in the carbon structure.



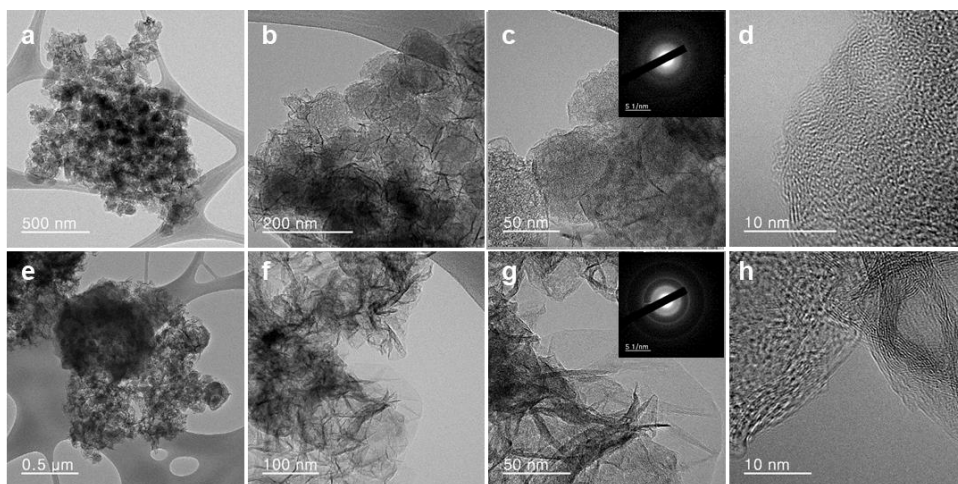


**Figure 5.13.** TEM image of D-BNC-700-LB (a-c), D-BNC-700-HB (e-g). HR-TEM images of D-BNC-700-LB (d) and D-BNC-700-HB (h).

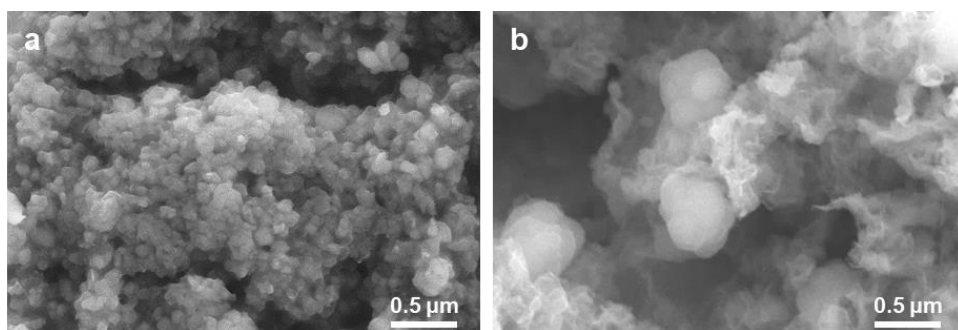


**Figure 5.14.** FE-SEM images of D-BNC-700-LB (a) and D-BNC-700-HB (b).

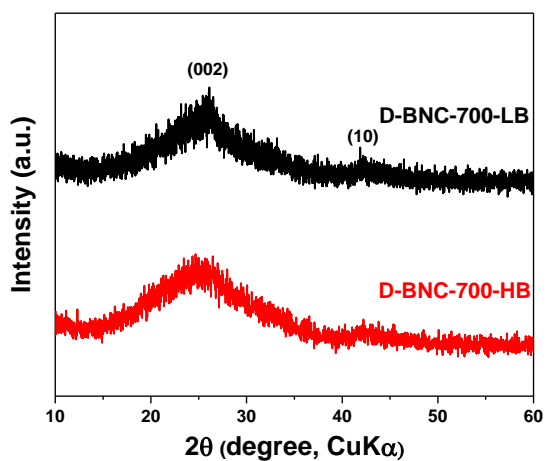


**Figure 5.15.** XRD of D-BNC-700-LB and -HB.

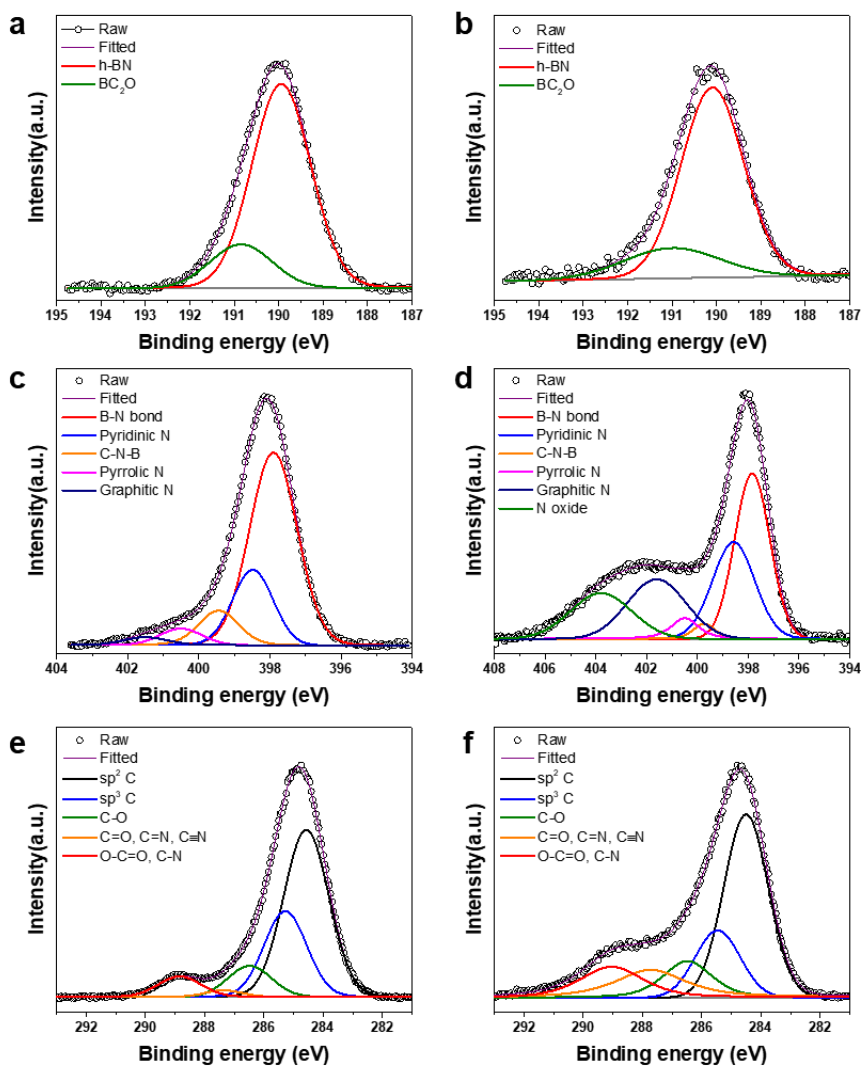


**Figure 5.16.** High resolution XPS B 1s spectra of D-BNC-700-LB (a) and D-BNC-700-HB (b), N 1s spectra of D-BNC-700-LB (c) and D-BNC-HB (d), and C 1s spectra of D-BNC-700-LB (e) and D-BNC-700-HB (f).

**Table 5.4.** The chemical composition of D-BNC-700s measured by XPS and N/C ratio calculated by XPS and EA.

Samples	XPS (at. %)				EA
	C	N	B	N/C	N/C
CN-800	94.5	5.3	N/D	0.06	
D-BNC-700-LB	71.6	16.2	12.2	0.23	0.26
D-BNC-700	54.2	24.0	18.9	0.44	0.40
D-BNC-700-HB	65.9	24.3	9.8	0.37	0.60

**Table 5.5.** Summary of the content of bond configuration of D-BNC-700-LB and – HB.

Samples	Sp <sup>2</sup> C (at. %)	h-BN (at. %)	BC <sub>2</sub> O (at. %)	BCO <sub>2</sub> (at. %)	Pyridic N (at. %)	Pyrrolic N	Graphitic N	N-oxide
D-BNC-700-LB	39.5	10.0	1.4	-	10.2	0.7	0.4	-
D-BNC-700-HB	29.1	7.9	1.9	-	3.03	1.5	4.0	4.9

**Table 5.6.** The BET SSA and pore volumes of BNC-700s.

Sample	BET SSA(m <sup>2</sup> /g)	Micro-pore volume (cm <sup>3</sup> /g)	Meso pore volume (cm <sup>3</sup> /g)	Total pore volume (cm <sup>3</sup> /g)
D-BNC-700-LB	940	0.35	0.41	2.37
D-BNC-700	1130	0.43	0.44	1.83
D-BNC-700-HB	790	0.30	0.46	2.83

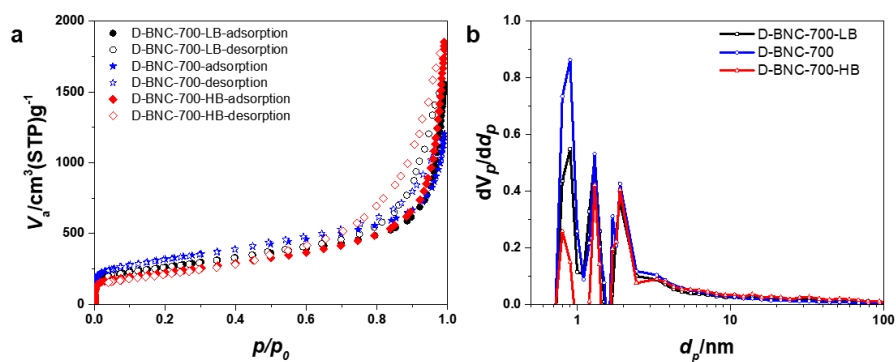


**Figure 5.17.** The N<sub>2</sub> sorption isotherm (a) and pore size distribution (b) of D-BNC-700s.

## 5.7. Formation mechanism of BNC

Based on the thermodynamic calculation and experiments, the proposed formation mechanism of D-BNCs is schematized in Figure 5.18.

When the chlorination temperature is low (400 °C and 600 °C), the C-N bond is maintained, and carbon ordering tendency is low. [5.29, 34] Thus, D-BNC retains the shape of raw-powder with the preserved interior CN. Boron atoms mainly associated with nitrogen at the surface of CN since B-N bonds are easily formed due to donor-acceptor interaction. [5.21] As a result, phase separation occurs in the D-BNC-400 and 600. That is CN (interior) and BN-rich phase (exterior) coexist in each BNC particle. The amount of interior CN phase is less at 600 °C than 400 °C.

In the chlorination process at 700 °C, the interior CN is mostly decomposed due to the low thermal stability of the C-N bond with increasing temperature. [5.46] On the surface of Ti(C,N), the diffused boron atom from TiB<sub>2</sub> can form BN as well as stabilize the carbon structure. Diffused boron atoms anchor the unstable nitrogen and carbon atoms in the carbon layer by forming a covalent bond [5.48, 49] and also facilitate the self-diffusion carbon atom in the carbon layer [5.50], which can promote the graphenization (establishing sp<sup>2</sup> C-C bond) of the carbon layer. As a result, a collapsed BNC shell where BN nano-domains are homogeneously distributed can be obtained.

When the chlorination temperature is higher than 800 °C, the sp<sup>2</sup> C-C bonds are

well established at the surface of CN, and significant loss of nitrogen occurs. The carbon structure linking effect by boron atoms is intensified, which facilitates the formation of carbon-rich shells. Thus, the solid carbon shell that retains the shape of the original raw particle is formed. Although BN rich phase can be partially formed during the chlorination, it hardly survives due to the decomposition by chlorine gas at the high temperature.

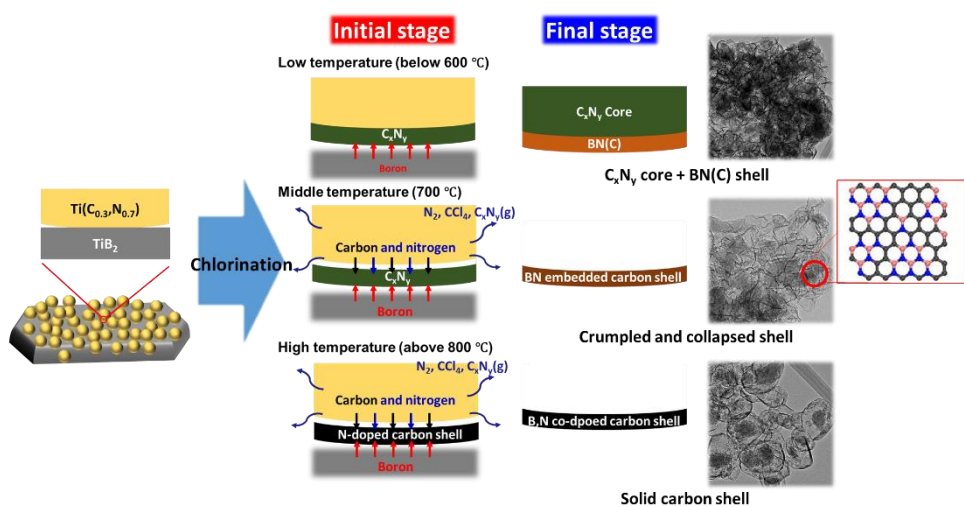


**Figure 5.18** The scheme of the formation mechanism of D-CNBs.

## 5.8. Oxygen reduction reaction performance of D-BNC

The oxygen reduction reaction (ORR) catalytic performance of D-BNCs was measured with a rotating ring-disk electrode (RRDE) setup. As mentioned above, the chlorination temperature greatly determines the characteristic of the B-C-N material, so we compared the catalytic activity according to the treated temperatures. Figure 5.19a shows the ORR polarization curves of D-BNCs, together with the  $\text{H}_2\text{O}_2$  production current detected by the ring electrode. The corresponding  $\text{H}_2\text{O}_2$  selectivity was plotted in Figure 5.19b as a function of potential. The activity of D-BNCs showed a steady increase as the chlorination temperature increased up to 800 °C and then decreased. D-BNC-400 and 600 had poor activities and current densities for ORR, which would be hard to be applied as electrocatalysts. D-BNC-800 showed a much higher disk current for ORR, and the ring current was much lower than others. The active center would be mainly the N-functional groups on N-doped carbon surfaces, which have previously been reported active for the  $4e^-$  ORR. The higher decrease in the activity of the D-BNC-1000 sample than that of D-BNC-800 could be explained in the content of nitrogen (or other functional groups) on the carbon surface. As shown in Table 5.1, the amount of nitrogen, oxygen species decreased dramatically in such a high temperature (at 1000 °C). Also, BET surface area results (Table 5.3) show that the D-BNC-1000 sample has a much lower surface area and pore volumes than D-BNC-800. Thus, we considered that this activity loss was contributed to the decreased active site number and physical surface area, which can occur in the transport issues in the porous carbon electrode.

To investigate how the treated temperature affects the electrocatalytic activities of D-BNCs based on the transport issues of reactant (oxygen and electrolyte ions) or electrical conductivity of the electrode, we conducted the electrochemical impedance spectroscopy (EIS) measurements. Impedance analysis has been used as a useful tool for studying the porous carbon structures with the electric double-layer capacitor performance in non-Faradaic conditions. The relaxation time constant ( $\tau_0$ ) of catalysts are obtained from EIS results through the complex capacitance analysis (Figures 5.19d and 5.20). The  $\tau_0$  indicates the rate capability of the porous carbon structure. D-BNC materials have higher peak frequency as the temperature rises. The D-BNC-1000 showed a peak at 14.98 Hz, and D-BNC-800 is at 11.38 Hz. Whereas D-BNC-400 and 600 do not show a peak in the measured frequencies (from 10 mHz to 100 kHz), which means the peak frequency of them might be below 10 mHz. Of note, the higher peak frequency of D-BNC-1000 indicates a shorter  $\tau_0$  than D-BNC-800, as well as better kinetics of the supercapacitor.

However, the ORR activity is quite the opposite. That is, the D-BNC-1000 sample has a severely decreased number of active sites, losing many functional groups on the surface at a higher heat-treated temperature. D-BNC-800 shows the superior ORR activity comparable to platinum-based catalysts in alkaline media following  $4e^-$  ORR, as it has a high surface area ( $\sim 1613 \text{ m}^2/\text{g}$ ) with plenty of micropores. Whereas, D-BNC-700 shows the highest activity, selectivity, and stability for electrochemical  $\text{H}_2\text{O}_2$  production than other D-BNCs, with a maximal  $\text{H}_2\text{O}_2$  selectivity of more than 88 %, and a high onset potential at about 0.81 V vs. RHE. This high onset potential in alkaline media represents facile kinetics of  $\text{H}_2\text{O}_2$  production with negligible overpotential. This indicates that there are distinct active

sites in D-BNC-700, probably the well-dispersed small domain of BN phases in carbon lattices, facilitating the 2e<sup>-</sup> ORR. We also conducted ORR measurement with different mixture ratio (C:B ratio) treated 700 °C, but they exhibited a similar electrochemical performance indicating the presence of similar active sites with these materials (Figure 5.21). D-BNC-700 showed superior activities than other configurations.

For the electrocatalyst application for fuel cells and electrosynthesis of liquid H<sub>2</sub>O<sub>2</sub> product, long-term stability is also an important criterion. To evaluate the stability of the D-BNC-700 sample, we conducted the stability test through the chronoamperometry method at 0.3 V vs. RHE in O<sub>2</sub>-saturated 0.1 M KOH electrolyte with 1600 rpm RRDE setup. Both the disk and ring currents were stable over 10 h (Figure 5.19c). To achieve a high current density of H<sub>2</sub>O<sub>2</sub> electrochemically production in the industrial scale (real device), we employed a D-BNC-700 catalyst as an efficient and stable 2e<sup>-</sup> ORR catalyst in our custom-made flow cell (Figure 5.19e). This flow cell was modified from a membrane-less reactor reported previously. A cell voltage of about 1.28 V was required to reach a cell current of 250 mA (50 mA/cm<sup>2</sup>), obtaining an H<sub>2</sub>O<sub>2</sub> Faradaic efficiency (FE) of ~ 61 % (Figure 5.19f). It was slightly lower than the selectivity delivered in the RRDE setup, but it would result from the mesoscopic effects related to H<sub>2</sub>O<sub>2</sub> molecules on the large-scale electrode. An impressive H<sub>2</sub>O<sub>2</sub> production rate of 4.65 mmol/h was obtained in our electrosynthetic cell. The continuous production of H<sub>2</sub>O<sub>2</sub> was conducted over 10 h with this cell, and the concentration of the final H<sub>2</sub>O<sub>2</sub> liquid solution product can be achieved with about 2.96 wt% in 1.0 M KOH solution. We measured the catalytic performance in neutral condition with flow cell (Figure 5.22), then the concentration



of  $\text{H}_2\text{O}_2$  in 1.0 M  $\text{Na}_2\text{CO}_3$  solution can be accumulated to about 2.58 wt. %.

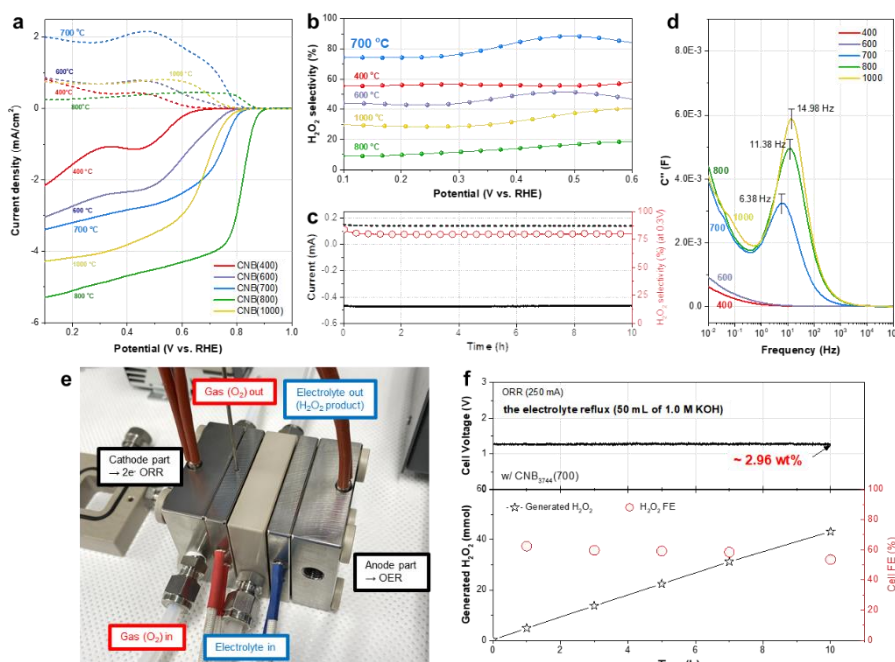


**Figure 5.19.** Polarization curves (solid lines) and simultaneous  $\text{H}_2\text{O}_2$  detection current at the ring electrode (dashed lines) at 1600 rpm with D-BNC materials, which were heat-treated under different temperature with Cl<sub>2</sub> (a). Calculated selectivity for  $\text{H}_2\text{O}_2$  production of samples (b), and the stability measurement of D-BNC-700 samples at 0.1 M KOH electrolyte (c). Imaginary capacitances plot for the complex capacitance analysis from EIS measurement (d). Digital images of our custom-made  $\text{H}_2\text{O}_2$  electrosynthetic flow cell (e) and  $\text{H}_2\text{O}_2$  generation performance in 1.0 M KOH electrolyte (f).

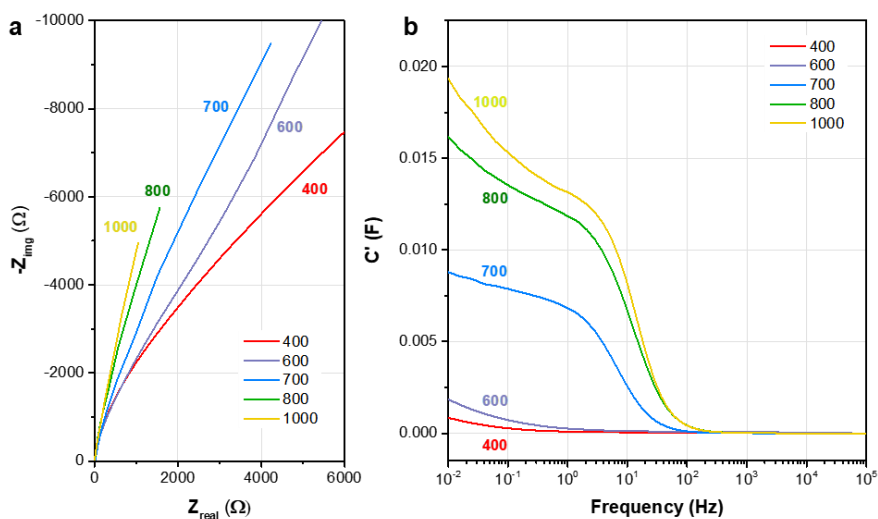


**Figure 5.20.** Nyquist plots of EIS results (a), and real capacitances plot for the complex capacitance analysis (b).

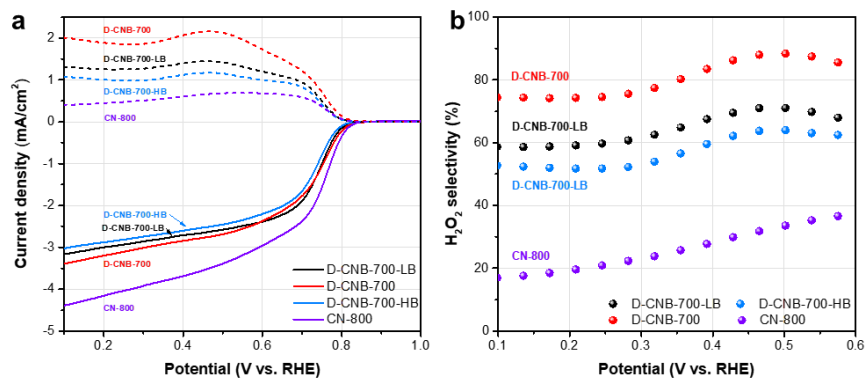


**Figure 5.21.** ORR polarization curves (a) and the selectivity for  $\text{H}_2\text{O}_2$  production (b) of D-BNC-700s using RRDE setup heat-treated at 700 °C.

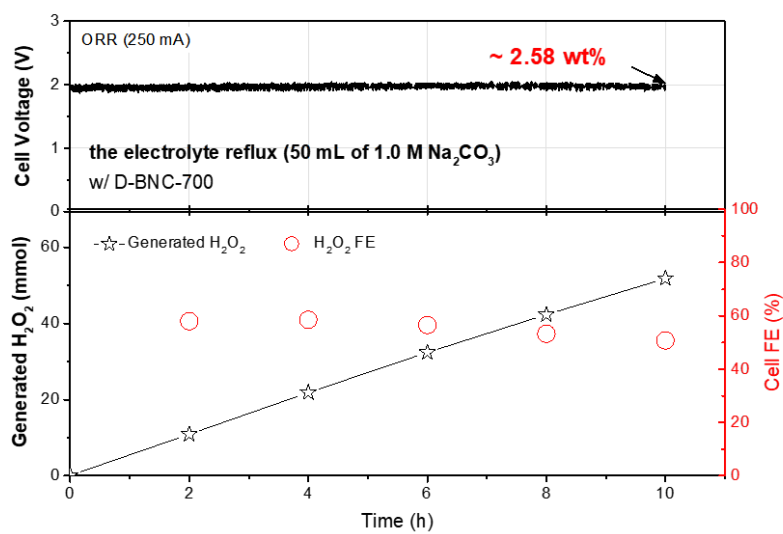


**Figure 5.22**  $\text{H}_2\text{O}_2$  generation performance of D-BNC-700 in the custom-made flow cell with the neutral 1.0 M  $\text{Na}_2\text{CO}_3$  electrolyte.

## 5.9. Conclusions

In this study, we design the novel one-pot chlorination synthetic process to produce the h-BN nano-domains incorporated porous carbon materials (D-BNCs) and demonstrates that these D-BNCs are promising electrocatalysts for  $\text{H}_2\text{O}_2$  production. Maximizing the proximity of B, C, and N in raw precursors ( $\text{Ti}(\text{C}_{0.3}\text{N}_{0.7})$  and  $\text{TiB}_2$ ) by leading the formation of nano-sized  $\text{Ti}(\text{C}_{0.3}\text{N}_{0.7})$  particles at the surface of micron  $\text{TiB}_2$  using the one-pot synthesis method is key for the implantation of BN phase. Because supplied boron atoms can facilitate the formation of the BN phase and also stabilize the BN embedded carbon layer by carbon structure linking effect during the chlorination process. The chlorination temperature and the composition of original raw powders are demonstrated as the major factor that determines the embedded BN composition and pore structure of D-BNCs. The moderate chlorination temperature (700 °C) and the moderate amount of boron (C:B molar ratio = 1:1 in the original raw materials) are optimal conditions to maximize both the formation of BN domains (32.2 at. %) in carbon layer and the development of the nanoporous structure of D-BNC (BET surface area: 1215  $\text{m}^2/\text{g}$ ). Thus, D-BNC-700 exhibited distinguished 2e-pathway oxygen reduction reaction (ORR) performance. It has superior maximum  $\text{H}_2\text{O}_2$  selectivity of 88.3 % in a rotating ring-disk electrode (RRDE) measurement in alkaline medium (1.0 M KOH). Furthermore, D-BNC-700 also shows excellent operation performance in the custom-made full flow cell condition. It has an outstanding  $\text{H}_2\text{O}_2$  production rate (4.65 mmol/h) and long-term stability with high  $\text{H}_2\text{O}_2$  faradaic efficiency (~ 61%) in 1.0 M KOH for 10 h. These results demonstrate that the B-C-N material can be the promising material as the electrocatalyst for  $\text{H}_2\text{O}_2$

production. Also, the chlorination of the carbonitride and boride mixture is an effective synthetic process to produce the high functional hetero-atom doped porous carbon, which is expected to give new insight into the synthesis of the carbon electrocatalyst research.

# **Chapter 6. Synthesis of atomically dispersed metal-CNB via one step chlorination**

## **6.1. Research highlight**

- Transition metals (Fe and Ni) and boron are concurrently introduced in the synthesis of N-doped carbon (CN) by the one step chlorination.
- Hand mixed  $\text{Ti}(\text{C}_{0.5}\text{N}_{0.5})\text{-TiB}_2$ -metal (Fe and Ni) acetylacetonate used as the original raw precursors
- The samples obtained by one step chlorination of raw precursors are denoted as M-CNB (M = Fe and Ni).
- The formation of metal boride nanoparticle and the increase in eutectic temperature of the metal boride-C system are revealed as critical factors that enables the synthesis of atomic dispersed M-CNB materials having high porosity by the chlorination process.
- In Fe-CNB, the atomic dispersion of Fe is feasible and it has highly porous structure thus, having outstanding electrocatalytic activity for oxygen reduction reaction (ORR) in alkaline medium.
- In Ni-CNB, the atomic dispersion of Ni is impossible and the severe graphitization occurs, no credit at all for the improvement of electrocatalytic activity for ORR in alkaline medium.

## 6.2. Introduction

Single-atom catalyst (SAC) has been recently in the spotlight as the key catalyst material in the energy and environmental applications since homogeneously distributed atomic metal species enable to maximize the catalytic activity and selectivity. [6.1-3] Among the various SACs, the atomic metal-N<sub>x</sub> (M-N<sub>x</sub>) catalyst has been most actively studied and expected to be a promising catalyst. To enhance the stability and recyclability, embedding the M-N<sub>x</sub> moieties into support is favorable. Carbon support is one of the most commonly used substrates, satisfying both durability and performance. [6.4] Nitrogen can readily incorporate into the carbon support, thus favorable to accommodate a large amount of M-N<sub>x</sub> moiety. [6.1, 5] Furthermore, carbon support can construct a strong covalent bond with M-N<sub>x</sub> moieties, stabilizing the M-N<sub>x</sub> moieties as well as modifying the electronic structure. [6.1, 5] Thus, both carbon support and M-N<sub>x</sub> moieties can be optimized to the adsorption and desorption of intermediates for improving catalytic performance. [6.1, 5] Furthermore, the carbon support has a high electrical conductivity enhancing the electron transfer in electrochemical reaction. [6.6] Therefore, numerous studies have been conducted on the synthesis of M-N<sub>x</sub> embedded carbon support (M-CN), especially transition metal M-CN that transition metal M-N<sub>x</sub> sites implanted in micropore. Depending on the type of transition metal, M-CN can show the extraordinary catalytic performance in various electrocatalytic reactions, including oxygen reduction reaction (ORR) [6.7-12], H<sub>2</sub> evolution reaction (HER) [6.13-15], and CO<sub>2</sub> reduction reaction (CO<sub>2</sub>RR) [6.16-18].

However, the facile synthesis of a robust M-CN catalyst is still unavailable. In

general, M-CN synthesis methods involve the pyrolysis of the mixtures of metal, nitrogen, and carbon precursors. The pyrolysis process accompanies high-temperature treatment ( $> 800\text{ }^{\circ}\text{C}$ ), which inevitably needs to endow the electric conductivity to the carbon support by constructing ordered structure as well as to improve the stability to  $\text{M-N}_x$  active sites. [6.19, 20] During the pyrolysis process, however, the atomic metals can establish  $\text{M-N}_x$  moieties and form metal-based nanoparticles. The preference to the  $\text{M-N}_x$  moieties or nanoparticles can be significantly varied depending on the experimental conditions. The formation of the metal-based nanoparticles, especially with transition metals, has a profound effect on the carbon structure since the transition metal-based particle acts as the graphitization catalyst well known in various carbon studies. [6.21-24] Therefore, the careful synthetic strategy based on the understanding of the interaction between carbon and metal precursors during the synthetic process is a prerequisite for producing practical M-CN catalysts.

Meanwhile, the introduction of boron to N-doped carbon (CN) is known as an effective method for improving the electrocatalytic properties. The electronic structure of carbon can be readily tuned by the synergetic effect of boron and nitrogen, which serves as the electron donor and electron acceptor, respectively, in carbon substrate. [6.25, 26] Therefore, boron and nitrogen co-doped carbon (CNB) produced by the various methods applied in multiple optical, electronic, and electrocatalytic applications. [6.27-30] In particular, in the electrocatalytic applications, numerous studies demonstrate that boron can induce the significant development of active sites, such as B-N bond and pyridinic nitrogen, having high catalytic activity. [6.31, 32]



In contrast to the active research on CNB and M-CN, few studies have been reported in the synthesis of M-CNB. Our group previously reported the facile synthesis and formation mechanism of CN and CNB via a one-pot chlorination process. [6.33-35] The addition of boron into CN significantly facilitated the formation of nitrogen-rich, especially pyridinic nitrogen-rich, carbon structure which had high CO<sub>2</sub> gas storage and ORR performance. [6.34, 36] Moreover, we also successfully synthesized the Fe-CNB catalyst having superior ORR performance via a one-pot chlorination process. [6.35] However, the mechanism of change in the structure and surface chemistry of Fe-CNB by the introduction of boron, directly related to the enhancement of electrocatalytic activity is still unrevealed.

In this study, we try to understand the influence of the boron to the structure change and electrocatalytic property (ORR) of M-CNB based on the experimental and thermodynamic analysis. For this purpose, Fe-CNB and Ni-CNB were synthesized via the one-pot chlorination process. TEM, XRD, EXAFS, and BET analysis were carried out to study their structure, and the nano-thermodynamic approach was applied to explain the fundamentals of the structure difference.

### 6.3. The ORR activity of Fe-CN/CNB and Ni-CN/CNB

To investigate the influence boron and transition metals (Fe and Ni) to the electrocatalytic properties of M-CNB materials, the oxygen reduction reaction (ORR) activities of M-CN and M-CNBs where M is Fe and Ni were evaluated using rotating ring-disk electrode (RRDE) measurement in alkaline media, exhibited in Figure 6.1. The linear sweep voltammetry (LSV) curve of Fe-CN in 0.1 M KOH (Figure 6.1a) demonstrates that the introduction of iron to CN effectively improves the ORR activity with lowering the onset potential and half-wave potential. Furthermore, the simultaneous introduction of boron and iron to CN enhances the ORR activity dramatically. The LSV curve of the Fe-CNB has the very high onset potential (0.92 V) and half-wave potential (0.85 V), which surpasses that of Pt/C catalyst (20 wt % Pt, Johnson-Matthey). This indicates that the concurrent incorporation of boron and iron during the synthesis of CN via the chlorination process dramatically stimulates the development of ORR active sites in the Fe-CNB. On the other hand, while the introduction of nickel enhances the ORR activity of CN shown in the LSV curve of Ni-CN, the simultaneous incorporation of boron and nickel barely improves the ORR activity (Figure 6.1b). In summary, the variation of ORR activity by the introduction of boron is different depending on the type of transition metal in M-CNB, despite their identical synthesis process.

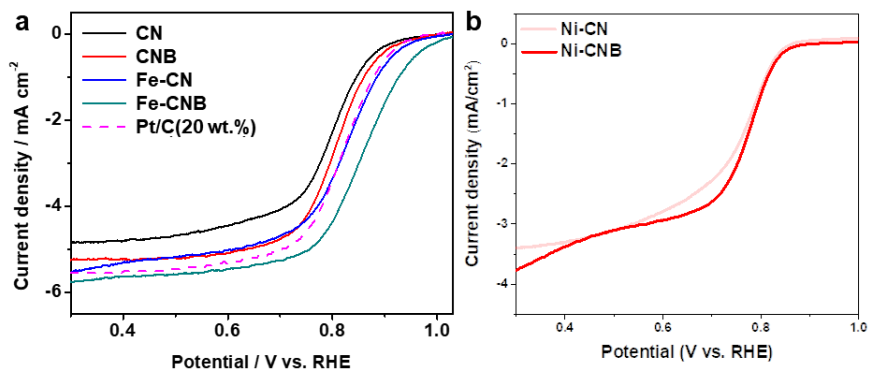


**Figure 6.1.** ORR activity comparison between (a) Fe-CN and Fe-CNB, and (b) Ni-CN and Ni-CNB in 0.1 M KOH. The measurements were conducted with the electrode rotation of 1600 rpm.

## 6.4. Structural variation of Fe-CN/CNB and Ni- CN/CNB

The structure variation of M-CN and M-CNB (M = Fe and Ni) depending on the incorporation of boron and transition metal was examined by the transmission electron microscopy (TEM) analysis. The TEM images of all samples are presented in Figures 6.2, 6.3, and 6.4. CN (Figure 6.2a), which is the control sample without boron and transition metal added, retains the shape of raw  $\text{Ti}(\text{C}_{0.5}\text{N}_{0.5})$  powder. This is a typical feature of carbon material produce by the chlorination method. [6.37] The HR-TEM image of CN (Figure 6.2b) shows the disordered carbon layer with the interlayer distance of 0.34-0.36 nm, indicating that CN has a turbostratic structure. The introduction of iron to CN (Fe-CN) barely changes the overall shape of Fe-CN (Figure 6.2c). There are both FeO nanoparticles covered with a thin disordered carbon layer (Figures 6.2d,e) and Fe nanoparticles covered with the thick graphitic carbon layer (Figures 6.2f-h), indicating that partial graphitization occurs at the interface between Fe-based particles and carbon substrate. Both particles are about a size of 5-30 nm size and exist at the surface of Fe-CN. The graphitization effect is more prominent in the Fe nanoparticle. In the case of Ni-CN (Figure 6.3), disorder carbon ribbons are developed at the entire surface of Ni-CN. In addition, residual nickel nanoparticles covered with the  $\text{Ni}_3\text{C}$  phase and ordered carbon layers are observed.

The selected area electron diffraction (SAED) patterns of Fe-CN and Ni-CN (insets of Figures 6.2c and 6.3a) exhibited two diffusive rings which indicate (100)/(101) and (110)/(112) patterns with 0.21 nm and 0.12 nm d-spacing,

respectively, along with one broad diffraction ring located at innermost indicating (002). These rings are also supporting evidence of the turbostratic structure of CN, Fe-CN, and Ni-CN. In addition, in the case of Fe-CN, additional spots are also observed in diffusive rings due to the partial graphitization that occurred around Fe nanoparticle, as shown in the HR-TEM image.

The morphologies of Fe-CNB and Ni-CNB are displayed in Figure 6.4. TEM images of CNB (Figures 6.4a,b) show that the shape and structure of CNB are similar to those of CN. The morphology of Fe-CNB shown in Figures 6.4c-e is analogous to CNB, having a turbostratic carbon structure and maintaining the shape of raw  $\text{Ti}(\text{C}_{0.5}\text{N}_{0.5})$  powder. Fe-based nanoparticles and graphitic layers observed in Fe-CN are not detected in Fe-CNB, although hollow disorder carbon rings, which are the traces of the existence of Fe or FeO nanoparticle, still remain (Figure 6.4d). In contrast, in the case of Ni-CNB, severe graphitization occurred at the surface of Ni-CNB (Figure 6.4g). The graphitic ribbons and layers which have the interlayer distance of 0.337 nm developed across the entire surface (Figure 6.4h). This is also verified in the SAED pattern of Ni-CNB (inset of Figure 6.4f). The distinct spots appear in the three diffusive rings indicating (002), (100)/(101), and (110)/(112) patterns with 0.34 nm, 0.21, 0.12 nm d-spacing, respectively. These results demonstrate that the significant development of surface graphitic structure co-existed with the turbostratic carbon core. This is quite different from the SAED pattern of CNB and Fe-CNB (inset of Figures 6.4a,c, respectively) only having diffusive rings. The TEM analysis results tell in Figure 6.4 that the effect of boron in the development of M-CNB (M= Fe and Ni) structure is different depending on the type of transition metals.

The X-ray diffraction(XRD) patterns of M-CN and M-CNB (M= Fe and Ni) are displayed in Figure 6.5. Both Fe-CN and Fe-CNB (Figure 6.5a) show two broad peaks centered at 26.5 ° and 44 ° assigned to (002) and (10) plane of turbostratic carbon, respectively, and no metal or metal compound peaks are detected. In contrast, the addition of boron in Ni-CNB (Figure 6.5b) causes the significant development of a sharp (002) peak accompanying the appearance of (10) and (004) peaks which are the indicator of graphitization. The XRD pattern of Ni-CN shows only broad (002) and (10) peaks. These results are consistent with TEM analysis results and demonstrate that the introduction of Ni to CN enhances graphitization, and the addition of boron to Ni-CN can further reinforce the graphitization.

To examine the local arrangement of metal atoms in M-CN and M-CNB (M= Fe and Ni), the fourier transform extended X-ray adsorption fine structure (FT-EXAFS) spectrometry analysis was conducted. Figure 6.6a exhibits the FT-EXAFS spectra of Fe-CN and Fe-CNB compared with Fe foil as the reference. Fe-CN shows one major peak (1.75 Å) and one minor peak (2.20 Å) attributed to Fe-O and Fe-Fe coordination, respectively. Fe-CNB has only one major peak at 1.5 Å assigned to Fe-N coordination, which is typically reported in Fe-CN catalyst studies. [6.10, 38] This reveals that the addition of boron can induce the atomic dispersion of Fe atom and the formation of Fe-N<sub>x</sub> site in Fe-CNB, while Fe atoms agglomerates and forms Fe and FeO nanoparticles in Fe-CN. On the other hand, when boron is introduced to Ni-CN (Figure 6.6b), the coordination of Ni in Ni-CNB is not changed. The one major peak (2.20 Å) corresponded Ni-Ni coordination of Ni metal and one minor peak (1.5 Å) attributed Ni-C coordination in Ni<sub>3</sub>C [6.39] are detected in both Ni-CN and Ni-

CNB, indicating that Ni in Ni-CN and Ni-CNB dominantly exists as the nanocluster. These results demonstrate that the addition of boron is beneficial for the atomic dispersion of metal in Fe-CNB but not for Ni-CNB.

The incorporation of transition metal (Fe and Ni) and boron to CN also change the pore structure of carbon. The N<sub>2</sub> adsorption and desorption isotherms of Fe-CN/CNB and Ni-CN/CNB at 77 K (Figures 6.7a,b) show that they have type I and IV pores. [6.40, 41] This tells that the micro- and mesopore are developed concurrently, as exhibited in the pore size distribution (PSD) plots (Figures 6.7c,d). The quantitative analysis of the pore texture of Fe-CN/CNB and Ni-CN/CNB was performed and was summarized in Table 6.1. The BET specific surface area and all pore volume values of Fe-CN and Ni-CN are decreased significantly compared to those of CN. This reduction is attributed to the partial ordering of carbon induced by the formation of the metal (Fe and Ni) nanoparticles. Compared to Fe-CN, the Fe-CNB has a higher BET specific surface area (820 → 1030 m<sup>2</sup>/g) and higher overall pore volumes, notably the micropore volume (0.29 → 0.38 cm<sup>3</sup>/g). In contrast, the introduction of boron to Ni-CN (Ni-CNB) significantly reduces the BET specific surface area (700 → 150 m<sup>2</sup>/g) and overall pore volumes, particularly micropore volume (0.25 → 0.05 cm<sup>3</sup>/g), which is due to severe graphitization, as observed in TEM and XRD analysis.

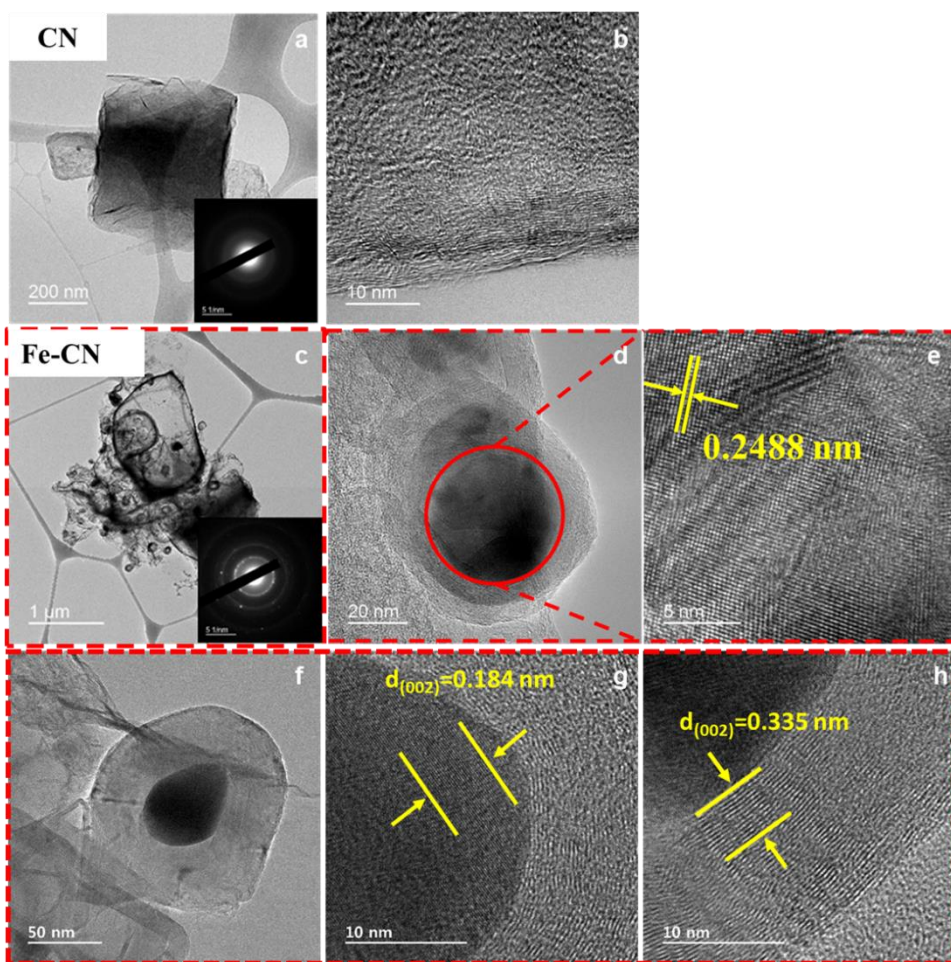


**Figure 6.2.** TEM images of (a,b) CN, (c-h) Fe-CN.



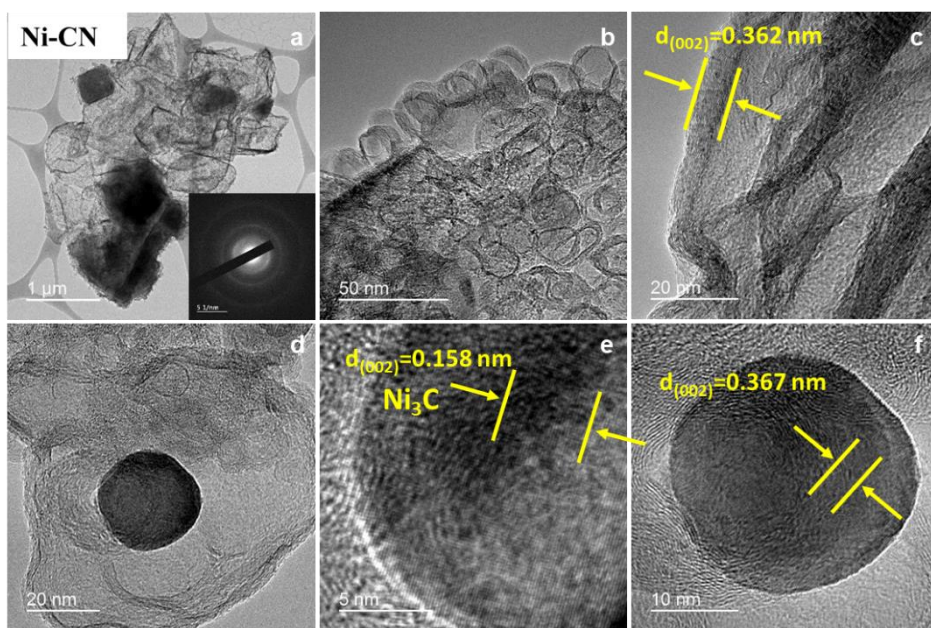


**Figure 6.3.** TEM images of Ni-CN.

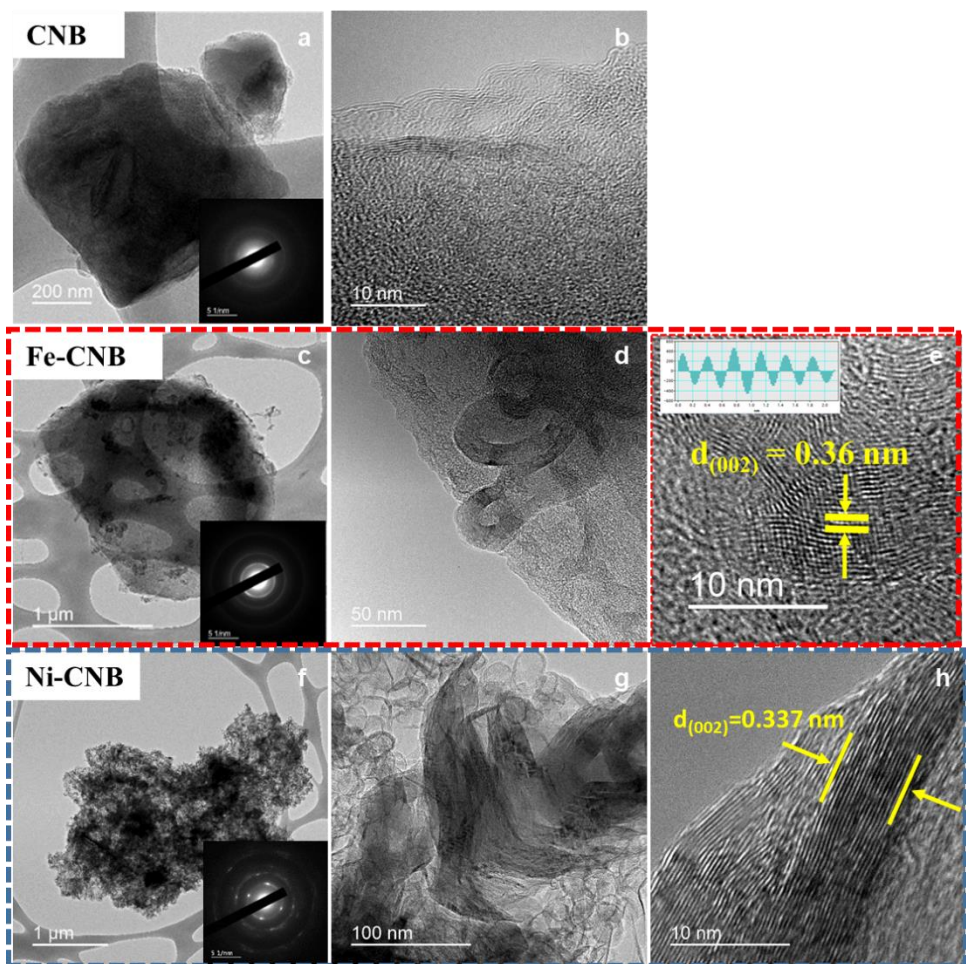


**Figure 6.4.** TEM images of (a-c) Fe-CNB and (d-f) Ni-CNB.

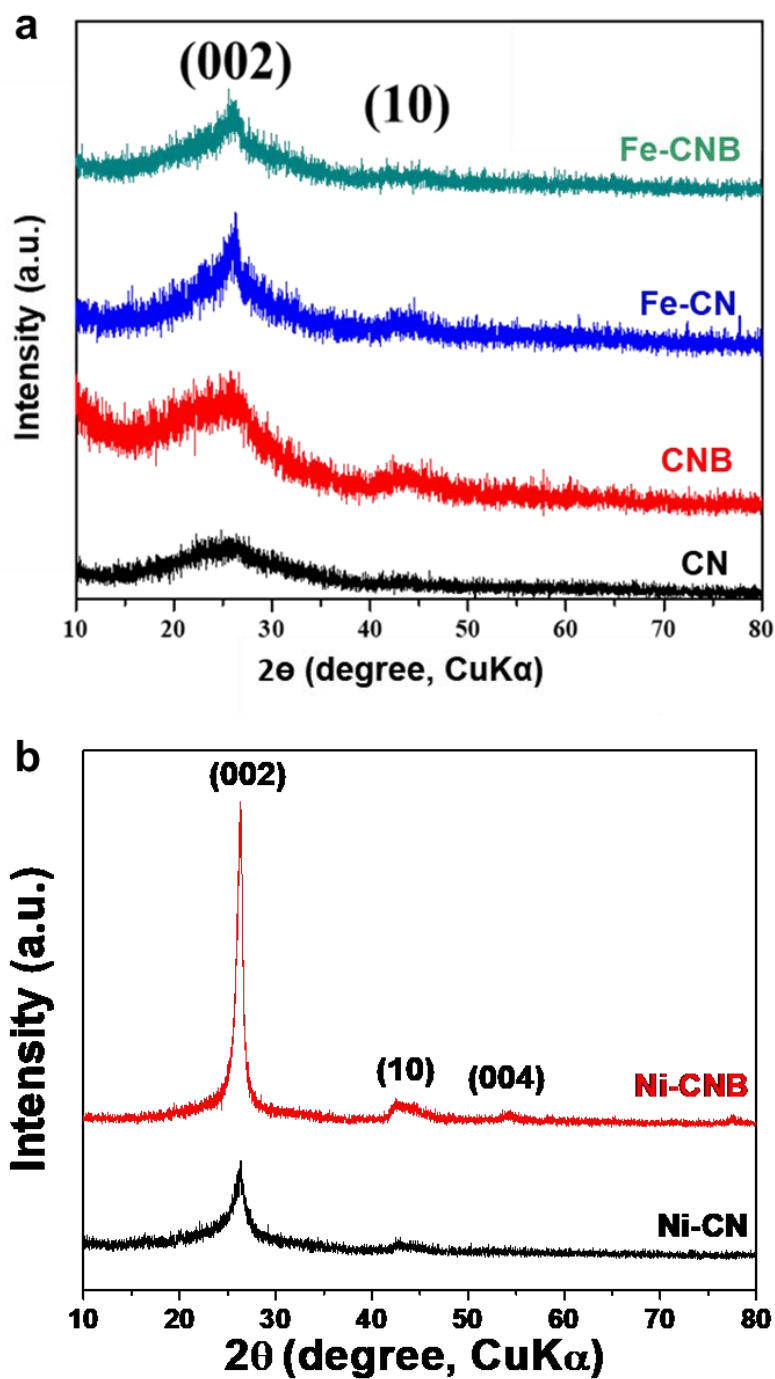


**Figure 6.5.** XRD patterns of (a) CN, CNB, Fe-CN, and Fe-CNB, and (b) Ni-CN and Ni-CNB.

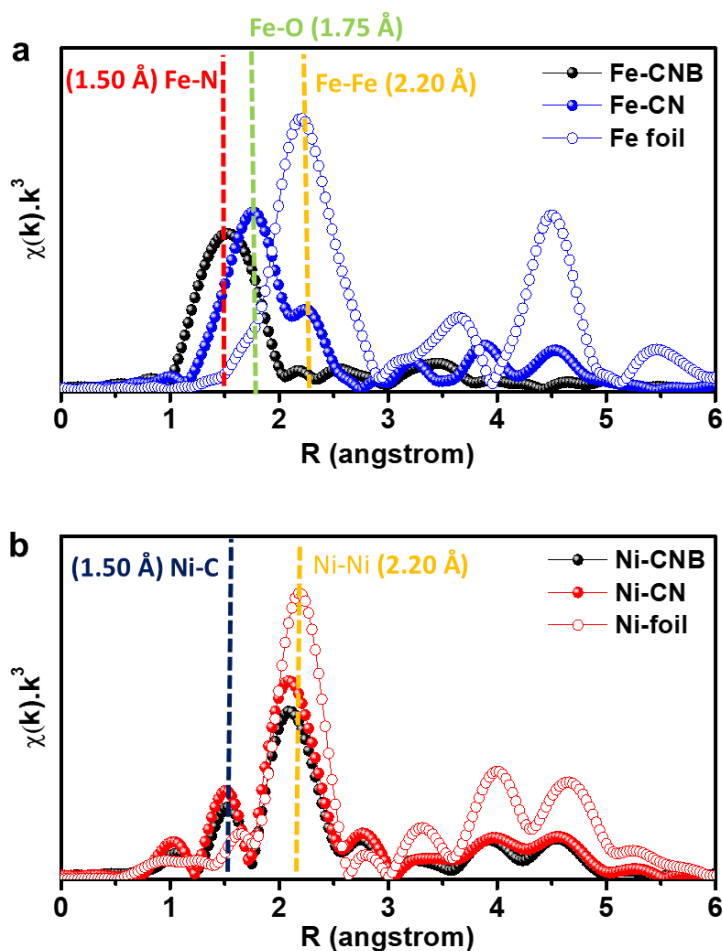


**Figure 6.6.** RDFs of FT  $k^3$ -weighted (a) Fe K-edge EXAFS spectra of Fe-CN and Fe-CNB and (b) Ni K-edge EXAFS spectra of Ni-CN and Ni-CNB.

**Table 6.1.** BET specific surface area and pore volumes of CN, CNB, Fe-CN, Fe-CNB, Ni-CN, Ni-CNB.

	SSA (m <sup>2</sup> /g)	Micropore volume (cm <sup>3</sup> /g)	Mesopore volume (cm <sup>3</sup> /g)	Total pore volume (cm <sup>3</sup> /g)
CN	1840	0.63	0.77	2.06
CNB	1470	0.55	0.47	1.46
Fe-CN	820	0.29	0.30	1.02
Fe-CNB	1030	0.38	0.33	1.24
Ni-CN	700	0.25	0.25	1.06
Ni-CNB	150	0.05	0.10	0.68

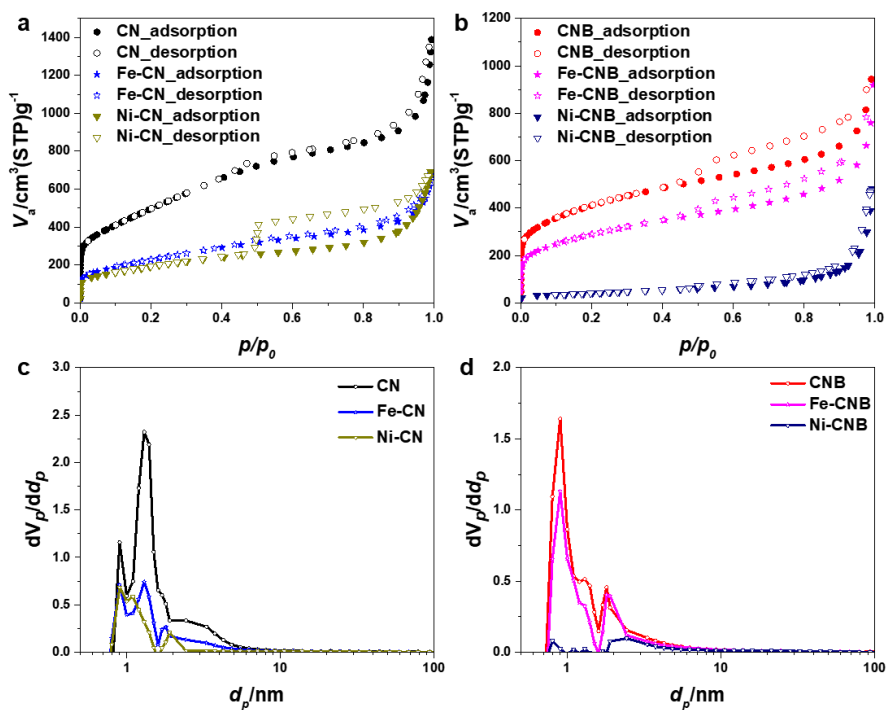


**Figure 6.7.** N<sub>2</sub> sorption isotherm of (a) CN, Fe-CN, and Ni-CN, and (b) CNB, Fe-CNB, and Ni-CNB. The pore size distribution (PSD) of (c) CN, Fe-CN, and Ni-CN, and (d) CNB, Fe-CNB, and Ni-CNB.

## **6.5. Formation of metal-based particles during the synthetic process of Fe-CN/CNB and Ni-CN/CNB**

Interestingly, despite using the identical synthesis method, the atomic dispersion of metal atoms in the porous carbon matrix was achieved in Fe-CNB, but not in Ni-CNB. This indicates that interaction between metal and boron during the synthesis of M-CNB is different depending on the metal type. Therefore, it is essential to clearly understand the formation mechanism of both Fe-CNB and Ni-CNB, which can give a clue for synthesizing a porous carbon-containing well-dispersed transition metal atoms. The transition metal-based nanoparticles can act as a strong graphitization catalyst. [6.42, 43] In order to synthesize atomically dispersed metals embedded in the nanoporous carbon the via chlorination method, therefore the suppression of the graphitization of carbon substrate causes by the metal-based nanoparticles and the rapid removal of these nanoparticles are indispensable. These two requirements were well achieved in the Fe-CNB, but not in the Fe-CN.

To figure out the initial state of Fe and Ni in Fe-CNB and Ni-CNB before chlorination process, the morphology of raw powder of Fe-CNB and Ni-CNB just before the chlorination process quenched samples just after heating up to 800 °C in Ar atmosphere was observed by TEM. In the case of the Fe-CNB system shown in Figures 6.8a,b, the FeO nanoparticles (identified by the d-spacing value) of size 5-30 nm are enclosed in the thick carbon nanotube and carbon ribbon are discovered at the surface of  $\text{Ti}(\text{C}_{0.5}\text{N}_{0.5})$  particle. The formation of the metal nanoparticle is also observed in Ni-CNB (Figures 6.8c,d). The Ni nanoparticles (confirmed by the d-

spacing) of about 5-30 nm located the surface of  $\text{Ti}(\text{C}_{0.5}\text{N}_{0.5})$ . They are predominantly naked, while few of them are covered in the thin carbon layers.

The formation of the nanoparticles was attributable to metal precursors ( $\text{Fe}(\text{acac})_3$  and  $\text{Ni}(\text{acac})_2$ ). [6.44, 45] The formation of the metal-based nanoparticle can also be understood through the Ellingham diagram shown in Figure 6.9. The  $\Delta G^\circ$  of metal (Fe and Ni) and carbon oxidation reaction with temperature are plotted. The relative oxidation tendency can be determined by comparing the  $\Delta G^\circ$  value of each oxidation reaction. The  $\Delta G^\circ$  value of Fe oxidation ( $2 \text{ Fe} + \text{O}_2 = 2 \text{ FeO}$ ) is lower than that of carbon oxidation ( $2 \text{ C} + \text{O}_2 = 2 \text{ CO}$ ) below 700 °C and this trend reverses above 700 °C. That is, iron oxide formation is thermodynamically more favorable than carbon oxidation below 700 °C ( $\text{Fe} + \text{CO} = \text{FeO} + \text{C} : \Delta G^\circ < 0$ ). Thus, iron oxide nanoparticles can be formed during the heat treatment with any available oxygen source. The carbon from the metal precursor, raw material, and impurities can construct carbon nanotube and graphitic ribbon. Although the reduction of iron oxide and the oxidation of carbon started over 700 °C, a certain amount of iron oxide particles may still remain at 800 °C, as shown in the above TEM analysis (Figure 6.2d). Thus, Fe and FeO nanoparticles can co-exist in the early stage of chlorination process. On the other hand, according to the Ellingham diagram in Figure 6.9,  $\Delta G^\circ$  of  $\text{Ni} + \text{CO} = \text{C} + \text{NiO}$  becomes positive above 450 °C. That is, NiO can be all reduced to Ni by carbon above 450 °C. As a result, Ni nanoparticle with little carbon layer coverage can prevail in Ni-CNB at 800°C before the chlorination process.



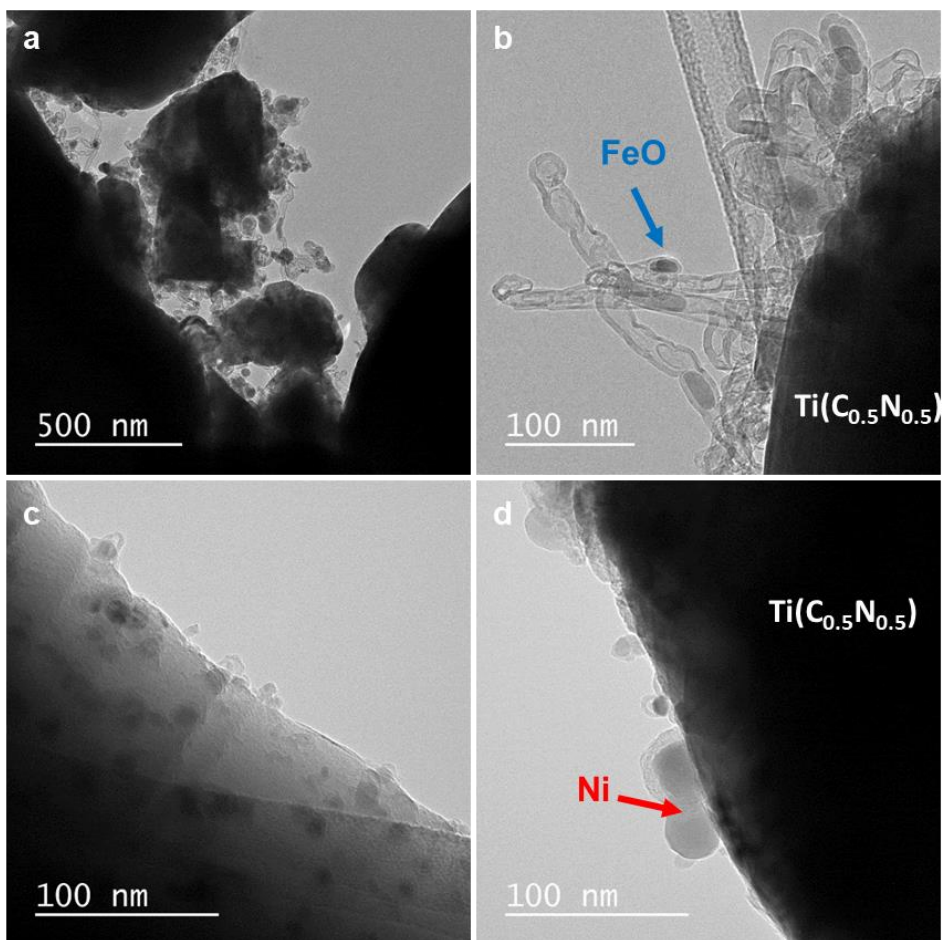


**Figure 6.8.** TEM images of just before chlorination (800 °C, Ar, 0 m) of (a,b) Fe-CNB and (c,d) Ni-CNB.



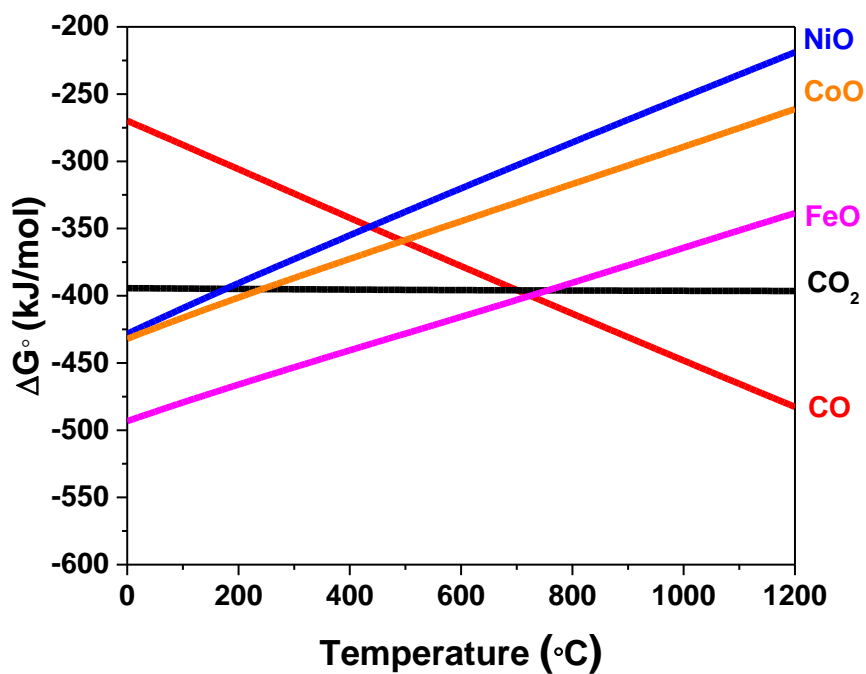


**Figure 6.9.** Ellingham diagram for the oxidation tendency of C and various metal (Fe, Ni, and Co):  $2\text{C} + \text{O}_2 = 2\text{CO}$ ,  $\text{CO} + \text{O}_2 = 2\text{CO}_2$ , and  $2\text{M} + \text{O}_2 = 2\text{MO}$ .

## 6.6. Thermodynamic calculation for the chlorination process

Thermodynamic calculations for the chlorination of Fe-CN/CNB and Ni-CN/CNB were performed using the FactSage thermodynamic calculation software [6.46], and the results were plotted in Figures 6.10 and 6.11. Although the hetero-atom doping on the carbon and nano-size effect (surface energy) could not be considered in the calculations, the general features of chlorination reactions and the influence of different chemistry of starting materials to the final products can be understood from the thermodynamic calculations.

The formation of carbon from solid Ti(C,N) by chlorination process can be well calculated. In the case of the Fe-CN (Figures 6.10a,b), TiC is firstly chlorinated to produce  $\text{TiCl}_4(\text{g})$  and carbon, followed by the chlorination of TiN to  $\text{TiCl}_4(\text{g})$  and  $\text{N}_2(\text{g})$ . Because Fe has less reactivity with  $\text{Cl}_2(\text{g})$  than Ti, thermodynamic calculations show that Fe is transformed to FeN and FeC (as part of fcc Ti(C,N) solid solution) until all Ti sources are chlorinated, then become  $\text{FeCl}_2(\text{g})$  or  $\text{FeCl}_3(\text{g})$ . In the case of the Ni-CN (Figures 6.10c,d), the calculations show that Ni metal remains until all Ti sources are chlorinated, then becomes  $\text{NiCl}_2(\text{g})$ . In the case of the M-CNB (Figures 6.11e,f), the results are more complex than M-CN. Due to the strong tendency to form BN, TiN is chlorinated prior to TiC. The calculated result of the Fe-CNB (Figures 6.11a,b) shows that FeC and FeN (as part of fcc Ti(C,N) solid solution) can progressively transform to  $\text{Fe}_2\text{B}$  during the chlorination process. In constant, in the case of the Ni-CNB,  $\text{Ni}_2\text{B}$  is formed from the early stage of the chlorination process. In the late stage, it transforms to  $\text{Ni}_3\text{B}$  and  $\text{NiCl}_2(\text{g})$ . This

difference between Fe-CNB and Ni-CNB is due to the relative stability of metal borides against the BN phase. In addition, in the case of the Fe-CNB,  $\text{FeCl}_2$  gas begins to form from the early stage of the chlorination process.

Although the general feature of the chlorination process is well explained in the thermodynamic calculations, the chemical reaction of Fe in the early chlorination process is incorrectly calculated, compared with the real experimental results. Because Fe or FeO nanoparticles are encapsulated in carbon layer, and physically separate from Ti(C,N) prior to the chlorination process (see Figures 6.8a,b), the chemical transition of Fe or FeO to FeC or FeN as part of Ti(C,N) solid solution hardly happen.

The formation of nickel boride phase in the early stage of the chlorination process can be proved by the experiment. The TEM image of Ni-CNB obtained after only 20 minutes of the chlorination process is presented in Figure 6.12, which confirms the presence of nickel boride nanoparticle of about 50 nm in size. The SAED pattern analysis (inset of Figure 6.12) shows three diffraction spots in three different diffusive rings assigned to (200), (201), and (301) plane of  $\text{Ni}_3\text{B}$ , respectively.

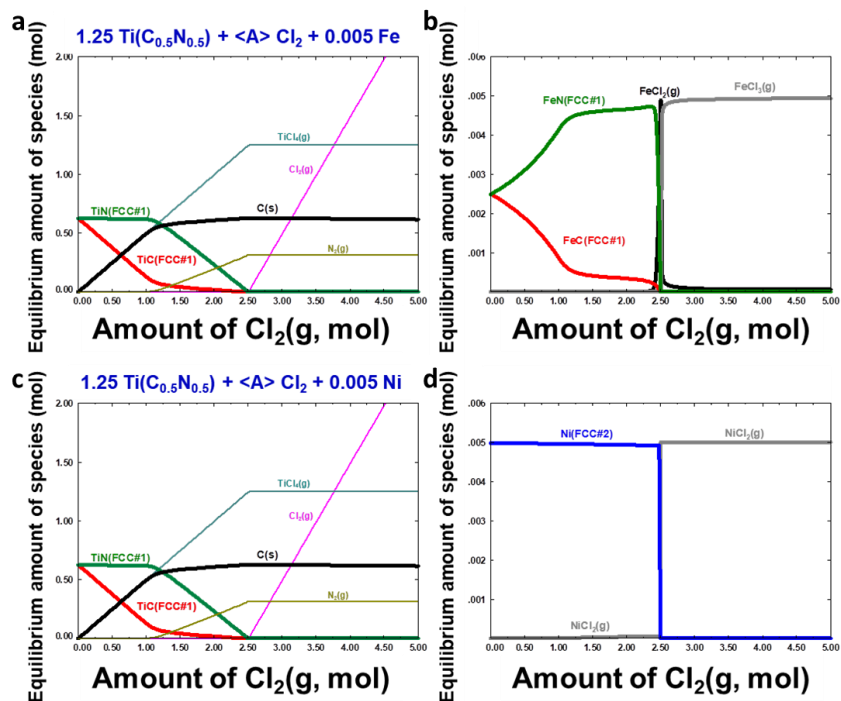


**Figure 6.10.** Thermodynamic calculation for chlorination of M-CN. FeO-CN (a,b), Fe-CN (c,d), and Ni-CN (e,f).

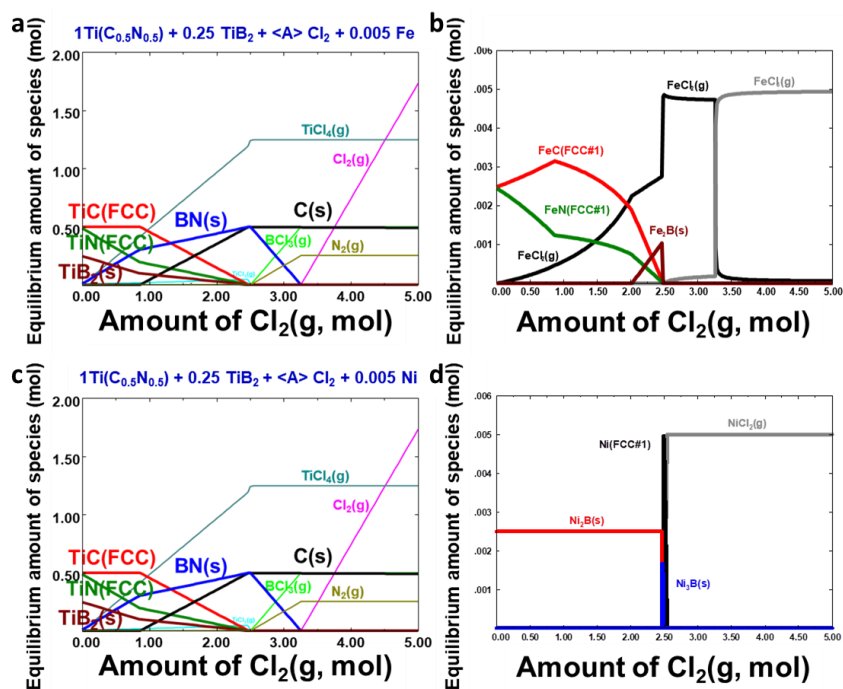


**Figure 6.11.** Thermodynamic calculation for chlorination of M-CNB. FeO-CNB (a,b), Fe-CNB (c,d), and Ni-CNB (e,f).

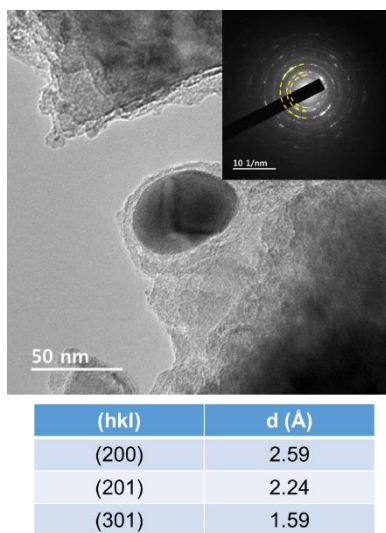


**Figure 6.12.** The existence of nickel boride particle ( $\text{Ni}_3\text{B}$ ) observed by TEM analysis.

## 6.7. Phase diagrams for the nano-sized M-C and MxB-C systems

As explained in Figure 6.4, the Ni-CNB has severe graphitization, but the Fe-CNB has no noticeable graphitization although both CNBs use transition metals. In order to explain these difference, further thermodynamic analysis has been carried. As well-known, transition metal-based nanoparticles can facilitate the graphitization of carbon. In particular, if the nanoparticles become liquid phases the graphitization can be significantly accelerated. [6.47] In this study, the melting behaviors of Fe- and Ni-based nanoparticles which can be formed in the synthetic process of the Fe-CNB and Ni-CNB were calculated to explain the difference between the graphitization process of two M-CNB materials.

Figure 6.13 illustrates the phase diagrams of the Ni-C, Ni<sub>2</sub>B-C and Ni<sub>3</sub>B-C systems. In the calculations, the nano-size effects (surface energies) of solid Ni-based particles (solid Ni, Ni<sub>2</sub>B and Ni<sub>3</sub>B phase) were taken into account. The variation of the phase diagram depending on the size of Ni-based particles is plotted in Figure 6.13. According to the calculated phase diagram, the eutectic temperatures of Ni-C, Ni<sub>2</sub>B-C and Ni<sub>3</sub>B-C bulk system are 1327 °C, 1133 °C, and 1158 °C, respectively. That is, the Ni boride-C systems have lower melting temperatures than Ni-C system. When 10 nm sized Ni-based particles are considered, the eutectic temperatures of all three systems are decreased significantly. In particular, the Ni<sub>2</sub>B-C and Ni<sub>3</sub>B-C system can have liquid phase around 800 °C or less. The phase diagrams of the Fe-C, and Fe<sub>2</sub>B-C systems are calculated in Figure 6.14. According

to the calculated phase diagram, the eutectic temperatures of Fe-C and Fe<sub>2</sub>B-C bulk system are 1153 °C and 1282 °C respectively, and they can be decreased to 711 °C and 972 °C, respectively, for 10 nm sized Fe and Fe<sub>2</sub>B system. Compared to the Ni-based system, the eutectic temperature of Fe-C is lower than that of Fe<sub>2</sub>B-C system. That is, the melting of nano-sized Fe-based particle at 800 °C can be expected in the Fe-C system, but not in the Fe<sub>2</sub>B-C system.

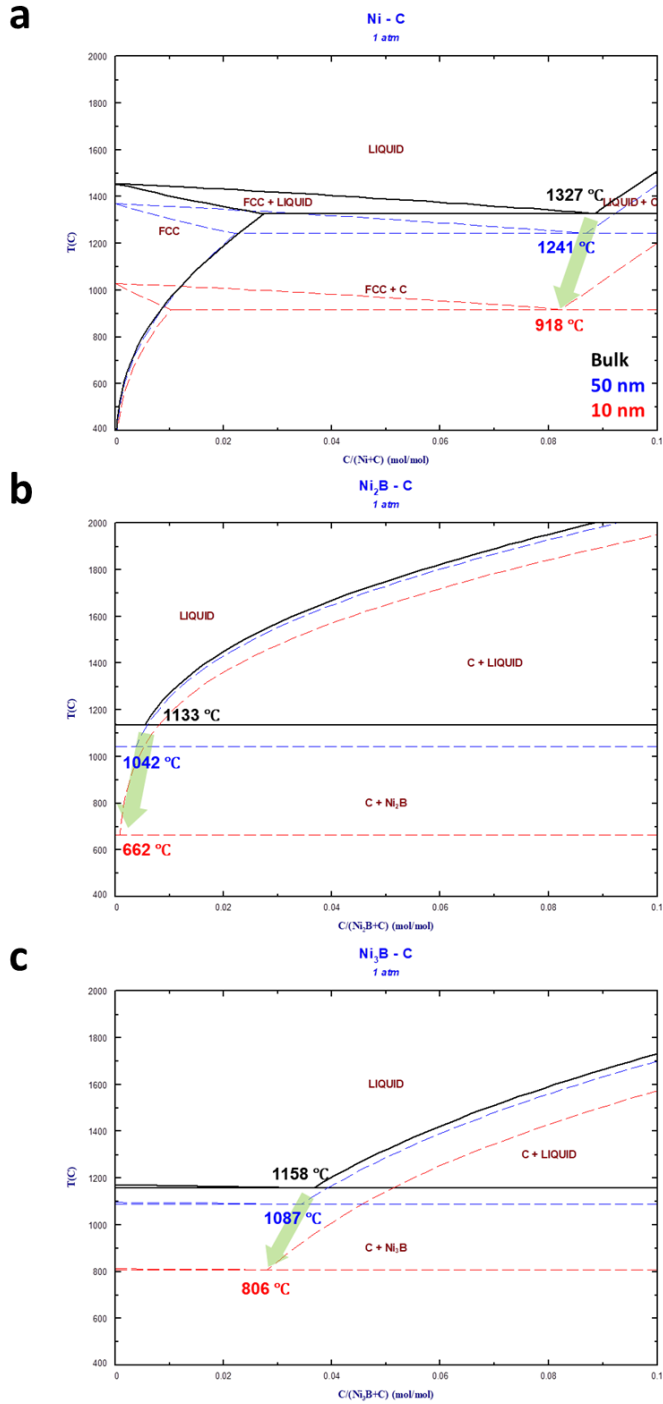


**Figure 6.13.** Phase diagrams of (a) Ni-C system, (b) Ni<sub>2</sub>B-C, (c) Ni<sub>3</sub>B-C system: bulk (black solid line), 50 nm (blue dashed line), and 10 nm (red dashed line).



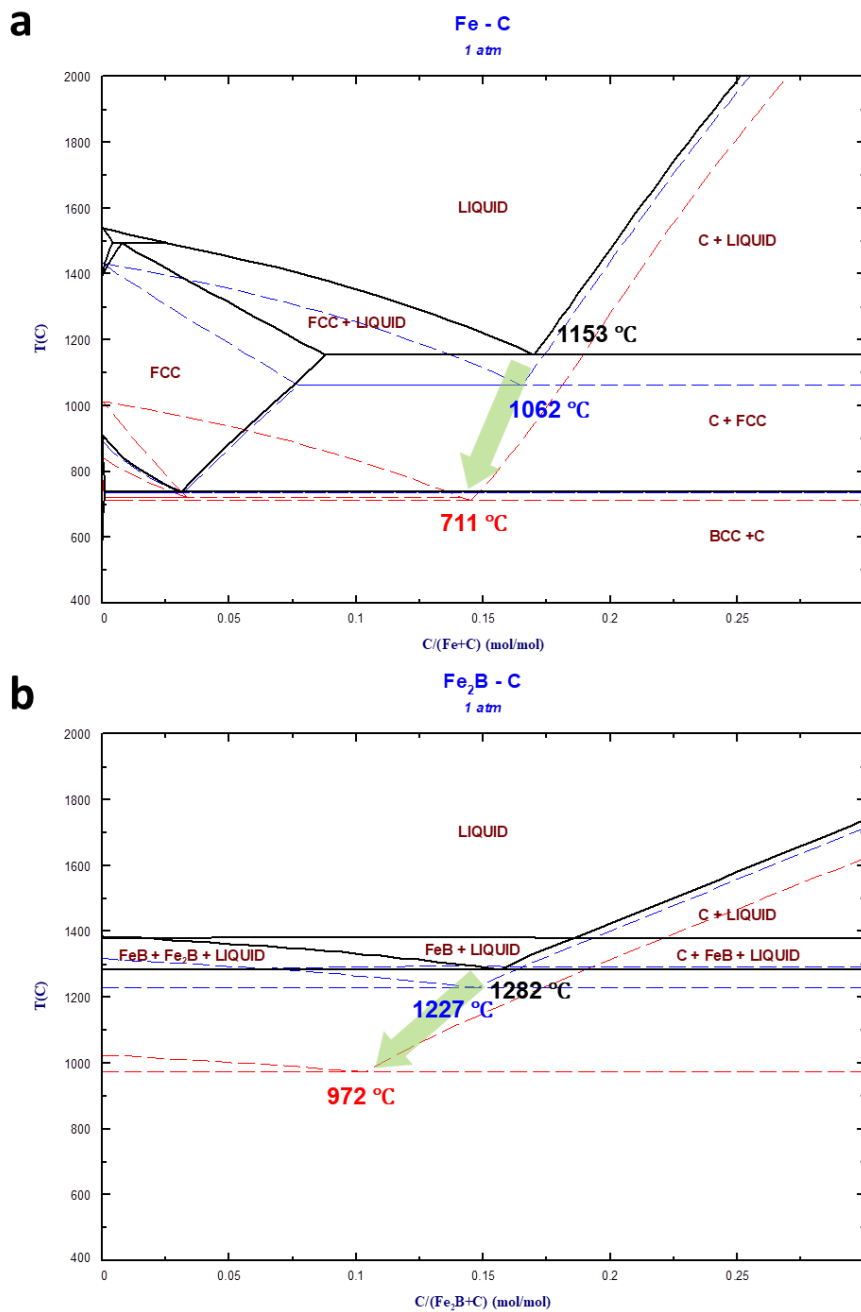


**Figure 6.14.** Phase diagrams of (a) Fe-C and (b) Fe<sub>2</sub>B-C: bulk (black solid line), 50 nm (blue dashed line), and 10 nm (red dashed line).

## 6.8. The proposed formation mechanism of Fe-CNB and Ni-CNB

The formation mechanism of Fe-CNB and Ni-CNB is proposed in Figure 6.15, based on the experimental results and thermodynamic analysis. In the case of Fe-CNB, both Fe (or FeO) nanoparticles firstly form from Fe(acac)<sub>3</sub> on the surface of raw Ti(C<sub>0.5</sub>,N<sub>0.5</sub>) powders during the heating to 800 °C in Ar atmosphere. In the early stage of the chlorination process, boron atoms are supplied to both Fe (or FeO) nanoparticles, and CN formed from Ti(C,N) through BCl<sub>3</sub>(g) and atomic diffusion. [6.34] Subsequently, part of Fe (or FeO) nanoparticles less enclosed by carbon structure are reacted with Cl<sub>2</sub>(g) to form FeCl<sub>2</sub>(g) and FeCl<sub>3</sub>(g). Fe (or FeO) nanoparticles enclosed by thick carbon layers can be gradually transformed to Fe<sub>2</sub>B nanoparticles. Consequently, the graphitization of the carbon substrate is inhibited, and the turbostratic carbon will remain. In the end, Fe<sub>2</sub>B nanoparticles are gradually removed by chlorine gas due to a porous carbon structure. Meanwhile, the incorporation of boron in carbon substrate (CN) also significantly facilitates the development of nitrogen-rich, especially pyridinic N, carbon layers, as shown in our previous study. [6.34] Therefore, some decomposed Fe content in FeCl<sub>3</sub> gas can readily bond with nitrogen functional groups in CN during the chlorination process. [6.48] Also, the atomic diffusion of Fe from Fe<sub>2</sub>B nanoparticles to N-doped site of porous carbon substrate is also feasible. [6.5, 49, 50] Thus, Fe-N<sub>x</sub> active sites are well-developed. As a result, the Fe-CNB has iron, boron, and nitrogen co-doped porous carbon structure with abundant Fe-N<sub>x</sub> active sites positioned in micropore thus exhibits an excellent ORR performance as shown in the above characterization

part of Fe-CNB.

In contrast, in Fe-CN, Fe (or FeO) particles remain and induce the formation of the thick graphitic structure enclosing these particles, as shown in the TEM image of Fe-CN (Figure 6.2f). This makes the atomic dispersion of Fe in carbon substrate to be difficult, and hinders the development of active sites, resulting in low ORR performance compared with Fe-CNB. To sum up, the introduction of boron through TiB<sub>2</sub> promotes the atomic dispersion of Fe atoms and minimizes the redundant graphitization at the surface of Fe-CNB, which are the keys for the superior ORR performance of Fe-CNB.

On the other hand, in the case of the Ni-CNB system, Ni nanoparticles form on the surface of Ti(C<sub>0.5</sub>N<sub>0.5</sub>) by the decomposition of Ni(acac)<sub>2</sub> during the heating in Ar atmosphere. Then, the boron contents originated from TiB<sub>2</sub> reacts with Ni to form nickel boride nanoparticles (Ni<sub>2</sub>B and Ni<sub>3</sub>B) from the early stage of the chlorination process. The surface melting of boride nanoparticles could actively occur due to significant decrease in the eutectic temperature of the nickel boride-carbon systems, compared to the nickel-carbon system. As a result, the severe graphitization throughout the surface of Ni-CNB occurs, which causes the degradation of active sites (micropore and nitrogen doping site) for an electrocatalytic reaction. The nickel boride nanoparticles are gradually removed by reacting with Cl<sub>2</sub> gas with the progress of the chlorination process. In brief, the introduction of boron to the Ni-CNB accelerates the surface graphitization, hindering the atomic dispersion of Ni atoms and the formation of M-N<sub>x</sub> active sites. Thus, the incorporation of boron in the Ni-CNB is unfavorable for the electrocatalytic activity for ORR.

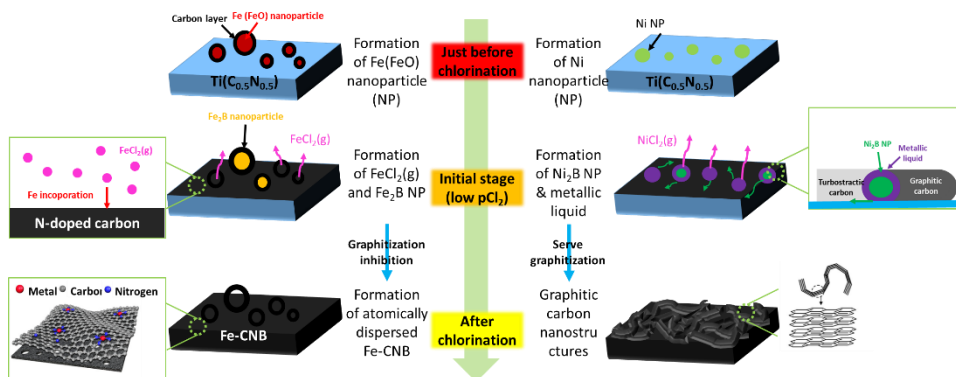


**Figure 6.15.** The proposed formation mechanism of Fe-CNB and Ni-CNB.

## 6.9. Conclusions

In summary, we demonstrate the influence of the introduction of boron and transition metal (Fe and Ni) in nitrogen-doped porous carbon (CN) synthesized by the chlorination of the titanium carbonitride, titanium boride, and transition metal precursor ( $M(\text{acac})_x$ ) mixture. Depending on the types of a transition metal, the addition of boron facilitates or impedes the atomic dispersion of metal in CN. The fast removal of metal-based nanoparticle and minimizing the graphitic catalytic effect of metal-based nanoparticle during the chlorination process are demonstrated as the critical factors that enable to produce the atomically dispersed M-CNB materials.

The metal-based nanoparticles are formed before the chlorination process due to the pyrolysis of metal precursor ( $M(\text{acac})_x$ ), and the addition of boron from  $\text{TiB}_2$  induces the phase transformation of metal-based nanoparticles to the metal boride nanoparticles. If the eutectic temperature of the metal boride-C system is higher than the chlorination temperature, the graphitization attributed to the surface melting of the metal-based nanoparticle is minimized. The boride nanoparticles are readily removed due to the high accessibility of  $\text{Cl}_2$  gas. Also, the carbon substrate retains the nanoporous structure, and introduced boron atoms to the carbon structure enhances the incorporation of nitrogen atoms. As a result, atomically dispersed metal embedded porous carbon having abundant  $M\text{-N}_x$  active site in nanopore can be obtained. In our study, the Fe-CNB system shows this trend; thus, Fe-CNB exhibits the superior ORR activity that surpasses the commercial Pt/C catalyst in the alkaline

medium.

In contrast, if the eutectic temperature of the metal boride-C system is lower than the chlorination temperature, the graphitization of carbon substrate is accelerated at the interface of nanoparticle-carbon substrate due to the severe surface melting of metal boride nanoparticles. Consequently, the nanopores (micro- and mesopore) and  $M-N_x$  active sites are degenerated. In this case, the addition of boron rather impedes the atomic dispersion of metal in the porous carbon substrate, unfavorable for enhancement of the electrocatalytic activity, and the Ni-CNB is a good example.

Through these results, not just about the understanding of one type of M-CNB system, taking a step forward, we demonstrate the overall view of the boron effect in the synthetic process the M-CNB materials. The introduction of boron can facilitate or hinder the atomic dispersion of metal on carbon structure depending on the variation of the eutectic temperature of formed metal-based nanoparticle – carbon system. Therefore, the interaction between the targeted metal type and boron source must be carefully considered to synthesize the atomically dispersed metal incorporated nanoporous carbon. Also, our result demonstrates the high applicability of the Fe-CNB material produced by the chlorination process as an electrocatalyst. Our results are expected to provide a useful guideline for the development of the synthetic method for the high functional M-CNB electrocatalysts.

## **Chapter 7. Synthesis of atomically dispersed M (Fe or Ni)-CNB via one-pot pyrolysis method**

### **7.1. Research highlight**

- Fe and boron are concurrently introduced in the synthesis of N-doped carbon (CN) by a one-pot pyrolysis process.
- PEG-Urea-boric acid-Fe nitrates mixture was used as the original raw precursors
- The samples obtained by one step pyrolysis of raw precursors are denoted as M-CNB(X)-T (M = Fe and Ni, X=boric acid molar percent with C in PEG, T = pyrolysis temperature).
- Boric acid is transformed to boron oxide in the early stage of pyrolysis process and coats the entire carbon structure, which inhibits the metal (Fe and Ni)-based nanoparticle by formation of liquid solution ( $\text{Fe-B}_2\text{O}_3$ ), demonstrating by the thermodynamic calculation and control experiment.
- Atomically dispersed Fe-CNB are obtained having carbon nanotube structure and nanoporous structure due to the introduction of boric acid.
- Similar result is obtained in the synthesis of the Ni-CNB using the identical synthesis process of the Fe-CNB.
- Introduction of boric acid enhances the electrocatalytic activity of the Fe-CNB and Ni-CNB.

## 7.2. Introduction

As demonstrated in Chapter 7, the introduction of boron to the iron and nitrogen co-doped carbon (Fe-CN) in the chlorination synthesis process is an effective method to homogenously distributed in Fe atoms in the boron and nitrogen co-doped porous carbon (CNB) which has an enhanced  $4e^-$  pathway ORR electrocatalytic activity. However, other transition metal systems like Ni and Co barely improve the ORR catalytic activity because the metals form metal boride nanoparticles instead of atomic distribution of metals, and induce the severe graphitization at the surface of CNB resulting in the degeneration of micropore. That is, carbide-derived carbon (CDC) process is not universal process to produce atomically distributed metal (M)-CNB materials.

In this chapter, pyrolysis method is used to synthesize the atomically dispersed M (Fe or Ni)-CNB to expand the applicability of M (Fe or Ni)-CNB for the electrocatalyst. The pyrolysis method widely used to synthesize the hetero-atom doped carbon material is introduced. [7.1-7] Boric acid was introduced in the synthesis of atomic dispersed M (Fe or Ni)-CNB. Boric acid is a well-known soft template in the nanostructuring field since it can readily be transformed to liquid boron oxide that forms the stable coating layer on unstable structure materials. [7.8-10] In addition, the boric acid is one of the representative boron doping sources thus is commonly used as the boron precursor for synthesizing CNB. [7.11-14] It is demonstrated that the addition of boric acid effectively inhibited the formation of metal-based nanoparticles, but facilitated the incorporation of nitrogen in carbon



substrate. As a result, abundant M (Fe or Ni)-N<sub>x</sub> embedded nanoporous carbon nanotubes having the excellent electrocatalytic activity are obtained.

For the convenience, the samples in the present study are denoted as M (Fe or Ni)-CN-T and M (Fe or Ni)-CNB(x)-T depending on the addition of the boric acid. x represents the mole percent of boric acid to the mole of carbon in the carbon precursor (Polyethylene glycol), and T indicates the pyrolysis temperature. Fe-CNB(20)-950, exhibits the most outstanding electrocatalytic activity for oxygen reduction reaction (ORR) in alkaline medium, surpassing the performance of commercial Pt/C catalyst. Ni-CNB(20)-950 also shows the good electrocatalytic activity for the carbon dioxide reduction reaction (CO<sub>2</sub>RR). This study demonstrates that the addition of boric acid in the pyrolysis of the Fe-CN can be a facile strategy to promote the atomic dispersion of transition metal atoms like Fe and Ni in N-doped nanoporous carbon structure.

### 7.3. Structural analysis of Fe-CN/CNB

Many samples of M-CNB-T where T = 600-1000 °C were synthesized and analyzed, summarized in appendix 3 section. Among them, the sample synthesized at 950 °C showed the most optimum results. Therefore, in the following section, the results of the samples at 950 °C were mainly presented.

The morphology of the Fe-CNB(20)-950 was observed by the transmission electron microscope (TEM) and scanning electron microscope. The TEM images (Figures 7.1a,b) and SEM images (Figures 7.1e,f) show that the Fe-CNB(20)-950 has a carbon nanotube structure. Also, the high-resolution TEM image (Figure 7.1d) demonstrates the turbostratic nature. This is further confirmed by selected area electron diffraction (SAED) (inset of Figure 7.1c) exhibiting three diffusive rings corresponded to (002), (100)/(101), and (110)/(112) patterns, typical in turbostratic carbon. [7.15] The high-angle annular dark-field scanning TEM (HAADF-STEM) analysis and Energy-dispersive X-ray spectroscopy (EDS) analysis were conducted to reveal the state of Fe in the Fe-CNB(20)-950. No Fe-based nanoparticles are observed in the HAADF-STEM image (Figure 7.2a). The EDS spectrum (Figure 7.2b-f) verifies uniformly dispersed elemental Fe, B, C, N, and O in the carbon structure.

In contrast to the Fe-CNB(20)-950, the HR-TEM images and SEM images in Figure 7.3 show that the Fe-CN-950 contains iron oxide ( $\text{Fe}_3\text{O}_4$ , magnetite) nanoparticles of about 10-50 nm and ordered carbon ribbons structure. The HAADF-

STEM image (Figure 7.3d) exhibits the bright spots indicating the Fe-based nanoparticles. In order to confirm the existence of  $\text{Fe}_3\text{O}_4$  magnetite, permanent magnet was applied to the sample Fe-CNB(20)-950 and Fe-CN-900. As shown in Figure 7.4, the Fe-CN-950 contains magnetite nanoparticles.

The X-ray diffraction (XRD) patterns of the Fe-CNB(20)-950 and Fe-CN-950 are presented in Figure 7.5. The XRD pattern of Fe-CNB(20)-950 shows two broad peaks at  $24.2^\circ$  and  $43^\circ$  without any crystalline peaks. This indicates the development of nanographene layer (turbostratic structure) without the formation of Fe-based nanoparticles. While, the XRD pattern of the Fe-CN-950 shows  $\text{Fe}_3\text{O}_4$  peaks appeared along with the development of broad (002) peak of at  $26.0^\circ$ . This could mean that Fe-based particles caused the partial graphitization in the Fe-CN-950.

From the TEM and XRD results for Fe-CNB(20)-950 and Fe-CN-950, it is proved that the addition of boric acid in the synthesis of Fe-CN facilitates the atomic dispersion of Fe atoms in the carbon nanotube structure.

The pore textures in Fe-CNB(20)-950 and Fe-CN-950 were examined by the  $\text{N}_2$  adsorption isotherm at 77 K in Figure 7.6. The isotherms of the Fe-CNB(20)-950 and Fe-CN-950 are Type 1 and Type 4 indicating co-existence of micro- and mesopore. [7.16, 17] This structure can be more clearly determined by the pore size distribution (PSD) results. The micropore is developed more in the Fe-CNB(20)-950 than the Fe-CN-950. The BET specific surface area and pore volumes of both samples are summarized in Table 7.1. The Fe-CNB(20)-950 has much higher BET specific surface ( $738 \text{ m}^2/\text{g}$ ), micropore volume ( $0.28 \text{ cm}^3/\text{g}$ ), and total pore volume

(0.92 cm<sup>3</sup>/g) than the Fe-CN-950 (373 m<sup>2</sup>/g, 0.15 cm<sup>3</sup>/g, and 0.37 cm<sup>3</sup>/g, respectively). This means that the introduction of boric acid to the Fe-CN could significantly improve the overall pore structure of carbon, which is favorable for both the formation of the active Fe-N<sub>x</sub> sites and the diffusion kinetic of reactant.

[7.18]

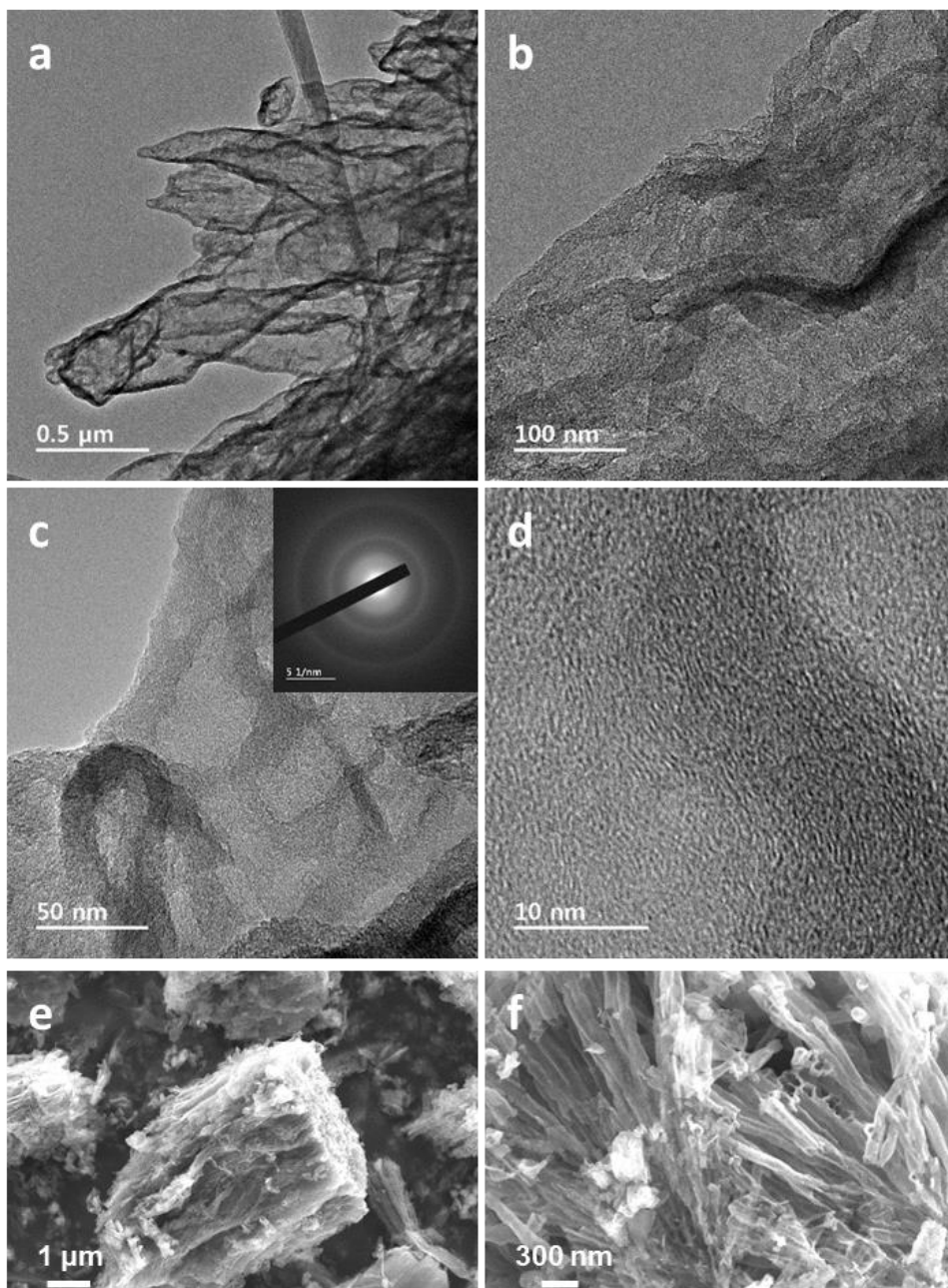


**Figure 7.1.** TEM images (a,b,c), HR-TEM image (d), and SEM images (e,f) of Fe-CNB(20)-950.

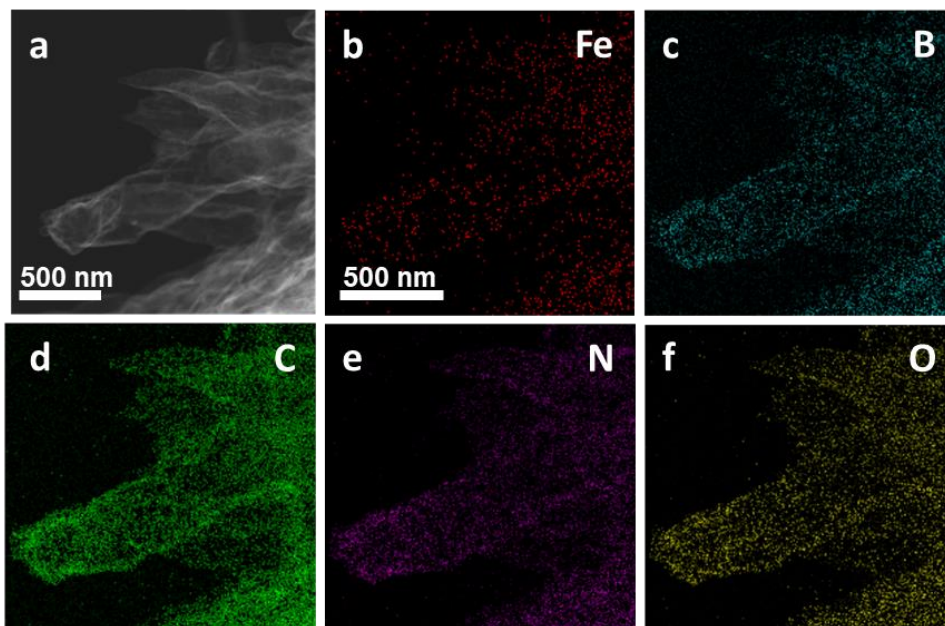


**Figure 7.2.** HADDF image (a) and EDS elemental mapping images (b-f) of Fe-CNB(20)-950.

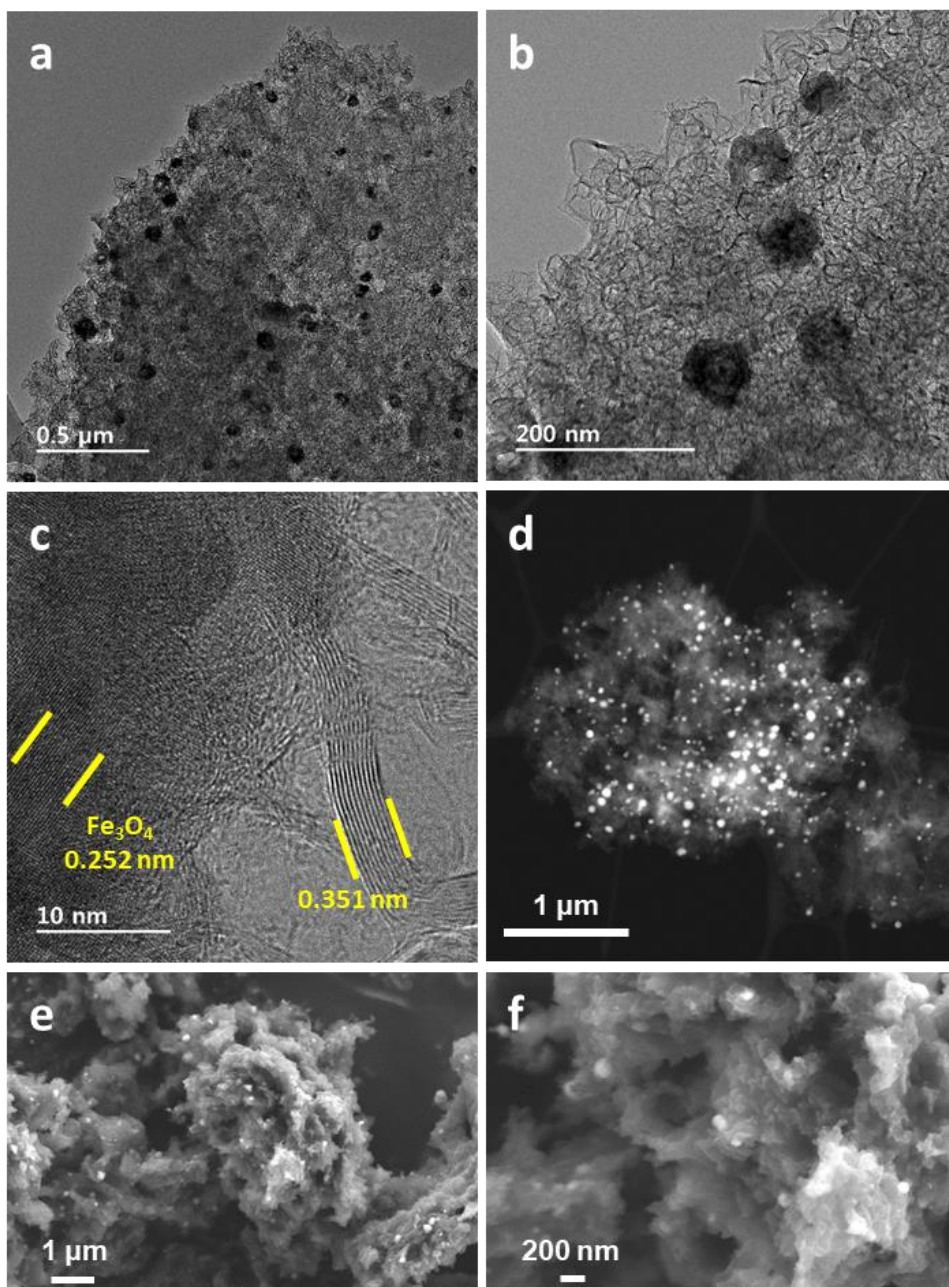


**Figure 7.3.** TEM images (a,b), HR-TEM image (c), HADDF images (d), and SEM images (e,f) of Fe-CN-950.



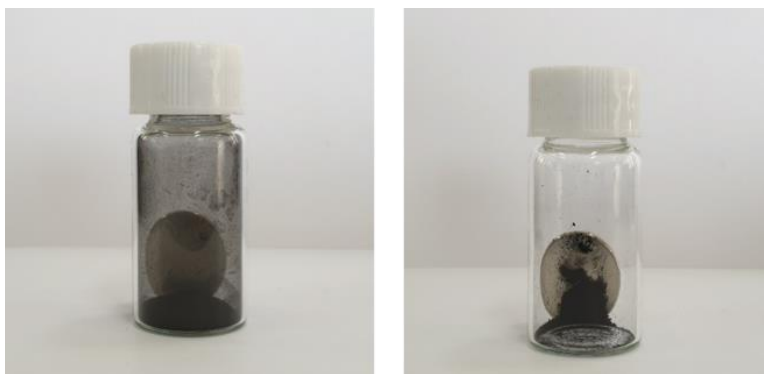


**Figure 7.4.** The optical images of Fe-CNB(20)-950 (left) and Fe-CN (right) that obtain to investigate the magnetism using magnet.

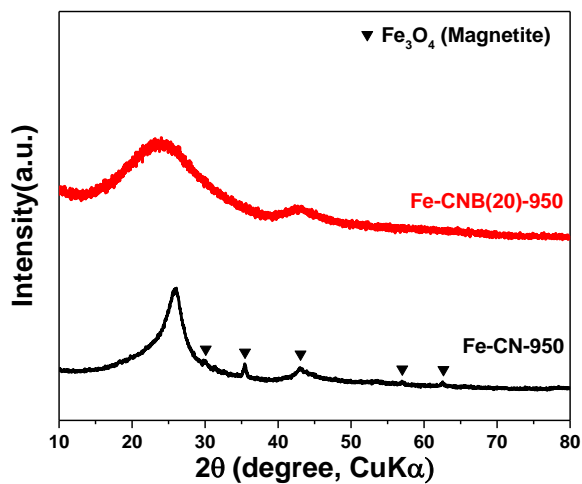


**Figure 7.5.** The XRD patterns of Fe-CNB(20)-950 and Fe-CN-950.



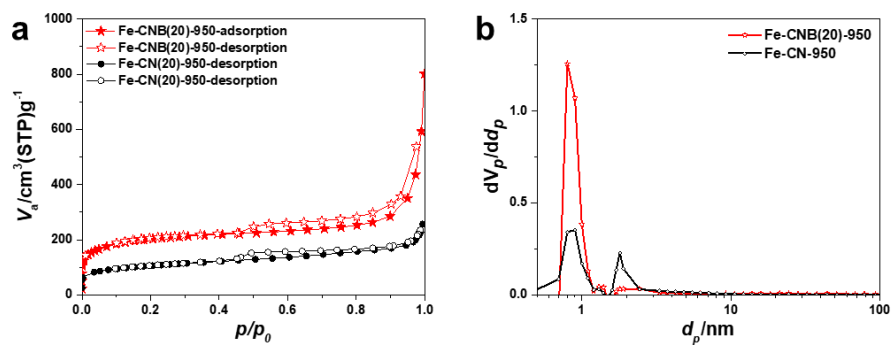


**Figure 7.6.** The  $N_2$  sorption isotherm (a) and pore size distribution (b) of Fe-CNB and Fe-CN.

**Table 7.1.** BET specific surface area and pore volumes of Fe-CNB and Fe-CN.

Sample	BET SSA( $\text{m}^2/\text{g}$ )	Micro pore volume ( $\text{cm}^3/\text{g}$ )	Meso pore volume ( $\text{cm}^3/\text{g}$ )	Total pore volume ( $\text{cm}^3/\text{g}$ )
Fe-CNB(20)-950	738	0.28	0.11	0.92
Fe-CN-950	373	0.15	0.1	0.37

## 7.4. Chemical configuration of Fe–CN/CNB

The X-ray photoelectron spectroscopy (XPS) analysis was performed to examine the surface chemistry of the Fe-CNB(20)-950 and the Fe-CN-950. The wide XPS spectra (Figure 7.7a) verify that both the Fe-CNB(20)-950 and Fe-CN-950 consist of C, N, O, and Fe. Of course, B appears in the Fe-CNB(20)-950. The content of each element obtained from the XPS quantitative analysis is summarized in Table 7.2. The nitrogen content of Fe-CNB(20)-950 is 15.2 at.%, much higher than that of Fe-CN-950 (2.7 at.%). The boron content in the Fe-CNB(20)-950 is 16.9 at.%. The high-resolution (HR) XPS spectra analysis was further performed to examine the bond figuration. The HR B1s spectra of the Fe-CNB(20)-950 (Figure 7.7b) can be divided into three components located at 190.3, 191.3, and 192.2 eV referring to B-N, BC<sub>2</sub>O, and BCO<sub>2</sub>, respectively. [7.12, 19-21] The HR N1s spectra of Fe-CNB(20)-950 (Figure 7.7c) can be deconvoluted into six components centered at 397.8, 398.2, 399.3, 400.3, and 401.5 eV corresponded to B-N, pyridinic N, Fe-N-C/B-N-C, pyrrolic N, graphitic N, and N-oxide, respectively. [7.12, 19-22] Compared with the HR N1s spectra of Fe-CN-950, the addition of boric acid greatly facilitates the development of B-N, pyridinic N, Fe-N-C, and B-N-C bond at the surface of the Fe-CNB(20)-950. The HR Fe<sub>2p</sub> spectra of the Fe-CNB(20)-950 can be deconvoluted into six components, as shown in Figure 7.7d. The component at 712.9 eV indicates an F-N bond. [7.23, 24] The two components centered at 710.7 eV and 714.9 eV are assigned to the 2p<sub>3/2</sub> orbitals of Fe<sup>2+</sup> and Fe<sup>3+</sup> species, respectively, and the other two components located at 724.7 eV and 728.8 eV are attributed to the 2p<sub>1/2</sub> orbitals of Fe<sup>2+</sup> and Fe<sup>3+</sup> species, respectively. [7.23, 24] The component at 719.4 eV is a satellite peak. [7.25] The HR Fe<sub>2p</sub> spectra of the Fe-CN-950, on the other hands, the

additional peak at 708.5 eV corresponding to the zero-valence metallic or iron carbide peak is observed. [7.23, 26] The XPS results indicate that the introduction of boric acid in the synthesis of the Fe-CN facilitates the development of pyridinic N functional group and B-N bond which are appropriate sites for atomic Fe to establish Fe-N<sub>x</sub> and Fe-N<sub>x</sub>-B moiety.

**Table 7.2.** The composition of Fe-CNB(20)-950 and Fe-CN-950 measured by XPS analysis.

Sample	C (at.%)	N (at.%)	B (at.%)	Fe (at.%)	O (at.%)
Fe-CNB(20)-950	49.2	15.2	16.9	0.2	18.5
Fe-CN-950	93.1	2.7	N/D	0.2	4.0

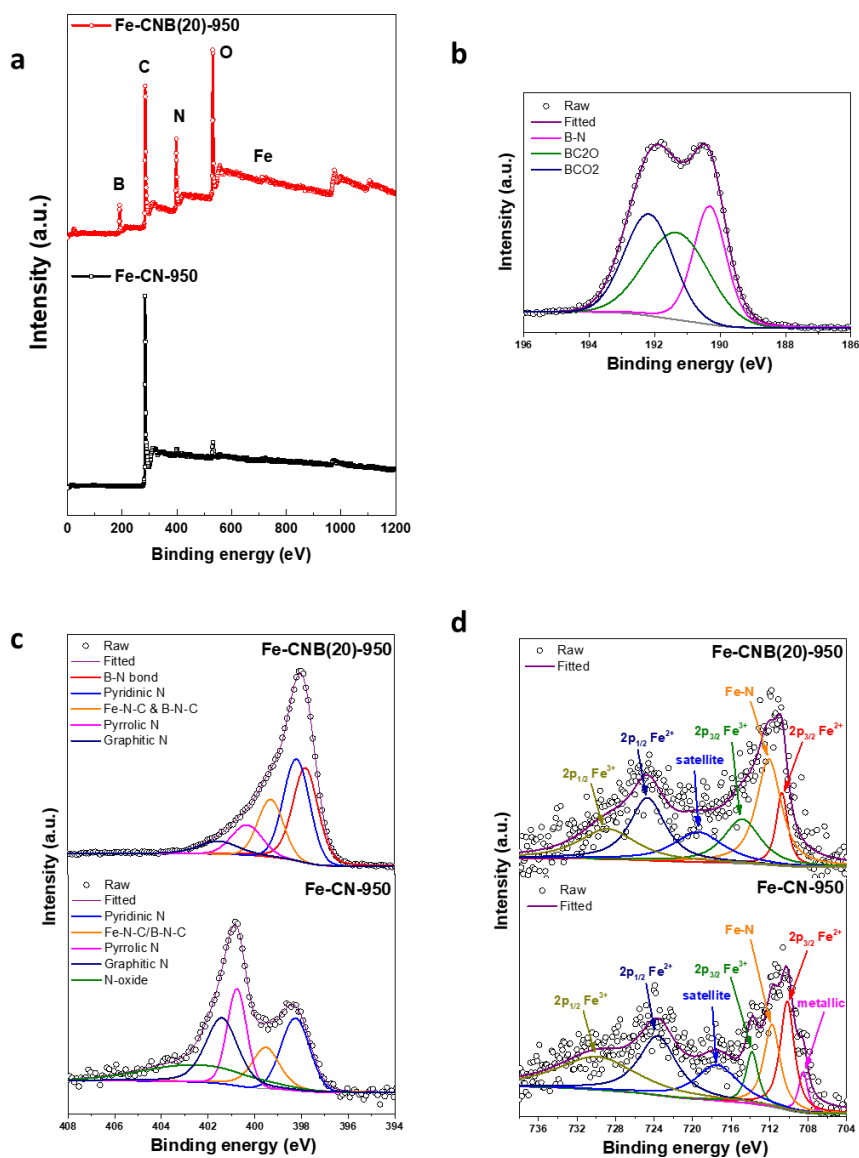


**Figure 7.7.** The wide scan XPS spectra of Fe-CNB(20)-950 and Fe-CN-950 (a). HR-B1s XPS spectra of Fe-CNB(20)-950 (b). HR-XPS N1s spectra (c) and F2p spectra (d) of Fe-CNB(20)-950 and Fe-CN-950.

## 7.5. Effect of boric acid for atomic dispersion of Fe in CNB

As presented in the above structural and surface chemistry analysis results, the introduction of boric acid in the pyrolysis of Fe-CNB facilitates the single atom doping of Fe in the nanoporous carbon. The roles of boric acid in the synthesis of Fe-CNB seems to be the followings. Firstly, boric acid can chemically and physically suppress the agglomeration of Fe ion in the precursor mixing step in the aqueous solution. The boric acid serves as the chelating agent in the precursor mixing step. The boric acid transforms to borate in the aqueous solution and borate chelated with Fe ion, which effectively prevents the formation of iron hydroxides and agglomeration of these hydroxides. The chelating effect of boric acid for transition metal ions in the aqueous solution was already reported in the electrodeposition field. For example, L.M. Graham et al. demonstrated that boric acid forms the nickel-borate complex, which isolates single Ni ion in the solution and leads to the homogenous nickel nanotube formation. [7.27]

Secondly, in the pyrolysis process, the formation of liquid boron oxide serves as the protective layer that impedes the formation of Fe-based nanoparticle and also acts as the template for the formation of a carbon nanotube structure simultaneously. Boric acid is the one of well-known soft-template agents for nanomaterial structuring. During the pyrolysis process, boric acid transforms to boron oxide (around 300°C) and melts in relatively low temperature (above 450 °C). The liquid boron oxide can enclose the newly formed nanostructures, which reduces the surface energy and prevents the agglomeration of the nanostructured materials. [7.21, 28-30] In present

study, as the protective layer for the N-doped carbon structure originated from the pyrolysis of PEG and urea, liquid boron oxide layer induces the formation of carbon nanotube structure in Fe-CNB. Furthermore, it seems that this liquid layer hinders the formation of the iron oxide nanoparticles and enables the incorporation of Fe atoms to the carbon nanotube structure.

The inhibitory effect of the boron oxide coating layer on the formation of iron oxide nanoparticles is verified by the control experiments. The Fe-CNB(1)-950 and The Fe-CNB(5)-950 containing insufficient amount of starting boric acid were synthesized. The XRD patterns of these controlled samples in Figure 7.8 show that insufficient amount of boric acid cannot inhibit the formation of Fe-based nanoparticles (iron and iron boride) during the synthesis of the Fe-CNB. The variations of BET specific surface (SSA) and the contents of boron and nitrogen depending on the starting amount of boric acid are summarized in Figure 7.9a. The BET SSA value ( $381 \text{ m}^2/\text{g}$ ) and nitrogen content (2.3 at.%) of the Fe-CNB(1)-950 are similar to those of the Fe-CN-950, and boron content of the Fe-CNB(1)-950 is very low (0.7 at.%). While, in the case of the Fe-CNB(5)-950, the BET SSA value ( $755 \text{ m}^2/\text{g}$ ), boron content (10.6 at.%), and nitrogen content (11.7 at.%) are greatly increased, and get close to those of the Fe-CNB(20)-950.

The amount of major bonding types of the Fe-CN-950 and Fe-CNB-950s calculated from the N1s and B1s HR-XPS spectra are plotted in Figure 7.9b. The B-N and pyridinic N content of the Fe-CNB(5)-950 are significantly increased, contrasted with those of the Fe-CNB(1)-950. Also, the B-N content is similar to that of the Fe-CNB(20)-950. From these results, it is demonstrated that the required

amount of boric acid for the atomic dispersion of Fe in CNB is larger than that for synthesizing CNB having high B and N content. The amount of doped boron in carbon substrate is already sufficient in the Fe-CNB(5)-950 having high BET SSA, boron content, and nitrogen content. However,  $\text{Fe}_3\text{O}_4$  and FeB nanoparticles exist in the Fe-CNB(5)-950 as shown in XRD analysis, indicating that the formation of a sufficient amount of boron oxide liquid which could cover the entire surface of the carbon structure is prerequisite for the atomic dispersion of Fe in CNB substrate.

In order to understand the role of liquid boron oxide in the inhibition of Fe-based nanoparticle formation, the thermodynamic calculations were performed using the FactSage thermodynamic software [7.31], and the results are presented in Figures 7.10 and 7.11. In the present Fe-CNB and Fe-CN material system, the elements which can form oxides are Fe and B. The pseudo-binary phase diagrams of the Fe- $\text{B}_2\text{O}_3$  at  $10^{-5}$  atm  $\text{P}_{\text{O}_2}$  condition is calculated in Figure 7.10. Unfortunately, it is hard to determine the  $\text{P}_{\text{O}_2}$  in the present experimental condition. Considering the formation of  $\text{Fe}_3\text{O}_4$  in Fe-CN-950 sample, the  $\text{P}_{\text{O}_2}$  is set to be  $10^{-5}$  atm. It should be noted that the Fe- $\text{B}_2\text{O}_3$  phase diagram can be varied depending on the  $\text{P}_{\text{O}_2}$ , but the general feature of the diagram is similar at  $\text{P}_{\text{O}_2} = 10^{-6} \sim 10^{-3}$  atm, as shown in the phase diagram of at 950 °C (Figure 7.11). According to the calculated diagram (Figure 7.10), Fe exists as Fe oxide ( $\text{Fe}_2\text{O}_3$  or  $\text{Fe}_3\text{O}_4$ ) and make liquid solution with  $\text{B}_2\text{O}_3$ . Liquid  $\text{B}_2\text{O}_3$  phase formed above 550 °C and the area of liquid oxide phase are enlarged rapidly with increasing temperature. In the present study, the at.% of (% Fe/(Fe+ $\text{B}_2\text{O}_3$ )) in the starting materials of Fe-CNB(1)-950, Fe-CNB(5)-950, and Fe-CNB(20)-950 are 32.9, 8.9, and 2.4 at.%, respectively. In all case, a significant amount of Fe oxide becomes liquid Fe-oxide- $\text{B}_2\text{O}_3$  from 450 °C.

Figure 7.12 shows the thermodynamic calculation results to simulate Fe-CN and Fe-CNB(20) synthesis process. That is, both PEG and Urea for carbon and nitrogen source are considered together with Fe and B<sub>2</sub>O<sub>3</sub>. All possible solids, liquid oxide, and gas phase were considered in the equilibrium calculation. As can be seen in Figure 7.12a, Fe source can change from Fe<sub>3</sub>O<sub>4</sub> to FeO and Fe at about 600 °C due to the reducing condition by carbon. In contrast, when the boron oxide is added for Fe-CNB (Figure 7.12b), all Fe source becomes liquid phase with B<sub>2</sub>O<sub>3</sub> between from 600 and 655 °C, and then the metallic Fe phase is gradually formed as the temperature increases. This process seems to generate very uniformly distributed atomic dispersion of Fe in Fe-CNB. In order to confirm this earlier stage of transformation of Fe oxide phase, Fe-CN and Fe-CNB(20) were prepared just after 1 min heat treatment at 700 °C. Their TEM images are presented in Figures 7.13 and 14. The Fe<sub>3</sub>O<sub>4</sub> nanoparticles exist in Fe-CN (Figure 7.13), whereas Fe-based nanoparticles were not detected in Fe-CNB (Figures 7.14a-e). In addition, the TEM-EDS mapping analysis shown in Figures 7.14f-h demonstrates that Fe, N and B are homogeneously distributed in the carbon structure.

It is well known that the addition of boron dramatically improves the incorporation of nitrogen in carbon structure by the acceptor-donor complementary effect. [7.32] During the pyrolysis, the active radical B<sub>2</sub>O<sub>2</sub>(g) attributed to the decomposition of liquid boron oxide can be formed at the high temperature (above 800 °C), and reacts with carbon and forms B-N. [7.14, 21] Thus, boron favorably incorporates into nitrogen-doped carbon nanotube structure, resulting in a great increase in nitrogen functional groups, especially pyridinic N and B-N even at high



temperature where pyridinic N is prone to pyrolysis. [7.33]

In the synthetic process of Fe-CNB, the formation of Fe-based nanoparticle which could be the strong graphitization catalyst was effectively suppressed by the formation of  $B_2O_3$  liquid phase. As a result, the redundant graphitization that caused the degeneration of a nanoporous carbon structure could be diminished and Fe could be atomically dispersed. Furthermore, boron doping effects enables the incorporation of a large amount of nitrogen in the nanoporous carbon structure. Therefore, to maximize the effectiveness of the addition of boric acid for developing abundant  $Fe-N_x$  active sites having high electrocatalytic activity in the porous carbon structure, the proper heat treatment temperature is important and 950 °C was experimentally found to be the optimum temperature in this study.

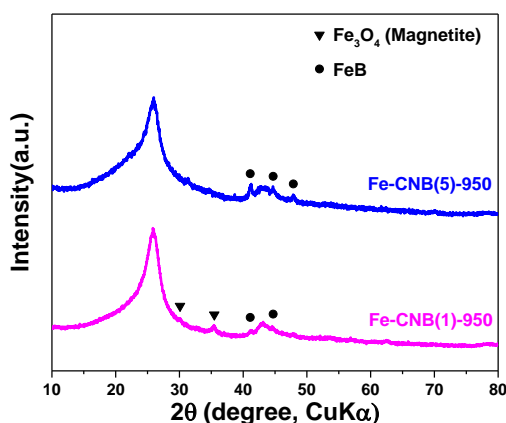


**Figure 7.8.** The XRD patterns of Fe-CNB(5)-950 and Fe-CNB(1)-950.

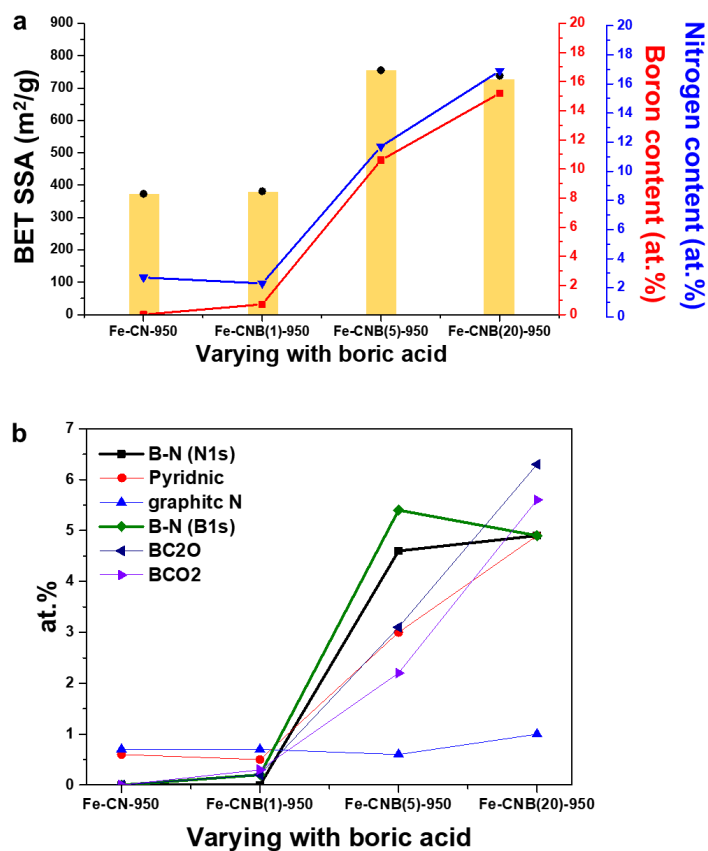


**Figure 7.9.** The BET specific surface area, boron, and nitrogen content of Fe-CN-950 and Fe-CNB(1, 5, and 20)-950 (a), and the content of deconvoluted peaks in N1s and B1s XPS of Fe-CN-950 and Fe-CNB(1, 5, and 20)-950, calculated by the peak area.

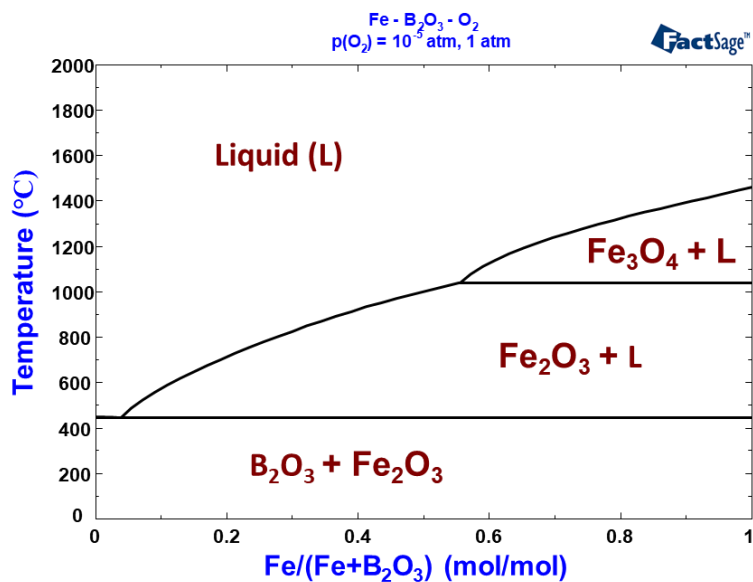


**Figure 7.10.** Phase diagram of the Fe-B<sub>2</sub>O<sub>3</sub> system at ( $p_{O_2}=10^{-5}$  atm), calculated from the thermodynamic software.

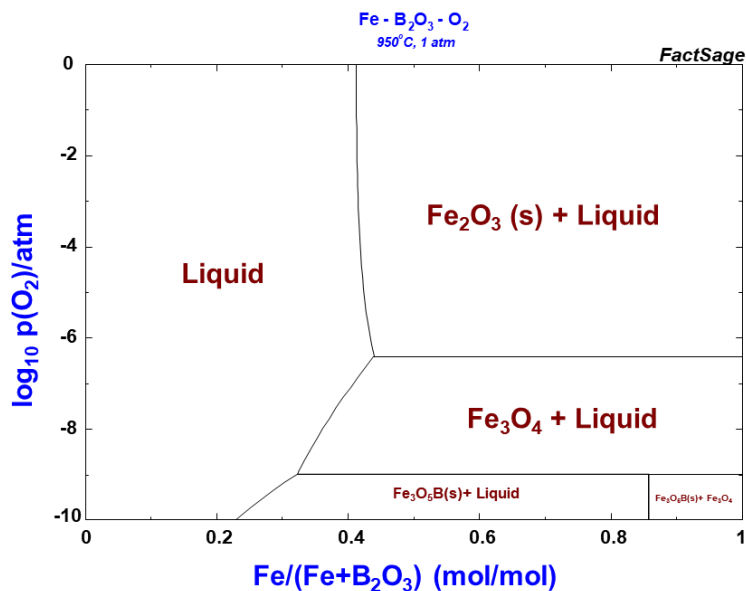


**Figure 7.11.** Phase diagram of the Fe-B<sub>2</sub>O<sub>3</sub>-O<sub>2</sub> system with oxygen partial pressure at 950 °C, calculated from the thermodynamic software.

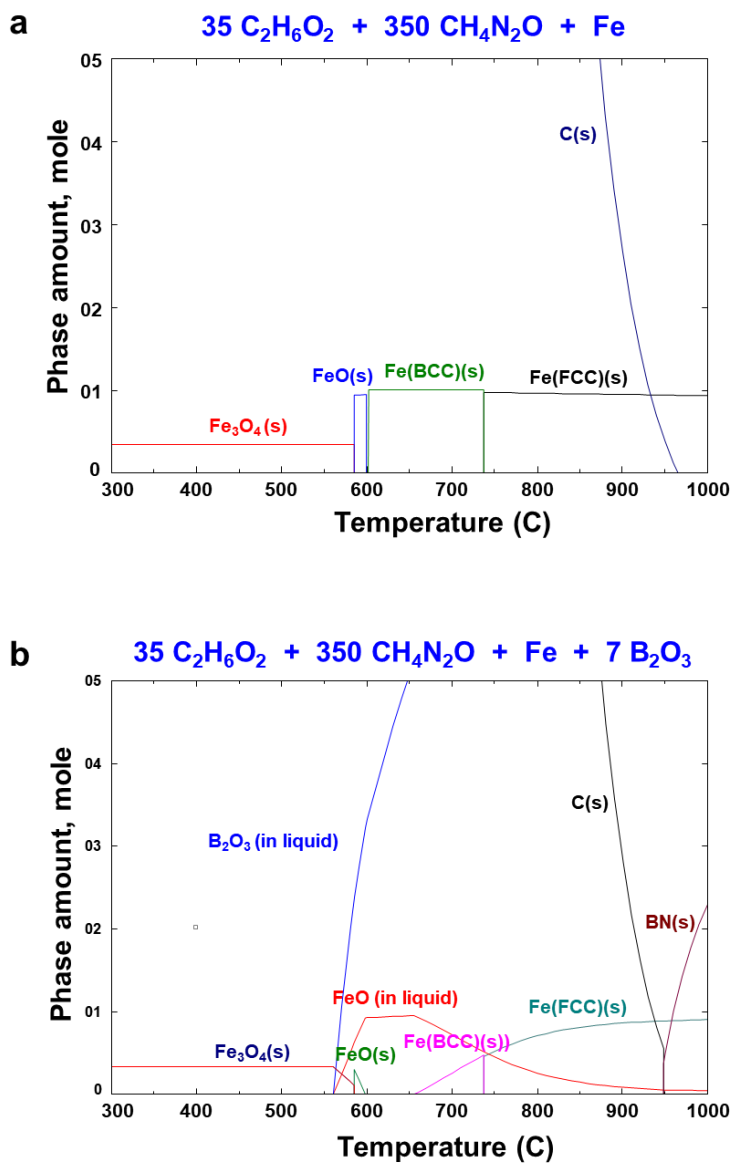


**Figure 7.12.** Thermodynamic calculations for the Fe-CN (PEG-urea-Fe) (a) and Fe-CNB(20) (PEG-urea-Fe-B<sub>2</sub>O<sub>3</sub>) (b).

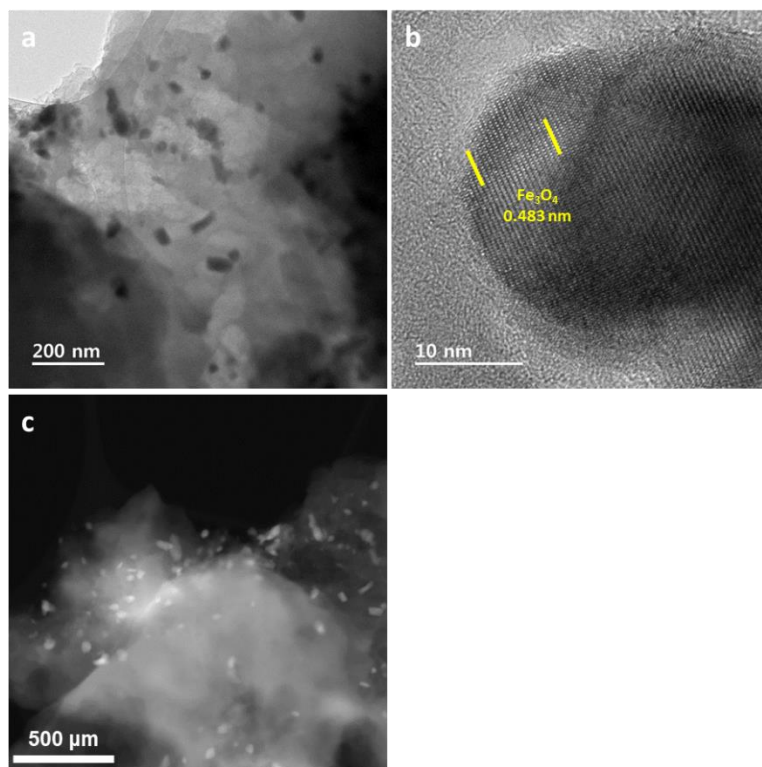


**Figure 7.13.** TEM image (a), HR-TEM image (b), HADDF image (c) of Fe-CN-700-1 min.

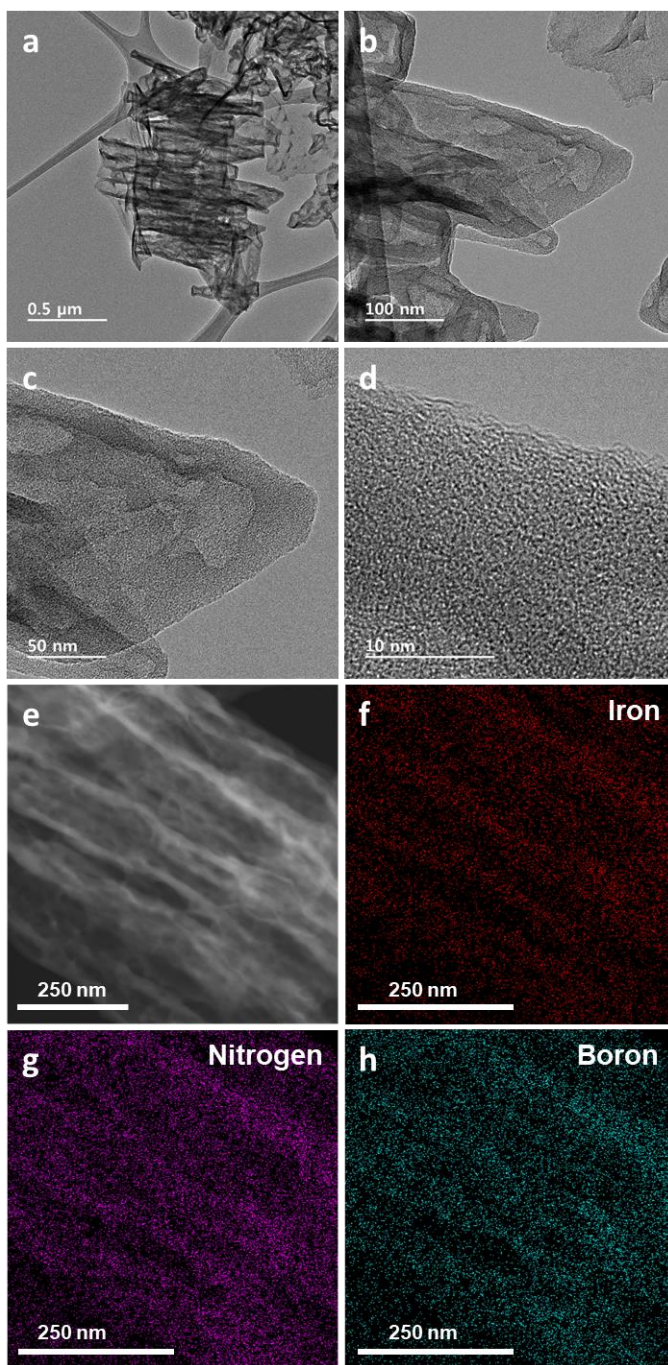


**Figure 7.14.** TEM images (a-c), HR-TEM image (d), HADDF image (e), and EDS elemental mappings (iron, nitrogen, and boron) (f-h) of Fe-CNB(20)-700-1 min.

## 7.6. Proposed formation mechanism of Fe-CNB

Based on experimental results and thermodynamic calculations, the formation mechanism of the Fe-CN-900 and Fe-CNB(20)-950 can be proposed as in Figure 7.15. In the Fe-CN system, the iron oxide nanoparticle formation starts at low temperature (300 °C) [7.34] before the construction of a robust N-doped carbon structure. As the temperature increases, growth of iron oxide nanoparticle occurs, and the reduction of iron oxide nanoparticle to Fe nanoparticles occurs above 600 °C. Fe nanoparticles induce partial graphitization, and thus the Fe-CN has graphitic ribbon and/or carbon ribbon structure having with less nanoporous and less Fe-N<sub>x</sub> active sites. [7.35, 36]

In contrast, when the boric acid is introduced for the Fe-CNB system, Fe ions are first chelated by borate thus Fe complex can be homogenously dispersed at the surface of urea and PEG in the mixing process. In the initial stage of pyrolysis (below 450 °C), Fe complex are transformed to Fe oxide. As the temperature increases continuously, the boron oxide melts and covers the surface of carbon structure originated from the pyrolysis of PEG. Fe oxide is dissolved into liquid boron to form liquid oxide solution phase, which effectively inhibit the formation of iron nanoparticle. Nitrogen-doped carbon is formed subsequently by the decomposition of melamine originated from urea (> 600 °C). [7.21] The reduction of Fe oxide to metallic Fe occurs in liquid B<sub>2</sub>O<sub>3</sub>, and reduced Fe atoms incorporate into carbon structure and forms Fe-N<sub>x</sub> moiety (> 700 °C). [7.34] The boron atoms doped into carbon structure at high temperature (> 800 °C) which leads to further development

of Fe-N<sub>x</sub>-B and Fe-N<sub>x</sub> sites. Leftover liquid B<sub>2</sub>O<sub>3</sub> is mostly evaporated to gas phase, and B<sub>2</sub>O<sub>3</sub> barely remains in the surface of carbon structure.

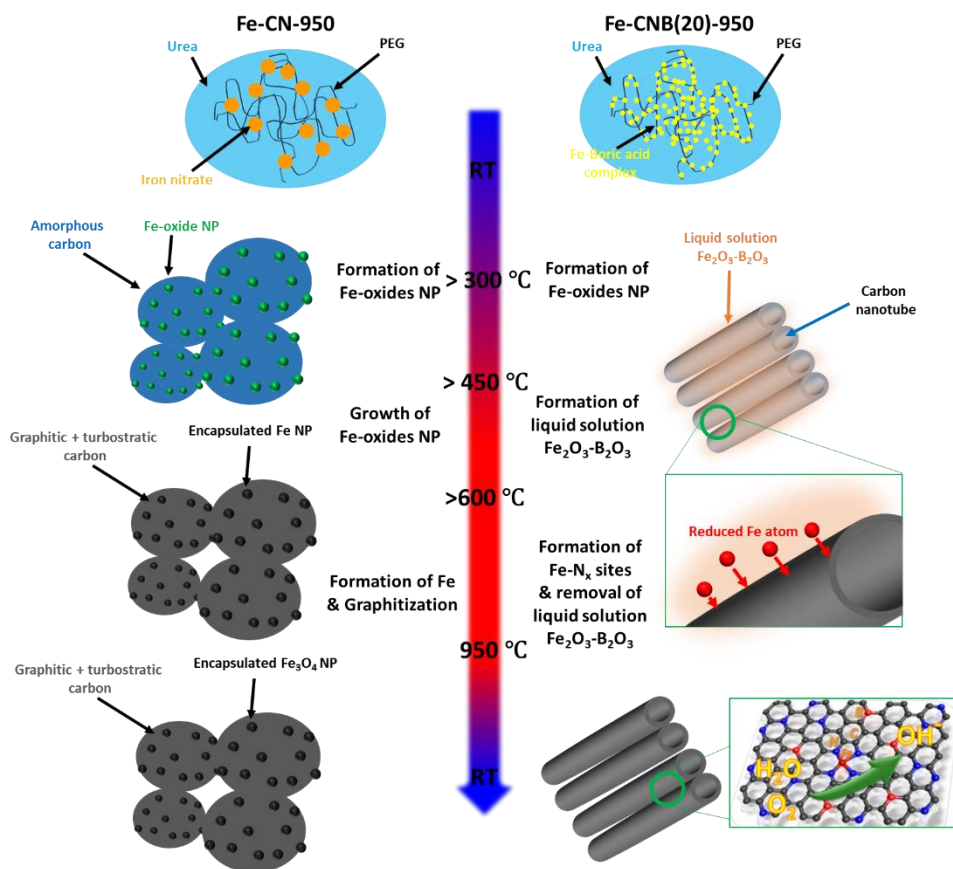


**Figure 7.15.** Formation mechanism of Fe-CN-950 and Fe-CNB(20)-950.



## 7.7. Electrocatalytic performance evaluation

The electrocatalytic activity of the Fe-CNB(20)-950 for ORR in alkaline medium was examined and compared with the results of the control samples (Fe-CN-950, CN-950, and CNB(20)-950) and commercial 20 wt.% Pt/C catalyst. The ORR performance was evaluated by a rotating ring disk electrode (RRDE) measurement in O<sub>2</sub> saturated 0.1 M KOH electrolyte. As shown in Figure 7.16, Fe-CNB had the highest onset potential (0.94 V) and half-wave potential (0.89 V), surpassing the commercial 20 wt.% Pt/C catalyst. This is significantly contrasted to the results of Fe-CN (control sample without boric acid) and CNB (control sample without Fe) showing the lower onset potential and half-wave potential.

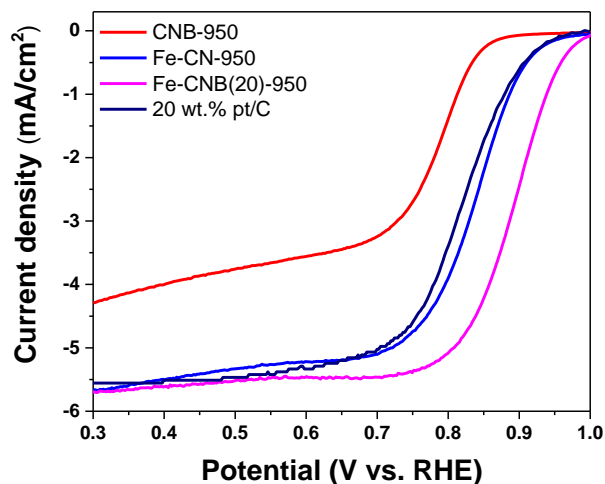


**Figure 7.16.** LSV curves of CN-950, CNB(20)-950, Fe-CN-950, Fe-CNB(20)-950, and commercial 20 wt.% Pt/C exhibiting ORR activity in 0.1 M KOH. The measurements were conducted with the electrode rotation of 1600 rpm.

## 7.8. Synthesis of Ni-CNB

We further applied boric acid for the synthesis of the Ni-CNB system. The TEM results of the Ni-CNB(20)-950 and Ni-CN-950 demonstrates that the addition of boric acid induces the atomic dispersion of Ni in CNB, similar to the Fe-CNB. Figures 7.17a,b show the TEM images of the Ni-CN. The Ni nanoparticles are observed along with carbon ribbons that enclose the Ni nanoparticle, and the partial graphitization occurs as shown in HR-TEM images of the Ni-CN (Figures 7.17 c,d). The HADDF image and EDS elemental mapping analysis also demonstrate the existence of Ni nanoparticles in the Ni-CN shown in Figures 7.17 e,f. In contrast, the TEM images of the Ni-CNB in Figure 7.18a-c show that carbon nanotubes are formed without the Ni-based nanoparticles. These carbon nanotubes have the turbostratic structure as shown in the SAED pattern (the inset of Figure 7.18c) and the HR-TEM image of the Ni-CNB (Figure 7.18d). The HADDF image and EDS elemental analysis in Figure 7.18 e-h also demonstrate that Ni, B, and N are homogenously incorporated into the carbon nanotube. The XRD pattern of Ni-CNB(20)-950 and Ni-CN-950 shown in Figure 7.19 exhibits that the Ni-CNB(20)-950 have the turbostratic carbon structure having two broad (002) and (10) peaks centered around  $26^\circ$  and  $43^\circ$ . While (002) peak of the Ni-CN-950 is less broad, and (002) and (10) peaks are slightly shifted to higher angle due to the partial graphitization attributed to the existence of Ni nanoparticles. The addition of boric acid in the Ni-CN also enhances the development of the nanoporous structure. The BET SSA and all pore volumes derived by the  $N_2$  isotherm at 77 K (Figure 7.20a) are greatly increased in the Ni-CNB compared to the Ni-CN, as summarized in Table

7.3. The improvement in the pore structure of the Ni-CNB is attributed to the formation of carbon nanotube structure and inhibition of Ni nanoparticle formation, induced by the addition of boric acid. The results of the Ni-CNB(20)-950 are the same as those of Fe-CNB(20)-950.

The applicability of the Ni-CNB(20)-950 for CO<sub>2</sub> reduction reaction (CO<sub>2</sub>RR) was evaluated. The electrochemical activities of the Ni-CNB(20)-950 and Ni-CN-950 were measured by a linear sweep voltammetry, shown in Figure 7.21. The Ni-CNB(20)-950 and Ni-CN-950 show low current densities in Ar atmosphere, which indicate the low hydrogen evolution reaction (HER) activity. In contrast, when the atmosphere is changed to CO<sub>2</sub>, the current densities of the Ni-CNB(20)-950 and Ni-CN-950 are significantly increased, especially more prominent in the Ni-CNB(20)-950. The current density of Ni-CNB(20)-950 is 35.8 mA/cm<sup>2</sup> at -1.0 V, almost twice of Ni-CN-950 (19.0 mA/cm<sup>2</sup>). Previous studies reported that the Ni-N<sub>x</sub> moiety is a major active site that endows the electrocatalytic activity for CO<sub>2</sub>RR.[37-39] In the Ni-CNB(20)-950, it is presumed that the introduction of boric acid facilitates the development of Ni-N<sub>x</sub> active sites, as reveals in the Fe-CNB system, resulting in a significant increase in the current density of the Ni-CNB(20)-950 after the CO<sub>2</sub> dissolution in the electrolyte.

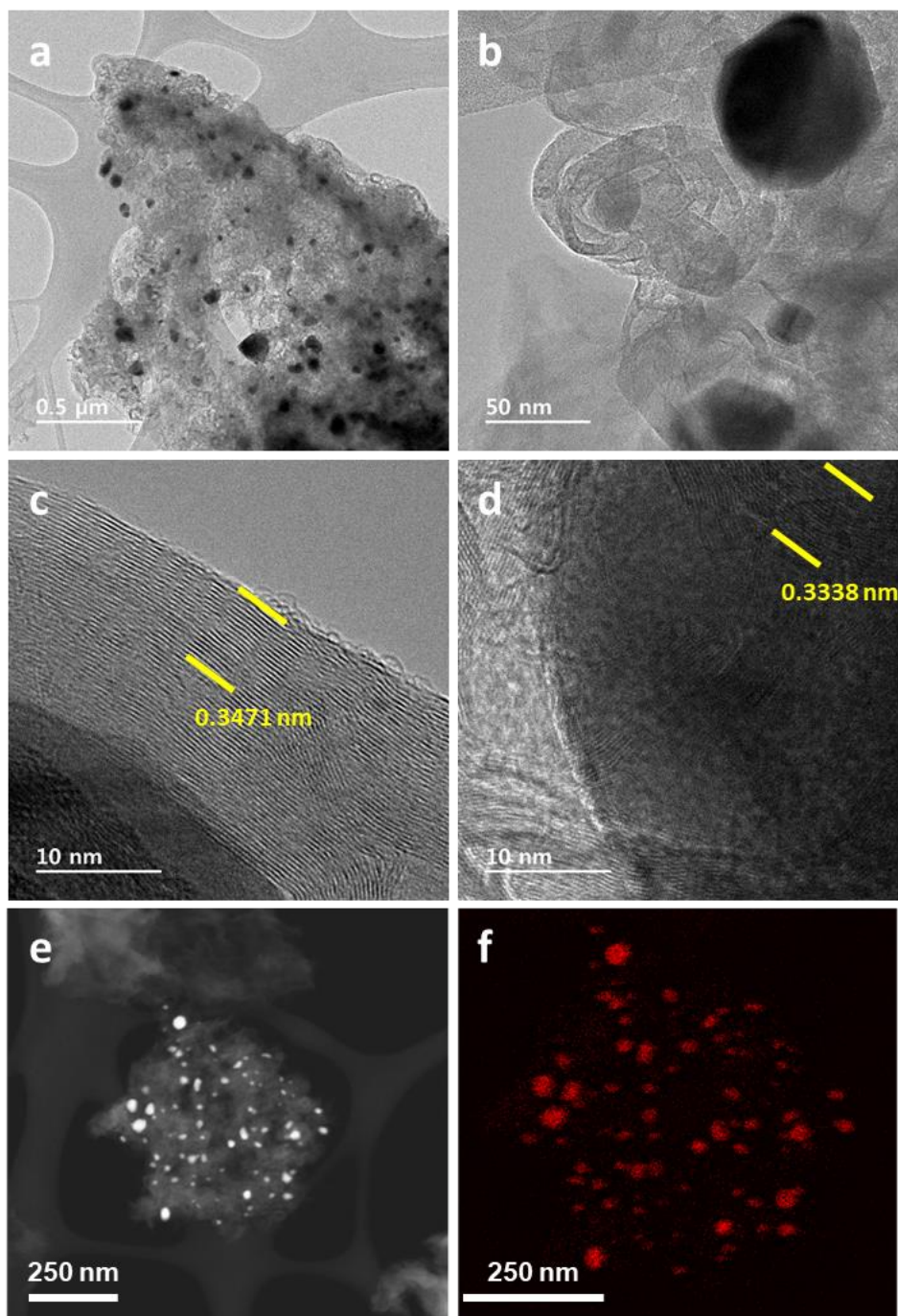


**Figure 7.17.** TEM images (a,b), HR-TEM image (c,d), HADDF image (e), and EDS elemental mappings (nickel) (f) of Ni-CN-950.

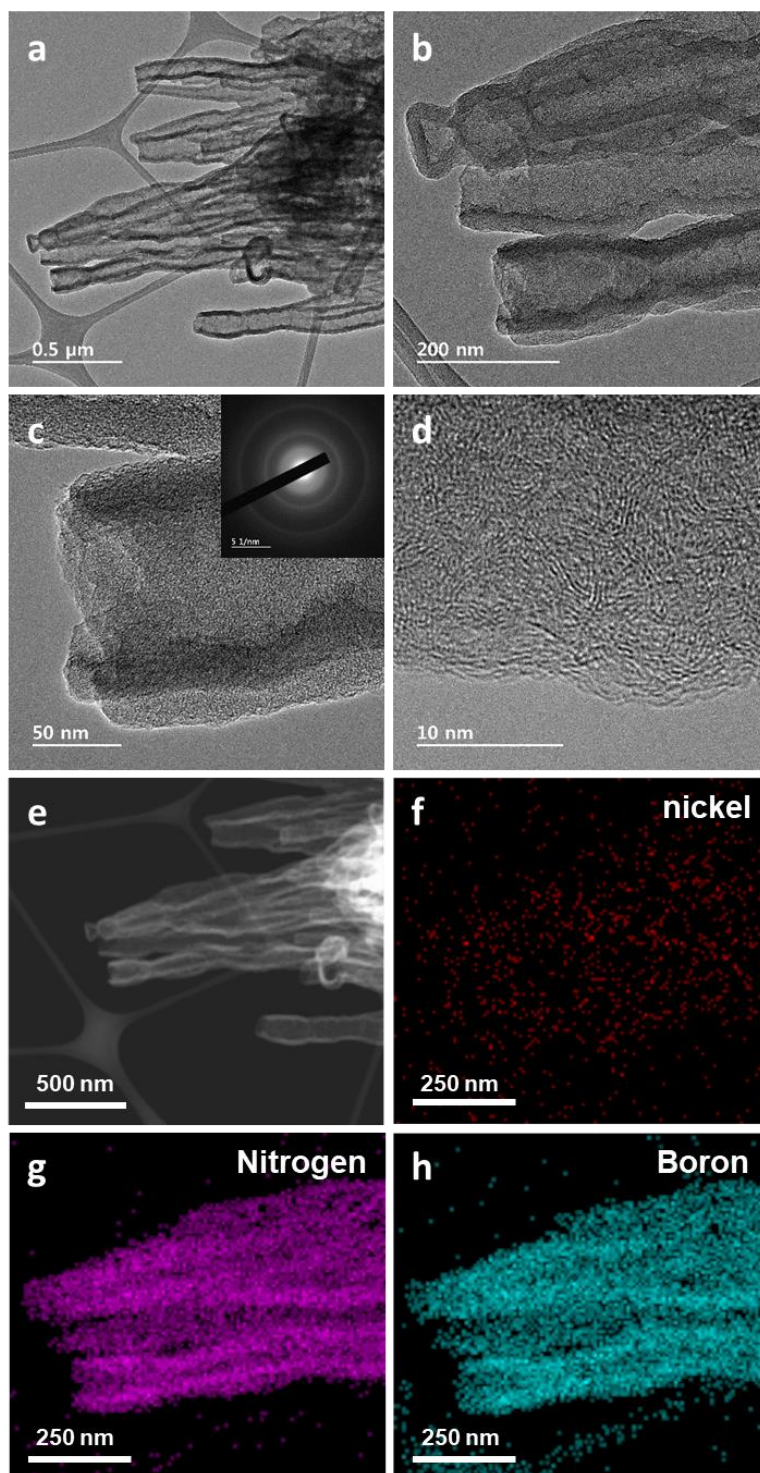


**Figure 7.18.** TEM images (a-c), HR-TEM image (d), HADDF image (e), and EDS elemental mappings (nickel, nitrogen, and boron) (f-h) of Ni-CNB(20)-950.

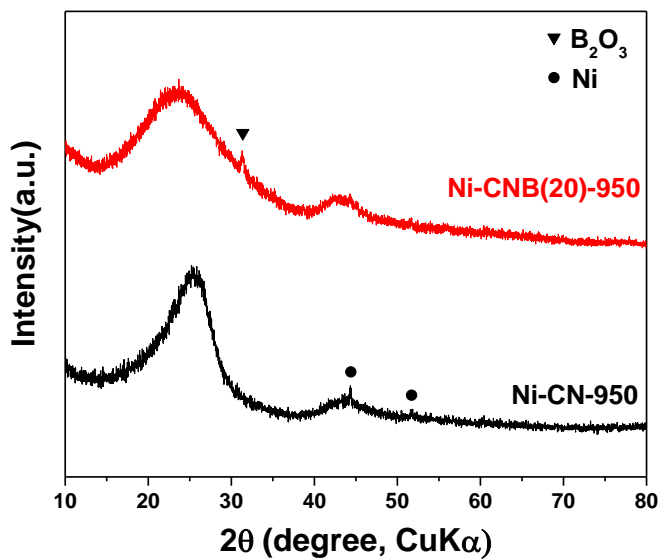


**Figure 7.19.** The XRD patterns of Ni-CNB(20)-950 and Ni-CN-950.

**Table 7.3.** BET specific surface area and pore volumes of Ni-CNB(20)-950 and Ni-CN-950.

Sample	BET SSA(m <sup>2</sup> /g)	Micro pore volume (cm <sup>3</sup> /g)	Meso pore volume (cm <sup>3</sup> /g)	Total pore volume (cm <sup>3</sup> /g)
Ni-CNB(20)-950	1336	0.51	0.16	1.37
Ni-CN-950	687	0.27	0.08	0.50

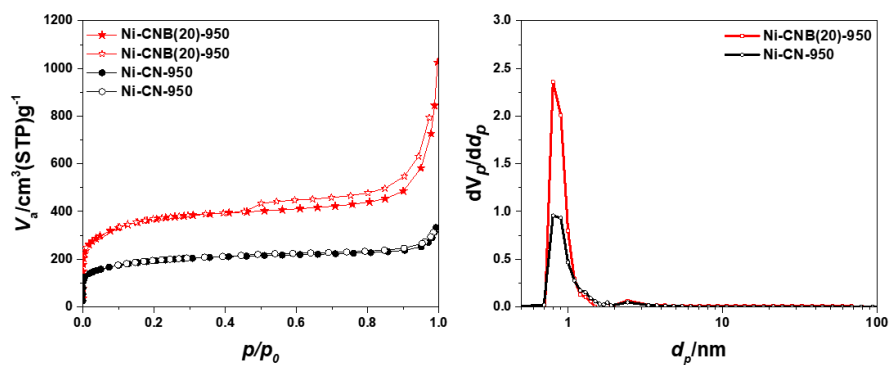


**Figure 7.20.** The  $N_2$  sorption isotherm (a) and pore size distribution (b) of Ni-CNB(20)-950 and Ni-CN-950.

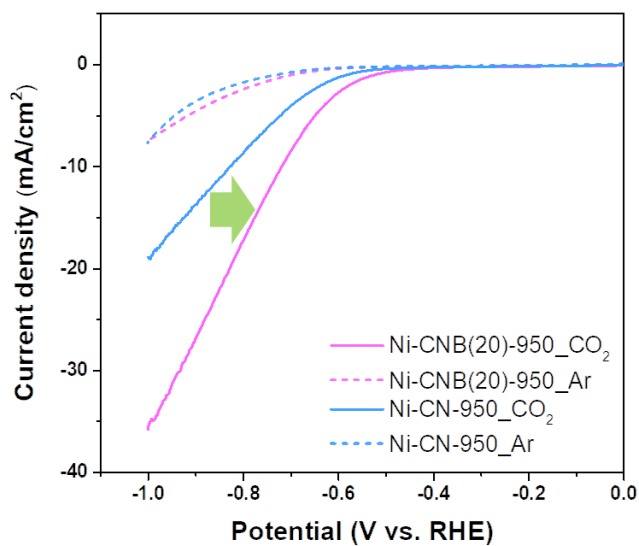


**Figure 7.21.** LSV curves of Ni-CNB(20)-950 and Ni-CN-950 measured in the Ar saturated or  $\text{CO}_2$  saturated 0.5 M  $\text{KHCO}_3$  electrolyte.

## 7.9. Conclusions

The pyrolysis synthesis for producing atomically dispersed M (Fe or Ni) – CNB was investigated. This study demonstrates that the introduction of boric acid is a facile method to embed M-N<sub>x</sub> active sites to a porous carbon structure. Boric acid plays the roles of both a protective layer that facilitates the development of an N-doped carbon nanotube structure and inhibits the formation of metal (Fe or Ni)-based nanoparticle and the B doping source that enhances the incorporation of N in the carbon structure. The formation process of the Fe-CNB was elucidated based on the experimental data and thermodynamics analysis. In the precursor mixing step, boric acid forms borate that is chelated with Fe ion, which can chemically and physically isolate Fe ion. During the early stage of the pyrolysis process (< 600 °C), boron oxide liquid is formed and coats the entire surface of carbon structure and Fe oxide is dissolved into boron oxide. Thus the formation of the metal-based nanoparticle is suppressed, and the formation of M-N<sub>x</sub> moiety in carbon substrate readily occurs along with the development of robust B and N-doping sites in carbon substrate at high temperature (> 700°C). As a result, the Fe-CNB(20)-950 having abundant Fe-N<sub>x</sub>-B and Fe-N<sub>x</sub> active sites was obtained. it exhibits an outstanding electrocatalytic activity for oxygen reduction reaction (ORR) with a half-wave potential of 0.89 V, superior to commercial Pt/C catalyst. The effect of boric acid is also manifested in the Ni-CNB system.

This study demonstrates that the introduction of boric acid can be a facile and effective approach to synthesize metal-N<sub>x</sub> active moiety incorporated boron and nitrogen co-doped porous carbon which is expected for various applications including electrocatalysis.



## Chapter 8. Overall Conclusion

### 8.1. Summary of results

In this study, the novel synthesis methods for heteroatoms-doped porous carbon materials having hierarchical pore structure and abundant active sites were investigated. The heteroatoms-doped porous carbon materials synthesized in this study show the high electrocatalyst performances. Furthermore, the interactions between carbon and heteroatoms during the synthesis process were elucidated from the thermodynamic analysis and controlled experiments. The formation mechanisms of heteroatoms-doped porous carbon materials are proposed, which are essential for the accurate control of the properties of porous carbon materials. The results of this study are summarized as follows:

(1) This study demonstrated that the availability of boron atoms in the initial stage of the chlorination process of TiC and Ti(C,N) for the carbide-derived porous carbon (C) and carbonitride-derived nitrogen-containing porous carbon (CN), respectively, is vital for maximizing the functionality of the carbon materials. The diffusion interface between boron, carbon, and nitrogen in the original raw precursors is maximized through a simple raw powder engineering. Thus, boron atoms could be diffused effectively from TiB<sub>2</sub> to the carbon structure in the early stage of the chlorination process. The boron atoms serve as the carbon structure linkers as well as dopants, facilitating the development of the heteroatoms-rich carbon layer in the harsh chlorination condition by establishing covalent connections with carbon and

nitrogen atoms.

(i) Using an one-pot chlorination process of  $\text{TiC-TiB}_2$  and  $\text{Ti(C,N)-TiB}_2$  mixture, it was possible to synthesize the boron-doped porous carbon (D-CB) having an oxygen-rich defective carbon layers, and boron and nitrogen co-doped carbon (D-CNB) having a thick boron and nitrogen co-doped shell. In particular, pyridinic N was exclusively developed in both D-CB and D-CNB. As a result, the D-CB and D-CNB show excellent activities for the  $2e^-$  pathway and  $4e^-$  pathway oxygen reduction reaction (ORR), respectively.

(ii) The novel synthetic process was designed to produce the h-BN nano-domains incorporated porous carbon materials (D-BNCs) using an one-pot chlorination of the nitrogen rich- $\text{Ti(C,N)-TiB}_2$  mixture. The optimum condition to produce the D-BNC was searched by varying the composition of original raw powder and chlorination temperature. As a result, the D-BNC-700 having the abundant h-BN-C interface and hierarchical pore structure was obtained. The D-BNC-700 exhibits one of the world-top class  $2e^-$  pathway oxygen reduction reaction (ORR) performance. It has a maximum  $\text{H}_2\text{O}_2$  selectivity of 88.3 % in a rotating ring-disk electrode (RRDE) measurement in alkaline medium (1.0 M KOH). Furthermore, D-BNC-700 shows an excellent operation performance in the custom-made full flow cell condition. It has an outstanding  $\text{H}_2\text{O}_2$  production rate (4.65 mmol/h) and long-term stability with high  $\text{H}_2\text{O}_2$  faradaic efficiency ( $\sim 61\%$ ) in 1.0 M KOH for 10 h. These results demonstrate that the B-C-N materials produced by the chlorination process can be a promising material for the electrocatalyst for  $\text{H}_2\text{O}_2$  production.

(2) The facile synthesis processes to produce atomically dispersed M-CNB materials having the outstanding electrocatalytic activity were searched. Major factors that determine the atomic dispersion of metal in porous carbon structure were investigated.

(i) The M (Fe and Ni)-CNBs were synthesized by the one-pot chlorination process of the titanium carbonitride, titanium boride, and transition metal precursor ( $M(\text{acac})_x$ ) ( $M = \text{Fe}$  and  $\text{Ni}$ ) mixture. Depending on the types of a transition metal, it was found that boron can facilitate or impede the atomic dispersion of metal in CNB. The metal-based nanoparticles were inevitably formed before the chlorination process due to the pyrolysis of the metal precursor ( $M(\text{acac})_x$ ), and the addition of boron from  $\text{TiB}_2$  induced the phase transformation of metal-based nanoparticles to the metal boride nanoparticles. The inhibition of the surface melting of metal-based nanoparticles that causes a severe graphitization is the critical factor that enables the development of  $M\text{-N}_x$  active sites in the porous carbon structure. Thermodynamic analysis shows that iron boride nanoparticle has higher melting temperature than iron nanoparticle, and the melting temperatures of both iron boride and iron nanoparticles is higher than the Fe-CNB processing temperature. Therefore, the redundant graphitization of the Fe-CNB was suppressed and the atomic Fe was readily incorporated to porous carbon structure of the Fe-CNB by  $\text{FeCl}_3$  gas during the chlorination. As a result, the  $\text{Fe-N}_x$  active sites were well-developed in the porous carbon structure. Therefore, the Fe-CNB shows outstanding oxygen reduction reaction (ORR) performance in the alkaline medium, superior to commercial Pt/C catalyst. In contrast, the melting temperature of nickel boride nanoparticles is much lower than nickel nanoparticles, and even lower than the Ni-CNB processing

temperature. That is, the surface melting of the nickel boride nanoparticles can occur during the chlorination process, which accelerates the severe graphitization. Thus, the addition of boron barely improves the ORR performance of Ni-CNB.

(ii) As an alternative process, pyrolysis process was also studied to produce M-CNB. The atomically dispersed M (Fe and Ni) – CNB was successfully synthesized by the one-pot pyrolysis of polyethylene glycol-urea-boric acid-metal nitrate (Fe and Ni). It was demonstrated that the introduction of boric acid is a facile tactic to embed M-N<sub>x</sub> active sites into a porous carbon structure. In the present pyrolysis process, the boric acid was transformed to the borate (boron oxide) that can chemically and physically isolate Fe ion by the chelating effect during the mixing process, which led to the homogenous distribution of Fe in the mixture of raw precursors. During the early stage of the pyrolysis process (< 600 °C), liquid boron oxide was formed and covered the entire surface of carbon structure and Fe became Fe oxide and dissolved in liquid boron oxide. In this way, the formation of the metal-based nanoparticle was inhibited, and the formation of Fe-N<sub>x</sub> moiety in carbon substrate readily occurred along with the development of robust B and N-doping sites in carbon substrate at high temperature (> 700°C). As a result, Fe-CNB having abundant Fe-N<sub>x</sub>-B and Fe-N<sub>x</sub> active sites exhibits a distinguished electrocatalytic activity for the oxygen reduction reaction (ORR) with a half-wave potential of 0.89 V, superior to commercial Pt/C catalyst. The effect of boric acid was also manifest in the Ni-CNB system. The Ni-CNB shows the applicability as the electrocatalyst for the CO<sub>2</sub> reduction reaction (CO<sub>2</sub>RR).

In summary, this study demonstrates the applicability of the chlorination process for the synthesis of the functional heteroatoms-doped porous carbon materials. The CNB and M-CNB materials produced through the chlorination process show the promising performances for the electrochemical applications. It is found that h-BN implantation and atomic dispersion of metals in the heteroatoms doped porous carbons are key factors for improving the electrochemical performance of CNB and M-CNB. The critical chemical and processing parameters that determine the characteristics of heteroatoms doped porous carbon in the chlorination and pyrolysis synthesis process were experimentally and thermodynamically investigated to provide the guidance for commercial production of such functional carbon materials.

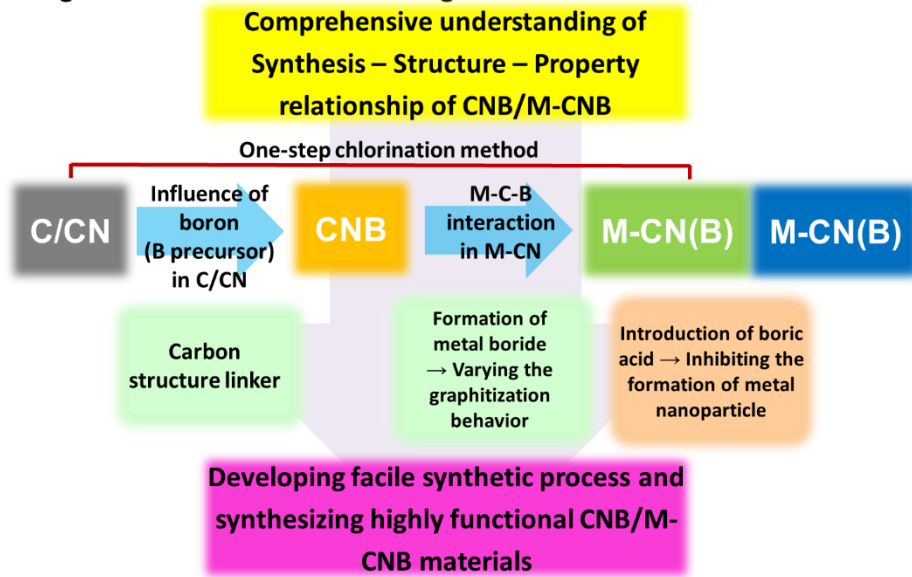
## 8.2. Original contribution

The original contribution of this study to knowledge is as follows:

First, this study demonstrates the versatility of the chlorination process to synthesize various heteroatoms-doped porous carbon materials. In general, the post-treatment process has to be accompanied to carbide-derived carbon to dope heteroatoms in nanoporous carbon structure, which is an inconvenient approach and has a limitation for the doping amount. In this study, the critical chemical and processing parameters for synthesizing the CNB and M-CNB materials thorough the chlorination process, essential to produce highly functional heteroatoms-doped porous carbon materials were revealed. This has not been addressed before in the conventional carbide-derived carbon research. It is expected that this study can present a new aspect to the chlorination process.

Second, this study demonstrates the effect of boron (or boron precursor) in the synthesis of the M-CNB materials. Depending on the experiment condition, the interaction between metal and boron can be totally different, which greatly affects the characteristics of the final porous carbon product. The mechanisms of the incorporation of metal atoms in porous carbon structure in the chlorination process and pyrolysis process are identified by thermodynamic and controlled experiments in this study. These understanding can be a cornerstone for the development of the practical synthesis of atomically dispersed M-CN materials.

❖ Original Contribution to Knowledge



## **8.3. Future suggestion**

### **8.3.1. Searching new metallic elements for M-CNB materials**

In this thesis, the facile synthesis of the CNB materials and M (Fe and Ni)–CNB materials using the chlorination process and the pyrolysis process. In this study, Fe, and Ni were tested comprehensively, and Co was also tested. In the literature, the synthesis of M-CN materials where M = Mn, Cu, Mo, and Pt have been actively studied, and these M-CN materials applied to various energy and environmental applications. [8.1, 2 ,3]

As future work, it would be interesting to test other metals for M-CNB using chlorination process and pyrolysis process. The present thermodynamic analysis shows the key parameters to determine the atomic dispersion of metals and graphitization of porous carbons: oxidation/reduction based on Ellingham diagram, melting temperature of nanoparticles, phase diagram of boron oxide-metal oxide, synthesis (processing) temperature, etc. Based on the thermodynamic analysis, some new metallic elements can be screened and tested for experiments.

### **8.3.2. Development of new thermodynamic model for heteroatoms doped carbon materials**

In the present study, we found that thermodynamic calculations are very useful to understand the chemical reactions during chlorination process. However, one of limitations of the present calculation is a missing thermodynamic model and database to reproduce heteroatoms doped carbon. In all simulations in the present study, carbon as pure carbon was used in the calculation. Recently, C. Patrice and co-workers proposed a model to reproduce carbons containing S and H on the surface



of carbon layer. [8.4, 5] The same model can be further expanded to describe N and B doped carbon materials. Then, more proper thermodynamic simulations can be achieved and the chlorination process can be more accurately understood. In addition, if proper thermodynamic model are further developed to treat the nano-size effect, the more accurate thermodynamic analysis would be possible.

# Reference

- [1.1] A. Hirsch, The era of carbon allotropes, *Nat Mater*, 9 (2010) 868-871.
- [1.2] G. Speranza, The Role of Functionalization in the Applications of Carbon Materials: An Overview, *C — Journal of Carbon Research*, 5 (2019).
- [1.3] R. Raccichini, A. Varzi, S. Passerini, B. Scrosati, The role of graphene for electrochemical energy storage, *Nat Mater*, 14 (2015) 271-279.
- [1.4] Q. Wu, L. Yang, X. Wang, Z. Hu, Carbon-Based Nanocages: A New Platform for Advanced Energy Storage and Conversion, *Adv Mater*, (2019) e1904177.
- [1.5] H. Jiang, P.S. Lee, C. Li, 3D carbon based nanostructures for advanced supercapacitors, *Energy Environ. Sci.*, 6 (2013) 41-53.
- [1.6] Z.W. Seh, J. Kibsgaard, C.F. Dickens, I. Chorkendorff, J.K. Nørskov, T.F. Jaramillo, Combining theory and experiment in electrocatalysis: Insights into materials design, *Science*, 355 (2017).
- [1.7] M.R. Benziger, S.N. Talapaneni, S. Joseph, K. Ramadass, G. Singh, J. Scaranto, U. Ravon, K. Al-Bahily, A. Vinu, Recent advances in functionalized micro and mesoporous carbon materials: synthesis and applications, *Chem Soc Rev*, 47 (2018) 2680-2721.
- [1.8] J. Zhang, Z. Xia, L. Dai, Carbon-based electrocatalysts for advanced energy conversion and storage, *Science advances*, 1 (2015) e1500564.
- [1.9] D. Higgins, P. Zamani, A. Yu, Z. Chen, The application of graphene and its composites in oxygen reduction electrocatalysis: a perspective and review of recent progress, *Energy & Environmental Science*, 9 (2016) 357-390.
- [1.10] X. Liu, L. Dai, Carbon-based metal-free catalysts, *Nature Reviews Materials*, 1 (2016).
- [1.11] D. Voiry, H.S. Shin, K.P. Loh, M. Chhowalla, Low-dimensional catalysts for hydrogen evolution and CO<sub>2</sub> reduction, *Nature Reviews Chemistry*, 2 (2018).
- [1.12] J. Lee, J. Kim, T. Hyeon, Recent Progress in the Synthesis of Porous Carbon Materials, *Advanced Materials*, 18 (2006) 2073-2094.
- [1.13] R.J. White, V. Budarin, R. Luque, J.H. Clark, D.J. Macquarrie, Tuneable porous carbonaceous materials from renewable resources, *Chem Soc Rev*, 38 (2009) 3401-3418.
- [1.14] C. Hu, L. Dai, Carbon-Based Metal-Free Catalysts for Electrocatalysis beyond the ORR, *Angew Chem Int Ed Engl*, 55 (2016) 11736-11758.
- [1.15] M. Terrones, A.R. Botello-Méndez, J. Campos-Delgado, F. López-Urías, Y.I. Vega-Cantú, F.J. Rodríguez-Macías, A.L. Elías, E. Muñoz-Sandoval, A.G. Cano-Márquez, J.-C. Charlier, Graphene and graphite nanoribbons: Morphology, properties, synthesis, defects and applications, *Nano today*, 5 (2010) 351-372.
- [1.16] J. Tang, J. Liu, N.L. Torad, T. Kimura, Y. Yamauchi, Tailored design of functional nanoporous carbon materials toward fuel cell applications, *Nano Today*, 9 (2014) 305-323.
- [1.17] W. Xia, A. Mahmood, Z. Liang, R. Zou, S. Guo, Earth-Abundant Nanomaterials for Oxygen Reduction, *Angew Chem Int Ed Engl*, 55 (2016) 2650-2676.

- [1.18] L. Dai, Y. Xue, L. Qu, H.J. Choi, J.B. Baek, Metal-free catalysts for oxygen reduction reaction, *Chem Rev*, 115 (2015) 4823-4892.
- [1.19] E.P. Randviir, D.A.C. Brownson, C.E. Banks, A decade of graphene research: production, applications and outlook, *Materials Today*, 17 (2014) 426-432.
- [1.20] J. Masa, W. Xia, M. Muhler, W. Schuhmann, On the Role of Metals in Nitrogen-Doped Carbon Electrocatalysts for Oxygen Reduction, *Angew Chem Int Ed Engl*, 54 (2015) 10102-10120.
- [1.21] X. Huang, T. Shen, T. Zhang, H. Qiu, X. Gu, Z. Ali, Y. Hou, Efficient Oxygen Reduction Catalysts of Porous Carbon Nanostructures Decorated with Transition Metal Species, *Advanced Energy Materials*, 10 (2019).
- [1.22] R. Jasinski, A new fuel cell cathode catalyst, *Nature*, 201 (1964) 1212-1213.
- [1.23] H. Chen, F. Sun, J. Wang, W. Li, W. Qiao, L. Ling, D. Long, Nitrogen Doping Effects on the Physical and Chemical Properties of Mesoporous Carbons, *The Journal of Physical Chemistry C*, 117 (2013) 8318-8328.
- [1.24] J. Yu, M. Guo, F. Muhammad, A. Wang, F. Zhang, Q. Li, G. Zhu, One-pot synthesis of highly ordered nitrogen-containing mesoporous carbon with resorcinol-urea-formaldehyde resin for CO<sub>2</sub> capture, *Carbon*, 69 (2014) 502-514.
- [1.25] J. Wei, D. Zhou, Z. Sun, Y. Deng, Y. Xia, D. Zhao, A Controllable Synthesis of Rich Nitrogen-Doped Ordered Mesoporous Carbon for CO<sub>2</sub>Capture and Supercapacitors, *Advanced Functional Materials*, 23 (2013) 2322-2328.
- [1.26] M. Sevilla, P. Valle-Vigón, A.B. Fuertes, N-Doped Polypyrrole-Based Porous Carbons for CO<sub>2</sub>Capture, *Advanced Functional Materials*, 21 (2011) 2781-2787.
- [1.27] L. Lai, J.R. Potts, D. Zhan, L. Wang, C.K. Poh, C. Tang, H. Gong, Z. Shen, J. Lin, R.S. Ruoff, Exploration of the active center structure of nitrogen-doped graphene-based catalysts for oxygen reduction reaction, *Energy & Environmental Science*, 5 (2012).
- [1.28] S. Agnoli, M. Favaro, Doping graphene with boron: a review of synthesis methods, physicochemical characterization, and emerging applications, *Journal of Materials Chemistry A*, 4 (2016) 5002-5025.
- [1.29] D.-W. Wang, F. Li, Z.-G. Chen, G.Q. Lu, H.-M. Cheng, Synthesis and Electrochemical Property of Boron-Doped Mesoporous Carbon in Supercapacitor, *Chemistry of Materials*, 20 (2008) 7195-7200.
- [1.30] S. Ding, S. Zheng, M. Xie, L. Peng, X. Guo, W. Ding, One-pot synthesis of boron-doped mesoporous carbon with boric acid as a multifunction reagent, *Microporous and Mesoporous Materials*, 142 (2011) 609-613.
- [1.31] N. kumar, K. Moses, K. Pramoda, S.N. Shirodkar, A.K. Mishra, U.V. Waghmare, A. Sundaresan, C.N.R. Rao, Borocarbonitrides, BxCyNz, *Journal of Materials Chemistry A*, 1 (2013).
- [1.32] L. Song, Z. Liu, A.L. Reddy, N.T. Narayanan, J. Taha-Tijerina, J. Peng, G. Gao, J. Lou, R. Vajtai, P.M. Ajayan, Binary and ternary atomic layers built from carbon, boron, and nitrogen, *Adv Mater*, 24 (2012) 4878-4895.

- [1.33] Y. Zhao, L. Yang, S. Chen, X. Wang, Y. Ma, Q. Wu, Y. Jiang, W. Qian, Z. Hu, Can boron and nitrogen co-doping improve oxygen reduction reaction activity of carbon nanotubes?, *J Am Chem Soc*, 135 (2013) 1201-1204.
- [1.34] J. da Rocha Martins, H. Chacham, Disorder and segregation in B–C–N graphene-type layers and nanotubes: tuning the band gap, *Acs Nano*, 5 (2011) 385-393.
- [1.35] T. Schiros, D. Nordlund, L. Palova, L. Zhao, M. Levendorf, C. Jaye, D. Reichman, J. Park, M. Hybertsen, A. Pasupathy, Atomistic Interrogation of B-N Co-dopant Structures and Their Electronic Effects in Graphene, *ACS Nano*, 10 (2016) 6574-6584.
- [1.36] S. Beniwal, J. Hooper, D.P. Miller, P.S. Costa, G. Chen, S.Y. Liu, P.A. Dowben, E.C. Sykes, E. Zurek, A. Enders, Graphene-like Boron-Carbon-Nitrogen Monolayers, *ACS Nano*, 11 (2017) 2486-2493.
- [1.37] C.N.R. Rao, K. Gopalakrishnan, Borocarbonitrides, BxCyNz: Synthesis, Characterization, and Properties with Potential Applications, *ACS Appl Mater Interfaces*, 9 (2017) 19478-19494.
- [1.38] G. Wu, P. Zelenay, Nanostructured nonprecious metal catalysts for oxygen reduction reaction, *Accounts of chemical research*, 46 (2013) 1878-1889.
- [1.39] Y. Liang, Y. Li, H. Wang, H. Dai, Strongly coupled inorganic/nanocarbon hybrid materials for advanced electrocatalysis, *J Am Chem Soc*, 135 (2013) 2013-2036.
- [1.40] X.-F. Yang, A. Wang, B. Qiao, J. Li, J. Liu, T. Zhang, Single-atom catalysts: a new frontier in heterogeneous catalysis, *Accounts of chemical research*, 46 (2013) 1740-1748.
- [1.41] C. Zhu, S. Fu, Q. Shi, D. Du, Y. Lin, Single-Atom Electrocatalysts, *Angew Chem Int Ed Engl*, 56 (2017) 13944-13960.
- [1.42] H. Zhang, G. Liu, L. Shi, J. Ye, Single-Atom Catalysts: Emerging Multifunctional Materials in Heterogeneous Catalysis, *Advanced Energy Materials*, 8 (2018).
- [1.43] C. Wan, Y.N. Regmi, B.M. Leonard, Multiple phases of molybdenum carbide as electrocatalysts for the hydrogen evolution reaction, *Angew Chem Int Ed Engl*, 53 (2014) 6407-6410.
- [1.44] X. Fan, Z. Peng, R. Ye, H. Zhou, X. Guo, M3C (M: Fe, Co, Ni) nanocrystals encased in graphene nanoribbons: an active and stable bifunctional electrocatalyst for oxygen reduction and hydrogen evolution reactions, *ACS nano*, 9 (2015) 7407-7418.
- [1.45] W.J. Jiang, L. Gu, L. Li, Y. Zhang, X. Zhang, L.J. Zhang, J.Q. Wang, J.S. Hu, Z. Wei, L.J. Wan, Understanding the High Activity of Fe-N-C Electrocatalysts in Oxygen Reduction: Fe/Fe3C Nanoparticles Boost the Activity of Fe-N(x), *J Am Chem Soc*, 138 (2016) 3570-3578.
- [1.46] C. Zhu, H. Li, S. Fu, D. Du, Y. Lin, Highly efficient nonprecious metal catalysts towards oxygen reduction reaction based on three-dimensional porous carbon nanostructures, *Chem Soc Rev*, 45 (2016) 517-531.
- [1.47] L. Zhao, Y. Zhang, L.B. Huang, X.Z. Liu, Q.H. Zhang, C. He, Z.Y. Wu, L.J. Zhang, J. Wu, W. Yang, L. Gu, J.S. Hu, L.J. Wan, Cascade anchoring strategy for general mass production of high-loading single-atomic metal-nitrogen catalysts, *Nat Commun*, 10 (2019) 1278.

- [1.48] G. Wu, K.L. More, C.M. Johnston, P. Zelenay, High-performance electrocatalysts for oxygen reduction derived from polyaniline, iron, and cobalt, *Science*, 332 (2011) 443-447.
- [1.49] L. Lin, Q. Zhu, A.W. Xu, Noble-metal-free Fe-N/C catalyst for highly efficient oxygen reduction reaction under both alkaline and acidic conditions, *J Am Chem Soc*, 136 (2014) 11027-11033.
- [1.50] Y.J. Sa, D.J. Seo, J. Woo, J.T. Lim, J.Y. Cheon, S.Y. Yang, J.M. Lee, D. Kang, T.J. Shin, H.S. Shin, H.Y. Jeong, C.S. Kim, M.G. Kim, T.Y. Kim, S.H. Joo, A General Approach to Preferential Formation of Active Fe-N<sub>x</sub> Sites in Fe-N/C Electrocatalysts for Efficient Oxygen Reduction Reaction, *J Am Chem Soc*, 138 (2016) 15046-15056.
- [1.51] G.A. Ferrero, K. Preuss, A. Marinovic, A.B. Jorge, N. Mansor, D.J. Brett, A.B. Fuertes, M. Sevilla, M.M. Titirici, Fe-N-Doped Carbon Capsules with Outstanding Electrochemical Performance and Stability for the Oxygen Reduction Reaction in Both Acid and Alkaline Conditions, *ACS Nano*, 10 (2016) 5922-5932.
- [1.52] A. Zitolo, N. Ranjbar-Sahraie, T. Mineva, J. Li, Q. Jia, S. Stamatina, G.F. Harrington, S.M. Lyth, P. Krtić, S. Mukerjee, E. Fonda, F. Jaouen, Identification of catalytic sites in cobalt-nitrogen-carbon materials for the oxygen reduction reaction, *Nat Commun*, 8 (2017) 957.
- [1.53] R. Jiang, L. Li, T. Sheng, G. Hu, Y. Chen, L. Wang, Edge-Site Engineering of Atomically Dispersed Fe-N<sub>4</sub> by Selective C-N Bond Cleavage for Enhanced Oxygen Reduction Reaction Activities, *J Am Chem Soc*, 140 (2018) 11594-11598.
- [1.54] W. Chen, J. Pei, C.T. He, J. Wan, H. Ren, Y. Zhu, Y. Wang, J. Dong, S. Tian, W.C. Cheong, S. Lu, L. Zheng, X. Zheng, W. Yan, Z. Zhuang, C. Chen, Q. Peng, D. Wang, Y. Li, Rational Design of Single Molybdenum Atoms Anchored on N-Doped Carbon for Effective Hydrogen Evolution Reaction, *Angew Chem Int Ed Engl*, 56 (2017) 16086-16090.
- [1.55] L. Cao, Q. Luo, W. Liu, Y. Lin, X. Liu, Y. Cao, W. Zhang, Y. Wu, J. Yang, T. Yao, S. Wei, Identification of single-atom active sites in carbon-based cobalt catalysts during electrocatalytic hydrogen evolution, *Nature Catalysis*, 2 (2018) 134-141.
- [1.56] C. Lei, Y. Wang, Y. Hou, P. Liu, J. Yang, T. Zhang, X. Zhuang, M. Chen, B. Yang, L. Lei, C. Yuan, M. Qiu, X. Feng, Efficient alkaline hydrogen evolution on atomically dispersed Ni-N<sub>x</sub> Species anchored porous carbon with embedded Ni nanoparticles by accelerating water dissociation kinetics, *Energy & Environmental Science*, 12 (2019) 149-156.
- [1.57] X. Li, W. Bi, M. Chen, Y. Sun, H. Ju, W. Yan, J. Zhu, X. Wu, W. Chu, C. Wu, Y. Xie, Exclusive Ni-N<sub>4</sub> Sites Realize Near-Unity CO Selectivity for Electrochemical CO<sub>2</sub> Reduction, *J Am Chem Soc*, 139 (2017) 14889-14892.
- [1.58] C. Zhao, X. Dai, T. Yao, W. Chen, X. Wang, J. Wang, J. Yang, S. Wei, Y. Wu, Y. Li, Ionic Exchange of Metal-Organic Frameworks to Access Single Nickel Sites for Efficient Electroreduction of CO<sub>2</sub>, *J Am Chem Soc*, 139 (2017) 8078-8081.
- [1.59] W. Ju, A. Bagger, G.P. Hao, A.S. Varela, I. Sinev, V. Bon, B. Roldan Cuenya, S. Kaskel, J. Rossmeisl, P. Strasser, Understanding activity and selectivity of metal-nitrogen-doped carbon catalysts for electrochemical reduction of CO<sub>2</sub>, *Nat Commun*, 8 (2017) 944.

- [1.60] F. Yang, P. Song, X. Liu, B. Mei, W. Xing, Z. Jiang, L. Gu, W. Xu, Highly Efficient CO<sub>2</sub> Electroreduction on ZnN<sub>4</sub>-based Single-Atom Catalyst, *Angew Chem Int Ed Engl*, 57 (2018) 12303-12307.
- [1.61] F. Pan, H. Zhang, K. Liu, D. Cullen, K. More, M. Wang, Z. Feng, G. Wang, G. Wu, Y. Li, Unveiling Active Sites of CO<sub>2</sub> Reduction on Nitrogen-Coordinated and Atomically Dispersed Iron and Cobalt Catalysts, *ACS Catalysis*, 8 (2018) 3116-3122.
- [1.62] J.P. Paraknowitsch, A. Thomas, Doping carbons beyond nitrogen: an overview of advanced heteroatom doped carbons with boron, sulphur and phosphorus for energy applications, *Energy & Environmental Science*, 6 (2013).
- [1.63] H. Cui, Y. Guo, L. Guo, L. Wang, Z. Zhou, Z. Peng, Heteroatom-doped carbon materials and their composites as electrocatalysts for CO<sub>2</sub> reduction, *Journal of Materials Chemistry A*, 6 (2018) 18782-18793.
- [1.64] M. Chen, Y. He, J.S. Spendelow, G. Wu, Atomically Dispersed Metal Catalysts for Oxygen Reduction, *ACS Energy Letters*, 4 (2019) 1619-1633.
- [1.65] C. Tang, Q. Zhang, Nanocarbon for Oxygen Reduction Electrocatalysis: Dopants, Edges, and Defects, *Adv Mater*, 29 (2017).
- [1.66] A. Öya, H. Marsh, Phenomena of catalytic graphitization, *Journal of Materials Science*, 17 (1982) 309-322.
- [1.67] F. Maldonado-Hódar, C. Moreno-Castilla, J. Rivera-Utrilla, Y. Hanzawa, Y. Yamada, Catalytic graphitization of carbon aerogels by transition metals, *Langmuir*, 16 (2000) 4367-4373.
- [1.68] A.G. Nasibulin, A. Moisala, D.P. Brown, E.I. Kauppinen, Carbon nanotubes and onions from carbon monoxide using Ni(acac)<sub>2</sub> and Cu(acac)<sub>2</sub> as catalyst precursors, *Carbon*, 41 (2003) 2711-2724.
- [1.69] D.H.Nam, Phase and structure control of metal compound and carbon hybrid nanofibers using thermodynamic redox reaction, Ph.D, thesis, Seoul national university, 2017.
- [1.70] V. Presser, M. Heon, Y. Gogotsi, Carbide-Derived Carbons - From Porous Networks to Nanotubes and Graphene, *Advanced Functional Materials*, 21 (2011) 810-833..
- [1.71] Y. Gogotsi, A. Nikitin, H. Ye, W. Zhou, J.E. Fischer, B. Yi, H.C. Foley, M.W. Barsoum, Nanoporous carbide-derived carbon with tunable pore size, *Nat Mater*, 2 (2003) 591-594.
- [1.72] G. Yushin, R. Dash, J. Jagiello, J.E. Fischer, Y. Gogotsi, Carbide-Derived Carbons: Effect of Pore Size on Hydrogen Uptake and Heat of Adsorption, *Advanced Functional Materials*, 16 (2006) 2288-2293
- [1.73] V. Presser, J. McDonough, S.-H. Yeon, Y. Gogotsi, Effect of pore size on carbon dioxide sorption by carbide derived carbon, *Energy & Environmental Science*, 4 (2011).
- [1.74] S. Porada, L. Borchardt, M. Oschatz, M. Bryjak, J.S. Atchison, K.J. Keesman, S. Kaskel, P.M. Biesheuvel, V. Presser, Direct prediction of the desalination performance of porous carbon electrodes for capacitive deionization, *Energy & Environmental Science*, 6 (2013).
- [1.75] J. Kortus, I. Mazin, K.D. Belashchenko, V.P. Antropov, L. Boyer, Superconductivity of metallic boron in MgB<sub>2</sub>, *Physical Review Letters*, 86 (2001) 4656.

- [1.76] T. Martins, R.d. Miwa, A.J. Da Silva, A. Fazzio, Electronic and transport properties of boron-doped graphene nanoribbons, *Physical review letters*, 98 (2007) 196803.
- [1.77] A.J. Mannix, X.-F. Zhou, B. Kiraly, J.D. Wood, D. Alducin, B.D. Myers, X. Liu, B.L. Fisher, U. Santiago, J.R. Guest, Synthesis of borophenes: Anisotropic, two-dimensional boron polymorphs, *Science*, 350 (2015) 1513-1516.
- [1.78] X. Wang, G.-H. Ma, W. Zhu, J. Glass, L. Bergman, K. Turner, R. Nemanich, Effects of boron doping on the surface morphology and structural imperfections of diamond films, *Diamond and Related Materials*, 1 (1992) 828-835.
- [1.79] M. Endo, H. Muramatsu, T. Hayashi, Y.-A. Kim, G.V. Lier, J.-C. Charlier, H. Terrones, M. Terrones, M.S. Dresselhaus, Atomic nanotube welders: boron interstitials triggering connections in double-walled carbon nanotubes, *Nano letters*, 5 (2005) 1099-1105.
- [1.80] Y. Waseda, H. Chen, A structural study of metallic glasses containing boron (Fe-B, Co-B, and Ni-B), *Physica status solidi (a)*, 49 (1978) 387-392.
- [1.81] K. Yuan, S. Sfaelou, M. Qiu, D. Lützenkirchen-Hecht, X. Zhuang, Y. Chen, C. Yuan, X. Feng, U. Scherf, Synergetic Contribution of Boron and Fe-Nx Species in Porous Carbons toward Efficient Electrocatalysts for Oxygen Reduction Reaction, *ACS Energy Letters*, 3 (2017) 252-260.
- [1.82] Y. Guo, P. Yuan, J. Zhang, Y. Hu, I.S. Amiinu, X. Wang, J. Zhou, H. Xia, Z. Song, Q. Xu, S. Mu, Carbon Nanosheets Containing Discrete Co-Nx-By-C Active Sites for Efficient Oxygen Electrocatalysis and Rechargeable Zn-Air Batteries, *ACS Nano*, 12 (2018) 1894-1901.
- [1.83] S. Kang, Y. Mo, S.P. Ong, G. Ceder, Nanoscale Stabilization of Sodium Oxides: Implications for Na-O<sub>2</sub> Batteries, *Nano Letter*, 2014, 14, 1016
- [1.84] W. Sun, S. Jayaraman, W. Chen, K. A. Persson, G. Ceder, Nucleation of metastable aragonite CaCO<sub>3</sub> in seawater, *Proceedings of the National Academy of Sciences of the United States of America*, 2015, 112, 3199
- [1.85] L. Shi, A. Xu, T.S. Zhao, Formation of Li<sub>3</sub>PO<sub>4</sub> nano particles in the discharge products of non-aqueous lithium-oxygen batteries leads to lower charge overvoltage, *Physical Chemistry Chemical Physics*. 2015, 17, 29859.
- [1.86] D.H. Nam, S. Lee, Y.J Lee, J.H Jo, E. Yoon, Gaseous Nanocarving-Mediated Carbon Framework with Spontaneous Metal Assembly for Structure-Tunable Metal/Carbon Nanofibers, *Advanced materials*, 2017, 29, 1702958.
- [1.87] <https://meijo-nano.com/en/applications/use.html>
- [2.1] V. Presser, M. Heon, Y. Gogotsi, Carbide-derived carbons—from porous networks to nanotubes and graphene, *Advanced Functional Materials*, 21 (2011) 810-833.
- [2.2] Z. Cambaz, G. Yushin, Y. Gogotsi, K. Vyshnyakova, L. Pereselensteva, Formation of Carbide-Derived Carbon on  $\beta$ -Silicon Carbide Whiskers, *Journal of the American Ceramic Society*, 89 (2006) 509-514.
- [2.3] J. Chmiola, G. Yushin, R. Dash, Y. Gogotsi, Effect of pore size and surface area of carbide derived carbons on specific capacitance, *Journal of Power Sources*, 158 (2006) 765-772.

- [2.4] G. Yushin, R. Dash, J. Jagiello, J.E. Fischer, Y. Gogotsi, Carbide-Derived Carbons: Effect of Pore Size on Hydrogen Uptake and Heat of Adsorption, *Advanced Functional Materials*, 16 (2006) 2288-2293.
- [2.5] J. Chmiola, G. Yushin, Y. Gogotsi, C. Portet, P. Simon, P.-L. Taberna, Anomalous increase in carbon capacitance at pore sizes less than 1 nanometer, *science*, 313 (2006) 1760-1763.
- [2.6] V. Presser, J. McDonough, S.-H. Yeon, Y. Gogotsi, Effect of pore size on carbon dioxide sorption by carbide derived carbon, *Energy & Environmental Science*, 4 (2011).
- [2.7] J. Chmiola, C. Largeot, P.-L. Taberna, P. Simon, Y. Gogotsi, Monolithic carbide-derived carbon films for micro-supercapacitors, *science*, 328 (2010) 480-483.
- [2.8] S. Porada, L. Borchardt, M. Oschatz, M. Bryjak, J. Atchison, K. Keesman, S. Kaskel, P. Biesheuvel, V. Presser, Direct prediction of the desalination performance of porous carbon electrodes for capacitive deionization, *Energy & Environmental Science*, 6 (2013) 3700-3712.
- [2.9] P. Huang, C. Lethien, S. Pinaud, K. Brousse, R. Laloo, V. Turq, M. Respaud, A. Demortiere, B. Daffos, P.-L. Taberna, On-chip and freestanding elastic carbon films for micro-supercapacitors, *Science*, 351 (2016) 691-695.
- [2.10] O. Hutchins, Method for the production of silicon tetrachlorid, *Google Patents*, 1918.
- [2.11] J. Leis, A. Perkson, M. Arulepp, M. Käärrik, G. Svensson, Carbon nanostructures produced by chlorinating aluminium carbide, *Carbon*, 39 (2001) 2043-2048.
- [2.12] R. Dash, A. Nikitin, Y. Gogotsi, Microporous carbon derived from boron carbide, *Microporous and Mesoporous Materials*, 72 (2004) 203-208.
- [2.13] E.N. Hoffman, G. Yushin, M.W. Barsoum, Y. Gogotsi, Synthesis of carbide-derived carbon by chlorination of  $Ti_2AlC$ , *Chemistry of materials*, 17 (2005) 2317-2322.
- [2.14] E.N. Hoffman, G. Yushin, T. El-Raghy, Y. Gogotsi, M.W. Barsoum, Micro and mesoporosity of carbon derived from ternary and binary metal carbides, *Microporous and Mesoporous Materials*, 112 (2008) 526-532.
- [2.15] T. Nguyen, J.-S. Bae, S. Bhatia, Characterization and adsorption modeling of silicon carbide-derived carbons, *Langmuir*, 25 (2009) 2121-2132.
- [2.16] A. Jänes, H. Kurig, E. Lust, Characterisation of activated nanoporous carbon for supercapacitor electrode materials, *Carbon*, 45 (2007) 1226-1233.
- [2.17] B. Carroll, Y. Gogotsi, A. Kovalchenko, A. Erdemir, M. McNallan, Effect of humidity on the tribological properties of carbide-derived carbon (CDC) films on silicon carbide, *Tribology Letters*, 15 (2003) 51-55.
- [2.18] H. Wang, Q. Gao, Synthesis, characterization and energy-related applications of carbide-derived carbons obtained by the chlorination of boron carbide, *Carbon*, 47 (2009) 820-828.
- [2.19] C.R. Pérez, S.-H. Yeon, J. Ségalini, V. Presser, P.-L. Taberna, P. Simon, Y. Gogotsi, Structure and Electrochemical Performance of Carbide-Derived Carbon Nanopowders, *Advanced Functional Materials*, 23 (2013) 1081-1089.
- [2.20] Y. Xiong, Y. Xie, X. Li, Z. Li, Production of novel amorphous carbon nanostructures from ferrocene in low-temperature solution, *Carbon*, 42 (2004) 1447-1453.



- [2.21] T. Kyotani, J. Chmiola, Y. Gogotsi, *Carbon Materials for Electrochemical Energy Storage Systems*, CRC Press/Taylor and Francis, 2009.
- [2.22] G. Yushin, A. Nikitin, Y. Gogotsi, *Carbon Nanomaterials*, Gogotsi (ed.) CRC Taylor & Francis, (2006) 211-254.
- [2.23] A. Kravchik, J.A. Kukushkina, V. Sokolov, G. Tereshchenko, Structure of nanoporous carbon produced from boron carbide, *Carbon*, 44 (2006) 3263-3268.
- [2.24] T. Thomberg, A. Jänes, E. Lust, Energy and power performance of electrochemical double-layer capacitors based on molybdenum carbide derived carbon, *Electrochimica acta*, 55 (2010) 3138-3143.
- [2.25] J. Xu, R. Zhang, P. Chen, D. Shen, X. Ye, S. Ge, Mechanism of formation and electrochemical performance of carbide-derived carbons obtained from different carbides, *Carbon*, 64 (2013) 444-455.
- [2.26] A. Jänes, T. Thomberg, E. Lust, Synthesis and characterisation of nanoporous carbide-derived carbon by chlorination of vanadium carbide, *Carbon*, 45 (2007) 2717-2722.
- [2.27] S. Gordeev, S. Kukushkin, A. Osipov, Y.V. Pavlov, Self-organization in the formation of a nanoporous carbon material, *Physics of the Solid State*, 42 (2000) 2314-2317.
- [2.28] Y. Gogotsi, A. Nikitin, H. Ye, W. Zhou, J.E. Fischer, B. Yi, H.C. Foley, M.W. Barsoum, Nanoporous carbide-derived carbon with tunable pore size, *Nature materials*, 2 (2003) 591-594.
- [2.29] R. Dash, J. Chmiola, G. Yushin, Y. Gogotsi, G. Laudisio, J. Singer, J. Fischer, S. Kucheyev, Titanium carbide derived nanoporous carbon for energy-related applications, *Carbon*, 44 (2006) 2489-2497.
- [2.30] C. de Tomas, I. Suarez-Martinez, F. Vallejos-Burgos, M.J. López, K. Kaneko, N.A. Marks, Structural prediction of graphitization and porosity in carbide-derived carbons, *Carbon*, 119 (2017) 1-9.
- [2.31] M.S. Seo, J.H. Kim, J.M. Kim, J.S. Han, S. Kang, J.S. Ihm, D.O. Kim, Tunable and selective formation of micropores and mesopores in carbide-derived carbon, *Carbon*, 60 (2013) 299-306.
- [2.32] M.K. Lee, Nitrogen-doped carbon produced by chlorination process of Ti (C, N) and its electrochemical properties, Ph.D. thesis, Seoul national university, 2019.
- [2.33] J. Han, S. Lee, K. Choi, J. Kim, D. Ha, C.G. Lee, B. An, S.H. Lee, H. Mizuseki, J.W. Choi, S. Kang, Effect of nitrogen doping on titanium carbonitride-derived adsorbents used for arsenic removal, *J Hazard Mater*, 302 (2016) 375-385.
- [2.34] J. Kim, J. Han, D. Ha, S. Kang, Synthesis of nitrogen and boron co-doped carbon (CNB) and their CO<sub>2</sub> capture properties: from porous to hollow granule structure, *J. Mater. Chem. A*, 2 (2014) 16645-16651.
- [2.35] J.-S. Han, D.Y. Chung, D.-G. Ha, J.-H. Kim, K. Choi, Y.-E. Sung, S.-H. Kang, Nitrogen and boron co-doped hollow carbon catalyst for the oxygen reduction reaction, *Carbon*, 105 (2016) 1-7.

- [2.36] L. Dai, Y. Xue, L. Qu, H.J. Choi, J.B. Baek, Metal-free catalysts for oxygen reduction reaction, *Chem Rev*, 115 (2015) 4823-4892.
- [2.37] S. Agnoli, M. Favaro, Doping graphene with boron: a review of synthesis methods, physicochemical characterization, and emerging applications, *Journal of Materials Chemistry A*, 4 (2016) 5002-5025.
- [2.38] C. Lowell, Solid solution of boron in graphite, *Journal of the American Ceramic Society*, 50 (1967) 142-144.
- [2.39] R. Faccio, L. Fernández-Werner, H. Pardo, C. Goyenola, O.N. Ventura, Á.W. Mombrú, Electronic and structural distortions in graphene induced by carbon vacancies and boron doping, *The Journal of Physical Chemistry C*, 114 (2010) 18961-18971.
- [2.40] X. Blase, J.-C. Charlier, A. De Vita, R. Car, P. Redlich, M. Terrones, W. Hsu, H. Terrones, D. Carroll, P. Ajayan, Boron-mediated growth of long helicity-selected carbon nanotubes, *Physical Review Letters*, 83 (1999) 5078.
- [2.41] M. Endo, H. Muramatsu, T. Hayashi, Y.-A. Kim, G.V. Lier, J.-C. Charlier, H. Terrones, M. Terrones, M.S. Dresselhaus, Atomic nanotube welders: boron interstitials triggering connections in double-walled carbon nanotubes, *Nano letters*, 5 (2005) 1099-1105.
- [2.42] D.P. Hashim, N.T. Narayanan, J.M. Romo-Herrera, D.A. Cullen, M.G. Hahm, P. Lezzi, J.R. Suttle, D. Kelkhoff, E. Munoz-Sandoval, S. Ganguli, A.K. Roy, D.J. Smith, R. Vajtai, B.G. Sumpter, V. Meunier, H. Terrones, M. Terrones, P.M. Ajayan, Covalently bonded three-dimensional carbon nanotube solids via boron induced nanojunctions, *Sci Rep*, 2 (2012) 363.
- [2.43] H. Muramatsu, T. Hayashi, K. Fujisawa, T. Tojo, Y.-I. Ko, A. Morelos-Gomez, K.-S. Yang, Y.A. Kim, M. Endo, M. Terrones, M.S. Dresselhaus, Boron-assisted coalescence of parallel multi-walled carbon nanotubes, *RSC Advances*, 3 (2013).
- [2.44] J. Bernholc, A. Antonelli, T.M. Del Sole, Y. Bar-Yam, S.T. Pantelides, Mechanism of self-diffusion in diamond, *Phys Rev Lett*, 61 (1988) 2689-2692.
- [2.45] A. Ōya, R. Yamashita, S. Ōtani, Catalytic graphitization of carbons by borons, *Fuel*, 58 (1979) 495-500.
- [2.46] J.-C. Pu, S.-F. Wang, C.-L. Lin, J.C. Sung, Characterization of boron-doped diamond-like carbon prepared by radio frequency sputtering, *Thin Solid Films*, 519 (2010) 521-526.
- [2.47] Y. Jeong, T.C. Mike Chung, The synthesis and characterization of a super-activated carbon containing substitutional boron (BCx) and its applications in hydrogen storage, *Carbon*, 48 (2010) 2526-2537.
- [2.48] L. Song, Z. Liu, A.L. Reddy, N.T. Narayanan, J. Taha-Tijerina, J. Peng, G. Gao, J. Lou, R. Vajtai, P.M. Ajayan, Binary and ternary atomic layers built from carbon, boron, and nitrogen, *Adv Mater*, 24 (2012) 4878-4895.
- [2.49] N. kumar, K. Moses, K. Pramoda, S.N. Shirodkar, A.K. Mishra, U.V. Waghmare, A. Sundaresan, C.N.R. Rao, Borocarbonitrides, BxCyNz, *Journal of Materials Chemistry A*, 1 (2013).

- [2.50] K.S. Novoselov, A.K. Geim, S.V. Morozov, D. Jiang, Y. Zhang, S.V. Dubonos, I.V. Grigorieva, A.A. Firsov, Electric field effect in atomically thin carbon films, *science*, 306 (2004) 666-669.
- [2.51] X. Blase, A. Rubio, S.G. Louie, M.L. Cohen, Quasiparticle band structure of bulk hexagonal boron nitride and related systems, *Phys Rev B Condens Matter*, 51 (1995) 6868-6875.
- [2.52] L. Song, L. Ci, H. Lu, P.B. Sorokin, C. Jin, J. Ni, A.G. Kvashnin, D.G. Kvashnin, J. Lou, B.I. Yakobson, P.M. Ajayan, Large scale growth and characterization of atomic hexagonal boron nitride layers, *Nano Lett*, 10 (2010) 3209-3215.
- [2.53] W. Liu, Z.F. Wang, Q.W. Shi, J. Yang, F. Liu, Band-gap scaling of graphene nanohole superlattices, *Physical Review B*, 80 (2009).
- [2.54] J. Bai, X. Zhong, S. Jiang, Y. Huang, X. Duan, Graphene nanomesh, *Nat Nanotechnol*, 5 (2010) 190-194.
- [2.55] R. Balog, B. Jorgensen, L. Nilsson, M. Andersen, E. Rienks, M. Bianchi, M. Fanetti, E. Laegsgaard, A. Baraldi, S. Lizzit, Z. Slijivancanin, F. Besenbacher, B. Hammer, T.G. Pedersen, P. Hofmann, L. Hornekaer, Bandgap opening in graphene induced by patterned hydrogen adsorption, *Nat Mater*, 9 (2010) 315-319.
- [2.56] M. Kawaguchi, B/C/N materials based on the graphite network, *Advanced Materials*, 9 (1997) 615-625.
- [2.57] J. Wu, M.T. Rodrigues, R. Vajtai, P.M. Ajayan, Tuning the Electrochemical Reactivity of Boron- and Nitrogen-Substituted Graphene, *Adv Mater*, 28 (2016) 6239-6246.
- [2.58] C.N.R. Rao, K. Gopalakrishnan, Borocarbonitrides, BxCyNz: Synthesis, Characterization, and Properties with Potential Applications, *ACS Appl Mater Interfaces*, 9 (2017) 19478-19494.
- [2.59] S. Wang, F. Ma, H. Jiang, Y. Shao, Y. Wu, X. Hao, Band gap-Tunable Porous Borocarbonitride Nanosheets for High Energy-Density Supercapacitors, *ACS Appl Mater Interfaces*, 10 (2018) 19588-19597.
- [2.60] S. Wang, E. Iyyamperumal, A. Roy, Y. Xue, D. Yu, L. Dai, Vertically aligned BCN nanotubes as efficient metal-free electrocatalysts for the oxygen reduction reaction: a synergetic effect by co-doping with boron and nitrogen, *Angew Chem Int Ed Engl*, 50 (2011) 11756-11760.
- [2.61] S. Wang, L. Zhang, Z. Xia, A. Roy, D.W. Chang, J.B. Baek, L. Dai, BCN graphene as efficient metal-free electrocatalyst for the oxygen reduction reaction, *Angew Chem Int Ed Engl*, 51 (2012) 4209-4212.
- [2.62] C.N.R. Rao, M. Chhetri, Borocarbonitrides as Metal-Free Catalysts for the Hydrogen Evolution Reaction, *Adv Mater*, 31 (2019) e1803668.
- [2.63] R. Kaner, Boron-carbon-nitrogen materials of graphite-like structure, (1986).
- [2.64] Y. Goto, M. Sasaki, M. Hashizume, M. Suzuki, Synthesis of BCN ceramics from pyrrolidine-Borane complex, *Journal of the European Ceramic Society*, 19 (1999) 2695-2700.

- [2.65] L. Ci, L. Song, C. Jin, D. Jariwala, D. Wu, Y. Li, A. Srivastava, Z. Wang, K. Storr, L. Balicas, Atomic layers of hybridized boron nitride and graphene domains, *Nature materials*, 9 (2010) 430-435.
- [2.66] G.H. Han, J.A. Rodríguez-Manzo, C.-W. Lee, N.J. Kybert, M.B. Lerner, Z.J. Qi, E.N. Dattoli, A.M. Rappe, M. Drndic, A.C. Johnson, Continuous growth of hexagonal graphene and boron nitride in-plane heterostructures by atmospheric pressure chemical vapor deposition, *Acs Nano*, 7 (2013) 10129-10138.
- [2.67] Y. Gong, G. Shi, Z. Zhang, W. Zhou, J. Jung, W. Gao, L. Ma, Y. Yang, S. Yang, G. You, Direct chemical conversion of graphene to boron-and nitrogen-and carbon-containing atomic layers, *Nature communications*, 5 (2014) 1-8.
- [2.68] S. Dou, X. Huang, Z. Ma, J. Wu, S. Wang, A simple approach to the synthesis of BCN graphene with high capacitance, *Nanotechnology*, 26 (2015) 045402.
- [2.69] J. Wu, M.T.F. Rodrigues, R. Vajtai, P.M. Ajayan, Tuning the Electrochemical Reactivity of Boron-and Nitrogen-Substituted Graphene, *Advanced Materials*, 28 (2016) 6239-6246.
- [2.70] M. Barua, M. Sreedhara, K. Pramoda, C. Rao, Quantification of surface functionalities on graphene, boron nitride and borocarbonitrides by fluorescence labeling, *Chemical Physics Letters*, 683 (2017) 459-466.
- [2.71] J. Hao, J. Wang, S. Qin, D. Liu, Y. Li, W. Lei, B/N co-doped carbon nanosphere frameworks as high-performance electrodes for supercapacitors, *Journal of materials Chemistry A*, 6 (2018) 8053-8058.
- [2.72] D.-W. Kim, H.-S. Kil, J. Kim, I. Mochida, K. Nakabayashi, C.K. Rhee, J. Miyawaki, S.-H. Yoon, Highly graphitized carbon from non-graphitizable raw material and its formation mechanism based on domain theory, *Carbon*, 121 (2017) 301-308.
- [2.73] A.G. Nasibulin, A. Moisala, D.P. Brown, E.I. Kauppinen, Carbon nanotubes and onions from carbon monoxide using Ni(acac)<sub>2</sub> and Cu(acac)<sub>2</sub> as catalyst precursors, *Carbon*, 41 (2003) 2711-2724.
- [2.74] M. Zhao, H. Song, X. Chen, W. Lian, Large-scale synthesis of onion-like carbon nanoparticles by carbonization of phenolic resin, *Acta Materialia*, 55 (2007) 6144-6150.
- [2.75] C.T. Wirth, C. Zhang, G. Zhong, S. Hofmann, J. Robertson, Diffusion-and reaction-limited growth of carbon nanotube forests, *ACS nano*, 3 (2009) 3560-3566.
- [2.76] J.P. Tessonnier, D.S. Su, Recent progress on the growth mechanism of carbon nanotubes: a review, *ChemSusChem*, 4 (2011) 824-847.
- [2.77] A. Ōya, H. Marsh, Phenomena of catalytic graphitization, *Journal of Materials Science*, 17 (1982) 309-322.
- [2.78] E. Charon, J.N. Rouzaud, J. Aléon, Graphitization at low temperatures (600–1200°C) in the presence of iron implications in planetology, *Carbon*, 66 (2014) 178-190.
- [2.79] H. Rastegar, M. Bavand-vandchali, A. Nemati, F. Golestani-Fard, Catalytic graphitization behavior of phenolic resins by addition of in situ formed nano-Fe particles, *Physica E: Low-dimensional Systems and Nanostructures*, 101 (2018) 50-61.

- [2.80] A. Gorbunov, O. Jost, W. Pompe, A. Graff, Role of the catalyst particle size in the synthesis of single-wall carbon nanotubes, *Applied surface science*, 197 (2002) 563-567.
- [2.81] J.H. Boer, Dynamical character of adsorption, (1968).
- [2.82] K. Oura, V.G. Lifshits, A.A. Saranin, A.V. Zotov, M. Katayama, *Surface Science, An Introduction*. Springer, (2003).
- [2.83] K. Autumn, Y.A. Liang, S.T. Hsieh, W. Zesch, W.P Chan, T.W. Kenny, R. Fearing, R.J. Full, Adhesive force of a single gecko foot-hair, *Nature*, 405 (2000) 681-685.
- [2.84] M. Nič, J. Jirát, B. Košata, A. Jenkins, A. McNaught, *IUPAC compendium of chemical terminology*, IUPAC, Research Triangle Park, NC, (2009).
- [2.85] S. Urbonaitė, Synthesis and characterisation of carbide derived carbons, Department of Physical, Inorganic and Structural Chemistry, Stockholm University 2008.
- [2.86] K.S. Sing, Assessment of surface area by gas adsorption, *Adsorption by Powders and Porous Solids: Principles, Methodology and Applications*, (2013) 237-263.
- [2.87] Q. Huo, D.I. Margolese, G.D. Stucky, Surfactant control of phases in the synthesis of mesoporous silica-based materials, *Chemistry of Materials*, 8 (1996) 1147-1160.
- [2.88] M. Kruk, M. Jaroniec, A. Sayari, Application of large pore MCM-41 molecular sieves to improve pore size analysis using nitrogen adsorption measurements, *Langmuir*, 13 (1997) 6267-6273.
- [2.89] G. Mason, The effect of pore space connectivity on the hysteresis of capillary condensation in adsorption—desorption isotherms, *Journal of Colloid and Interface Science*, 88 (1982) 36-46.
- [2.90] M. Thommes, K. Kaneko, A.V. Neimark, J.P. Oliver, F. Rodriguez-Reinoso, J. Rouquerol, K.W. sing, *Pure and Applied Chemistry*, 87(9-10) (2015) 1051-1069.
- [2.91] M. Kruk, M. Jaroniec, Gas adsorption characterization of ordered organic– inorganic nanocomposite materials, *Chemistry of materials*, 13 (2001) 3169-3183.
- [2.92] 오승모, 전기화학, 자유아카데미, 2014.
- [2.93] A.J Bard, L.R Faulkner, *Electrochemical methods, fundamentals and applications*, Wiley & Sons, Inc., New York, NY.
- [2.94] D. Yu, E. Nagelli, F. Du, and L. Dai, Metal-Free Carbon Nanomaterials Become More Active than Metal Catalysts and Last Longer, *The Journal of Physical Chemistry Letters*, 2010, 1, 14, 2165–2173.
- [2.95] J. Zhang *PEM Fuel Cell Electrocatalysts and Catalyst Layers*, Springer, 2008.
- [2.96] W. Xia, Z. Liang, R. Zou, S. Guo, *Earth-Abundant Nanomaterials for Oxygen Reduction*, *Angewandte chemie International edition*, 55 (2016) 2650-2676.
- [2.97] J. K. Nørskov, J. Rossmeisl, A. Logadottir, L. Lindqvist, J. R. Kitchin, T. Bligaard, and H. Jónsson, Origin of the Overpotential for Oxygen Reduction at a Fuel-Cell Cathode, *The Journal of Physical Chemistry*, 108, 46, (2004) 17886–17892.
- [2.98] Dynamical character of adsorption B.HammerJ.K.Nørskov *Theoretical surface science and catalysis—calculations and concepts*, *Advances in Catalysis*, 45, 2000, 71-129.

- [2.99] J. K. Nørskov, T. Bligaard, J. Rossmeisl & C. H. Christensen, Towards the computational design of solid catalysts, *Nature Chemistry*, 1, (2009), 37–46.
- [2.100] Z.W. She, J. Kibsgaard, C.F. Dickens, I. Chorkendorff, J.K. Nørskov, T.F. Jaramillo, Combining theory and experiment in electrocatalysis: Insights into materials design, *Science*, 355, 146, (2017).
- [2.101] Y. Jiao, Y. Zheng, M. Jaroniec, S. Z. Qiao, Origin of the Electrocatalytic Oxygen Reduction Activity of Graphene-Based Catalysts: A Roadmap to Achieve the Best Performance, *Journal of the American Chemical Society*, 136, 11, (2014), 4394–4403.
- [2.102] D.R. Gaskell, D.E. Laughlin, *Introduction to the Thermodynamics of Materials*, CRC press, 2017.
- [2.103] D.A. Porter, K.E. Easterling, *Phase transformations in metals and alloys*, CRC press, 2009.
- [2.104] Kaptay, George. ‘The chemical (not mechanical) paradigm of thermodynamics of colloid and interface science’, *Advances in colloid and interface science*, 256, (2018), 163-192.
- [2.105] Guthrie, Roderick IL, and T. Iida, *The physical properties of liquid metals*, Clarendon press, 1987.
- [3.1] Kaptay, George. "The chemical (not mechanical) paradigm of thermodynamics of colloid and interface science." *Advances in colloid and interface science* 256 (2018): 163-192.
- [3.2] Guthrie, Roderick IL, and T. Iida. *The physical properties of liquid metals*. Clarendon press, 1987.
- [3.3] Hillert, Mats. "The compound energy formalism." *Journal of Alloys and Compounds* 320.2 (2001): 161-176.
- [4.1] J.P. Paraknowitsch, A. Thomas, Doping carbons beyond nitrogen: an overview of advanced heteroatom doped carbons with boron, sulphur and phosphorus for energy applications, *Energy & Environmental Science*, 6 (2013).
- [4.2] H. Cui, Y. Guo, L. Guo, L. Wang, Z. Zhou, Z. Peng, Heteroatom-doped carbon materials and their composites as electrocatalysts for CO<sub>2</sub> reduction, *Journal of Materials Chemistry A*, 6 (2018) 18782-18793.
- [4.3] X. Wang, G. Sun, P. Routh, D.H. Kim, W. Huang, P. Chen, Heteroatom-doped graphene materials: syntheses, properties and applications, *Chem Soc Rev*, 43 (2014) 7067-7098.
- [4.4] D. Jariwala, V.K. Sangwan, L.J. Lauhon, T.J. Marks, M.C. Hersam, Carbon nanomaterials for electronics, optoelectronics, photovoltaics, and sensing, *Chem Soc Rev*, 42 (2013) 2824-2860.
- [4.5] H. Chen, F. Sun, J. Wang, W. Li, W. Qiao, L. Ling, D. Long, Nitrogen Doping Effects on the Physical and Chemical Properties of Mesoporous Carbons, *The Journal of Physical Chemistry C*, 117 (2013) 8318-8328.
- [4.6] J. Yu, M. Guo, F. Muhammad, A. Wang, F. Zhang, Q. Li, G. Zhu, One-pot synthesis of highly ordered nitrogen-containing mesoporous carbon with resorcinol–urea–formaldehyde resin for CO<sub>2</sub> capture, *Carbon*, 69 (2014) 502-514.
- [4.7] J. Wei, D. Zhou, Z. Sun, Y. Deng, Y. Xia, D. Zhao, A Controllable Synthesis of Rich Nitrogen-Doped Ordered Mesoporous Carbon for CO<sub>2</sub> Capture and Supercapacitors, *Advanced Functional Materials*, 23 (2013) 2322-2328.

- [4.8] L. Lai, J.R. Potts, D. Zhan, L. Wang, C.K. Poh, C. Tang, H. Gong, Z. Shen, J. Lin, R.S. Ruoff, Exploration of the active center structure of nitrogen-doped graphene-based catalysts for oxygen reduction reaction, *Energy & Environmental Science*, 5 (2012).
- [4.9] M. Sevilla, P. Valle-Vigón, A.B. Fuertes, N-Doped Polypyrrole-Based Porous Carbons for CO<sub>2</sub>Capture, *Advanced Functional Materials*, 21 (2011) 2781-2787.
- [4.10] S. Agnoli, M. Favaro, Doping graphene with boron: a review of synthesis methods, physicochemical characterization, and emerging applications, *Journal of Materials Chemistry A*, 4 (2016) 5002-5025.
- [4.11] S. Ding, S. Zheng, M. Xie, L. Peng, X. Guo, W. Ding, One-pot synthesis of boron-doped mesoporous carbon with boric acid as a multifunction reagent, *Microporous and Mesoporous Materials*, 142 (2011) 609-613.
- [4.12] D.-W. Wang, F. Li, Z.-G. Chen, G.Q. Lu, H.-M. Cheng, Synthesis and Electrochemical Property of Boron-Doped Mesoporous Carbon in Supercapacitor, *Chemistry of Materials*, 20 (2008) 7195-7200.
- [4.13] W. Lei, D. Portehault, R. Dimova, M. Antonietti, Boron carbon nitride nanostructures from salt melts: tunable water-soluble phosphors, *J Am Chem Soc*, 133 (2011) 7121-7127.
- [4.14] C. Sun, F. Ma, L. Cai, A. Wang, Y. Wu, M. Zhao, W. Yan, X. Hao, Metal-free Ternary BCN Nanosheets with Synergetic Effect of Band Gap Engineering and Magnetic Properties, *Sci Rep*, 7 (2017) 6617.
- [4.15] J. Hao, J. Wang, S. Qin, D. Liu, Y. Li, W. Lei, B/N co-doped carbon nanosphere frameworks as high-performance electrodes for supercapacitors, *Journal of materials Chemistry A*, 6 (2018) 8053-8058.
- [4.16] F. Guo, P. Yang, Z. Pan, X.N. Cao, Z. Xie, X. Wang, Carbon-Doped BN Nanosheets for the Oxidative Dehydrogenation of Ethylbenzene, *Angew Chem Int Ed Engl*, 56 (2017) 8231-8235.
- [4.17] L. Ci, L. Song, C. Jin, D. Jariwala, D. Wu, Y. Li, A. Srivastava, Z.F. Wang, K. Storr, L. Balicas, F. Liu, P.M. Ajayan, Atomic layers of hybridized boron nitride and graphene domains, *Nat Mater*, 9 (2010) 430-435.
- [4.18] T. Schiros, D. Nordlund, L. Palova, L. Zhao, M. Levendorf, C. Jaye, D. Reichman, J. Park, M. Hybertsen, A. Pasupathy, Atomistic Interrogation of B-N Co-dopant Structures and Their Electronic Effects in Graphene, *ACS Nano*, 10 (2016) 6574-6584.
- [4.19] J. Wu, M.T. Rodrigues, R. Vajtai, P.M. Ajayan, Tuning the Electrochemical Reactivity of Boron- and Nitrogen-Substituted Graphene, *Adv Mater*, 28 (2016) 6239-6246.
- [4.20] X. Blase, J.-C. Charlier, A. De Vita, R. Car, P. Redlich, M. Terrones, W. Hsu, H. Terrones, D. Carroll, P. Ajayan, Boron-mediated growth of long helicity-selected carbon nanotubes, *Physical Review Letters*, 83 (1999) 5078.
- [4.21] M. Endo, H. Muramatsu, T. Hayashi, Y.-A. Kim, G.V. Lier, J.-C. Charlier, H. Terrones, M. Terrones, M.S. Dresselhaus, Atomic nanotube welders: boron interstitials triggering connections in double-walled carbon nanotubes, *Nano letters*, 5 (2005) 1099-1105.
- [4.22] M.S. Seo, J.H. Kim, J.M. Kim, J.S. Han, S. Kang, J.S. Ihm, D.O. Kim, Tunable and selective

- formation of micropores and mesopores in carbide-derived carbon, *Carbon*, 60 (2013) 299-306.
- [4.23] V. Presser, M. Heon, Y. Gogotsi, Carbide-Derived Carbons - From Porous Networks to Nanotubes and Graphene, *Advanced Functional Materials*, 21 (2011) 810-833.
- [4.24] Y. Gogotsi, A. Nikitin, H. Ye, W. Zhou, J.E. Fischer, B. Yi, H.C. Foley, M.W. Barsoum, Nanoporous carbide-derived carbon with tunable pore size, *Nat Mater*, 2 (2003) 591-594.
- [4.25] J. Kim, J. Han, D. Ha, S. Kang, Synthesis of nitrogen and boron co-doped carbon (CNB) and their CO<sub>2</sub> capture properties: from porous to hollow granule structure, *J. Mater. Chem. A*, 2 (2014) 16645-16651.
- [4.26] J. Han, S. Lee, K. Choi, J. Kim, D. Ha, C.G. Lee, B. An, S.H. Lee, H. Mizuseki, J.W. Choi, S. Kang, Effect of nitrogen doping on titanium carbonitride-derived adsorbents used for arsenic removal, *J Hazard Mater*, 302 (2016) 375-385.
- [4.27] C.R. Pérez, S.-H. Yeon, J. Ségalini, V. Presser, P.-L. Taberna, P. Simon, Y. Gogotsi, Structure and Electrochemical Performance of Carbide-Derived Carbon Nanopowders, *Advanced Functional Materials*, 23 (2013) 1081-1089.
- [4.28] R. Dash, J. Chmiola, G. Yushin, Y. Gogotsi, G. Laudisio, J. Singer, J. Fischer, S. Kucheyev, Titanium carbide derived nanoporous carbon for energy-related applications, *Carbon*, 44 (2006) 2489-2497.
- [4.29] A. Sadezky, H. Muckenhuber, H. Grothe, R. Niessner, U. Pöschl, Raman microspectroscopy of soot and related carbonaceous materials: Spectral analysis and structural information, *Carbon*, 43 (2005) 1731-1742.
- [4.30] S.J. Gregg, K.S.W. Sing, H. Salzberg, Adsorption surface area and porosity, *Journal of The Electrochemical Society*, 114 (1967) 279C-279C.
- [4.31] J. Rouquerol, F. Rouquerol, P. Llewellyn, G. Maurin, K.S. Sing, Adsorption by powders and porous solids: principles, methodology and applications, Academic press 2013.
- [4.32] H.W. Kim, M.B. Ross, N. Kornienko, L. Zhang, J. Guo, P. Yang, B.D. McCloskey, Efficient hydrogen peroxide generation using reduced graphene oxide-based oxygen reduction electrocatalysts, *Nature Catalysis*, 1 (2018) 282-290.
- [4.33] Y.J. Sa, J.H. Kim, S.H. Joo, Active Edge-Site-Rich Carbon Nanocatalysts with Enhanced Electron Transfer for Efficient Electrochemical Hydrogen Peroxide Production, *Angew Chem Int Ed Engl*, 58 (2019) 1100-1105.
- [4.34] Y. Zhao, L. Yang, S. Chen, X. Wang, Y. Ma, Q. Wu, Y. Jiang, W. Qian, Z. Hu, Can boron and nitrogen co-doping improve oxygen reduction reaction activity of carbon nanotubes?, *J Am Chem Soc*, 135 (2013) 1201-1204.
- [4.35] J. Jin, F. Pan, L. Jiang, X. Fu, A. Liang, Z. Wei, J. Zhang, G. Sun, Catalyst-free synthesis of crumpled boron and nitrogen Co-doped graphite layers with tunable bond structure for oxygen reduction reaction, *ACS nano*, 8 (2014) 3313-3321.
- [4.36] Z. Ling, Z. Wang, M. Zhang, C. Yu, G. Wang, Y. Dong, S. Liu, Y. Wang, J. Qiu, Sustainable Synthesis and Assembly of Biomass-Derived B/N Co-Doped Carbon Nanosheets with Ultrahigh Aspect Ratio for High-Performance Supercapacitors, *Advanced Functional*



Materials, 26 (2016) 111-119.

- [4.37] J. Bernholc, A. Antonelli, T. Del Sole, Y. Bar-Yam, S. Pantelides, Mechanism of self-diffusion in diamond, *Physical review letters*, 61 (1988) 2689.
- [4.38] J.-C. Pu, S.-F. Wang, C.-L. Lin, J.C. Sung, Characterization of boron-doped diamond-like carbon prepared by radio frequency sputtering, *Thin Solid Films*, 519 (2010) 521-526.
- [4.39] R. Faccio, L. Fernández-Werner, H. Pardo, C. Goyenola, O.N. Ventura, Á.W. Mombrú, Electronic and structural distortions in graphene induced by carbon vacancies and boron doping, *The Journal of Physical Chemistry C*, 114 (2010) 18961-18971.
- [4.40] Y.A. Kim, K. Fujisawa, H. Muramatsu, T. Hayashi, M. Endo, T. Fujimori, K. Kaneko, M. Terrones, J. Behrends, A. Eckmann, Raman spectroscopy of boron-doped single-layer graphene, *ACS nano*, 6 (2012) 6293-6300.
- [4.41] M. Kawaguchi, B/C/N materials based on the graphite network, *Advanced Materials*, 9 (1997) 615-625.
- [4.42] Y.-J. Lee, Y. Uchiyama, L.R. Radovic, Effects of boron doping in low- and high-surface-area carbon powders, *Carbon*, 42 (2004) 2233-2244.
- [4.43] E. Rodríguez, R. García, Characterisation of boron-doped coal-derived carbon foams and their oxidation behaviour, *Fuel*, 93 (2012) 288-297.
- [4.44] M.-K. LEE, Nitrogen-doped carbon produced by chlorination process of Ti (C, N) and its electrochemical properties, Ph.D thesis, Seoul national university, 2019.
- [4.45] Z. Lu, G. Chen, S. Siahrostami, Z. Chen, K. Liu, J. Xie, L. Liao, T. Wu, D. Lin, Y. Liu, T.F. Jaramillo, J.K. Nørskov, Y. Cui, High-efficiency oxygen reduction to hydrogen peroxide catalysed by oxidized carbon materials, *Nature Catalysis*, 1 (2018) 156-162.
- [4.46] N. Ramaswamy, S. Mukerjee, Influence of Inner- and Outer-Sphere Electron Transfer Mechanisms during Electrocatalysis of Oxygen Reduction in Alkaline Media, *The Journal of Physical Chemistry C*, 115 (2011) 18015-18026.
- [4.47] Q. Lv, W. Si, J. He, L. Sun, C. Zhang, N. Wang, Z. Yang, X. Li, X. Wang, W. Deng, Y. Long, C. Huang, Y. Li, Selectively nitrogen-doped carbon materials as superior metal-free catalysts for oxygen reduction, *Nat Commun*, 9 (2018) 3376.
- [4.48] D. Guo, R. Shibuya, C. Akiba, S. Saji, T. Kondo, J. Nakamura, Active sites of nitrogen-doped carbon materials for oxygen reduction reaction clarified using model catalysts, *Science*, 351 (2016) 361-365.
- [4.49] C.H. Choi, H.K. Lim, M.W. Chung, J.C. Park, H. Shin, H. Kim, S.I. Woo, Long-range electron transfer over graphene-based catalyst for high-performing oxygen reduction reactions: importance of size, N-doping, and metallic impurities, *J Am Chem Soc*, 136 (2014) 9070-9077.
- [4.50] T. Prasad Yadav, R. Manohar Yadav, D. Pratap Singh, Mechanical Milling: a Top Down Approach for the Synthesis of Nanomaterials and Nanocomposites, *Nanoscience and Nanotechnology*, 2 (2012) 22-48.
- [4.51] S. Wang, E. Iyyamperumal, A. Roy, Y. Xue, D. Yu, L. Dai, Vertically aligned BCN nanotubes as efficient metal-free electrocatalysts for the oxygen reduction reaction: a synergetic effect

- by co-doping with boron and nitrogen, *Angew Chem Int Ed Engl*, 50 (2011) 11756-11760.
- [5.1] Y. Jiang, P. Ni, C. Chen, Y. Lu, P. Yang, B. Kong, A. Fisher, X. Wang, Selective Electrochemical H<sub>2</sub>O<sub>2</sub> Production through Two-Electron Oxygen Electrochemistry, *Advanced Energy Materials*, 8 (2018).
- [5.2] W. Zhou, X. Meng, J. Gao, A.N. Alshawabkeh, Hydrogen peroxide generation from O<sub>2</sub> electroreduction for environmental remediation: A state-of-the-art review, *Chemosphere*, 225 (2019) 588-607.
- [5.3] J. Zhang, H. Zhang, M.J. Cheng, Q. Lu, Tailoring the Electrochemical Production of H<sub>2</sub> O<sub>2</sub> : Strategies for the Rational Design of High-Performance Electrocatalysts, *Small*, 16 (2020) e1902845.
- [5.4] C.H. Choi, W.S. Choi, O. Kasian, A.K. Mechler, M.T. Sougrati, S. Bruller, K. Strickland, Q. Jia, S. Mukerjee, K.J.J. Mayrhofer, F. Jaouen, Unraveling the Nature of Sites Active toward Hydrogen Peroxide Reduction in Fe-N-C Catalysts, *Angew Chem Int Ed Engl*, 56 (2017) 8809-8812.
- [5.5] E. Jung, H. Shin, B.H. Lee, V. Efremov, S. Lee, H.S. Lee, J. Kim, W. Hooch Antink, S. Park, K.S. Lee, S.P. Cho, J.S. Yoo, Y.E. Sung, T. Hyeon, Atomic-level tuning of Co-N-C catalyst for high-performance electrochemical H<sub>2</sub>O<sub>2</sub> production, *Nat Mater*, 19 (2020) 436-442.
- [5.6] Y. Sun, I. Sinev, W. Ju, A. Bergmann, S. Drespe, S. Kühn, C. Spöri, H. Schmies, H. Wang, D. Bernsmeier, B. Paul, R. Schmack, R. Kraehnert, B. Roldan Cuenya, P. Strasser, Efficient Electrochemical Hydrogen Peroxide Production from Molecular Oxygen on Nitrogen-Doped Mesoporous Carbon Catalysts, *ACS Catalysis*, 8 (2018) 2844-2856.
- [5.7] Y.J. Sa, J.H. Kim, S.H. Joo, Active Edge-Site-Rich Carbon Nanocatalysts with Enhanced Electron Transfer for Efficient Electrochemical Hydrogen Peroxide Production, *Angew Chem Int Ed Engl*, 58 (2019) 1100-1105.
- [5.8] H.W. Kim, M.B. Ross, N. Kornienko, L. Zhang, J. Guo, P. Yang, B.D. McCloskey, Efficient hydrogen peroxide generation using reduced graphene oxide-based oxygen reduction electrocatalysts, *Nature Catalysis*, 1 (2018) 282-290.
- [5.9] Z. Lu, G. Chen, S. Siahrostami, Z. Chen, K. Liu, J. Xie, L. Liao, T. Wu, D. Lin, Y. Liu, T.F. Jaramillo, J.K. Nørskov, Y. Cui, High-efficiency oxygen reduction to hydrogen peroxide catalysed by oxidized carbon materials, *Nature Catalysis*, 1 (2018) 156-162.
- [5.10] L. Han, Y. Sun, S. Li, C. Cheng, C.E. Halbig, P. Feicht, J.L. Hübner, P. Strasser, S. Eigler, In-Plane Carbon Lattice-Defect Regulating Electrochemical Oxygen Reduction to Hydrogen Peroxide Production over Nitrogen-Doped Graphene, *ACS Catalysis*, 9 (2019) 1283-1288.
- [5.11] C.N.R. Rao, K. Gopalakrishnan, Borocarbonitrides, B<sub>x</sub>C<sub>y</sub>N<sub>z</sub>: Synthesis, Characterization, and Properties with Potential Applications, *ACS Appl Mater Interfaces*, 9 (2017) 19478-19494.
- [5.12] C. Chen, D. Yan, Y. Wang, Y. Zhou, Y. Zou, Y. Li, S. Wang, BN Pairs Enriched Defective Carbon Nanosheets for Ammonia Synthesis with High Efficiency, *Small*, 15 (2019) e1805029.

- [5.13] L. Song, Z. Liu, A.L. Reddy, N.T. Narayanan, J. Taha-Tijerina, J. Peng, G. Gao, J. Lou, R. Vajtai, P.M. Ajayan, Binary and ternary atomic layers built from carbon, boron, and nitrogen, *Adv Mater*, 24 (2012) 4878-4895.
- [5.14] N. kumar, K. Moses, K. Pramoda, S.N. Shirodkar, A.K. Mishra, U.V. Waghmare, A. Sundaresan, C.N.R. Rao, Borocarbonitrides, BxCyNz, *Journal of Materials Chemistry A*, 1 (2013).
- [5.15] R. Kumar, K. Gopalakrishnan, I. Ahmad, C.N.R. Rao, BN-Graphene Composites Generated by Covalent Cross-Linking with Organic Linkers, *Advanced Functional Materials*, 25 (2015) 5910-5917.
- [5.16] S. Wang, L. Zhang, Z. Xia, A. Roy, D.W. Chang, J.B. Baek, L. Dai, BCN graphene as efficient metal-free electrocatalyst for the oxygen reduction reaction, *Angew Chem Int Ed Engl*, 51 (2012) 4209-4212.
- [5.17] J. Jin, F. Pan, L. Jiang, X. Fu, A. Liang, Z. Wei, J. Zhang, G. Sun, Catalyst-free synthesis of crumpled boron and nitrogen Co-doped graphite layers with tunable bond structure for oxygen reduction reaction, *ACS nano*, 8 (2014) 3313-3321.
- [5.18] S. Wang, E. Iyyamperumal, A. Roy, Y. Xue, D. Yu, L. Dai, Vertically aligned BCN nanotubes as efficient metal-free electrocatalysts for the oxygen reduction reaction: a synergetic effect by co-doping with boron and nitrogen, *Angew Chem Int Ed Engl*, 50 (2011) 11756-11760.
- [5.19] Y. Zhao, L. Yang, S. Chen, X. Wang, Y. Ma, Q. Wu, Y. Jiang, W. Qian, Z. Hu, Can boron and nitrogen co-doping improve oxygen reduction reaction activity of carbon nanotubes?, *J Am Chem Soc*, 135 (2013) 1201-1204.
- [5.20] S. Chen, Z. Chen, S. Siahrostami, D. Higgins, D. Nordlund, D. Sokaras, T.R. Kim, Y. Liu, X. Yan, E. Nilsson, R. Sinclair, J.K. Nørskov, T.F. Jaramillo, Z. Bao, Designing Boron Nitride Islands in Carbon Materials for Efficient Electrochemical Synthesis of Hydrogen Peroxide, *J Am Chem Soc*, 140 (2018) 7851-7859.
- [5.21] M. Kawaguchi, B/C/N materials based on the graphite network, *Advanced Materials*, 9 (1997) 615-625.
- [5.22] S. Wang, F. Ma, H. Jiang, Y. Shao, Y. Wu, X. Hao, Band gap-Tunable Porous Borocarbonitride Nanosheets for High Energy-Density Supercapacitors, *ACS Appl Mater Interfaces*, 10 (2018) 19588-19597.
- [5.23] V. Presser, M. Heon, Y. Gogotsi, Carbide-Derived Carbons - From Porous Networks to Nanotubes and Graphene, *Advanced Functional Materials*, 21 (2011) 810-833.
- [5.24] Y. Gogotsi, A. Nikitin, H. Ye, W. Zhou, J.E. Fischer, B. Yi, H.C. Foley, M.W. Barsoum, Nanoporous carbide-derived carbon with tunable pore size, *Nat Mater*, 2 (2003) 591-594.
- [5.25] J. Chmiola, C. Largeot, P.-L. Taberna, P. Simon, Y. Gogotsi, Monolithic carbide-derived carbon films for micro-supercapacitors, *science*, 328 (2010) 480-483.
- [5.26] Y. Korenblit, M. Rose, E. Kockrick, L. Borchardt, A. Kvit, S. Kaskel, G. Yushin, High-rate electrochemical capacitors based on ordered mesoporous silicon carbide-derived carbon, *Acs Nano*, 4 (2010) 1337-1344.

- [5.27] M.E. Suss, S. Porada, X. Sun, P.M. Biesheuvel, J. Yoon, V. Presser, Water desalination via capacitive deionization: what is it and what can we expect from it?, *Energy & Environmental Science*, 8 (2015) 2296-2319.
- [5.28] G. Yushin, R. Dash, J. Jagiello, J.E. Fischer, Y. Gogotsi, Carbide-Derived Carbons: Effect of Pore Size on Hydrogen Uptake and Heat of Adsorption, *Advanced Functional Materials*, 16 (2006) 2288-2293.
- [5.29] M.S. Seo, J.H. Kim, J.M. Kim, J.S. Han, S. Kang, J.S. Ihm, D.O. Kim, Tunable and selective formation of micropores and mesopores in carbide-derived carbon, *Carbon*, 60 (2013) 299-306.
- [5.30] J. Kim, J. Han, D. Ha, S. Kang, Synthesis of nitrogen and boron co-doped carbon (CNB) and their CO<sub>2</sub> capture properties: from porous to hollow granule structure, *J. Mater. Chem. A*, 2 (2014) 16645-16651.
- [5.31] J.-S. Han, D.Y. Chung, D.-G. Ha, J.-H. Kim, K. Choi, Y.-E. Sung, S.-H. Kang, Nitrogen and boron co-doped hollow carbon catalyst for the oxygen reduction reaction, *Carbon*, 105 (2016) 1-7.
- [5.32] J. Kim, J. Han, M. Seo, S. Kang, D. Kim, J. Ihm, High-surface area ceramic-derived boron-nitride and its hydrogen uptake properties, *J. Mater. Chem. A*, 1 (2013) 1014-1017.
- [5.33] C.W. Bale, E. Bélisle, P. Chartrand, S.A. Decterov, G. Eriksson, K. Hack, I.H. Jung, Y.B. Kang, J. Melançon, A.D. Pelton, C. Robelin, S. Petersen, FactSage thermochemical software and databases — recent developments, *Calphad*, 33 (2009) 295-311.
- [5.34] J. Sui, J.-J. Lu, Synthesis of carbon nitride powder by selective etching of TiC<sub>0.3</sub>N<sub>0.7</sub> in chlorine-containing atmosphere at moderate temperature, *Materials Chemistry and Physics*, 123 (2010) 264-268.
- [5.35] Y. Gong, H. Fei, X. Zou, W. Zhou, S. Yang, G. Ye, Z. Liu, Z. Peng, J. Lou, R. Vajtai, B.I. Yakobson, J.M. Tour, P.M. Ajayan, Boron- and Nitrogen-Substituted Graphene Nanoribbons as Efficient Catalysts for Oxygen Reduction Reaction, *Chemistry of Materials*, 27 (2015) 1181-1186.
- [5.36] M. Kawaguchi, T. Kawashima, T. Nakajima, Syntheses and structures of new graphite-like materials of composition BCN (H) and BC<sub>3</sub>N (H), *Chemistry of materials*, 8 (1996) 1197-1201.
- [5.37] E. Raymundo-Pinero, D. Cazorla-Amorós, A. Linares-Solano, J. Find, U. Wild, R. Schlögl, Structural characterization of N-containing activated carbon fibers prepared from a low softening point petroleum pitch and a melamine resin, *Carbon*, 40 (2002) 597-608.
- [5.38] H. Zhu, J. Yin, X. Wang, H. Wang, X. Yang, Microorganism-Derived Heteroatom-Doped Carbon Materials for Oxygen Reduction and Supercapacitors, *Advanced Functional Materials*, 23 (2013) 1305-1312.
- [5.39] T. Hemraj-Benny, S. Banerjee, S. Sambasivan, D.A. Fischer, W. Han, J.A. Misewich, S.S. Wong, Investigating the structure of boron nitride nanotubes by near-edge X-ray absorption fine structure (NEXAFS) spectroscopy, *Phys Chem Chem Phys*, 7 (2005) 1103-1106.

- [5.40] I. Caretti, I. Jiménez, Point defects in hexagonal BN, BC<sub>3</sub> and BC<sub>x</sub>N compounds studied by x-ray absorption near-edge structure, *Journal of Applied Physics*, 110 (2011).
- [5.41] L.S. Zhang, X.Q. Liang, W.G. Song, Z.Y. Wu, Identification of the nitrogen species on N-doped graphene layers and Pt/NG composite catalyst for direct methanol fuel cell, *Phys Chem Chem Phys*, 12 (2010) 12055-12059.
- [5.42] W. Lei, D. Portehault, R. Dimova, M. Antonietti, Boron carbon nitride nanostructures from salt melts: tunable water-soluble phosphors, *J Am Chem Soc*, 133 (2011) 7121-7127.
- [5.43] J. Huang, Y.T. Zhu, H. Mori, Structure and phase characteristics of amorphous boron–carbon–nitrogen under high pressure and high temperature, *Journal of Materials Research*, 16 (2011) 1178-1184.
- [5.44] S.J. Gregg, K.S.W. Sing, H. Salzberg, Adsorption surface area and porosity, *Journal of The electrochemical society*, 114 (1967) 279C.
- [5.45] J. Rouquerol, F. Rouquerol, P. Llewellyn, G. Maurin, K.S. Sing, *Adsorption by powders and porous solids: principles, methodology and applications*, Academic press 2013.
- [5.46] M.-K. LEE, Nitrogen-doped carbon produced by chlorination process of Ti (C, N) and its electrochemical properties, *Materials Science and Engineering*, Seoul National University, 2019.
- [5.47] J. Tang, J. Liu, N.L. Torad, T. Kimura, Y. Yamauchi, Tailored design of functional nanoporous carbon materials toward fuel cell applications, *Nano Today*, 9 (2014) 305-323.
- [5.48] X. Blase, J.-C. Charlier, A. De Vita, R. Car, P. Redlich, M. Terrones, W. Hsu, H. Terrones, D. Carroll, P. Ajayan, Boron-mediated growth of long helicity-selected carbon nanotubes, *Physical Review Letters*, 83 (1999) 5078.
- [5.49] M. Endo, H. Muramatsu, T. Hayashi, Y.-A. Kim, G.V. Lier, J.-C. Charlier, H. Terrones, M. Terrones, M.S. Dresselhaus, Atomic nanotube welders: boron interstitials triggering connections in double-walled carbon nanotubes, *Nano letters*, 5 (2005) 1099-1105.
- [5.50] J. Bernholc, A. Antonelli, T.M. Del Sole, Y. Bar-Yam, S.T. Pantelides, Mechanism of self-diffusion in diamond, *Phys Rev Lett*, 61 (1988) 2689-2692.
- [6.1] X.-F. Yang, A. Wang, B. Qiao, J. Li, J. Liu, T. Zhang, Single-atom catalysts: a new frontier in heterogeneous catalysis, *Accounts of chemical research*, 46 (2013) 1740-1748.
- [6.2] C. Zhu, S. Fu, Q. Shi, D. Du, Y. Lin, Single-Atom Electrocatalysts, *Angew Chem Int Ed Engl*, 56 (2017) 13944-13960.
- [6.3] H. Zhang, G. Liu, L. Shi, J. Ye, Single-Atom Catalysts: Emerging Multifunctional Materials in Heterogeneous Catalysis, *Advanced Energy Materials*, 8 (2018).
- [6.4] Y. Peng, B. Lu, S. Chen, Carbon-Supported Single Atom Catalysts for Electrochemical Energy Conversion and Storage, *Adv Mater*, 30 (2018) e1801995.
- [6.5] J. Guo, J. Huo, Y. Liu, W. Wu, Y. Wang, M. Wu, H. Liu, G. Wang, Nitrogen-Doped Porous Carbon Supported Nonprecious Metal Single-Atom Electrocatalysts: from Synthesis to Application, *Small Methods*, 3 (2019).
- [6.6] L. Zhao, Y. Zhang, L.B. Huang, X.Z. Liu, Q.H. Zhang, C. He, Z.Y. Wu, L.J. Zhang, J. Wu, W. Yang, L. Gu, J.S. Hu, L.J. Wan, Cascade anchoring strategy for general mass production

- of high-loading single-atomic metal-nitrogen catalysts, *Nat Commun*, 10 (2019) 1278.
- [6.7] G. Wu, K.L. More, C.M. Johnston, P. Zelenay, High-performance electrocatalysts for oxygen reduction derived from polyaniline, iron, and cobalt, *Science*, 332 (2011) 443-447.
- [6.8] L. Lin, Q. Zhu, A.W. Xu, Noble-metal-free Fe-N/C catalyst for highly efficient oxygen reduction reaction under both alkaline and acidic conditions, *J Am Chem Soc*, 136 (2014) 11027-11033.
- [6.9] G.A. Ferrero, K. Preuss, A. Marinovic, A.B. Jorge, N. Mansor, D.J. Brett, A.B. Fuertes, M. Sevilla, M.M. Titirici, Fe-N-Doped Carbon Capsules with Outstanding Electrochemical Performance and Stability for the Oxygen Reduction Reaction in Both Acid and Alkaline Conditions, *ACS Nano*, 10 (2016) 5922-5932.
- [6.10] Y.J. Sa, D.J. Seo, J. Woo, J.T. Lim, J.Y. Cheon, S.Y. Yang, J.M. Lee, D. Kang, T.J. Shin, H.S. Shin, H.Y. Jeong, C.S. Kim, M.G. Kim, T.Y. Kim, S.H. Joo, A General Approach to Preferential Formation of Active Fe-N<sub>x</sub> Sites in Fe-N/C Electrocatalysts for Efficient Oxygen Reduction Reaction, *J Am Chem Soc*, 138 (2016) 15046-15056.
- [6.11] A. Zitolo, N. Ranjbar-Sahraie, T. Mineva, J. Li, Q. Jia, S. Stamatini, G.F. Harrington, S.M. Lyth, P. Krtil, S. Mukerjee, E. Fonda, F. Jaouen, Identification of catalytic sites in cobalt-nitrogen-carbon materials for the oxygen reduction reaction, *Nat Commun*, 8 (2017) 957.
- [6.12] R. Jiang, L. Li, T. Sheng, G. Hu, Y. Chen, L. Wang, Edge-Site Engineering of Atomically Dispersed Fe-N<sub>4</sub> by Selective C-N Bond Cleavage for Enhanced Oxygen Reduction Reaction Activities, *J Am Chem Soc*, 140 (2018) 11594-11598.
- [6.13] W. Chen, J. Pei, C.T. He, J. Wan, H. Ren, Y. Zhu, Y. Wang, J. Dong, S. Tian, W.C. Cheong, S. Lu, L. Zheng, X. Zheng, W. Yan, Z. Zhuang, C. Chen, Q. Peng, D. Wang, Y. Li, Rational Design of Single Molybdenum Atoms Anchored on N-Doped Carbon for Effective Hydrogen Evolution Reaction, *Angew Chem Int Ed Engl*, 56 (2017) 16086-16090.
- [6.14] L. Cao, Q. Luo, W. Liu, Y. Lin, X. Liu, Y. Cao, W. Zhang, Y. Wu, J. Yang, T. Yao, S. Wei, Identification of single-atom active sites in carbon-based cobalt catalysts during electrocatalytic hydrogen evolution, *Nature Catalysis*, 2 (2018) 134-141.
- [6.15] C. Lei, Y. Wang, Y. Hou, P. Liu, J. Yang, T. Zhang, X. Zhuang, M. Chen, B. Yang, L. Lei, C. Yuan, M. Qiu, X. Feng, Efficient alkaline hydrogen evolution on atomically dispersed Ni-N<sub>x</sub> Species anchored porous carbon with embedded Ni nanoparticles by accelerating water dissociation kinetics, *Energy & Environmental Science*, 12 (2019) 149-156.
- [6.16] X. Li, W. Bi, M. Chen, Y. Sun, H. Ju, W. Yan, J. Zhu, X. Wu, W. Chu, C. Wu, Y. Xie, Exclusive Ni-N<sub>4</sub> Sites Realize Near-Unity CO Selectivity for Electrochemical CO<sub>2</sub> Reduction, *J Am Chem Soc*, 139 (2017) 14889-14892.
- [6.17] F. Pan, H. Zhang, K. Liu, D. Cullen, K. More, M. Wang, Z. Feng, G. Wang, G. Wu, Y. Li, Unveiling Active Sites of CO<sub>2</sub> Reduction on Nitrogen-Coordinated and Atomically Dispersed Iron and Cobalt Catalysts, *ACS Catalysis*, 8 (2018) 3116-3122.
- [6.18] F. Yang, P. Song, X. Liu, B. Mei, W. Xing, Z. Jiang, L. Gu, W. Xu, Highly Efficient CO<sub>2</sub> Electroreduction on ZnN<sub>4</sub>-based Single-Atom Catalyst, *Angew Chem Int Ed Engl*, 57 (2018) 12303-12307.

- [6.19] D. Zhao, Z. Zhuang, X. Cao, C. Zhang, Q. Peng, C. Chen, Y. Li, Atomic site electrocatalysts for water splitting, oxygen reduction and selective oxidation, *Chem Soc Rev*, 49 (2020) 2215-2264.
- [6.20] M.B. Gawande, P. Fornasiero, R. Zbořil, Carbon-Based Single-Atom Catalysts for Advanced Applications, *ACS Catalysis*, 10 (2020) 2231-2259.
- [6.21] B. Bokhonov, M. Korchagin, The formation of graphite encapsulated metal nanoparticles during mechanical activation and annealing of soot with iron and nickel, *Journal of alloys and compounds*, 333 (2002) 308-320.
- [6.22] M. Sevilla, A.B. Fuertes, Graphitic carbon nanostructures from cellulose, *Chemical Physics Letters*, 490 (2010) 63-68.
- [6.23] J. Hoekstra, A.M. Beale, F. Soulimani, M. Versluijs-Helder, J.W. Geus, L.W. Jenneskens, Base Metal Catalyzed Graphitization of Cellulose: A Combined Raman Spectroscopy, Temperature-Dependent X-ray Diffraction and High-Resolution Transmission Electron Microscopy Study, *The Journal of Physical Chemistry C*, 119 (2015) 10653-10661.
- [6.24] C.J. Thambiliyagodage, S. Ulrich, P.T. Araujo, M.G. Bakker, Catalytic graphitization in nanocast carbon monoliths by iron, cobalt and nickel nanoparticles, *Carbon*, 134 (2018) 452-463.
- [6.25] L. Song, Z. Liu, A.L. Reddy, N.T. Narayanan, J. Taha-Tijerina, J. Peng, G. Gao, J. Lou, R. Vajtai, P.M. Ajayan, Binary and ternary atomic layers built from carbon, boron, and nitrogen, *Adv Mater*, 24 (2012) 4878-4895.
- [6.26] C.-K. Chang, S. Kataria, C.-C. Kuo, A. Ganguly, B.-Y. Wang, J.-Y. Hwang, K.-J. Huang, W.-H. Yang, S.-B. Wang, C.-H. Chuang, Band gap engineering of chemical vapor deposited graphene by in situ BN doping, *ACS nano*, 7 (2013) 1333-1341.
- [6.27] W. Lei, D. Portehault, R. Dimova, M. Antonietti, Boron carbon nitride nanostructures from salt melts: tunable water-soluble phosphors, *J Am Chem Soc*, 133 (2011) 7121-7127.
- [6.28] C.N.R. Rao, K. Gopalakrishnan, Borocarbonitrides, *BxCyNz*: Synthesis, Characterization, and Properties with Potential Applications, *ACS Appl Mater Interfaces*, 9 (2017) 19478-19494.
- [6.29] C.H. Choi, S.H. Park, S.I. Woo, Binary and ternary doping of nitrogen, boron, and phosphorus into carbon for enhancing electrochemical oxygen reduction activity, *ACS nano*, 6 (2012) 7084-7091.
- [6.30] J. Jin, F. Pan, L. Jiang, X. Fu, A. Liang, Z. Wei, J. Zhang, G. Sun, Catalyst-free synthesis of crumpled boron and nitrogen Co-doped graphite layers with tunable bond structure for oxygen reduction reaction, *ACS nano*, 8 (2014) 3313-3321.
- [6.31] Y. Gong, H. Fei, X. Zou, W. Zhou, S. Yang, G. Ye, Z. Liu, Z. Peng, J. Lou, R. Vajtai, B.I. Yakobson, J.M. Tour, P.M. Ajayan, Boron- and Nitrogen-Substituted Graphene Nanoribbons as Efficient Catalysts for Oxygen Reduction Reaction, *Chemistry of Materials*, 27 (2015) 1181-1186.
- [6.32] D. Guo, R. Shibuya, C. Akiba, S. Saji, T. Kondo, J. Nakamura, Active sites of nitrogen-doped carbon materials for oxygen reduction reaction clarified using model catalysts, *Science*, 351

(2016) 361-365.

- [6.33] M.S. Seo, J.H. Kim, J.M. Kim, J.S. Han, S. Kang, J.S. Ihm, D.O. Kim, Tunable and selective formation of micropores and mesopores in carbide-derived carbon, *Carbon*, 60 (2013) 299-306.
- [6.34] J. Kim, J. Han, D. Ha, S. Kang, Synthesis of nitrogen and boron co-doped carbon (CNB) and their CO<sub>2</sub> capture properties: from porous to hollow granule structure, *J. Mater. Chem. A*, 2 (2014) 16645-16651.
- [6.35] M.-K. Lee, Nitrogen-doped carbon produced by chlorination process of Ti (C, N) and its electrochemical properties, Seoul national university, 2019.
- [6.36] J.-S. Han, D.Y. Chung, D.-G. Ha, J.-H. Kim, K. Choi, Y.-E. Sung, S.-H. Kang, Nitrogen and boron co-doped hollow carbon catalyst for the oxygen reduction reaction, *Carbon*, 105 (2016) 1-7.
- [6.37] V. Presser, M. Heon, Y. Gogotsi, Carbide-Derived Carbons - From Porous Networks to Nanotubes and Graphene, *Advanced Functional Materials*, 21 (2011) 810-833.
- [6.38] W.J. Jiang, L. Gu, L. Li, Y. Zhang, X. Zhang, L.J. Zhang, J.Q. Wang, J.S. Hu, Z. Wei, L.J. Wan, Understanding the High Activity of Fe-N-C Electrocatalysts in Oxygen Reduction: Fe/Fe<sub>3</sub>C Nanoparticles Boost the Activity of Fe-N(x), *J Am Chem Soc*, 138 (2016) 3570-3578.
- [6.39] R.P. Struis, D. Bachelin, C. Ludwig, A. Wokaun, Studying the formation of Ni<sub>3</sub>C from CO and metallic Ni at T= 265 C in situ using Ni K-Edge x-ray absorption spectroscopy, *The Journal of Physical Chemistry C*, 113 (2009) 2443-2451.
- [6.40] S.J. Gregg, K.S.W. Sing, H. Salzberg, Adsorption surface area and porosity, *Journal of The Electrochemical Society*, 114 (1967) 279C-279C.
- [6.41] J. Rouquerol, F. Rouquerol, P. Llewellyn, G. Maurin, K.S. Sing, Adsorption by powders and porous solids: principles, methodology and applications, Academic press 2013.
- [6.42] F. Derbyshire, A. Presland, D. Trimm, Graphite formation by the dissolution—precipitation of carbon in cobalt, nickel and iron, *Carbon*, 13 (1975) 111-113.
- [6.43] A. Ōya, H. Marsh, Phenomena of catalytic graphitization, *Journal of Materials Science*, 17 (1982) 309-322.
- [6.44] L. Zhang, R. He, H.-C. Gu, Oleic acid coating on the monodisperse magnetite nanoparticles, *Applied Surface Science*, 253 (2006) 2611-2617.
- [6.45] A.G. Nasibulin, A. Moisala, D.P. Brown, E.I. Kauppinen, Carbon nanotubes and onions from carbon monoxide using Ni(acac)<sub>2</sub> and Cu(acac)<sub>2</sub> as catalyst precursors, *Carbon*, 41 (2003) 2711-2724.
- [6.46] C.W. Bale, E. Bélisle, P. Chartrand, S.A. Decterov, G. Eriksson, K. Hack, I.H. Jung, Y.B. Kang, J. Melançon, A.D. Pelton, C. Robelin, S. Petersen, FactSage thermochemical software and databases — recent developments, *Calphad*, 33 (2009) 295-311.
- [6.47] E. Charon, J.N. Rouzaud, J. Aléon, Graphitization at low temperatures (600–1200°C) in the presence of iron implications in planetology, *Carbon*, 66 (2014) 178-190.
- [6.48] J. Li, L. Jiao, E. Wegener, L.L. Richard, E. Liu, A. Zitolo, M.T. Sougrati, S. Mukerjee, Z.



- Zhao, Y. Huang, Evolution Pathway from Iron Compounds to FeI (II)-N<sub>4</sub> Sites through Gas-Phase Iron during Pyrolysis, *Journal of the American Chemical Society*, 142 (2019) 1417-1423.
- [6.49] Z. Huang, X. Gu, Q. Cao, P. Hu, J. Hao, J. Li, X. Tang, Catalytically active single-atom sites fabricated from silver particles, *Angew Chem Int Ed Engl*, 51 (2012) 4198-4203.
- [6.50] J. Yang, Z. Qiu, C. Zhao, W. Wei, W. Chen, Z. Li, Y. Qu, J. Dong, J. Luo, Z. Li, Y. Wu, In Situ Thermal Atomization To Convert Supported Nickel Nanoparticles into Surface-Bound Nickel Single-Atom Catalysts, *Angew Chem Int Ed Engl*, 57 (2018) 14095-14100.
- [7.1] A. Zitolo, N. Ranjbar-Sahraie, T. Mineva, J. Li, Q. Jia, S. Stamatini, G.F. Harrington, S.M. Lyth, P. Krtić, S. Mukerjee, E. Fonda, F. Jaouen, Identification of catalytic sites in cobalt-nitrogen-carbon materials for the oxygen reduction reaction, *Nat Commun*, 8 (2017) 957.
- [7.2] A. Han, W. Chen, S. Zhang, M. Zhang, Y. Han, J. Zhang, S. Ji, L. Zheng, Y. Wang, L. Gu, C. Chen, Q. Peng, D. Wang, Y. Li, A Polymer Encapsulation Strategy to Synthesize Porous Nitrogen-Doped Carbon-Nanosphere-Supported Metal Isolated-Single-Atomic-Site Catalysts, *Adv Mater*, 30 (2018) e1706508.
- [7.3] R. Jiang, L. Li, T. Sheng, G. Hu, Y. Chen, L. Wang, Edge-Site Engineering of Atomically Dispersed Fe-N<sub>4</sub> by Selective C-N Bond Cleavage for Enhanced Oxygen Reduction Reaction Activities, *J Am Chem Soc*, 140 (2018) 11594-11598.
- [7.4] Y. Li, X. Liu, L. Zheng, J. Shang, X. Wan, R. Hu, X. Guo, S. Hong, J. Shui, Preparation of Fe-N-C catalysts with FeN<sub>x</sub> (x = 1, 3, 4) active sites and comparison of their activities for the oxygen reduction reaction and performances in proton exchange membrane fuel cells, *Journal of Materials Chemistry A*, 7 (2019) 26147-26153.
- [7.5] X. Wang, Y. Jia, X. Mao, D. Liu, W. He, J. Li, J. Liu, X. Yan, J. Chen, L. Song, A. Du, X. Yao, Edge-Rich Fe-N<sub>4</sub> Active Sites in Defective Carbon for Oxygen Reduction Catalysis, *Adv Mater*, 32 (2020) e2000966.
- [7.6] M.B. Gawande, P. Fornasiero, R. Zboril, Carbon-Based Single-Atom Catalysts for Advanced Applications, *ACS Catalysis*, 10 (2020) 2231-2259.
- [7.7] D. Zhao, Z. Zhuang, X. Cao, C. Zhang, Q. Peng, C. Chen, Y. Li, Atomic site electrocatalysts for water splitting, oxygen reduction and selective oxidation, *Chem Soc Rev*, 49 (2020) 2215-2264.
- [7.8] H.I. Lee, J.H. Kim, D.J. You, J.E. Lee, J.M. Kim, W.S. Ahn, C. Pak, S.H. Joo, H. Chang, D. Seung, Rational Synthesis Pathway for Ordered Mesoporous Carbon with Controllable 30- to 100-Angstrom Pores, *Advanced Materials*, 20 (2008) 757-762.
- [7.9] H.I. Lee, G.D. Stucky, J.H. Kim, C. Pak, H. Chang, J.M. Kim, Spontaneous phase separation mediated synthesis of 3D mesoporous carbon with controllable cage and window size, *Adv Mater*, 23 (2011) 2357-2361.
- [7.10] F.U. Shah, S. Glavatskih, O.N. Antzutkin, Boron in Tribology: From Borates to Ionic Liquids, *Tribology Letters*, 51 (2013) 281-301.
- [7.11] C.H. Choi, S.H. Park, S.I. Woo, Binary and ternary doping of nitrogen, boron, and phosphorus into carbon for enhancing electrochemical oxygen reduction activity, *ACS nano*, 6 (2012)

7084-7091.

- [7.12] Y. Gong, H. Fei, X. Zou, W. Zhou, S. Yang, G. Ye, Z. Liu, Z. Peng, J. Lou, R. Vajtai, B.I. Yakobson, J.M. Tour, P.M. Ajayan, Boron- and Nitrogen-Substituted Graphene Nanoribbons as Efficient Catalysts for Oxygen Reduction Reaction, *Chemistry of Materials*, 27 (2015) 1181-1186.
- [7.13] H. Tabassum, R. Zou, A. Mahmood, Z. Liang, S. Guo, A catalyst-free synthesis of B, N co-doped graphene nanostructures with tunable dimensions as highly efficient metal free dual electrocatalysts, *Journal of Materials Chemistry A*, 4 (2016) 16469-16475.
- [7.14] H. Tabassum, R. Zou, A. Mahmood, Z. Liang, Q. Wang, H. Zhang, S. Gao, C. Qu, W. Guo, S. Guo, A Universal Strategy for Hollow Metal Oxide Nanoparticles Encapsulated into B/N Co-Doped Graphitic Nanotubes as High-Performance Lithium-Ion Battery Anodes, *Adv Mater*, 30 (2018).
- [7.15] C.R. Pérez, S.-H. Yeon, J. Ségalini, V. Presser, P.-L. Taberna, P. Simon, Y. Gogotsi, Structure and Electrochemical Performance of Carbide-Derived Carbon Nanopowders, *Advanced Functional Materials*, 23 (2013) 1081-1089.
- [7.16] S.J. Gregg, K.S.W. Sing, H. Salzberg, Adsorption surface area and porosity, *Journal of The electrochemical society*, 114 (1967) 279C.
- [7.17] J. Rouquerol, F. Rouquerol, P. Llewellyn, G. Maurin, K.S. Sing, *Adsorption by powders and porous solids: principles, methodology and applications*, Academic press 2013.
- [7.18] J. Tang, J. Liu, N.L. Torad, T. Kimura, Y. Yamauchi, Tailored design of functional nanoporous carbon materials toward fuel cell applications, *Nano Today*, 9 (2014) 305-323.
- [7.19] M. Kawaguchi, T. Kawashima, T. Nakajima, Syntheses and structures of new graphite-like materials of composition BCN (H) and BC<sub>3</sub>N (H), *Chemistry of materials*, 8 (1996) 1197-1201.
- [7.20] J.-i. Ozaki, N. Kimura, T. Anahara, A. Oya, Preparation and oxygen reduction activity of BN-doped carbons, *Carbon*, 45 (2007) 1847-1853.
- [7.21] J. Jin, F. Pan, L. Jiang, X. Fu, A. Liang, Z. Wei, J. Zhang, G. Sun, Catalyst-free synthesis of crumpled boron and nitrogen Co-doped graphite layers with tunable bond structure for oxygen reduction reaction, *ACS nano*, 8 (2014) 3313-3321.
- [7.22] H. Zhu, J. Yin, X. Wang, H. Wang, X. Yang, Microorganism-Derived Heteroatom-Doped Carbon Materials for Oxygen Reduction and Supercapacitors, *Advanced Functional Materials*, 23 (2013) 1305-1312.
- [7.23] W.J. Jiang, L. Gu, L. Li, Y. Zhang, X. Zhang, L.J. Zhang, J.Q. Wang, J.S. Hu, Z. Wei, L.J. Wan, Understanding the High Activity of Fe-N-C Electrocatalysts in Oxygen Reduction: Fe/Fe<sub>3</sub>C Nanoparticles Boost the Activity of Fe-N(x), *J Am Chem Soc*, 138 (2016) 3570-3578.
- [7.24] Z. Huang, H. Pan, W. Yang, H. Zhou, N. Gao, C. Fu, S. Li, H. Li, Y. Kuang, In Situ Self-Template Synthesis of Fe-N-Doped Double-Shelled Hollow Carbon Microspheres for Oxygen Reduction Reaction, *ACS Nano*, 12 (2018) 208-216.
- [7.25] L. Lin, Q. Zhu, A.W. Xu, Noble-metal-free Fe-N/C catalyst for highly efficient oxygen

- reduction reaction under both alkaline and acidic conditions, *J Am Chem Soc*, 136 (2014) 11027-11033.
- [7.26] S.H. Ahn, X. Yu, A. Manthiram, "Wiring" Fe-Nx -Embedded Porous Carbon Framework onto 1D Nanotubes for Efficient Oxygen Reduction Reaction in Alkaline and Acidic Media, *Adv Mater*, 29 (2017).
- [7.27] L.M. Graham, S. Cho, S.K. Kim, M. Noked, S.B. Lee, Role of boric acid in nickel nanotube electrodeposition: a surface-directed growth mechanism, *Chem Commun (Camb)*, 50 (2014) 527-529.
- [7.28] J. Geng, D.A. Jefferson, B.F. Johnson, Exploring the structural complexities of metal-metalloid nanoparticles: the case of Ni<sub>3</sub>B as catalyst, *Chemistry*, 15 (2009) 1134-1143.
- [7.29] V. Singh, V. Srinivas, Evolution of Ni<sub>3</sub>B<sub>2</sub>O<sub>3</sub> core-shell structure and magnetic properties on devitrification of amorphous NiB particles in air, *Journal of Applied Physics*, 106 (2009).
- [7.30] A.M. Alexander, J.S. Hargreaves, Alternative catalytic materials: carbides, nitrides, phosphides and amorphous boron alloys, *Chem Soc Rev*, 39 (2010) 4388-4401.
- [7.31] C.W. Bale, E. Béglise, P. Chartrand, S.A. Decterov, G. Eriksson, K. Hack, I.H. Jung, Y.B. Kang, J. Melançon, A.D. Pelton, C. Robelin, S. Petersen, FactSage thermochemical software and databases — recent developments, *Calphad*, 33 (2009) 295-311.
- [7.32] N. kumar, K. Moses, K. Pramoda, S.N. Shirodkar, A.K. Mishra, U.V. Waghmare, A. Sundaresan, C.N.R. Rao, Borocarbonitrides, BxCyNz, *Journal of Materials Chemistry A*, 1 (2013).
- [7.33] J. Kim, J. Han, D. Ha, S. Kang, Synthesis of nitrogen and boron co-doped carbon (CNB) and their CO<sub>2</sub> capture properties: from porous to hollow granule structure, *J. Mater. Chem. A*, 2 (2014) 16645-16651.
- [7.34] J. Li, L. Jiao, E. Wegener, L.L. Richard, E. Liu, A. Zitolo, M.T. Sougrati, S. Mukerjee, Z. Zhao, Y. Huang, F. Yang, S. Zhong, H. Xu, A.J. Kropf, F. Jaouen, D.J. Myers, Q. Jia, Evolution Pathway from Iron Compounds to Fe(I)-N<sub>4</sub> Sites through Gas-Phase Iron during Pyrolysis, *J Am Chem Soc*, 142 (2020) 1417-1423.
- [7.35] F. Maldonado-Hódar, C. Moreno-Castilla, J. Rivera-Utrilla, Y. Hanzawa, Y. Yamada, Catalytic graphitization of carbon aerogels by transition metals, *Langmuir*, 16 (2000) 4367-4373.
- [7.36] C.J. Thambiliyagodage, S. Ulrich, P.T. Araujo, M.G. Bakker, Catalytic graphitization in nanocast carbon monoliths by iron, cobalt and nickel nanoparticles, *Carbon*, 134 (2018) 452-463.
- [7.37] X. Li, W. Bi, M. Chen, Y. Sun, H. Ju, W. Yan, J. Zhu, X. Wu, W. Chu, C. Wu, Y. Xie, Exclusive Ni-N<sub>4</sub> Sites Realize Near-Unity CO Selectivity for Electrochemical CO<sub>2</sub> Reduction, *J Am Chem Soc*, 139 (2017) 14889-14892.
- [7.38] C. Zhao, X. Dai, T. Yao, W. Chen, X. Wang, J. Wang, J. Yang, S. Wei, Y. Wu, Y. Li, Ionic Exchange of Metal-Organic Frameworks to Access Single Nickel Sites for Efficient Electroreduction of CO<sub>2</sub>, *J Am Chem Soc*, 139 (2017) 8078-8081.
- [7.39] H.-Y. Jeong, M. Balamurugan, V.S.K. Choutipalli, E.-s. Jeong, V. Subramanian, U. Sim, K.T.

- Nam, Achieving highly efficient CO<sub>2</sub> to CO electroreduction exceeding 300 mA cm<sup>-2</sup> with single-atom nickel electrocatalysts, *Journal of Materials Chemistry A*, 7 (2019) 10651-10661.
- [8.1] C. Wan, Y.N. Regmi, B.M. Leonard, Multiple phases of molybdenum carbide as electrocatalysts for the hydrogen evolution reaction, *Angew Chem Int Ed Engl*, 53 (2014) 6407-6410.
- [8.2] C. Lu, D. Tranca, J. Zhang, F.N. Rodri Guez Hernandez, Y. Su, X. Zhuang, F. Zhang, G. Seifert, X. Feng, Molybdenum Carbide-Embedded Nitrogen-Doped Porous Carbon Nanosheets as Electrocatalysts for Water Splitting in Alkaline Media, *ACS Nano*, 11 (2017) 3933-3942.
- [8.3] F. Li, G.-F. Han, H.-J. Noh, S.-J. Kim, Y. Lu, H.Y. Jeong, Z. Fu, J.-B. Baek, Boosting oxygen reduction catalysis with abundant copper single atom active sites, *Energy & Environmental Science*, 11 (2018) 2263-2269.
- [8.4] P. Ouzilleau, A.E. Gheribi, G. Eriksson, D.K. Lindberg, P. Chartrand, A size-dependent thermodynamic model for coke crystallites: The carbon–hydrogen system up to 2500K, *Carbon*, 85 (2015) 99-118.
- [8.5] P. Ouzilleau, A.E. Gheribi, D.K. Lindberg, P. Chartrand, A Size-Dependent Thermodynamic Model for Coke Crystallites: The Carbon-Sulfur System Up to 2500 K (2227 °C), *Metallurgical and Materials Transactions B*, 47 (2016) 1817-1831.

## 요약 (국문 초록)

탄질화물, 붕화물 및 전이금속 전구체의 단일  
염소반응 공정을 통한 고기능성 이중원소 치환  
다공성 탄소소재 합성 및 응용과 열역학을 통한  
구조 제어 인자의 이해

하 대 권

재료공학부

공과대학 대학원

서울대학교

다공성 나노 탄소소재에 이중 원자를 치환하는 방법은 탄소소재의 표면 반응성을 특정 응용분야에 적합하게 극대화 시키는 대표적인 방법이다. 지난 수 십 년간, 질소를 비롯한 비 금속 원자들 및 전이 금속 원자들의 치환에 대한 연구가 여러 방면으로 진행되어 왔다. 그러나, 현재까지도 합성-구조-물성 관계의 종합적인 이해를 바탕으로 한 실용적인 이중 원자가 치환된 다공성 나노탄소소재의 합성법 개발에 대한 연구는 부족한 실정이다.

염화반응을 통한 탄화물에서 유도된 탄소소재 (CDC) 합성법은 다공성 나노탄소소재를 손쉽게 합성할 수 있는 대표적인 방법이다. 염소

기체 분자와 탄화물 구조 내에 금속 원자들 간의 선택적인 제거 반응을 통하여, CDC 소재에 수 nm 이내의 미세기공들을 다량으로 발달 시킬 수 있다. 또한, 정밀한 합성 조건 조절을 통하여 미세기공들을 옹스트롬 (Å) 단위로 조절하는 것이 가능하다. 이러한 장점들 때문에 CDC 방법을 통해 합성된 다공성 나노 탄소소재는 에너지 저장 분야에서 폭넓게 연구되었다. 그러나, CDC 소재를 합성하는 과정에서 불가피하게 염소와 같은 반응성 높은 부식성 화학물질을 사용하는 공정을 수반한다. 이 때문에, CDC 소재에 탄소 이외에 다른 이종 원자를 담지하는 것에 한계가 있어왔다. 본 연구 그룹을 포함한 몇몇 연구에서 탄화물이 아닌 탄질화물 및 붕화물의 염화반응을 통해 이종 원자가 치환된 다공성 나노 탄소소재를 합성하는 연구가 보고 되었지만, 이종원자의 치환량 및 종류에 한계가 있는 실정이다.

본 학위논문에서는 기존의 CDC 합성법의 한계를 넘어, 열역학 계산과 실험을 바탕으로 한 이종원자가 치환된 다공성 나노 탄소 소재 합성의 새로운 접근법을 제시하고자 한다. 평형 열역학 계산을 통하여 탄소소재 합성과정에서 이종 원자 치환에 핵심이 되는 공정인자들을 예측하고 이를 실험적으로 증명한다. 또한, 합성된 탄소 소재들의 전기화학반응 촉매제로의 응용가능성에 대하여 평가한다.

첫 번째 주제는 타이타늄 탄질화물과 붕화물 혼합물( $\text{Ti}(\text{C}_{1-x}\text{N}_x) - \text{TiB}_2$ )의 원-팟(one-pot) 염화반응을 이용한 다공성 나노 B-C-N 소재의 합성이다. 먼저, 다공성 나노 탄소소재의 구조 형성과정에서 붕소를 도입 시 붕소가 탄소소재의 구조와 표면특성 변화에 미치는

영향에 대해 논의하였다. 염화반응 과정에서 붕화물-탄질화물 계면 형성을 통해 붕소 원자들을 고상 확산을 통해 탄소 구조 형성 과정에 효과적으로 공급하였으며, 공급된 붕소 원자들이 탄소 구조 연결자 역할을 하여 질소 혹은 산소 원자들이 담지된 탄소층의 형성을 촉진하는 것을 실험적으로 규명하였다. 또한, 이러한 붕소 공급 방법을 통하여, 질소 혹은 산소가 원자 단위로 다량으로 다공성 탄소체들에 담지 할 수 있음을 보이고, 이 탄소체들이 높은 산소 환원 반응 촉매 활성도를 갖는 것을 규명하였다.

더 나아가,  $Ti(C_{1-x}N_x)-TiB_2$ 의 원-팟(one-pot) 염화반응을 통한, 나노의 크기의 질화붕소 상(h-BN)이 다량으로 담지된 다공성 나노 탄소소재의 합성법 개발에 대해 논의한다. 평형 열역학 계산을 통하여,  $Ti(C_{1-x}N_x)-TiB_2$ 의 염화 반응에서 핵심 반응식과 h-BN 상 담지에 적합한 합성 조건을 예측하였다. 이를 바탕으로 원-팟(one-pot) 염화 반응 합성법 설계하였다. 공급된 붕소의 탄소 구조 연결자 역할이 탄소 구조에 h-BN 상을 담지를 가능케 함을 규명하였다. 또한, 다량의 h-BN-탄소 층 계면 형성이 2전자 산소 환원 반응의 촉매 활성도를 향상시키는 핵심인자임을 규명하였다. 이를 이용하여, 대량 생산에 적합한 플로우 셀(flow cell) 환경에서 높은 과산화수소 생산효율을 갖는 h-BN 상이 나노 크기로 담지된 다공성 탄소 촉매 소재가 합성가능함을 보였다.

두 번째 주제에서는 타이타늄 탄질화물, 붕화물, 전이 금속을 포함한 전구체 혼합물( $Ti(C,N)-TiB_2-M(acac)_x$ )의 원-팟(one-pot)

염화 반응을 이용한 전이 금속이 원자 단위로 담지된 다공성 나노 Fe-CNB 소재의 합성에 대해 논의한다. 평형 열역학 계산과 나노 효과를 고려한 평형 열역학 상태도 계산을 통하여, 전이 금속을 포함한 전구체에 의해 형성된 전이 금속 기반 나노 입자에 공급된 붕소가 금속 기반 나노 입자의 녹는점의 변화를 유발함을 예측하였다. 또한, Fe-CNB 시스템과 Ni-CNB 시스템의 대조 실험을 통하여, 붕소의 도입을 통한 금속 기반 나노 입자의 녹는점 상승이 탄소 구조체 내에 전이 금속 원자를 원자 단위로 분산 시키는 핵심인자임을 규명하였다. 이를 통하여, 우수한 4전자 산소 환원 반응 활성도를 갖는 원자 단위로 분산된 Fe-CNB 촉매 소재를  $(\text{Ti}(\text{C},\text{N})-\text{TiB}_2-\text{M}(\text{acac})_x)$ 의 원-팟(one-pot) 염화 반응을 통해 합성가능함을 보였다.

마지막으로, 에틸렌 글라이콜-붕산-전이 금속 질산염의 원-팟(one-pot) 열분해를 통한 원자 단위로 분산된 M-CNB (M= Fe 와 Ni) 소재의 합성에 대해 논의한다. 평형 열역학 계산을 이용하여, 열분해 과정에서 분산이 액상의 산화 붕소 층으로 상변화하여 전이금속 기반 나노 입자의 형성을 억제 할 수 있음을 예측하였다. 또한, 붕산의 도입이 전이 금속을 질소와 붕소가 치환되어 있는 다공성 탄소 구조체에 원자 단위로 전이 금속을 분산 시킬 수 있는 핵심 요인임을 실험을 통하여 입증하였다. 이를 통하여, 전이 금속이 원자 단위로 분산된 Fe-CNB와 Ni-CNB 소재를 원-팟(one-pot) 열분해 방법을 통해 합성가능함을 보였으며, 이 소재들이 각각 우수한 산소 환원 반응 촉매 성능과 이산화탄소 환원 반응 촉매 성능을 나타냄을 확인하였다.



본 학위논문이 이중 원자가 치환된 고기능성 다공성 나노 탄소소재 합성법 개발에 새로운 관점을 제시하고, 다공성 나노 탄소소재의 활용가능성을 한층 높일 수 있을 것으로 기대한다.

---

**표제어:** 탄화물 유도 탄소, 염화 반응 공정, 열분해 공정, 붕소 및 질소 이중치환 다공성 탄소, M-N<sub>x</sub> 작용기 담지 다공성 탄소, 금속의 원자 단위 분산, 산소 환원 반응.

**학번:** 2013-20630

# Appendix

## 1.1. Structural analysis of raw $\text{Ti}(\text{C}_{1-x},\text{N}_x)\text{-TiB}_2$ powder

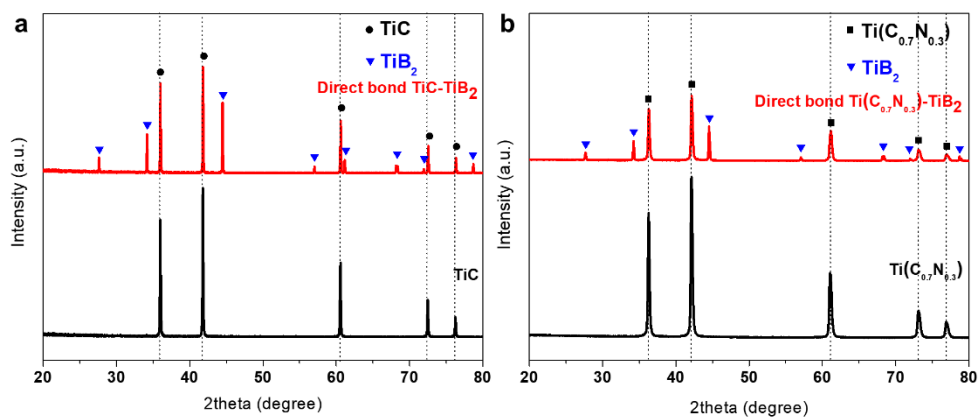


**Figure A.1.** XRD pattern of TiC and direct bond method  $\text{TiC-TiB}_2$  powders (a),  $\text{Ti}(\text{C}_{0.7},\text{N}_{0.3})$  and direct bond method  $\text{Ti}(\text{C}_{0.7},\text{N}_{0.3})\text{-TiB}_2$  powders (b).

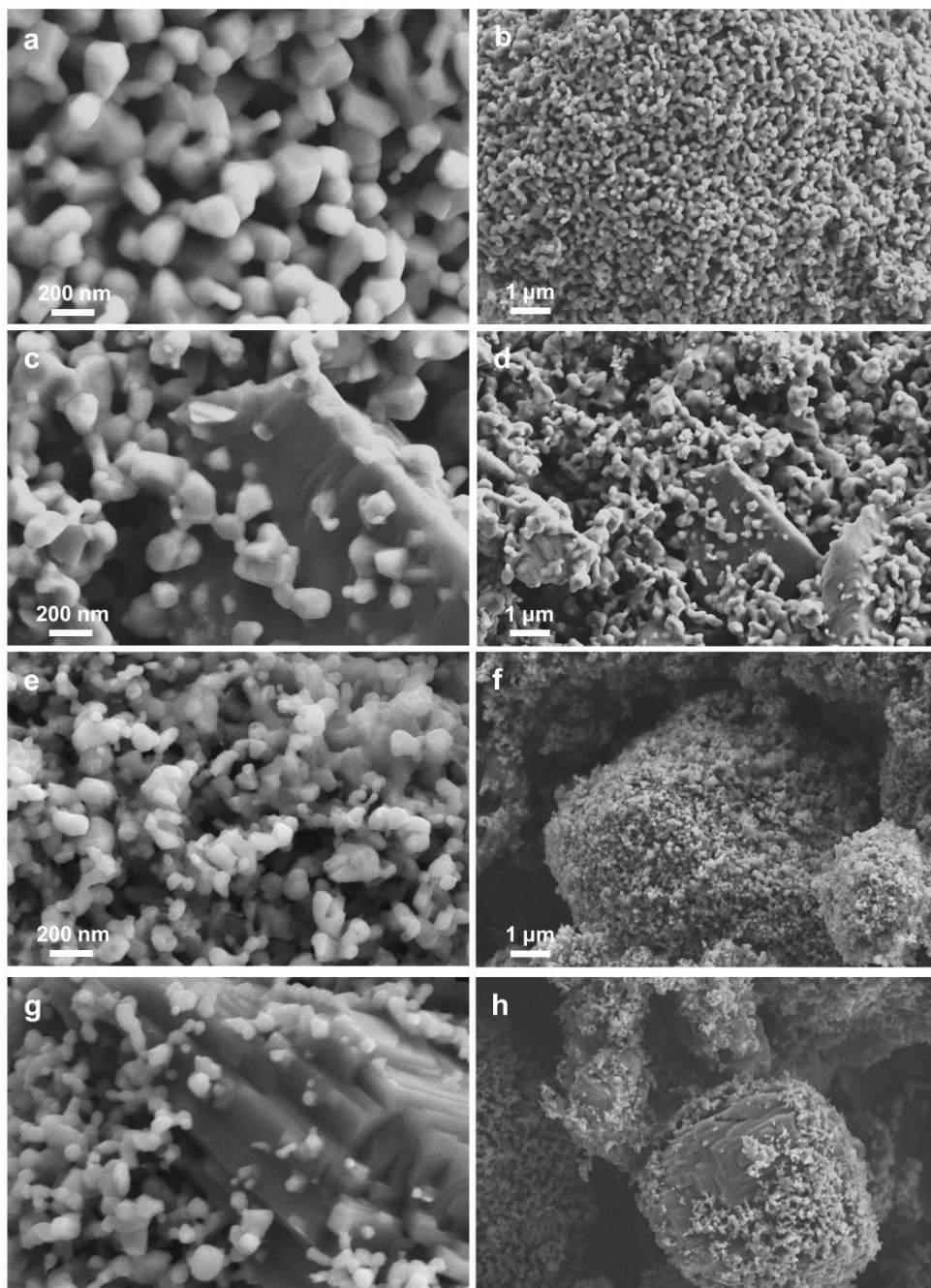


**Figure A.2.** FE-SEM image of TiC (a, b), direct bond method TiC-TiB<sub>2</sub> (c, d), Ti(C<sub>0.7</sub>N<sub>0.3</sub>) (e, f), and direct bond method Ti(C<sub>0.7</sub>N<sub>0.3</sub>)-TiB<sub>2</sub> (g, h).

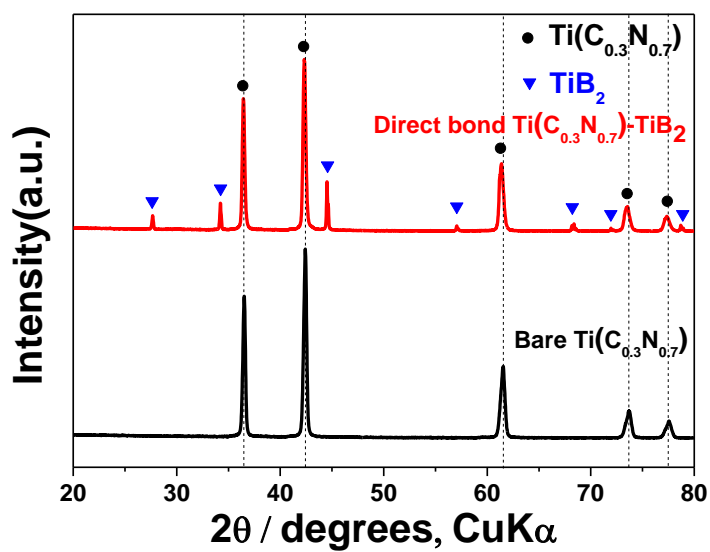


**Figure A.3.** XRD pattern of  $\text{Ti}(\text{C}_{0.3}\text{N}_{0.7})$  and direct bond method  $\text{Ti}(\text{C}_{0.3}\text{N}_{0.7})\text{-TiB}_2$  powders.

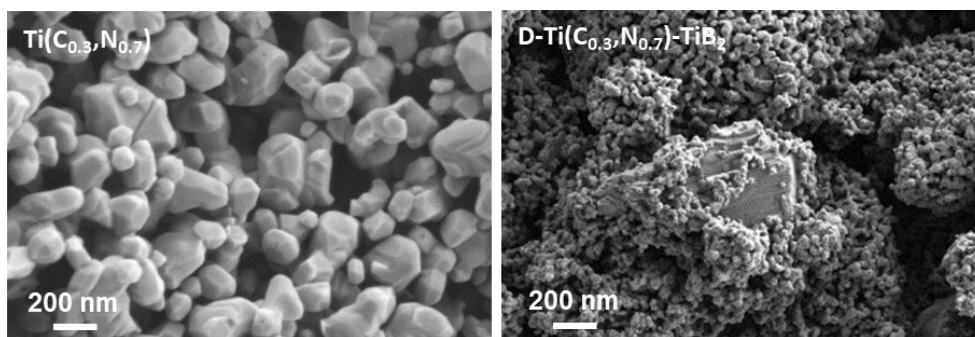


**Figure A.4.** FE-SEM image of  $\text{Ti}(\text{C}_{0.3}\text{N}_{0.7})$  (left), direct bond method  $\text{Ti}(\text{C}_{0.3}\text{N}_{0.7})\text{-TiB}_2$  (right).

## **1.2. Synthesis of BN embedded porous carbon via one-step chlorination process and its application for the H<sub>2</sub>O<sub>2</sub> production.**

### **1.2.1. Electrochemical properties of BNC in bulk scale**

To control the effect of the electric conductivity on the electrocatalytic activity of boron-nitride (BN) phases, we prepared the electrode with various ratio of BN sheet and carbon mixtures. The BN sheets were obtained urea-assisted exfoliation with ball milling method. The pristine h-BN was milled with urea powders, as NH<sub>2</sub> species from urea attached to BN during ball-milling can help the exfoliation to few-layer h-BN sheets. We blended these BN sheets and Vulcan carbon as a conducting agent with various ratios, and made the catalyst inks. The catalytic performance for ORR on 0.1 M KOH media was measured with RRDE setup with three-electrode system. We also measured a pure carbon electrode (non-BN sample, same carbon loading in the other BN/C cases). Although the carbon itself showed some activities in alkaline media, the onset potential and selectivity for H<sub>2</sub>O<sub>2</sub> production were enhanced increasing the content of BN sheets. The polarization curves suggest that ORR activity is quietly influenced by the amount of BN. However, the ORR activities were saturated and decreased at the high BN ratio (> 40%). It might reveal that the activity would be disturbed and hidden under the poor electronic conductivity properties. To investigate the effect of the electrical resistance (conductivity) of BN composites, we conducted the electrochemical impedance spectroscopy (EIS) with three-electrode cell which is same with the electrochemical ORR measurement. Recently, there were several efforts to characterization of the

electrode conductivity using complex capacitance plots or frequency dependent capacitance. Complex capacitance  $C(\omega)$  is defined as follows:

$$Z(\omega) = \frac{1}{j\omega C(\omega)}, \text{ where } Z(\omega) \text{ is impedance and } \omega \text{ is the frequency}$$

$$C(\omega) = C'(\omega) - j C''(\omega)$$

$$C'(\omega) = \frac{-Z''(\omega)}{\omega|Z(\omega)|^2}, \quad C''(\omega) = \frac{Z'(\omega)}{\omega|Z(\omega)|^2}$$

$C'(\omega)$  indicates the capacitance as a function of frequency, and  $C''(\omega)$  is related to the energy dissipation of the capacitor by an irreversible process, such as the irreversible faradaic charge transfer. We can estimate the electric conductivity with calculating the relaxation time constant ( $\tau_0$ ) from  $C''(\omega)$  plot.

$$\tau_0 = (2\pi f_0)^{-1}, \text{ where } f_0 \text{ is the peak frequency}$$

The relaxation time indicates the kinetic performance of the electrode structure. Our results showed that large time constants (small peak frequencies) were acquired as increasing the amount of BN sheets, as well as slower kinetics. That is, the kinetics were reduced by the amount of inactive BNs that is not in electrical contact with the conductive Vulcan carbon network. Also, as  $C'(\omega)$  detected at low frequency indicates to the static capacitance, the capacitance of BN sheet/carbon composites decreased as the carbon ratio was reduced. Our result reveals that the electrically activating BN phases in B-C-N materials is the most critical point to apply these materials as electrocatalysts. Thus, we made various B-C-N carbonaceous materials with various configurations through effective CDC method.

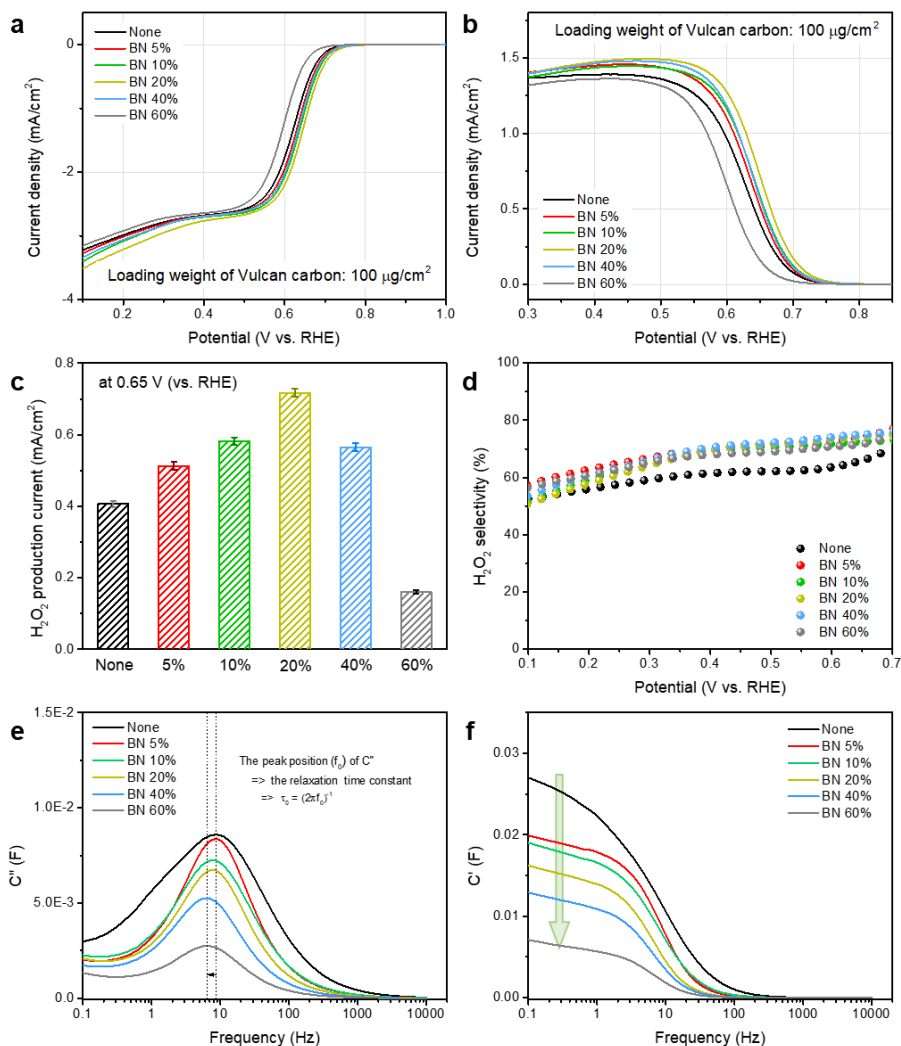


**Figure A.5.** Polarization curves (a) and simultaneous  $\text{H}_2\text{O}_2$  detection current at the ring electrode (b) at 1600 rpm with BNCs in bulk scale.  $\text{H}_2\text{O}_2$  production current of samples at 0.65 V (c) and calculated selectivity (d) of samples. Imaginary capacitances (e) and real capacitances (f) plot for the complex capacitance analysis of samples from EIS measurement.

### 1.2.2. Demonstration of the novelty of synthesis of D-BNC through the controlled experiments.

The importance of the proximity between carbon, nitrogen and boron source is very obvious by comparison of D-BNCs with the control. The control denoted as G-BNC is produced by the gas-transport method. In the process of synthesizing G-BNC,  $\text{TiB}_2$  is physically separated with  $\text{Ti}(\text{C}_{0.3}\text{N}_{0.7})$  thus only  $\text{BCl}_3(\text{g})$  served as a source of boron supplied to CN during the chlorination of  $\text{Ti}(\text{C}_{0.3}\text{N}_{0.7})\text{-TiB}_2$ . In Figure 6,7 and Table 1 the process yield and the content of boron, carbon, and nitrogen of BNCs are compared (the contents are measured by XPS analysis). The yield of G- BNC is extremely lower than D- BNC in entire chlorination temperature (600, 700, and 800 °C) and raw powder mixture ratio range (C:B molar ratio, from 1:1 to 1:4), unsuitable for the mass production. To make matters worse, comparing the BNC (14)-700 and 800 samples that excess boron precursor is added, the carbon content of G-BNC(14)-700 and 800 are very low while that of boron and nitrogen is too high. On the other hand, D-BNC(14)-700 and 800 have the high carbon content along with the high boron and nitrogen content. These results demonstrate that G-BNC(14)-700 and 800 are predominant with carbon-doped BN whereas D-BNC(14)-700 and 800 are prevailed with BN-doped carbon due to the extreme carbon loss. This discrepancy is obvious in the optical image of G-BNC(14)s and D-BNC(14)s (Figure 7). These disparities in yield and phase are due to the difference in the role of boron. In G-GNB, boron originated from  $\text{BCl}_3(\text{g})$  only serves as the BN source. BN phase formation dominantly occurred from the exterior of CN. Thus,  $\text{BCl}_3(\text{g})$  facilitates the premature outflow of nitrogen before the carbon shell formation in CN, which causes



the collapse and decomposition of the entire CN structure resulting in a catastrophic carbon and nitrogen loss. Thus, only a small amount of carbon-doped BN phase remains as a residual in BNC(14)s (excess boron precursor added) while nothing left at all in BNC(44)s (adequate boron precursor added) since BN phase formed during the chlorination is easily decomposed by the chlorine gas. The difference in the morphology of the D-BNC(44) and G-BNC(44) synthesized in the early stage of chlorination (10 min) at 800 °C shown in Figure 8 further demonstrates the difference in the formation mechanism between D-CNB and G-CNB. The TEM image of D-CNB clearly shows the formation of the shell that retains the shape of raw  $\text{Ti}(\text{C}_{0.3}\text{N}_{0.7})$  particle despite the loss of interior. In contrast, the G-CNB particle has been tearing apart without the formation of the shell. Taken together, how to supply  $\text{TiB}_2$  (boron source) to CN is a major parameter to produce CNB via chlorination and supplying boron atoms directly to CN by the direct-bond method is key to synthesize CNB that h-BN domain embedded in the porous carbon matrix.

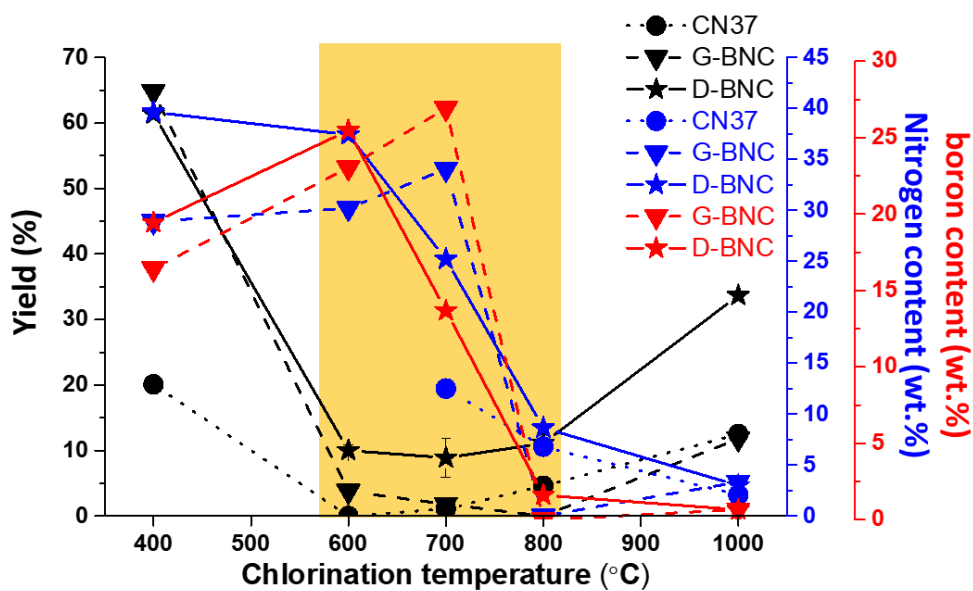


**Figure A.6.** The yield and chemical composition of BNCs measured by XPS.

**Table A.1.** The yield and chemical composition of BNCs measured by XPS.

<b>Sample</b>	<b>Yield (%, C+N)</b>	<b>C (wt.%)</b>	<b>N (wt.%)</b>	<b>B (wt.%)</b>	<b>O (wt.%)</b>
CN37-400	20.1				
G-BNC-400	64.8	24.4	28.9	16.4	30.3
D-BNC-400	61.4	23.6	39.6	19.4	17.3
CN37-600	0.0	-	-	-	-
G-BNC-600	3.8	24.7	30.2	23.0	22.1
D-BNC-600	10	24.2	37.4	25.5	12.9
CN37-700	0.0	-	-	-	-
G-BNC-700	1.8	15.9	34.1	26.9	23.2
D-BNC-700	8.9	55.8	25.2	13.7	5.3
CN37-800	4.6	89.5	6.8	-	3.7
G-BNC-800	0.6	88.7	7.1	0.3	4.0
D-BNC-800	11.1	84.2	8.7	1.6	2.2
CN37-1000	12.5	95.9	2.1	-	2.1
G-BNC-1000	11.8	94.2	3.3	0.7	1.8
D-BNC-1000	33.7	94.7	3.0	0.7	1.6

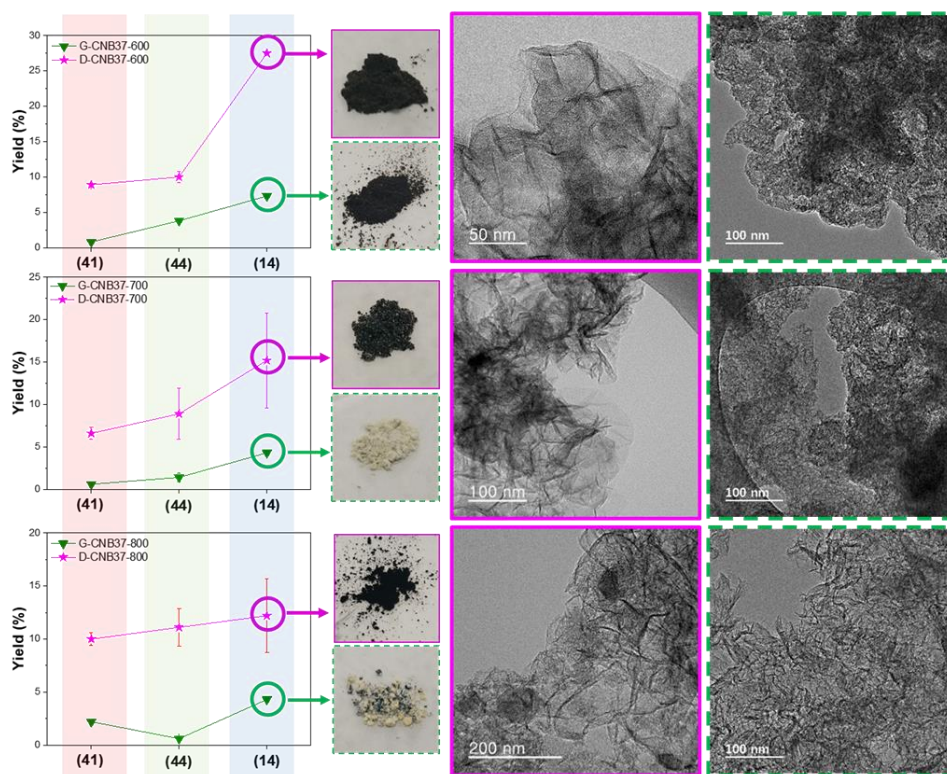


**Figure A.7.** The comparison of the yield, appearance, and morphology of D-BNCs and G-BNCs (control samples).

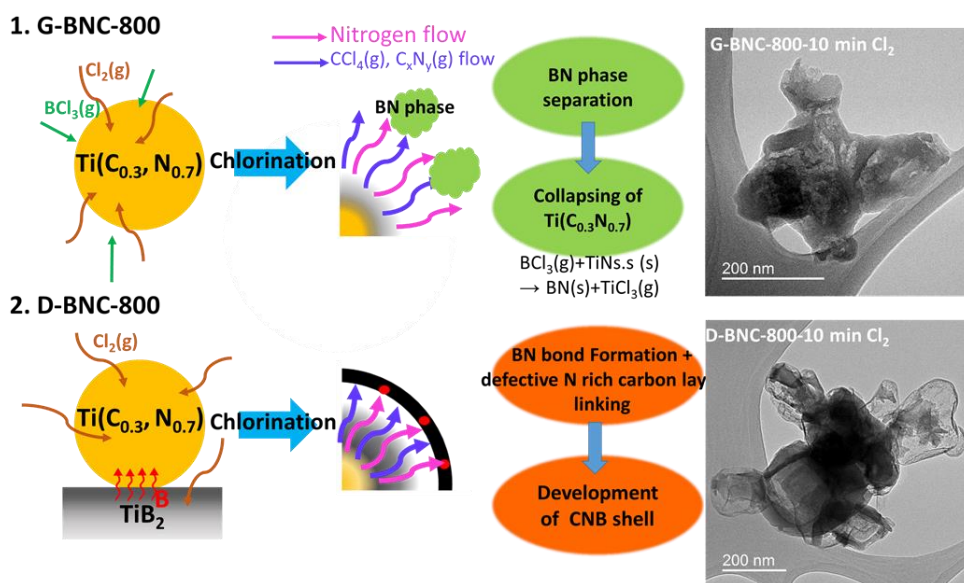


**Figure A.8.** The comparison of formation mechanism of G-BNC-800 and D-BNC-800.

## 2. Demonstration to other M-CNB system (Co-CNB)

Not just limited to Fe- and Ni-CNB, we try to extend our understanding of the influence of boron in the synthesis of M-CNB to another metal type system. For example, in the case of the Co-CNB system, comparing the Co-C binary phase diagram and Co<sub>2</sub>B-C pseudo-binary phase diagram (Figure A.9), the eutectic temperature of Co<sub>2</sub>B-C is slightly decreased (1310 °C → 1270 °C) along with a decrease in carbon composition of the eutectic point. Hence, it is presumed that the introduction of boron in Co-CN enhances the graphitization of Co-CN unfavorable for improving the electrocatalytic performance, which is proved by the experiment. The TEM images of Co-CN and Co-CNB shown in Figure A.10 demonstrate that the partially ordered carbon layer is detected in Co-CN and Co-CNB. Also, the XRD patterns of Co-CN and Co-CNB (Figure A.12a) show that sharp (002) peak along with broad peak centered at 26.5° appeared in Co-CNB, more prominent than Co-CN. This indicates that the tendency for partially ordering of carbon is intensified due to the introduction of boron. In line with the result of TEM and XRD analysis, the variation of pore texture (Table A.2 and Figure A.11) also illustrates that the micropore and small mesopore (<5 nm) presented the significant decline accompanying decrease in BET specific surface area, one of the indicators showing the intensification of graphitization of Co-CNB. The fourier transform extended X-ray adsorption fine structure (FT-EXAFS) spectrometry analysis further supports the enhancement of carbon ordering effect attributed by the addition of boron in Co-CNB, as shown in Figure A.12b. The FT-EXAFS spectra of Co-CN has one major peak (1.87 Å) probably corresponded to the combination of Co-Co coordination in

Co metal (2.20 Å) and Co-Co coordination (1.75 Å) in Co<sub>2</sub>C. Also, it has the one minor peak (1.24 Å) assigning to Co-C coordination in Co<sub>2</sub>C.<sup>49</sup> These two peaks indicate the coexistent of Co metal clusters and Co<sub>2</sub>C. Co<sub>2</sub>C was a metastable phase formed at Co-C interface, where the graphitization occurs.<sup>19</sup> On the other hand, in Co-CNB, Co metal-related pick disappears and only Co<sub>2</sub>C related peaks are dominant. The spectra of Co-CNB has one major peak at 1.75 Å only composed of Co-Co coordination in Co<sub>2</sub>C along with one minor peak at 1.2 Å. These results demonstrate that the addition of boron facilitate the interaction between Co-based nanoparticle and C, corresponding to the acceleration of surface melting attributed to the cobalt boride nanoparticle formation that intensifies the graphitization of Co-CNB. Therefore, the introduction of boron in Co-CNB barely promotes the ORR activity in the alkaline medium compared with Co-CN, as displayed in Figure A.13.

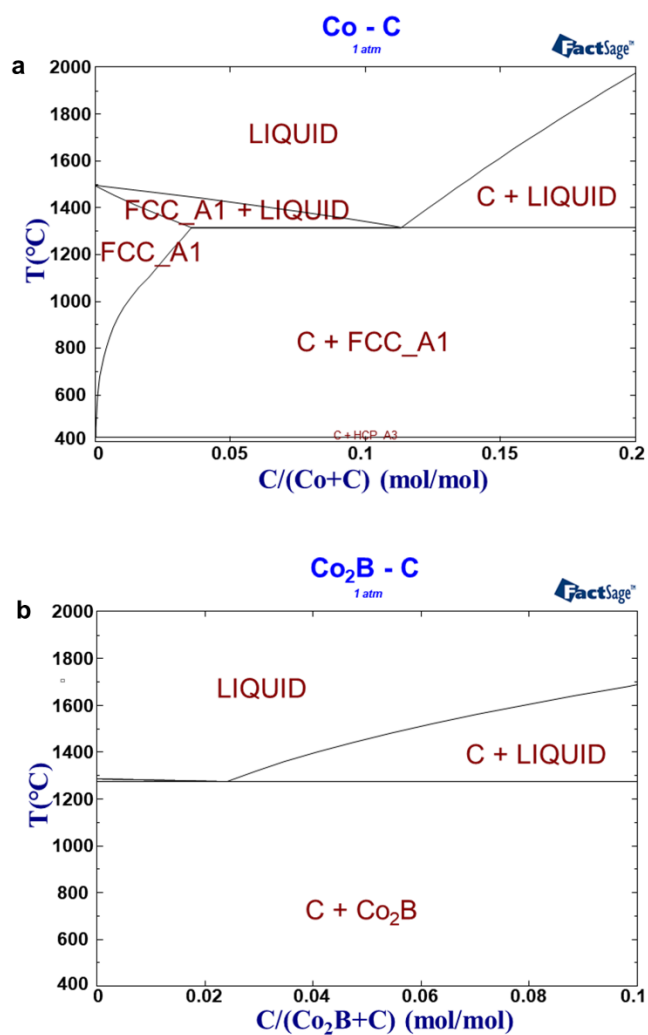


**Figure A.9.** (a) Binary phase diagram of Co-C system and (b) Pseudo-binary phase diagram of  $\text{Co}_2\text{B}$ -C.

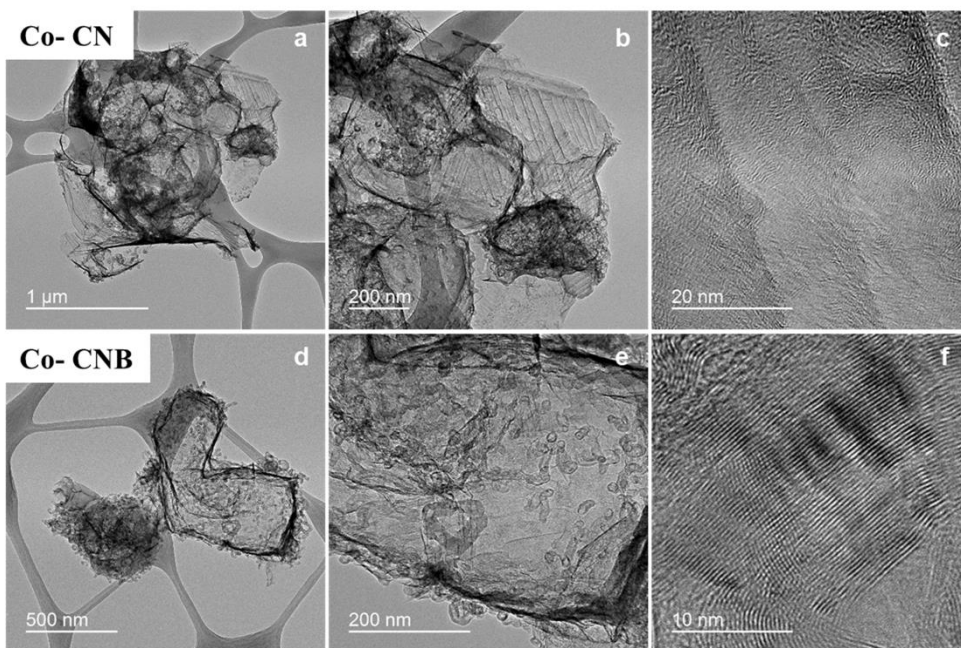


**Figure A.10.** TEM image of (a-c) Co-CN55-800 and (d-f) Co-CNB55-800.

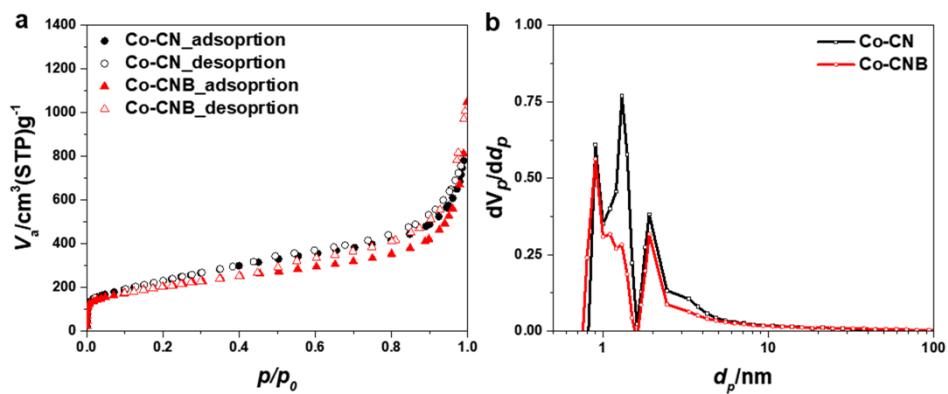


**Figure A.11.** (a)  $N_2$  sorption isotherm of Co-CN and Co-CNB. (b) The pore size distribution (PSD) of Co-CN and Co-CNB.



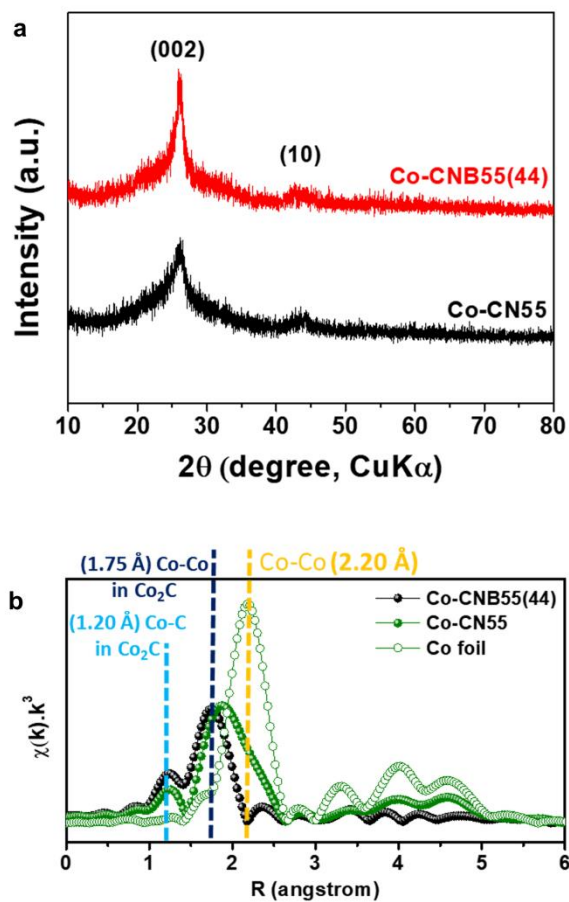


**Figure A.12.** (a) XRD patterns of Co-CN and Co-CNB. (b) RDFs of FT  $k^3$ -weighted Co K-edge EXAFS spectra of Co-CN and Co-CNB. (c) ORR activity comparison between Co-CN and Co-CNB in 0.1 M KOH. The measurements were conducted with the electrode rotation of 1600 rpm.

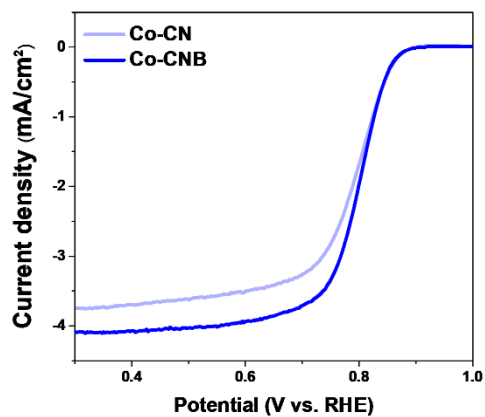


**Figure A.13.** ORR activity comparison between Co-CN and Co-CNB in 0.1 M KOH.

The measurements were conducted with the electrode rotation of 1600 rpm.

**Table A.2.** BET specific surface area and pore volumes of Co-CN and Co-CNB.

	SSA (m <sup>2</sup> /g)	Micropore volume (cm <sup>3</sup> /g)	Mesopore volume (cm <sup>3</sup> /g)	Total pore volume (cm <sup>3</sup> /g)
Co-CN	840	0.29	0.46	1.20
Co-CNB	720	0.27	0.39	1.29

### 3. Optimization of Fe-CNB(20)

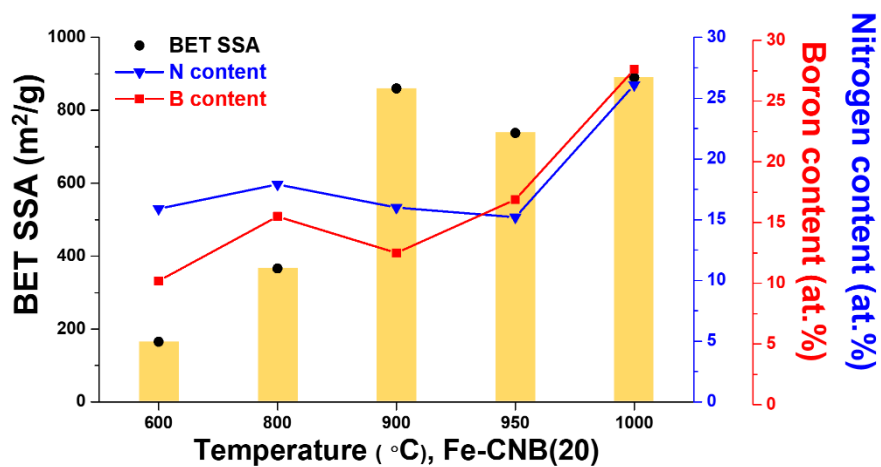


**Figure A.14.** BET surface area, nitrogen content, and boron content of Fe-CNB(20)s with pyrolysis temperature.

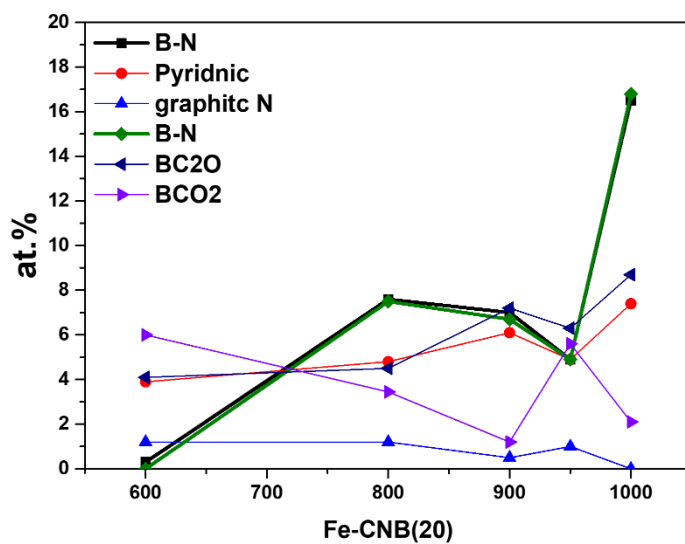


**Figure A.15.** Variation of Functional groups in Fe-CNB(20)s with pyrolysis temperature.